https://doi.org/10.15388/vu.thesis.464
https://orcid.org/0000-0001-7106-5328

VILNIUS UNIVERSITY
CENTER FOR PHYSICAL SCIENCES AND TECHNOLOGY

Rokas Gegevičius

Charge Carrier Transport in Hybrid Perovskites

DOCTORAL DISSERTATION

Natural Sciences,
Physics (N 002)

VILNIUS, 2023

The dissertation was prepared between 2018 and 2022 (at the Center for Physical Sciences and Technology). The research was supported by Research Council of Lithuania, with scholarships that were granted for academic accomplishments three times: 2018, 2019, 2021.

Academic supervisor – Dr. Marius Franckevičius (Center for Physical Sciences and Technology, Natural Sciences, Physics, N 002).

This doctoral dissertation will be defended in a public meeting of the Dissertation Defence Panel:

Chairman – Prof. Dr. Ramūnas Aleksiejūnas (Vilnius University, Natural Sciences, Physics, N 002).
Members:
Prof. Habil. Dr. Dariusz Hreniak (Institute of Low Temperature and Structure Research, Poland, Natural Sciences, Physics, N 002),
Dr. Sergėjus Balčiūnas (Vilnius University, Natural Sciences, Physics, N 002),
Dr. Rokas Kondrotas (Center for Physical Sciences and Technology, Natural Sciences, Chemistry, N 003),
Dr. Artiom Magomedov (Kaunas University of Technology, Natural Sciences, Chemistry, N 003).

The dissertation shall be defended at a public meeting of the Dissertation Defence Panel at 10:00 on May 31, 2023 in Conference Hall A101 of the National Center for Physical Sciences and Technology.
Address: Saulėtekio av. 3, Vilnius, Lithuania.
Tel. +370 5 264 8884; e-mail: office@ftmc.lt

The text of this dissertation can be accessed at the libraries of Center for Physical Sciences and Technology and Vilnius University, as well as on the website of Vilnius University:
www.vu.lt/lt/naujienos/ivykiu-kalendorius

https://doi.org/10.15388/vu.thesis.464
https://orcid.org/0000-0001-7106-5328

VILNIAUS UNIVERSITETAS
FIZINIŲ IR TECHNOLOGIJOS MOKSLŲ CENTRAS

Rokas Gegevičius

Krūvininkų pernaša hibridiniuose perovskituose

DAKTARO DISERTACIJA

Gamtos mokslai,
Fizika (N 002)

VILNIUS, 2023

Disertacija rengta 2018–2022 metais Fizinių ir technologijos mokslų centre.
Mokslinius tyrimus rėmė Lietuvos mokslo taryba skirdama stipendijas 2018, 2019, 2021 metais už akademinius pasiekimus.

Mokslinis vadovas – dr. Marius Franckevičius (Fizinių ir technologijos mokslų centras, gamtos mokslai, fizika, N 002).

Gynimo taryba:
Pirmininkas – prof. dr. Ramūnas Aleksiejūnas (Vilniaus universitetas, gamtos mokslai, fizika, N 002).
Nariai :
prof. habil. dr. Dariusz Hreniak (Žemų temperatūrų ir struktūrinių tyrimų institutas, Lenkija, gamtos mokslai, fizika, N 002),
dr. Sergėjus Balčiūnas (Vilniaus universitetas, gamtos mokslai, fizika, N 002),
dr. Rokas Kondrotas (Fizinių ir technologijos mokslų centras, gamtos mokslai, chemija, N 003),
dr. Artiom Magomedov (Kauno technologijos universitetas, gamtos mokslai, chemija, N 003).

Disertacija ginama viešame Gynimo tarybos posėdyje 2023 m. gegužės mėn. 31 d. 10:00 val. Nacionalinio fizinių ir technologijos mokslų centro A101 konferencijų salėje. Adresas: Saulėtekio al. 3, Vilnius, Lietuva,
tel. +370 5 264 8884; el. paštas: office@ftmc.lt

Disertaciją galima peržiūrėti Fizinių ir technologijos mokslų centro ir Vilniaus universiteto bibliotekose bei VU interneto svetainėje adresu:
https://www.vu.lt/naujienos/ivykiu-kalendorius

Contents

1 Introduction

> Simplicity is a great virtue but it requires hard work to achieve it and education to appreciate it. And to make matters worse: complexity sells better.
>
> Edsger Wybe Dijkstra

Perovskite is a calcium titanate $CaTiO_3$ mineral. It was discovered in 1839 by the German mineralogist Gustav Rose in the Ural Mountains and named after mineralogist Count Lev Alekseyevich von Perovski. Natural crystals have a hardness of 5.5–6 and a density from 3.98 to 4.26 g/cm^3. Due to impurities, they are usually dark brown to black, but when pure, they are clear and have a refractive index of about 2.38. The term perovskite now refers to a broad class of materials that have the same type of structure as $CaTiO_3$ and have the general formula ABX_3. Currently, many hundreds of compounds are known to have the perovskite structure. In fact, one mineral with perovskite structure, bridgmanite $(Fe, Mg)SiO_3$, is the most common solid phase in the Earth's interior, accounting for 38 % of the total mass. The phase occurs at depths of 660–2900 km, but is stable only at high temperatures and pressures and therefore does not occur at the Earth's surface. In the 1940s, the importance of perovskites was highlighted by the discovery of the dielectric and ferroelectric properties of barium titanate, $BaTiO_3$. This material was quickly used not only in electronics as capacitors and electromechanical transducers or in nonlinear optics, but also in medicine as nanocarrier for drug delivery. In the following decades, attempts to improve the material properties of $BaTiO_3$ led

to intensive research into the structure-property relationships of a large number of nominally ionic ceramic perovskite-related phases with the overall composition ABO_3, with the result that a large number of new phases were synthesized. It was soon recognized that these materials as a group have very useful physical and chemical properties far beyond those of $BaTiO_3$, and research was extended to a number of structures and phases, all of which may be structurally related to the perovskite family.

One of the most interesting branches developed during this period is hybrid perovskites, which combine a metal-halide framework with a small organic cation. First synthesized and structurally described by Dieter Weber in 1978,[1] later variants were investigated in the 1990s and early 2000s for use in organic electronic devices such as light-emitting diodes[2] and field-effect transistors.[3] However, the particularly intriguing properties of these materials did not emerge until metal halide perovskites were used as absorber materials. In 2009, methylammonium lead iodide ($MAPbI_3$) became the first perovskite to be used in a dye-sensitized solar cell (DSSC), achieving an efficiency of 3.8 %.[4] Four years later, the efficiency increased to 15 %[5] and became the fastest developing solar technology in the field. Since then, improvements in light management, charge carrier transport, and structural composition have enabled the production of solar cells with certified efficiencies above 25 %,[6] one step closer to the predicted theoretical limit of 31 %.[7] These results already surpass current records for CdTe solar cells, the second technology on the market. Metal halide perovskites have subsequently also been used with great success in photodetectors, both visible[8] and X-ray,[9] and LEDs,[10] with these devices now exhibiting remarkable responsivities and high external quantum efficiencies.

The radical change in perspective associated with hybrid perovskites was driven primarily by their remarkable properties, such as low carrier recombination rates which are responsible for the impressive diffusion lengths, tunable bandgaps, and large optical absorption coefficients typically associated with traditional crystalline semiconductors.[11] At the same time, hybrid perovskites exhibit remarkable tolerance to crystalline defects and can be processed directly from solution in a manner

similar to organic devices. However, the added advantages of quasi-organic properties and their ionic nature come at a price. They have the same problems with device stability and short operating times.[12]

1.1 The Aim of the Thesis

In recent years, knowledge of the fundamental processes in hybrid perovskite materials has greatly increased. However, many aspects of charge carrier transport are still poorly understood and require further investigation. These include charge carrier generation, extraction, and recombination. Another important topic that is not yet sufficiently understood is the influence of ionic motion on charge carrier dynamics. This knowledge is crucial to fully understand the operation of hybrid perovskites and to further improve the performance and stability of perovskite devices. Therefore, this work was carried out with the aim of investigating charge carrier dynamics in various hybrid perovskites with different device architectures and identifying mechanisms linking ion migration to charge carrier extraction, recombination, and their trapping and mobility parameters.

1.2 Task of the Research Work

- To implement and apply experimental technique for measuring transient electroluminescence in hybrid perovskite optoelectronic devices.
- To relate and understand charge carrier dynamics in the context of transient electroluminescence kinetics in hybrid perovskites optoelectronic devices.
- To implement, improve and apply transient electro-optical measurement techniques that allow direct tracking of ion motion in hybrid perovskites.
- To trace and identify the extraction, recombination, and trapping of photogenerated charge carriers and explain the influence of ion motion on charge carrier transport in hybrid perovskites.

1.3 Statements of the Thesis

1. The accumulation of charge carriers in the perovskite layer under forward voltage causes the electroluminescence overshoot effect, while the ion redistribution induced by the electric field minimizes the accumulation of charge carriers and the overshoot effect in perovskite solar cells.

2. An unfavorable space charge distribution leads to a roll-off of the external quantum efficiency in hybrid perovskite light-emitting diodes, which can be avoided by a balanced injection current.

3. Electric field-induced redistribution of ions of a single type in the perovskite layer causes complex multiphase dynamics of electroluminescence and current in $MAPbI_3$ perovskite light emitting diodes.

4. Electric field-induced luminescence quenching in $MAPbI_3$ perovskites is determined by the direct effect of the electric field on the charge carrier distributions and the influence on the spatial redistribution of ions in the perovskite layer.

5. There are potential barriers to lateral carrier movement in the polycrystalline hybrid perovskite films that affect carrier mobility, diffusion and recombination rates.

1.4 Novelty and Relevance

- The developed transient electroluminescence spectroscopy proved to be very sensitive to ion accumulation and its spatial distribution and is a powerful tool to study ion dynamics and related electronic processes in hybrid perovskite solar cells and LEDs.

- The measurement technique, which uses different electrical pulses and their duration, was developed to study the current-induced stressing effect in per-

ovskite LEDs. It allows to follow the stress-induced changes of various parameters over time.

- The electroluminescence overshoot effect in hybrid perovskite solar cells was discovered.
- Mobile negative ions were found to play a dominant role in the complex dynamics of electroluminescence and current occurring during the operation of $MAPbI_3$ PeLEDs.
- A developed modification of the conventional time-delayed collection field measurement technique was found to be effective for measuring the energy barriers to charge carrier motion in polycrystalline hybrid perovskite films.

1.5 Layout of the Thesis

This dissertation is a collection of scientific papers prepared during the doctoral studies at Vilnius University/Center for Physical Sciences and Technology. After the introduction, Chapter 2 presents the basic concepts of optoelectronic properties and modern investigation techniques from the current literature in the field of hybrid perovskites. Chapter 3 discusses the experimental methods and investigation details used in this thesis. Chapter 4 discusses new findings on charge carrier transport of hybrid perovskites and presents their results. Chapter 5 summarises the main conclusions from all the articles presented in this thesis.

1.6 Contribution of Author

The author realized all newly presented implementations of measurement techniques for hybrid perovskites. He performed all time-resolved spectroscopic experiments, processed and analyzed the obtained data. The author participated in the discussions and preparation of all presented manuscripts. The PeLEDs studied in

this work were fabricated by Karim Elkhoully from Paul Hereman's group at Interuniversity Microelectronics Centre (IMEC) Belgium. The perovskite solar cells were fabricated at École polytechnique fédérale de Lausanne (EPFL) Switzerland and the hybrid perovskite samples on an interdigitated comb of electrodes were fabricated by the author.

2 Literature Overview

2.1 Chemical Structure

2.1.1 Crystal Structure

The Hybrid Organic-Inorganic Perovskite (HOIP) crystal structure has the stoichiometric formula ABX_3 and is characterized by $[BX_6]^{4-}$ octahedra that share common corners in all three orthogonal directions and form infinite three-dimensional (3D) $[BX_3]$ frameworks. The A-side cations occupy the cavities between them and serve as a structural template (Figure 2.1). Their shape, size, and charge distribution play an important role in stabilizing the perovskite structure. The ions in the ABX_3 structure obey size constraints defined by the Goldschmidt tolerance factor[13]

$$t = \frac{(r_A + r_X)}{\sqrt{2}(r_B + r_X)} \tag{2.1}$$

where r_A, r_B and r_X are the ionic radii of the respective ions. The idealized structure (ideal cubic perovskite) can form when t is close to one. In this case, the structure consists of BX_6 octahedra distributed over the corners and A cations occupying the voids between them. When t depart from one, perovskite motifs with edge- and face-sharing octahedra can form over the corner-sharing structure.[14] Unlike perovskite oxides, $A^+B^{2+}X_3^-$ compounds are much rarer in nature and can only be formed with certain combinations of elements. This is because the halide anions (X = Cl, Br, I) have two major differences compared to the O^{2-} anions: first of all, they carry a lower negative charge, which is only sufficient to compensate for metal ions

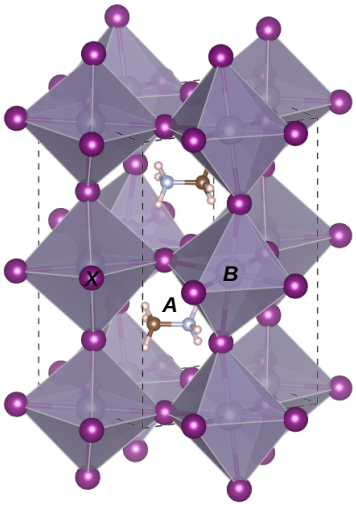

Figure 2.1: Orthorhombic perovskite crystal structure ABX_3. Organic cations A occupies the cavities, metallic cations B lies at the octahedral centres, and the halogens X forms the corners of the BX_6 octahedra.

in lower oxidation states, and second they have a much larger ionic radius, which precludes the incorporation of small metal ions into the octahedral coordination geometry. Because of these limitations, the metal anion M^{2+} can only be selected from a small group of elements, including the alkaline earths, the divalent rare earths (Ca^{2+}, Eu^{2+}, Yb^{2+}), and the heavier group 14 elements (Ge^{2+} , Sn^{2+} , Pb^{2+}).[15–17] Surprisingly, there are no transition metals that can adopt the halide perovskite structure, with a few notable exceptions.[18] Only a few A cations known so far are able to stabilize the perovskite structure in heavy halides. Thus, the 3D structure is predicted to be stable when the tolerance factor is between 0.8 and 1.0, and this condition is only true for cesium - (Cs^+), methylammonium - (MA^+), hydroxylammonium - (NH_3OH^+), hydrazinium - ($NH_2NH_3^+$), azetidinium - ($(CH_2)_3NH_2^+$), formamidinium - (FA^+) and imidazolium - ($C_3N_2H_5^+$) cations.[19] But the actual sit-

uation is even more complicated. It has been shown that only Cs^+ is large enough to obtain the perovskite, and for organic cations it seems that not only the size is important, but also the distribution of the net positive charge. Thus, MA^+ and FA^+ and are able to stabilize the perovskite, but cations of similar size such as $HONH_3^+$, $CH_3CH_2NH_3^+$, or $(CH_3)_2NH_2^+$ are not and stabilize a different structure. When the cation is too small, the preferred structure is the NH_4CdCl_3 type, which can be described as double chains of $[BI_5]^{3-}$. When the cation is too large, the preferred structure is the $CsNiBr_3$ type, which consists of single chains of face-dividing octahedra. On the other hand, too large densely packed cations can lead to perovskite-like structures, although with a lower dimensionality.[20,21]

2.1.2 Bonding and Different Phases

The flexible nature of the perovskite framework, due to the double bridging halide ion (B – X bond), gives perovskites another characteristic feature: phase transitions. Perovskites undergo a series of structural changes when external stimuli (temperature, pressure, etc.) act on them, starting from the ideal basic cubic structure in which all B – X – B angles are 180° (space group 221). This ideal structure responds to changes in temperature or pressure by forcing the $[BX_6]$ octahedra to tilt about one or more of their axes of symmetry, reducing the symmetry in a way that depends on the properties of the particular compound. Tilting does not change the overall 3D architecture, but can reduce the B – X – B angle from an ideal 180° to as low as 150°, below which the structure type changes or becomes amorphous (Figure 2.2a). One reason for the structural changes is that the molecular cation has a dipole moment and lower symmetry than the ideal $[BX_6]$ octahedra. In addition, the molecules in the neighbourhood can align differently on different length scales, leading to symmetry breaking even when the Goldschmidt tolerance factor t is close to one. This leads to a large structural diversity accessible at a given temperature and can be associated with a complex bonding profile manifested in HOIPs.[23,24] The cohesive energy (for which ionic bonding is an important driving force) of HOIPs is much lower than that of perovskite oxides. This is reflected in the electronic struc-

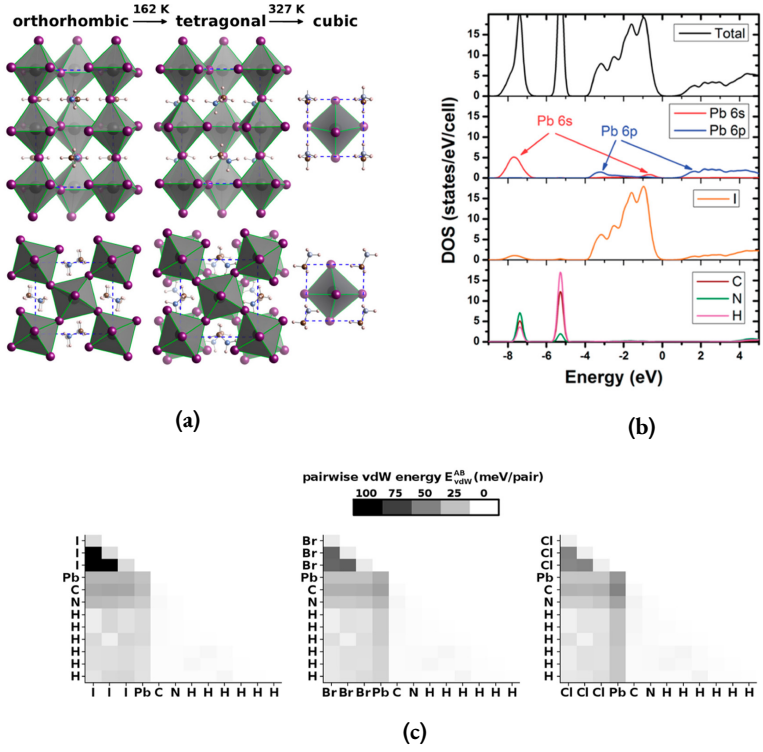

Figure 2.2: (a) Schematic representation of methylammonium lead iodide ($MAPbI_3$) and its crystal structures at different temperatures. Upper (lower) panels show side (top) views. Dashed lines represent unit cell boundaries. (b) Total and projected density of states of tetragonal $MAPbI_3$, showing orbital-specific contributions. (c) Graphical summary of pairwise dispersive energies, E^{AB}_{vdW}, between atomic sites A and B in the unit cell of $MAPbI_3$ (left panel), $MAPbBr_3$ (center panel), and $MAPbCl_3$ (right panel). Reproduced with permission from ref. [22] Copyright 2015 American Chemical Society.

ture of $MAPbI_3$ (Figure 2.2b),[25] which is characterized by an iodide valence band and a lead conduction band.[25,26] The oxidation state of X is lower (−1) in halide perovskites than in oxides (−2) and the Madelung potential is much less binding. This can be associated with a large structural diversity of HOIPs. Also in HOIPs, for example $MAPbI_3$ Pb and I interact covalently as well through the interaction

of the 6 s electrons of the lone pair of Pb with the 5 p electrons of I, which contribute to the top of the valence band (Figure 2.2b).[25,26] Moreover, because the halogen atoms in HOIPs have a large polarization ability, they can support significant dispersive interactions. Therefore, weak interactions such as van der Waals and hydrogen bonding supported by the organic cation atoms also play an important role in the structure of HOIPs. The importance of van der Waals interactions between the inorganic atoms, and hydrogen bonds between the organic species and the inorganic octahedra, has been demonstrated in the first-principles calculations. (Figure 2.2c).[27,28] Important contributions of the organic cation to the perovskite band structure are found only a few eV below the valence band maximum (Figure 2.2b),[25,26] i.e., besides the hydrogen bonding, there is no hybridization between the organic and inorganic parts of the HOIPs. Instead, the molecule acts as a sufficiently large framework for the formation of lead halide perovskites at room temperature. The large size of MA is important because the similar inorganic $CsPbI_3$ perovskite has the angular NH_4CdCl_3 structure at room temperature instead of the cubic perovskite structure, with a significantly different electronic structure that is less favorable for photovoltaics.[29] It is already clear that the chemical bonds in HOIPs are not rigid. In fact, the lattice constants of the ideal cubic $MAPbX_3$ are 5.7 Å–6.3 Å, much higher than the 3.8 Å–4.2 Å for common oxide perovskites.[30] Moreover, the experimental and theoretical Young and bulk moduli of various HOIPs[31] are in the range of 10 GPa–25 GPa, i.e., at least several tens of GPa lower than the values for typical oxide perovskites or inorganic semiconductors. This means that HOIPs readily accept changes in their equilibrium bond lengths and offer great conformational freedom compared to other semiconductors with similar electronic properties. The rich structural diversity combined with the material flexibility of HOIPs can lead to the presence of locally distinct phases in HOIP films and surfaces. Density functional theory calculations (DFT) have shown that near equilibrium many different structures are locally stable and differ in energy by only a few meV per formula unit.[32] Theoretical work on XRD spectra has also shown that the patterns are

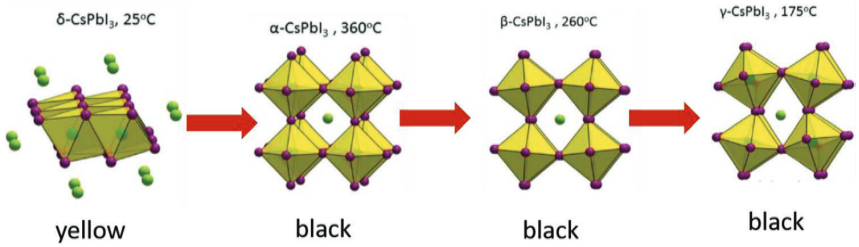

Figure 2.3: Phase transition flow in $CsPbI_3$ (based on synchrotron based powder diffraction). Reproduced with permission from ref. [23] Copyright 2015 American Chemical Society.

compatible with different coexisting phases,[33] and that systems can deviate from the ideal structure on a sub-ps time scale.[34]

2.1.3 Structural Phase Transitions

HOIPs undergo successive structural phase transitions. Figure 2.2a shows a schematic representation of the $MAPbI_3$ crystal structure, which was first synthesized and structurally described by Weber.[1] There are four major phases: The alpha (α)-phase, characterized by an ordered cubic structure, is stable at > 330 K. After the first transition near or below room temperature < 300 K, $MAPbI_3$ adopts the beta (β)-phase. β-$MAPbI_3$ exhibits spontaneous electric polarization caused mainly by the alignment of the MA molecules along the z-axis together with a marginal atomic distortion of the Pb – I octahedra. Although the presence of ferroelectricity in halide perovskites has been theoretically predicted, its experimental manifestation is not obvious and strogly depends on the experimental details.[35] After the second phase transition at low temperatures < 130 K, $MAPbI_3$ exhibits an orthorhombic gamma (γ)-phase consisting of twisted octahedra. This phase is a non-perovskite structure (either $NH_4CdCl_3^-$ or $CsNiBr_3^-$ structure type). All of phase transitions are fully reversible, although in some cases the phase change can be blocked kinetically or the transition can be delayed up to several days. A characteristic example of reversible transitions can be found in the $CsBI_3$ (B = Sn, Pb), as shown in Figure 2.3. $CsPbI_3$

stable δ (yellow) phase converts upon heating above 360 °C to the black perovskite α-phase. On cooling, the perovskite structure remains kinetically stabilized converting to the black perovskite β- and γ-phases at 260 °C and 175 °C, respectively. Full conversion of the γ- to the initial yellow δ-phase occurs after ≈48 h.

Although not a phase transition in the strict sense, the reference halide perovskite $MAPbI_3$ can also adopt the δ-phases in the form of $CH_3NH_3PbI_3 - X$ solvates, where any solvent with hydrogen bonding ability, such as $X = H_2O$, DMF, DMSO, etc.[36] can cause the collapse of the perovskite crystal lattice. This process is the origin of the apparent temporal instability of $MAPbI_3$ perovskites. Remarkably, the solvation process in $MAPbI_3$ occurs at temperatures where the α/β-phase transition also occurs (≈40 °C), suggesting a change in the transition pathway in the presence of certain solvents. Fortunately, it has been shown that this destructive phase transition can be circumvented by maintaining the temperature above the transition point during crystal growth[37] or by using solvents with low hydrogen bonding ability.[38]

2.1.4 Molecular Rotations

A unique aspect of HOIPs compared to conventional semiconductors is that the organic molecule can move in the crystal and undergo rearrangements. Typical organic cations used in perovskites, such as MA^+, can have multiple low energy orientations in the perovskite structure. They can be aligned with corners, edges, or faces of the inorganic cages (Figure 2.4a).[39] The energy barriers for such rotations can be as low as a few meV,[32,40] so significant motion of the molecules can be expected at finite temperatures.[41] Using quasi-elastic neutron scattering measurements in conjunction with Monte Carlo simulations for $MAPbI_3$ perovskite, Leguy et al. found two primary molecular motions that dominate at room temperature (Figure 2.4b)[39] motions of the CH_3 and NH_3 groups about the C – N axis and rotation of the entire MA unit perpendicular to the C – N axis. These movements can occur via several possible pathways (Figure 2.4a). The activation energies for these motions are different and therefore occur on different time scales: The CH_3 – or

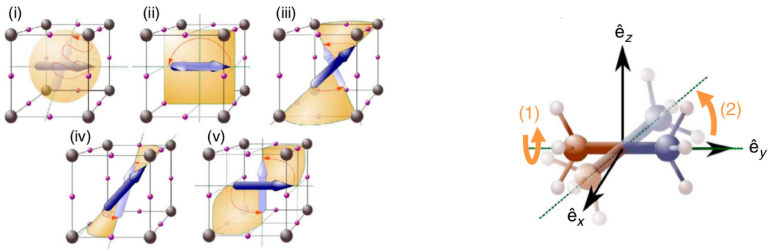

Figure 2.4: (a) Possible minimum-energy orientations and associated reorientation pathways, indexed from (i) to (v), for MA^+ in $MAPbI_3$, based on rotation (2) in panel (b). (b) Two modes of rotation of MA^+: (1) rotation of CH_3 or NH_3; (2) rotation of MA^+, swapping locations of C and N. Reproduced with permission from ref. [39]. Copyright 2015 Nature Publishing Group.

NH_3 – related motions occur on a time scale of less than one ps, whereas the large MA molecular unit aligns more slowly, at about 3 ps–14 ps.[42,43] Molecular rotations in HOIPs are strongly temperature dependent.[44] While molecules in HOIPs have a large conformational freedom at room temperature, rotations become restricted once HOIPs are cooled and undergo phase transitions into tetragonal and orthorhombic structures. Experimental and theoretical results have shown that at lower temperatures the molecular orientations are bound to the highly symmetric directions of the crystal[42] and energy barriers to reorientation are increased.[45] When T is lowered, the AX_{12} cuboctahedra shrinks due to octahedral BX_6 rotations, leaving less room for molecular rearrangements. Since BX_6 distortions and molecular rotations are coupled, the bond lengths and angles of the BX_6 octahedra change significantly with molecular rotations.[39,40] This coordinated effect of molecular rotations and octahedral distortions suggests that a snapshot of a single HOIP structure cannot account for important dynamical effects and does not provide sufficient information about its properties. For example, the bandgap size may change with molecular rotation.[40] However, in a Sn-based HOIPs, molecular rearrangements affect the band structure[46] through electrostatic and hydrogen bonding effects on the inorganic ions, which are primarily responsible for the electronic

structure of the band edge. Therefore, structural fluctuations at room temperature can lead to dynamic changes in important parameters of the electronic structure, e.g., band gap, effective masses, and possibly carrier lifetime. Such effects have also been reported for Pb-based HOIPs, with time-dependent changes in the bandgap predicted to range from 0.1–0.2 eV at 320 K.[33,34] Molecular rotations, octahedral distortions, and phase transitions are also closely related to ferroelectricity. There is still debate in the perovskite community about the ferroelectric nature of HOIPs. Theoretically, it is possible because lower temperature phases can crystallize in polar space groups,[35] but there are many reports claiming either the presence or absence of ferroelectricity. Berry phase calculations in HOIPs predicted a polarization of ≈4–12 $\mu C\,cm^{-2}$ for the low temperature phases of $MAPbX_3$ (X = I, Br, Cl),[26,47] which is significantly lower than the values reported for ferroelectric oxides, e.g., $BaTiO_3$. Although the measurement of ferroelectric hysteresis in HOIPs is a difficult task because due to the small band gap and the large number of mobile charge carriers, it can lead to significant leakage currents.[26] Due to the large structural diversity and molecular flexibility of HOIPs, it would probably be very difficult to stabilize large ferroelectric domains in HOIPs at room temperature, but another possibility would be to consider short-lived ferroelectric domains.[48,49] Interestingly, long-range electrostatic interactions of molecular dipoles can lead to polar domains via regions with aligned dipoles.[49] Such domains can alter the HOIP bandgap,[50] separate the wavefunctions of electrons and holes,[51] and suppress carrier recombination.[52] These polar domains can also serve as channels for the separate transfer of electrons and holes, for example, by forming domain walls,[49,50] which could partly explain the long carrier lifetimes of HOIPs.

2.2 Excitons

2.2.1 Excitons and Free Charge Carriers

An exciton is a mobile neutral quasiparticle consisting of an electrostatically bound electron-hole pair. The interaction between electron and hole can be strong or weak,

leading to two different types of excitons Frenkel excitons, found mainly in organic semiconductors, and Wanier-Mott excitons, associated with classical inorganic semiconductors.[53] Semiconductors with high exciton binding energies are more suitable for light-emitting applications because radiation racombination by excitons can be very effective at low carrier concentrations. In contrast, a low exciton binding energy is desirable for photovoltaic applications because easy dissociation or spontaneous generation of free charge carriers is essential for effective current generation in photovoltaic devices. Surprisingly, hybrid perovskites can function in both excitonic[5] and planar[54] configurations. Therefore, the electrostatic interaction strength between the correlated electron and hole, i.e., the exciton binding energy (E_b), is an important parameter for predicting and modelling the operation of optoelectronic devices.

2.2.2 Determination of Exciton Binding Energy

Temperature-dependent photoluminescence (PL),[55,56] optical[57,58] and magneto absorption[59,60] are used together with theoretical calculations[28,61] to study the exciton binding energy in HOIPs.

Temperature-dependent photoluminescence is a common method for determining the exciton binding energy E_b. In this method, E_b is extracted by fitting the Arrehnius equation to the experimentally determined integrated PL intensity at different temperatures.[62] In general, the PL intensity decreases with increasing temperature, which is due to the temperature-activated exciton dissociation processes.[55] Since this method is widely used, large variations of E_b are reported in the literature, ranging from 19 meV (10 K–300 K)[63] to 32 meV (80 K–300 K)[64] for $MAPbI_3$. This deviation may be due to the complex tempreture-dependent radiative recombination process in hybrid perovskites.[65]

Another approach to determine E_b is to measure optical absorption and analyse it using Elliott theory.[66] This theory involves the continuum and excitonic states in the relationship of the absorption coefficient. Using this method, Yang et al. found an E_b of 9 meV at room temperature.[57] Saba et al. estimated 25 meV at both 300 K

and 170 K.[67] Yamada et al. found a gradual increase from 6 meV to 30 meV as the temperature drops from 300 K to 13 K.[68] These remarkable discrepancies may be due to the fitting uncertainties caused by the fact that the assignment of exciton, Coulomb interaction, and continuum absorption is not clear when the values of exciton binding energy E_b and homogeneous line broadening in the materials are comparable.[66]

Magnetoabsorption is also a commonly used method for determining the exciton binding energy. In this method, magnetoabsorption spectra are measured as a function of magnetic field for both circular polarizations, resulting in an energy shift and splitting equivalent to diamagnetic shift and Zeeman splitting. Hirasawa et al. determined E_b =37 meV for the polycrystalline $MAPbI_3$ film at 4.2 K.[59] Tanaka et al. later redetermined the value of Hirasawa et. al. by performing magnetoabsorption experiments in which no photoluminescence induced by a magnetic field was observed. They found that the binding energy for $MAPbI_3$ is 50 meV at 4.2 K.[69] The value obtained by Tanaka agrees well with a theoretical calculation of E_b using density functional theory (DFT) based on the Wannier-Mott model with the frequency dielectric constant, where E_b for $MAPbI_3$ was estimated to be 48 meV.[28]

2.2.3 Dissociation of Excitons

It is generally believed that free charge carriers dominate in hybrid perovskites under working conditions.[68,71] Although there is some research where free charge carriers have been directly observed,[71,72] another view on this subject has recently emerged. It states that after photoexcitation, free charge carriers and excitons coexist in equilibrium[71,73,74] and the balance can be determined by the Saha-Langmuir equation.[75] This model states that the fraction of free charge carriers relative to the total excitation density ϕ_{fc} for a 3D system can be described as follows

$$\frac{\phi_{fc}^2}{1-\phi_{fc}} = \frac{1}{n}\left(\frac{2\pi m_r k_B T}{h^2}\right)^{\frac{3}{2}} \exp\left[-\frac{E_b}{k_B T}\right] \tag{2.2}$$

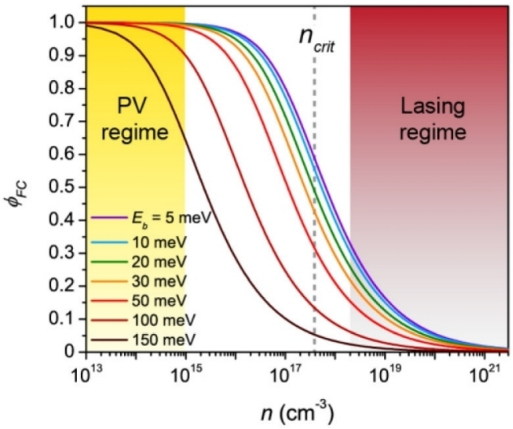

Figure 2.5: Quantum yield of free carriers ϕ_{fc} as a function of excitation density according to the Saha-Langmuir equation (2.2) for various values of E_b at room temperature, with $m_r = 0.1m_0$. Densities relevant for PV and lasing applications are highlighted, along with the critical carrier density, n_{crit}, above which manybody effects limit exciton formation (for $E_b = 15$ meV). Reproduced with permission from ref. [70] Copyright 2016 American Chemical Society.

where n is the total excitation density, m_r is the reduced effective mass, and h is Planck's constant. The application of the Saha-Langmuir equation for different values of E_b at room temperature is shown in Figure 2.5. At low excitation densities ($n \leq 10^{15}$ cm^{-3}), the population of the abandoned state consists mainly of free carriers for $E_b \leq 100$ meV. This state is very advantageous for photovoltaic applications. When the excitation density increases, the fraction of free carriers starts to decrease, increasing the exciton population. When the excitation density exceeds 10^{18} cm^{-3}, the excitonic fraction begins to dominate. The value of $n \approx 10^{18}$ cm^{-3} is consistent with the onset of the excitation density of amplified spontaneous emission in $MAPbI_3$ (2×10^{18} cm^{-3}).[76] The model implies that excitons would contribute to lasing at high excitation density for all binding energies. However, this is at odds with experimental results indicating that excitons generally undergo a transition to free carriers before lasing at high excitation density.[77] Excited states consisting mainly of free charge carriers at high excitation intensity have also been re-

ported.[67,78] Since the Saha-Langmuir model does not account for the contributions of many-body effects that occur at high excitation density, this deviation from experimental results is understandable. At high excitation density, the electrostatic interaction between the electron and hole would be screened by the presence of other charge carriers, leading to the dissociation of the exciton into free charge carriers. This transition is called the Mott transition and manifests at a critical excitation density (n_{crit}), where $n_{crit} = k_B T/(11\pi E_b r_B^3)$. The dashed line in Figure 2.5 represents the critical density ($n_{crit} \approx 4 \times 10^{17}$ cm^{-3}) of the Mott transition for $E_b = 15$ meV and $r_B = 5$ nm, at which the Saha-Langmuir equation no longer applies. Even below the critical density of the Mott transition, the excitonic state in bulk perovskites is usually short-lived. This leads to rapid dissociation of excitons to free charge carriers.[79–81] According to Valverde-Chavez et al, photogenerated excitons in $MAPbI_3$ single crystals dissociate to free charge carriers in a time scale of 1 ps, with an E_b value of 17 meV.[79] Jha et al. recently reported from 2D spectroscopy that the dissociation of excitons to free charge carriers in $MAPbI_3$ thin film occurs within 50 fs.[81] This is considered to be one of the main reasons why perovskite photovoltaics exhibit very high efficiency.

2.2.4 Exciton Dynamics

To study the ultrafast dynamics of excitons and charge carriers, the most popular technique is transient absorption (TA). Most of these studies have shown that excitons, when formed at room temperature, dissociate rapidly into free charge carriers, on a sub-ps time scale. However, using the ultrafast pump-probe technique with excitation densities (n) ranging from 3.8×10^{16} cm^{-3} to 5.5×10^{18} cm^{-3}, Yang et al. found that the contribution of excitons to the transient absorption spectrum (TA) of $MAPbI_3$ films cannot be neglected.[57] The study clearly showed that at excitation intensities of less than $\approx 1 \times 10^{18}$ cm^{-3} the TA spectrum is dominated by excitonic bleaching, while at larger excitation densities the continuum contribution by free carriers begins to dominate. It should be noted, however, that the intensities used in the TA measurements are much higher compared to steady-state ab-

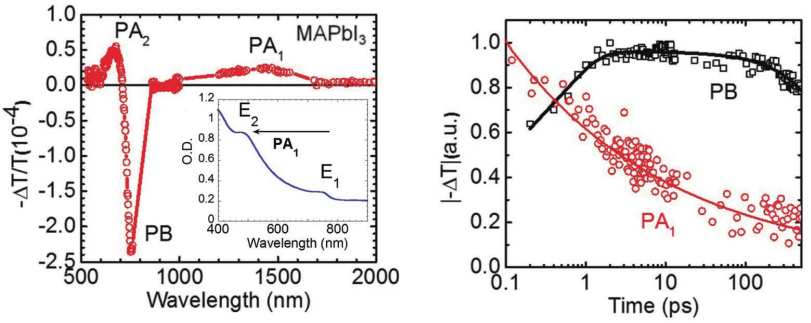

Figure 2.6: (a) Transient photomodulation spectra measured at t = 0 ps for $MAPbI_3$ thin films, with the 400 nm excitation wavelength. Inset shows the corresponding absorption spectra for the film, where two different excitons, E_1 and E_2 and the interband PA_1 transition between them, are assigned. (b) Decay dynamics of PB and PA_1 bands up to 500 ps. Reproduced with permission from ref. [82] Copyright 2016, Wiley-VCH.

sorption measurements or actual working conditions. This means that free charge carriers will dominate in perovskites with exciton binding energies comparable to or even larger than the thermal energy at room temperature. Another interesting study by Zhai et al. revealed that the TA spectrum of $MAPbI_3$ films obtained by pump-probe spectroscopy in the visible to mid-IR (450−4000 nm) consists of a large photoinduced bleaching band (PB) at 750 nm and an adjacent photoinduced absorption band (PA_2) at shorter wavelengths, as well as another photoinduced absorption band (PA_1) peaking at 1500 nm (Figure 2.6a). PA_1 showed different decay dynamics compared to PB and PA_2 (Figure 2.6b) and was therefore assigned to different existing species. In particular, PB and PA_2 were interpreted as a result of the band filling effect caused by the photocarriers. For the PA_1 since the energy peak of the PA_1 band (1500 nm, 0.8 eV) perfectly matched the separation between the excitonic states at 750 nm (E_1 = 1.66 eV) and 500 nm (E_2 = 2.48 eV), as seen in the steady-state absorption spectrum. The PA_1 band was therefore assigned to an optically allowed excitonic transition from E_1 to E_2.[82] Many other studies using transient techniques in perovskite films show the ultrafast behavior of localized

excitons,[83] biexcitons,[84] trions,[85] and multiple exciton generation.[86] For example, He et al. reported that the radiative recombination of photogenerated species in solution-processed $MAPbX_3$ is dominated by excitons weakly localized in band tail states under the excitation level near the working regime of solar cells, and such an exciton localization effect was generally found in several solution-processed perovskite films.[83] Interestingly, Weerd et al. have demonstrated highly efficient carrier multiplication in $CsPbI_3$ nanocrystals, with a threshold close to the energy conservation limit of twice the bandgap.[86] Such efficient carrier multiplication may lead to next generation solar cells that can overcome the Shockley-Queisser limit.

2.3 Free Charge Carriers

2.3.1 Carrier Motion

The transport of free charge carriers in semiconductors is mainly governed by two mechanisms: drift and diffusion.[87] Diffusion with characteristic parameter D refers to the movement of charge carriers from regions of high to regions of low charge carrier density without an externally applied electric field. Drift with the characteristic parameter (μ) mobility refers to the charge carrier movement caused by an external electric field. The diffusion coefficient and the charge carrier mobility can be related via the Einstein relation[88]

$$\mu = \frac{q}{k_B T} D \tag{2.3}$$

where q is the electric charge. This relationship provides the ability to determine D by experimentally evaluating the charge carrier mobility. This is much easier than determining it by solving various diffusion models. On the other hand, carrier mobility can be determined by knowing the diffusion coefficient. In hybrid lead-based perovskites, the highly efficient charge carrier collection strongly depends on the long charge carrier diffusion length (µm), which is due to sufficient charge carrier

lifetimes.[89] Whereas the carrier mobility is modest at best compared to classical inorganic semiconductors.

2.3.2 Diffusion Length

Diffusion processes occur in every semiconductor material. Generally, charge carriers generated by light or electricity appears near the surface, creating a gradient of charge carrier density in the direction of the mass of the material. When a gradient of carrier concentration exists, carriers are moved by random motion through diffusion from areas of high carrier concentration to areas of low concentration. The diffusion length is the average length that a charge carrier travels between generation and recombination, and is defined as $L_D = \sqrt{D\tau}$.[90] Here τ is the lifetime of the charge carriers. As mentioned earlier, L_D affects the efficiency of charge carrier extraction in semiconductors and is therefore an important property to consider. The carrier lifetime τ is usually determined from transient measurements, while D can be derived from the diffusion model in the absence of an electric field.[70] Methods such as PL quenching,[91] time- and spatially-resolved transient absorption microscopy (TAM),[92] transient PL-scanned imaging microscopy[93] have been applied in perovskites to determine D and thus the diffusion length L_D. The diffusion length in perovskites varies between 100 nm and more than 100 µm depending on the determination method.[91–93]

Transient PL quenching (PLQ) is a common method for determining the carrier lifetime and diffusion length for perovskites by measuring different configurations (with quenching layers) and modeling the PL decay with the diffusion model (Figure 2.7a). Using the PL quenching technique, Stranks was one of the first to demonstrate that the diffusion lengths for electrons and holes were similar ((129 ± 41) nm for electrons and (105 ± 32) nm for holes) in the $MAPbI_3$ films.[94] Not surprisingly, a number of studies have shown that the carrier diffusion lengths measured on polycrystalline thin films were significantly shorter than those of single crystals due to the existence of grain boundaries - less than a few µm versus more than 100 µm.[95,96] While ensemble methods for determining diffusion length are not able to monitor

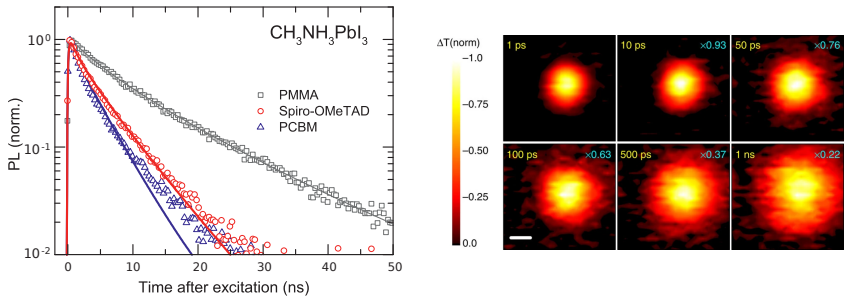

(a) (b)

Figure 2.7: a) Photoluminescence quenching method. Time-resolved PL measurements of $MAPbI_3$ films with a hole (spiro – OMeTAD, red) quenching layer, or an electron (PCBM, blue) quenching layer or an insulating PMMA (black) layer. Reproduced with permission from ref. [94] Copyright 2013, Science Publishing Group. b) Transient absorption microscopy method. The figure shows 2D imaging of the carrier density profile in $MAPbI_3$ at different pump–probe delay times. The scale bar in the figure is 300 nm. Reproduced with permission from ref. [92] Copyright 2015, Nature Publishing Group.

the influence of grain boundaries on charge carrier transport, transient absorption microscopy (TAM) is a suitable tool to study the behavior of charge carriers both in time and in space. In TAM, the pump beam is fixed at a known position while the probe beam is scanned relative to the pump position and an image is formed. In such images, the spatial distribution of carrier density can be directly visualized as a function of pump-probe delay. At 0 ps, the TAM image represents the initial carrier population generated by the pump pulse. At later delay times, the TAM image reflects carrier diffusion away from the initial excitation volume. Carrier diffusion is represented by the evolution of the carrier distribution profile over time (Figure 2.7b). Charge carrier diffusion of polycrystalline $MAPbI_3$ in space and time was demonstrated by Guo et al. using TAM.[92] A diffusion length of ≈ 220 nm was directly visualized using the probe delay window of 2 ns. Using the PL lifetime of ≈ 50 ns derived from modeling the time- and space-dependent carrier density with the in-plane 2D diffusion model, an estimated diffusion length of ≈ 1.2 μm was obtained. Imaging time-resolved PL-scanned microscopy is another tool to directly

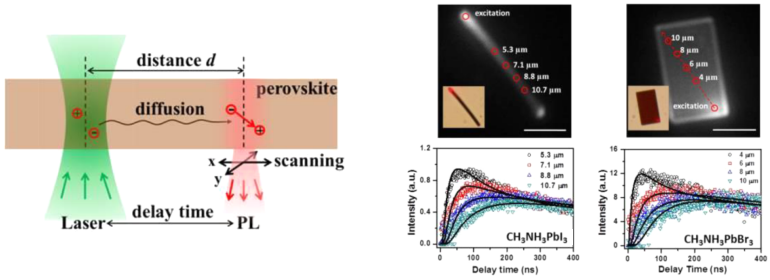

Figure 2.8: (a) A schematic presentation of the charge carrier excitation, diffusion, and recombination processes in perovskites. (b) PL intensity images (upper panels) and a set of PL kinetics collected at different diffusion distances (lower panels) of a $CH_3NH_3PbI_3$ NW (a) and NP (b) and a $CH_3NH_3PbBr_3$ NW. The red circles indicate the positions and diffusion distances where the PL kinetics is extracted. Black solid lines are the fits of the PL kinetics by the diffusion model. Reproduced with permission from ref. [93] Copyright 2015, American Chemical Society.

study charge carrier diffusion in time and space for the perovskites. Using this technique, Tian et al. have studied single crystal $MAPbI_3$ and $MAPbBr_3$ nanowires and nanoplates. The measurement was based on the diffusion of charge carriers after an excitation pulse from an excitation point to another position, where the change in charge carrier density can be observed by the time-resolved PL as a function of the delay time (Figure 2.8a). The diffusion parameters (diffusion coefficient, charge mobility, and recombination constants) can then be extracted (Figure 2.8b) from the fits of the PL kinetics by a diffusion model. The core of imaging microscopy is the use of a galvano-mirror in the PL collection path. By rotating this mirror, the PL collection point is scanned over the entire sample with a fixed excitation position. In this way, a PL intensity image is generated that reflects the spatial distribution of charge carriers in the perovskite sample. The delay time between the excitation and the emitted photons is detected using the time-correlated single photon counting model. By globally fitting the PL kinetics at different positions to the in-plane 2D diffusion model, the diffusion coefficient was estimated to average (14.0 ± 5.1) μm

HOIP	Architecture	Carrier Type	Mobility ($cm^2/V\,s$)	Technique	Ref.
$MAPbI_3$	film	e^-	1.4	PLQ	[91]
	film	h^+	0.9	PLQ	[91]
	film	e^-	0.7	PLQ	[94]
	film	h^+	0.4	PLQ	[94]
	film	$\sum$	35	TRTS	[97]
	film	$\sum$	20	TRTS	[98]
	film	$\sum$	29	MWC	[99]
	film	$\sum$	71	MWC	[100]
	film	$\sum$	8	Hall	[101]
	film	$\sum$	12.8	Hall	[102]
	sc	h^+	2.5	SCSL	[38]
	sc	h^+	164	SCSL	[37]
	sc	h^+	105	Hall	[37]
	sc	h^+	24	TOF	[37]
	film	$\sum$	2.0 (lateral)	PhC	[103]
	film	$\sum$	1.1 (lateral)	TPC	[104]

Table 2.1: Experimentally determined values for charge carrier mobility in $MAPbI_3$ perovskite

for $MAPbI_3$ and (6.0 ± 1.6) µm for $MAPbBr_3$, regardless of the shape of the nanostructures.[93]

2.3.3 Carrier Mobility

There are two categories of measurement methods for the experimental determination of charge carrier mobility, namely non-contact and contact probing techniques.[76,93,98,105–107] The table 2.1 shows experimentally determined values for the charge carrier mobility of hybrid perovskites. It is easy to see that the reported values are very different even for perovskites of the same composition, which means that they strongly depend on the measurement technique used.

Non-contact techniques include the above mentioned PLQ, TAM and transient PL - scanned imaging microscopy. In these techniques, the charge carrier mobility is determined from the derived diffusion coefficient via the Einstein relation. An-

other very widely used technique is time-resolved THz spectroscopy (TRTS).[98,105] This method is sensitive only to free carriers and excludes any excitonic contribution. The advantage of TRTS is that it studies material properties without contact artifacts. Due to the high frequency of THz radiation, TRTS investigates charge carrier transport in a relatively short range. Contact probing techniques are also commonly used to determine the charge carrier mobility of perovskites. Space Charge Limited Current (SCLC) is one of the reference techniques that measures current density (J) as a function of applied voltage (V).[37,38,110] The curve obtained can be divided into three regions: 1) a linear ohmic region at low bias where the electrical conductivity (s) can be calculated, 2) a trap-filled region at medium bias where an estimation of the trap density is possible, and 3) a trap-free SCLC region at high bias where the charge carrier mobility is determined. (Figure 2.9a) The mobility is then calculated according to the Mott-Guerney law[111] $J = 9\epsilon\mu V^2/(8L^3)$, where ϵ is the dielectric constant and L is the thickness of the sample, is used to derive the charge carrier mobility. The derivation of μ assumes that the current is generated by only one type of charge carrier and that the current flow is limited by drift and not by trapping or energetic disorder. Another commonly used electrical measurement technique is the time-of-flight (TOF) measurement, which is based on the transit time T_t required for the charge carriers to drift through the sample under the applied electric field.[37,38] The TOF method can measure both hole and electron mobilities separately (fixed positive and negative biases are applied to measure hole and electron mobilities, (Figure 2.9b) respectively) and determine different levels of trap states, while light illumination and relatively thick films (4500 nm) are required to ensure that charge carriers traverse the depletion region to reach accurate mobility values. The transit time T_t can be determined by measuring the photocurrent flowing through the sample. The carrier mobility μ can then be extracted from the relationship[112] $\mu = L/(E \cdot T_t)$, where L is the thickness of the sample and E is the applied electric field. A variation on the TOF theme is the charge extraction by linearly increasing voltage (CELIV) method. To measure charge carrier mobility, a triangular voltage is applied instead of a rectangular voltage pulse to extract

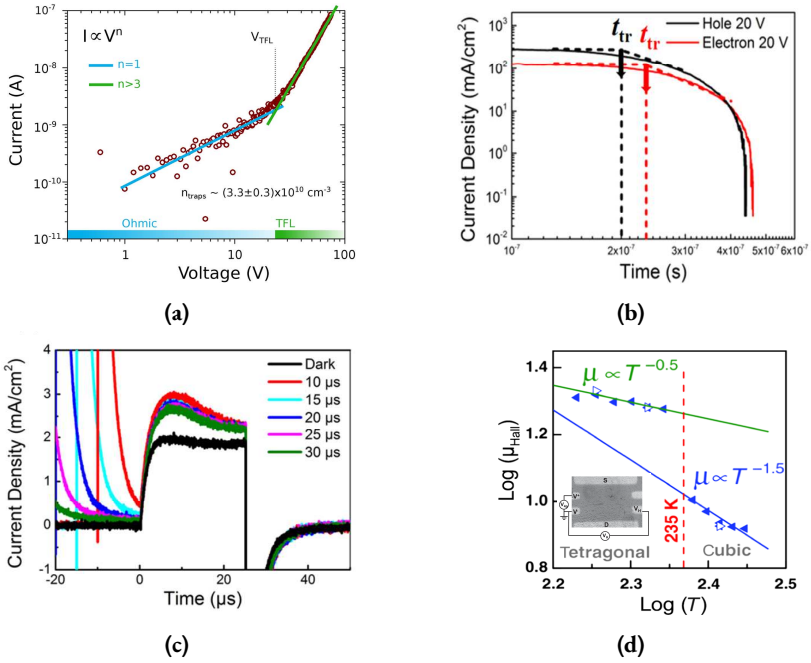

Figure 2.9: (a) Characteristic SCLC measurement $I - V$ trace (purple markers) showing three different regimes for $MAPbI_3$ (at 225 K). A linear ohmic regime ($I \propto V$, blue line) is followed by the trap-filled regime, marked by a steep increase in current ($I \propto V^{n>3}$, green line). Reproduced with permission from ref. [38] Copyright 2015, Science Publishing Group. (b) Characteristic TOF measurement logarithm $I - t$ profiles measuring the hole and electron mobilities of $MAPbI_3$ neat film. (c) Characteristic TOF measurement logarithmic $I - t$ profiles with the hole and electron measurement regimes of $MAPbI_3$ neat film. Reproduced with permission from ref. [108] Copyright 2015, American Chemical Society. (d) Temperature dependence of Hall mobility in $MAPbBr_3$ single crystal, inset shows a optical micrograph of a $MAPbBr_3$ single crystal with metal contacts in a Hall bar geometry. Reproduced with permission from ref. [109] Copyright 2015, Science Publishing Group.

the intrinsic or photogenerated charge carriers by dark or photo CELIV, but no distinction can be made between the type of charge carriers (Figure 2.9c). The carrier mobility can be determined from $\mu = 2d^2/3(\Delta/V\Delta t)t_{max}^2$, where d is the thickness of the active layer, $\Delta V/\Delta t$ is the voltage of the ramp of the applied triangular voltage

pulse, and t_{max} is the time at which the value of the current density is maximum.[113] The magnetic field is also used to determine the charge carrier mobility. The principle of Hall effect measurement is based on the deflection of charge carriers in a magnetic field, resulting in a generated Hall voltage (V_H) across the sample (Figure 2.9d).[35,38,79] The mobility can be extracted from $\mu = \sigma L V_H / (I \cdot B)$, where σ is the conductivity obtained from resistance measurements, L is the sample thickness, I is the current and B is the magnetic field.

In summary, the contact techniques better characterize the properties of a single charge carrier, since either the electron or the hole is extracted. However, the measurements made are affected by the type and quality of the contacts. It seems that the large differences in mobility values even between perovskites with the same composition and measurement technique are related to the systemic errors and limitations of the different measurement techniques. For example, the hole mobility values of single-crystal $MAPbI_3$ from SCSL measurements vary from 2.5 $cm^2\ V^{-1}\ s^{-1}$ to 164 $cm^2\ V^{-1}\ s^{-1}$, making it very difficult to obtain an appropriate mobility value for a given perovskite type in a given morphology. As suggested by Herz,[114] it is more informative to determine the average mobility values for the perovskites using the available data. As shown, the averaged carrier mobility for polycrystalline $MAPbI_3$ thin films with the contributions of electrons and holes is 2.4 $cm^2\ V^{-1}\ s^{-1}$from the long-range PLQ measurements and 37 $cm^2\ V^{-1}\ s^{-1}$ from the short-range THz and microwave conductivity measurements (MWC), indicating the effect of grain boundaries slowing carrier motion.

The difference in charge carrier mobility of perovskites and organic semiconductors is considerable, but small compared to typical inorganic semiconductors such as Si or GaAs. Therefore, it is very important to understand the mechanism that limits the carrier mobility in hybrid perovskites. Limiting mechanisms can be divided into intrinsic and extrinsic categeories. Intrinsic properties are fundamental, while extrinsic ones are related to material defects and fabrication quality. From Drude's model of electrical conduction[115] where $\mu = q\tau_s / m^*$, it is known that the charge carrier mobility μ is influenced only by the the charge carrier effective mass

m^* and electron-phonon scattering time τ_s. The experimentally determined effective masses of charge carriers in hybrid lead perovskites are very similar to those of Si or GaAs,[29] so that the lower mobility can be attributed to the shorter scattering times. The interaction of charge carriers with the vibrations of the crystal lattice involves the scattering of the acoustic phonon deformation potential scattering and Fröhlich coupling with the longitudinal optical (LO) phonons.[116] It has been demonstrated both theoretically[117] and experimentally[118] that, in particular, Fröhlich coupling with LO phonons in hybrid lead perovskites affects the charge carrier mobility at room temperature. Thus strong ionic character of metal-halide bond of hybrid perovskite induce large Fröhlich coupling constants (γ_{LO}). Also relatively low energy modes of the coupled LO phonons ($E_{LO} = \hbar\omega_{LO}$) for perovskites for examples ≈4.2 – 25 meV for $MAPbI_3$[118,119] vs ≈31 meV for GaAs[120] leads to easier Fröhlich interactions at room temperature. The same logic could be applied in order to explain higher carrier mobilities found in Iodide as compared to Bromide hybrid perovskites. Since Pb – I bond has lower ionicity as compared to Pb – Br bond, Fröhlich coupling will be reduced, thus higher carrier mobility at room temperature.[118] Using this model, it is possible to determine the highest possible charge carrier mobility if all extrinsic limiting properties are ignored. For $MAPbI_3$, it is 200 $cm^2\,V^{-1}s^{-1}$.[121] Extrinsic properties, however, are unavoidable and will significantly reduce the carrier mobility in real systems. For example, crystal grain size is one of the most important limiting factors for carrier mobility, as evidenced by mobility measurements from thin films to single crystals. Impurities in the material create additional scattering centers that also negatively affect carrier mobility, as does energetic disorder with regions of structural instability or structural transitions in perovskites. Therefore, to maximise the benefits of perovskite semiconductors, proper manufacturing quality control is essential.

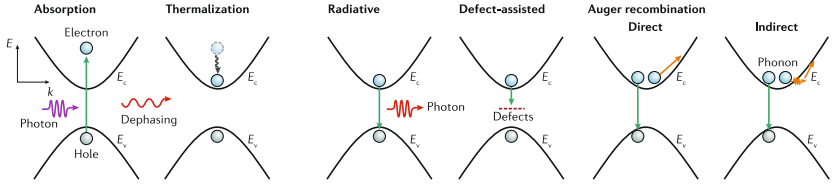

Figure 2.10: Generalized carrier generation and recombination scheme, including radiative, defect-assisted, and direct and indirect Auger recombination pathways.

2.4 Charge Carrier Recombination

2.4.1 General Recombination Model

In general, there are three pathways by which photoexcited energy is released. The initial decay begins with a very radip cooling of hot carriers and the additional energy of the excited species is released by radiative and non-radiative recombination mechanisms. In radiative recombination, the energy is released by light emission, while in non-radiative recombination the excess energy is converted to heat. Charge carrier recombination can also be divided into important classes: 1) excitonic recombination, 2) bimolecular radiative recombination, 3) trap-assisted recombination (Shockley-Read-Hall), and 4) nonradiative Auger recombination (Figure 2.10). The first recombination process is inherently excitonic, while the others involve free charge carriers. In bimolecular recombination, an electron moves from the conduction band to the empty valence band (hole). This band-to-band transition is usually a radiative transition. Trap-assisted recombination refers to the recombination of trapped charge carriers. When an electron gets trapped (falls into a different energy level due to an impurity or defect in the lattice), the trapped electron moves into an empty valence band in a second step and thus recombines. Auger recombination is a three-body process in which an electron and hole recombine in a band-to-band transition, but the resulting energy is released to another electron or hole.

To study the recombination dynamics of charge carriers, stationary PL measurements are usually used together with time-resolved PL kinetics.[106,122] Figure 2.11a

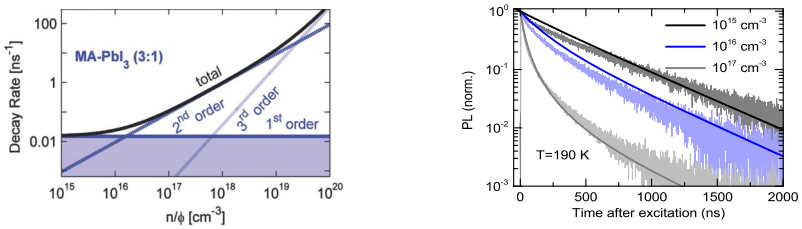

(a) **(b)**

Figure 2.11: (a) Trap-mediated (1^{st} order), bimolecular (2^{nd} order), and Auger (3^{rd} order) recombination decay rates of $MAPbI_3$ as a function of injected carrier density, respectively. Reproduced with permission from ref. [106] Copyright 2014, Wiley-VCH. (b) PL decays from $MAPbI_3$ with different initial photoexcitation densities. Solid lines are fits from the model. Reproduced with permission from ref. [123] Copyright 2014, American Physical Society

plots various recombination components as a function of charge carrier density (n). At low carrier densities with $n \ 10^{16}$ cm^{-3}, first-order trap-assisted recombination dominates, second-order bimolecular radiative recombination manifests in the carrier density range of $\approx 10^{17} \leq n \leq 10^{19}$ cm^{-3}, and the third-order Auger process begins to play at $n \ 10^{19}$ cm^{-3}. Different carrier density ranges (or excitation intensities) thus lead to different domminant recombination mechanisms. In real systems, however, these mechanisms usually intertwine and lead to very complicated carrier recombination dynamics (Figure 2.11b). A universal kinetic model is usually used to model the carrier dynamics[70]

$$\frac{dn}{dt} = G - k_1 n - k_2 n^2 - k_3 n^3 \tag{2.4}$$

where n is the time-dependent total carrier density, G is carrier generation term which depends on exitentaion intensity by $G = \alpha I_{ex}$ and k_1 (s^{-1}), k_2 ($cm^3 s^{-1}$) and k_3 ($cm^6 s^{-1}$) are the monomolecular, bimolecular, and three-body Auger recombination rate constants, respectively. Normally generation term G can be excluded by using ultrashort laser pulses. Since k_1, k_2, and k_3 are proportional to n, n^2, and n^3, they are also termed as the 1^{st}, 2^{nd}, and 3^{rd} order recombination rate constants.

2.4.2 Recombination Rates in Perovskites

Transient absorption (pump-probe),[70,78] transient PL (TRPL),[67,123] transient THz (TRTS),[106,124] and microwave spectroscopy (MWC)[55,98] are used to study the dynamics of charge carrier recombination and to extract the corresponding recombination rates from the kinetic model for perovskites. Although k_1 could be derived from fitting the kinetic data, it is usually determined by TRPL and used as a fixed parameter in the global fitting analyses to determine the higher-order rates because the monomolecular process can be isolated from the higher-order processes by applying low charge carrier densities. Typical values for recombination rate constants are summarised in the Table 2.2.

The monomolecular k_1 rate constant is highly dependent on the quality and crystallinity of the perovskite. For $MASnI_3$, for example, k_1 is almost three orders of magnitude higher than the same constant in $MAPbI_3$. It is known that $MaSnI_3$ undergoes very rapid oxidation from Sn^{2+} to Sn^{4+}, resulting in faster recombination of electrons.[125] The same k_1 acceleration is also observed in the $FAPbI_3$ system, which is known for compositional instabilities and amorphous morphologies.[65] These studies suggest that k_1 can be controlled by the fabrication process. By improving the quality of the material, it is possible to suppress the energy loss channel in perovskites. While the bimolecular k_2 rate is a fundamental property of the material that does not depend on external factors, but on the bright side k_2 values for perovskites are comparable to GaAs (3.7×10^{-10} cm^3 s^{-1}).[126] The simple Langevin model is commonly used to predict the k_2 rates. The model relates the bimolecular k_2 constant to the charge carrier mobility μ by $k_2 = \mu e/(\epsilon_0 \epsilon_r)$,[127] where e is the elementary charge, ϵ_0 is the dielectric constant of free space, and $epsilon_r$ is the relative dielectric constant of the material. This model assumes that recombination occurs as soon as an electron and a hole move within their common capture radius, which is presumably larger than their mean free path length. From the Langevin model, it appears that k_2 can be accelerated by increasing the mobility μ and slowed down by increasing ϵr due to the screening of the electron-hole interaction. Hertz has shown that the experimentally determined value of k_2 to carrier mobility ration

HOIP	Architecture	k_1 (s^{-1})	k_2 ($cm^3\ s^{-1}$)	k_3 ($cm^6\ s^{-1}$)	Ref.
$MAPbI_3$	flat film	15×10^6	0.6×10^{-10}	1.6×10^{-28}	[97]
	meso Al_2O_3	14×10^6	9.2×10^{-10}	1.3×10^{-28}	[106]
$MAPbI_{3-x}Cl_x$	flat film	12×10^6	1.1×10^{-10}	0.2×10^{-28}	[106]
$FAPbI_3$	flat film	7×10^6	1.1×10^{-10}	0.2×10^{-28}	[65]
$FAPbBr_3$	flat film	21×10^6	11×10^{-10}	1.5×10^{-28}	[65]
$FAPbBr_3$	meso TiO_2	8×10^6	14×10^{-10}		[125]

Table 2.2: Experimentally determined recombination parameters for different HOIPs.

for $MaPbI_3$ was four orders of magnitude lower than the value predicted by the Langevin model.[128] This deviation is highly desirable because it allows for long carrier diffusion lengths, L_D. Probably the most accurate bimolecular recombination constant, k_2, was obtained by Blancon et al. using confocal TRPL spectroscopy, which allows suppression of other decay channels. At excitation intensities relevant to photovoltaic applications, k_2 is on the order of 10^{-9} $cm^3\ s^{-1}$.[129] Auger recombination in normal cell operation conditions is relatively weak and can be neglected for photovoltaic applications. However, higher nonradiative Auger energy losses may occur in high charge density applications such as lasers. It has been found that k_3 varies in a small range of $(0.2–0.6) \times 10^{-28}$ $cm^6\ s^{-1}$ for various organic cations, halides, and film architectures. This is twenty five times higher than for GaAs.[130]

Methods for determining recombination rate are often combined with temperature dependent to gain further insight into recombination mechanisms. Millot et al. have shown that in the temperature range (8 K–360 K), which includes all crystal phases of perovskites, the k_1 value increases monotonically with increasing temperature, implying that monomolecular recombination occurs mainly by charge trapping by ionized impurities. The bimolecular constant k_2 decreases significantly with increasing temperature, along with the decrease in charge carrier mobility as predicted by the Langevin model.[97] The Auger rate constant k_3 is also strongly temperature dependent and phase specific in $MAPbI_3$, as the energy and momentum conservation requirements in this process make the many-body interactions sensi-

tive to the electronic structure. Although the universal kinetic model only considers processes that occur in the bulk, it neglects diffusion of charge carriers and non-radiative recombination at the surface. It is nevertheless a very useful and widely used model for determining the fundamental recombination rate constants. While there are several papers claiming that the recombination kinetics in polycrystalline $MAPbI_3$ can be completely determined by the dynamics of carrier diffusion and non-radiative recombination at the surfaces, based on a diffusion-surface recombination model,[131,132] the universal kinetic model is much easier to apply.

2.5 Migrating Species

In the course of the development of HOIP devices, several puzzling phenomena occurred. The first was the hysteresis in the $I-V$ curves[133] (dependence of the curve on the direction and speed of the bias scan). Second, it was observed that changing the polarity of the poling of $MAPbI_3$ films, photovoltage and currents can be inverted[134] and third, it was found that the dielectric response in the low-frequency range increases by three orders of magnitude when illuminated with photons above the bandgap.[135] None of the above observations can be explained by semiconductor theory, so other mechanisms must be considered. In principle, all ions that make up a perovskite material can migrate under an electric field and contribute to mentioned effects.[136] How easily an ion moves in a solid material is characterized by the activation energy (E_a) of an ion and the migration rate (r_m).

The migration rate (r_m) is proportional to ($-E_a/k_BT$). The E_a depends on the crystal structure, ionic radius, and ionic charge. For inorganic halide perovskites, ionic conduction is already well studied and has been attributed to the migration of halide vacancies with E_a of 0.2 eV–0.4 eV.[138] Ion migration in $MAPbI_3$ has also been studied both theoretically[137] and experimentally.[139] However, there is still a debate on the origin, types, and mechanisms of ion migration in hybrid perovskites. Temperature-dependent conductivity measurements showed that $MAPbI_3$ is a mixed ionic-electronic conductor in the dark. The activation energy for the moving

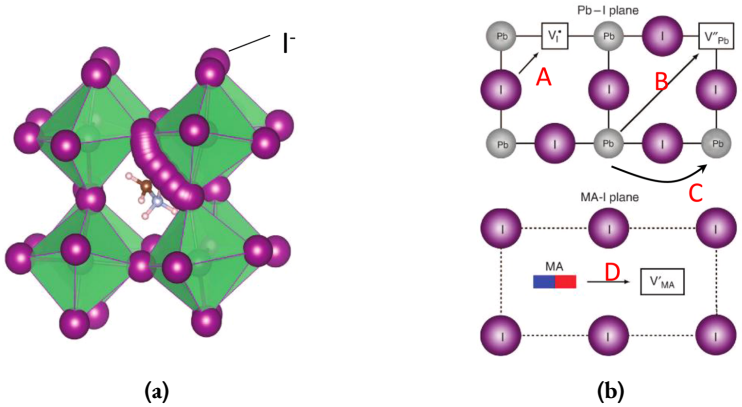

Figure 2.12: (a) Migration path of I^- ions along the $I^- - I^-$ edge of the PbI_6^{4-} octahedron in the $MAPbI_3$ crystal calculated from density functional theory (DFT) method. (b) Illustration of the migration paths for I^- ions (A), Pb^{2+} ions (B,C) in the Pb – I plane, and MA^+ ions (D) in the MA – I plane that was used for the calculation of activation energies. Reproduced with permission from ref. [137] Copyright 2015 Nature Publishing Group.

species was found to be 0.43 eV.[134] This value compares well with values for all inorganic perovskites. The similarity of E_a is not surprising considering that the film morphology, defect concentration, or grain boundaries are very similar in both materials. However, the question of what actually migrates in $MAPbI_3$ and how large the diffusion coefficient is is still open. By applying photocurrent relaxation experiments to $MAPbI_3$ perovskite, Enames et al. estimated E_a to be 0.60 eV–0.68 eV and compared this value with theoretical results obtained from first-principles calculations for different ions in $MAPbI_3$ perovskite. In the theoretical model, I^- was assumed to move with a curved pathway (Figure 2.12a) along the I – I edge of the PbI_6 octahedron (path A, Figure 2.12b) with a lowest E_a of 0.58 eV. Pb^{2+} along the diagonal of the unit cell (path B, Figure 2.12b) was found to have the highest E_a of 2.31 eV. MA^+ in the (100) plane along the [100] direction (path D, Figure 2.12b) was determined to have an E_a in between of 0.84 eV. The calculated result for I^- ions agreed well with the experimental results. From this, Enames et al. concluded that I^- is the most mobile ion in the $MAPbI_3$ perovskite lattice.[137] In another the-

oretical work by Azpiroz et al, E_a was calculated to be 0.08, 0.80 and 0.46 eV for I^-, Pb^{2+} and MA^+ respectively. From these values it was concluded that I^- ions can migrate through the $MAPbI_3$ film within a very short time scale of µs. This value is in contradiction with experimental results where the hysteresis effect or the photovoltaic switching rate in the $MAPbI_3$ based devices are usually observed in a time scale of seconds. For this reason, the observed slow current response was attributed to the MA^+ or Pb^{2+} (path C, Figure 2.12b) ions.[140] Although different publications give different numerical values for E_a, all agree that I^- ions are more easily mobile in the perovskite lattice than MA^+ or Pb^{2+} ions.

The first direct observation of ionic motion was found for MA^+ ions using photothermally induced resonance microscopy (PTIR). This technique allows direct imaging of MA^+ distribution by combining the chemical signal of Fourier transform infrared spectroscopy (FTIR) and atomic force microscopy (AFM) imaging. Yuan et al. presented images of the redistribution of MA^+ ions after electrical poling in $MAPbI_3$. After applying a small electric field of 1.6 V µm^{-1} for 100 s, MA^+ ions depleted from the center and the anode region and gathered around the cathode region (Figure 2.13a).[134] This was the first direct evidence of MA^+ migration in hybrid perovskites. From these experiments, E_a was determined to be 0.36 eV based on the conductivity changes (σ) of the $MAPbI_3$ films. The value obtained is slightly smaller than the 0.46 or 0.84 eV predicted by first-principles calculation methods.[137] This discrepancy is not surprising, since the calculated E_a is responsible for ion migration in a bulk crystal, while the measured ionic conductivity might be dominated by ion migration at the grain boundaries. Although theoretical calculations predicted that the I^- ions are the most mobile ions in the $MAPbI_3$ films, there is no direct observation of I^- ions at room temperature to date. Experiments performed with energy dispersive X-ray spectroscopy (EDX) showed no obvious redistribution of I^- ions, so it remains unclear whether the I^- ions migrate at room temperature.[134].

A study by Yang et al. showed a possibility that I^- ions migrate at elevated temperature.[139] In their study, the $MAPbI_3$ film was embedded in a solid-state electro-

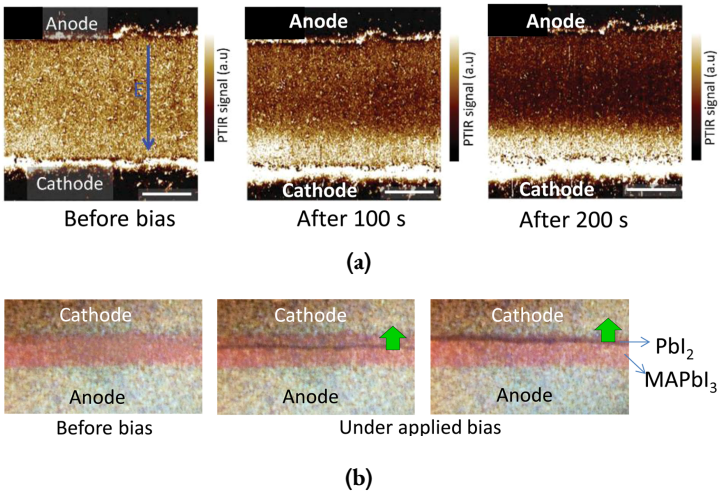

Figure 2.13: (a) PTIR images of the distribution of MA^+ before and after electrical poling for 100 s and 200 s, where the electrode spacing is 100 µm. Reproduced with permission form ref. [134] Copyright 2015 Wiley-VCH. (b) Optical images of the lateral $MAPbI_3$ perovskite solar cell with a mobile PbI_2 thread, which formed and migrated at 330 K along the applied electrical field direction. Reproduced with permission form ref. [141] Copyright 2015 Wiley-VCH.

chemical cell. After applying a bias voltage for one week at 323 K, the formation of lead iodide (PbI_2) was observed at the interface between the Pb anode and $MAPbI_3$, which could be the reaction product of the migrated I^- with the Pb anode, However, this observation is more likely due to the instability of the $MAPbI_3$ perovskite and can be explained by the decomposition of the $MAPbI_3$ crystal due to the leaving of MA^+ ions from the near-anode region, which was observed in another study by Xiao et al.[142] Another study by Yuan et al. investigated the electric poling effect on the lateral $MAPbI_3$ solar cells at 330 K and observed the formation of PbI_2 clusters with a width of 5 µm–15 µm, which could migrate along the applied electric field (Figure 2.13b).[141] This migration was explained by a reversible transformation between $MAPbI_3$ and PbI_2 phases driven by the electric field due to a massive migration of MA^+ and I^- ions. This study provided the first experimental evidence

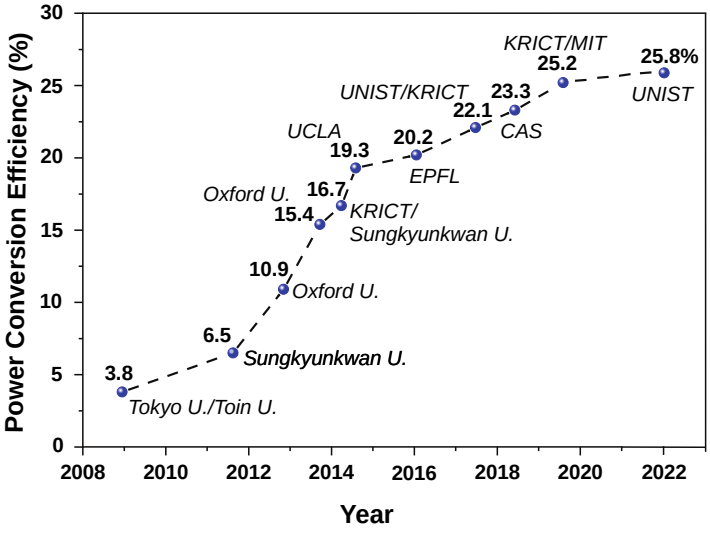

Figure 2.14: The progress of efficiency in the perovskite solar cells.

for the massive migration of I^- vacancies at elevated temperature. The results obtained demonstrate that both the MA^+ ions and the I^- ions in the $MAPbI_3$ films migrate at a relatively small electric field of 3 V/µm at 330 K, while the Pb^{2+} remains immobile within the resolution of the EDX measurement.

2.6 Applications

Not surprisingly, hybrid perovskites with the properties already mentioned are very versatile in application. In general, 3D bulk perovskites with low exciton binding energies are used in photovoltaics from solar cells to field-effect transistors and photodetectors. Low-dimensional perovskites, on the other hand, which tend to have excitonic properties due to the higher exciton binding energies, are more suitable for light-emitting diodes and lasers. One application that has attracted enormous attention since the first demonstration of a working device with an efficiency of 3.8 %[4] is perovskite solar cells (PSCs). Over time, immense efforts have been

made to increase the efficiency of perovskite solar cells (the increase in efficiency over time is shown in Figure 2.14) using various tactics, from changing the material composition to modifying the interfaces. For example, McMeekin et al. found that the incorporation of Cs^{2+} cation into the perovskite lattice leads to higher crystallisation and improved stability. Thus, perovskite cells prepared with the composition $FA_{0.83}Cs_{0.17}Pb(I_{0.6}Br_{0.4})_3$ achieved a over 17 % power conversion efficiency (PCE).[124] Saliba et al. showed that a triple Cs/MA/FA cation blend $(Cs_x(MA_{0.17}FA_{0.83})_{1-x}Pb(I_{0.83}Br_{0.17})_3, 0 \leq x \leq 0.15)$ with improved structural and thermal stability can yield a stabilised PCE of over 21 %.[143] Yang et al. presented a mixed perovskite of $(FAPbI_3)_{0.95}(MAPbBr_3)_{0.05}$ with potentially reduced intrinsic defects for non-radi-ative recombination and extended PL lifetime by introducing additional I^- ions into the organic cation solution. The resulting perovskite solar cells had a certified PCE of 22.1 %.[144] Jeon et al. fabricated highly efficient and thermally stable PSCs by using a fluorene-terminated hole transport material whose HOMO energy level is well matched to a mixed perovskite $((FAPbI_3)_{0.95}(MAPbBr_3)_{0.05})$. The PCE of these cells was reported to be 23.2 %, with a certified PCE of 22.6 %.[145] In 2022, Min et al. achieved a new efficiency record for perovskite solar cells by forming an interlayer between a SnO_2 electron-transporting layer and a halide perovskite with a PCE of 25.8 % and retaining 90 % of their original efficiency after 500 hours of continuous light exposure. The authors claim that the interlayer has atomically coherent features that enhance charge extraction and transport from the perovskite layer and form fewer interfacial defects.[6]

Another much investigated area of application is hybrid perovskites as active layers in light-emitting diodes, as they have great colour purity and easy wavelength tunability[148] (Figure 2.15c) First working device was presented by Tan et al. with 0.1 % external quantum efficiency.[149]. Strategy to improve performace was to apply reduced dimmesnionallity perosvkties with larger exciton binding energies for exciton emission which can improve the PLQY at low excitation intensity and thus to some extent overcomes the limitation of bimolecular recombination (low PLQY)

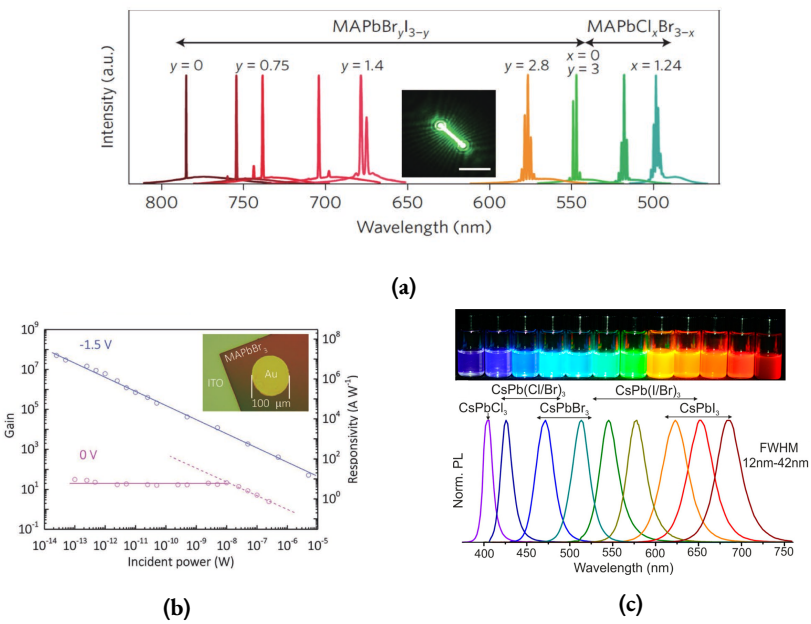

Figure 2.15: a) Widely wavelength-tunable lasing from single-crystal $MAPbX_3$ (X = Cl, Br, I and mixed Cl/Br and Br/I) nanowires at room temperature. Inset: optical image of a single $MAPbBr_3$ nanowire with a length of 13.6 μm under excitation above the lasing threshold. Reproduced with permission from ref. [146] Copyright 2015, Nature Publishing Group. b) Gain and responsivity of a single-crystal $MAPbBr_3$ photodetector. The highest gain and responsivity are about 5×10^7 and 1.6×10^7 A W^{-1}, respectively. Inset: optical image of the photodetector device. Reproduced with permission from ref. [147] Copyright 2018, Wiley-VCH. c) $CsPbX_3$ NCs (X = Cl, Br, I) colloidal solutions in toluene under UV lamp (λ = 365 nm) and representative PL spectra (λ = 400 nm for all but 350 nm for $CsPbCl_3$ samples) Reproduced with permission from ref. [148] Copyright 2015, American Chemical Society.

in the bulk perovskites. Wang et al. demonstrated PeLEDs based on self-organized multiple quantum wells with EQE of 11.7 %.[150] Alternatively, external passivation of the perovskite materials was also used to improve the EQE of PeLEDs by supressing the nonradiative recombination. Lin et al. mixed a $CsPbBr_3$ perovskite with a MABr additive. Obtained sructure passivates the nonradiative defects in $CsPbBr_3$ crystals, which greatly enhanced the PLQY and resulted in a record EQE of 20.3 %

of the based PeLEDs.[151] Cao et al. fabricated PeLEDs with a peak EQE of 20.7 %, by simply introducing amino-acid additives into the perovskite precursor solutions for effectively passivating the perovskite surface defects and thus reducing the nonradiative recombination.[152] Whereas, unlike the above discussed multilayered PeLEDs, the single-layered PeLED device is fabricated of a perovskite emitter sandwiched between two electrodes. The EQE of a single-layered PeLED device was found to be of 5.7 % for a $CsPbBr_3$ based thin film device.[153]

Perovskites are also excellent gain materials for developing high-performance lasing devices. Xing et al. was first to report spontaniuos amplified emmision of $MAPbX_3$ perovskite thin film processed at low temperature.[76] Room temperature perovskite lasing was demonstrated by Deschler et al. via embedding $MAPbI_{3-x}Cl_x$ perovskite thin films into a DBR Fabry–Pérot Cavity.[78] Beyond the usage of thin films coupled with external cavities, perovskite nanostructures such as nanoplates, nanowires and quantum dots that can serve as both active media and microcavities are also demonstrated to be good candidates for small solid-state lasers. Zhu et al. in this area demonmstrated wavelength-tunable lasing effect from $MAPbX_3$ (X = Cl, Br, I) nanowires (Figure 2.15a) with pretty low lasing threshold (220 nJ cm^{-2}).[146]

In addition to typical applications in photovoltaics, LEDs and lasers, perovskites have also attracted much attention as visible light region photodetectors. Yang et al. reported a photodetector based on a single-crystal $MAPbBr_3$ thin film with a gain of 50 million, a gain bandwidth of 70 GHz, and a detection limit of 100 photons at a modulation bandwidth of 180 Hz.[147] This remarkable performance (Figure 2.15b) was achieved by replacing the polycrystalline thin film with the single-crystal thin film. As well as perovskite photodetectors fabricated on rigid substrates, the construction of flexible perovskite photodetectors with perovskite films on flexible substrates was also demonstrated, with sensitivity (R) values ranging from a few to hundreds of mA W^{-1}.[154] For example, Hu et al. demonstrated high-performance flexible $MAPbI_3$ photodetector by developing a novel evaporation method to fabricate uniform and hole-free perovskite films on flexible substrates. The device sensitivity was 81 A W^{-1} at a low working voltage of 1 V, which is three orders of magni-

tude higher than previously known flexible perovskite thin film photodetectors.[155] These flexible photodetectors showed excellent bending stability and durability under various bending situations while maintaining their optoelectronic performance. Zhang et al. fabricated a novel perovskite-erbium-silicate nanosheet hybrid photodetector with a remarkable spectral response at 1.54 μm .[156] Outstanding sensitivity and external quantum efficiency comparable to previously reported microscale silicon-based sub-bandgap photodetectors have been demonstrated in these devices. More importantly, the response speed is 900 μs, which is five orders of magnitude faster than previously reported silicon-based hot electron photodetectors at telecommunication wavelengths.

3 Experimental Methods

3.1 Transient Photoluminescence

Time-Correlated Single Photon Counting

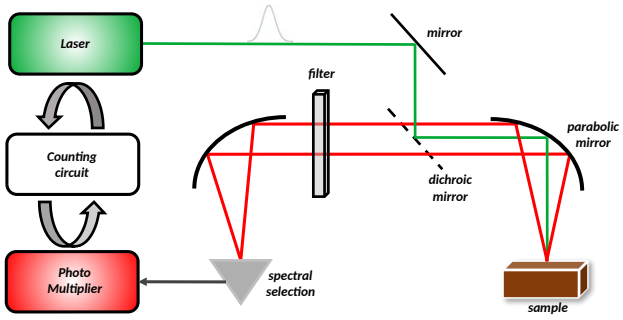

Figure 3.1: Schematic representation of TCSPC measurement setup.

Transient PL is one of the most important measurement methods for investigating questions about charge carrier recombination processes. Time-correlated single photon counting (TCSPC) is a statistical technique for recording time-resolved fluorescence data that provides kinetic information about the excited state. This technique uses a pulsed laser with a high repetition rate that repeatedly excites the sample. The fluorescence of the sample is collected by parabolic mirrors, passed through a monochromator and detected with a single photon counting detector. Single photon detection is performed with an avalanche photodiode or other photomultiplier. Schematic representation of the TCSPC setup is show in Figure 3.1.

The photoluminescence decay kinetics in this work were measured using the Edinburgh Instruments TCSPC fluorescence spectrometer F900. The pulsed picosecond diode laser EPL-470, which produces 72 ps pulses at 470 nm with a repetition rate of 500 kHz (interval 2 μs) was used for the sample excitation.

3.2 Electric Field-Induced Luminescence Quenching

Electric field-induced luminescence quenching is an advanced PL measurement technique that uses an electric field to modulate PL properties. It is possible to use this technique with continuous illumination to directly observe the changes in luminescence due to the electric field, or to use it in a pulsed mode and observe modulated PL transients. A typical measurement setup and kinetics is shown in Figure 3.2. For steady-state liuminescence registration, fast spectrometers or photomultiplier tubes are used, depending on the time constants of the occurring processes. The electric field is generated by a function generator and the sample is excited with a stable CW diode laser.

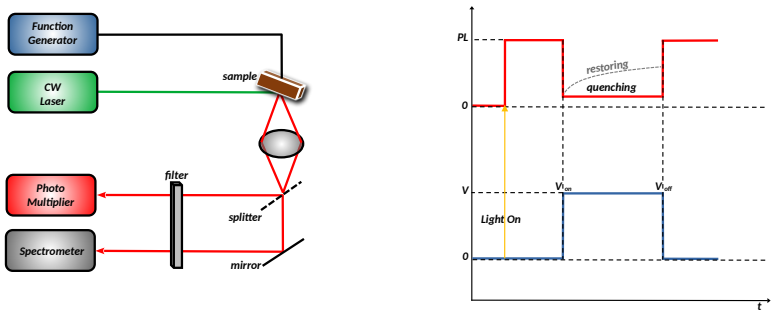

Figure 3.2: a) Schematic representation of an EFILQ measurement setup in steady state operation. b) Conceptual representation of EFILQ measurement kinetics.

In this work, EFILQ in stedy-state mode was measured with AvaSpec-HS1024 x58 fiber-optic spectrometer (Avantes) or the photomultiplier tube (Hamamatsu H10721-20), depending on the duration of the applied voltage. The sample was biased with function generator (Tektronix AFG3101) and Continuous-wave 635 nm 5mW diode laser (CPS635, ThorLabs) was used for sample excitation.

EFILQ in ultrafast mode were performed by Hamamatsu Streak camera operating in synchroscan regime. The samples were excited by 515 nm, 80 fs duration light pulses generated by Femtosecond Yb:KGW laser (Light Conversion Ltd.). Excitation intensity was of about 100 nJ/cm2. The laser operated at a repetition rate of 80 MHz, however mechanical chopper was additionally used to produce pulse packets of 500 μs duration at 15 Hz repetition rate. The pulse packets were synchronized with the electrical pulses of 25 ms duration. This setup enabled measurements of the PL kinetics at different times before and after the electrical pulse onset by turning the pulse packet arrival time relatively to the onset of the electrical pulses. The time resolution of the entire system was approximately 13.0 ps.

3.3 Transient Electroluminescence

Transient EL is a commonly used technique to study the properties of optoelectronic devices. It can be used to obtain a dispersion parameter related to structural disorder as well as information on carrier dynamics, mobility, and trapping. This technique also allows high excitation densities to be achieved in the devices under investigation, which can be used to study the lasing effect in new materials. he transient EL signal is obtained by exciting the sample with selected waveform voltage pulses. The obtained emission is collected with optical lenses and passed to a photomultiplier tube connected to the oscilloscope. The general scheme of the transient EL measurement is shown in Figure 3.3. The voltage V_1 across the resistor R_L measures the external current flowing through the sample; the voltage V_2 across R_{PM} measures the current generated by light.

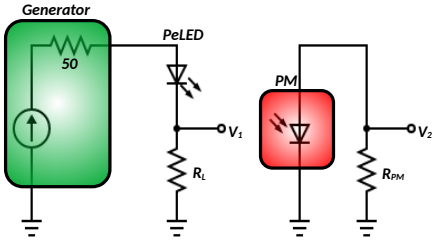

Figure 3.3: Schematic representation of an Tr-EL measurement scheme.

The transient EL in this work was measured with a Hamamatsu H10721-20 photomultiplier tube. The devices under investigation were exited with rectangular voltage pulses generated by the Tektronix AFG3101 function generator. The current was measured with an Agilent Technologies DSO5054A oscilloscope with an input resistance of 50 Ω.

3.4 Transient Photocurrent

In transient photocurrent (TPC) measurement, the device under investigation is irradiated with modulated light (typically a short laser pulse) and the transient photocurrent decay is measured in the time domain, from which important information about the charge carrier dynamics can be obtained. An advantage of this technique is that it is relatively easy to implement and that such measurements can be performed on complete devices under conditions that approximate real operating conditions. A typical schematic representation of the measurement setup is shown in Figure 3.4a. The sample is kept in a short-circuit condition, i.e. it is connected to a small resistor (50 Ω). An external electric field is generated by a fuction generator for carrier extraction and the laser pulse creates a perturbation in the device current, which is measured on the oscilloscope as a voltage drop V_1 across the resistor, which can be converted into a transient current by applying Ohm's law (Figure

3.4b). Analysis of the decay provides information about the recombination and extraction processes of the charge carriers. It is important to note that the RC current from the sample is subtracted from the photocurrent to obtain the current generated only by light.

The photocurrent transients in this work were measured with an Agilent Technologies DSO5054A oscilloscope with an input resistance of 50 Ω using excitation laser pulses from the Topas-C optical parametric amplifier (Light Conversion Ltd.) pumped through the Integra-C femtosecond Ti:Sapphire laser (Quantronix Inc.), which generates pulses of ≈150 fs with 430 Hz repetition rate. The samples under investigation were biassed with rectangular voltage pulses generated with the Tektronix AFG3101 function generator.

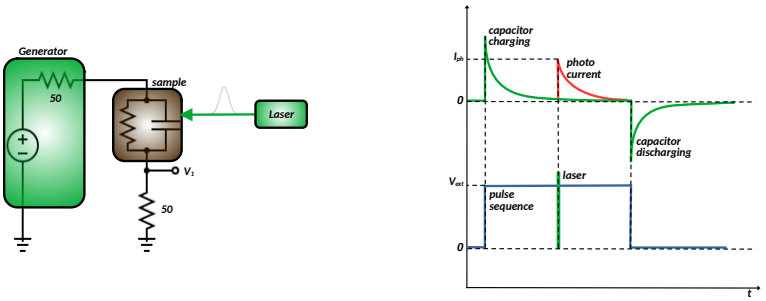

Figure 3.4: a) Schematic representation of an TPC measurement setup. b) Conceptual representation of TPC measurement kinetics.

3.5 Time-Delayed Collection Field

Time-delayed collection field (TDCF) measurement technique is a variant of TPC measurement method performed with the same equipment. It provides additional information on carrier density decay and mobility kinetics. In the conventional implementation, the sample is excited at zero voltage (V_{gen}) while the extraction voltage (V_{ext}) is applied after a variable time delay (Figure 3.5a). The dependence of the to-

tal extracted charge (cumulative current) on the delay time between the optical excitation and the application of the extraction voltage represents the decrease of the charge carrier density at zero bias voltage. On the other hand, the initial photocurrent is equal to the product of charge carrier density and charge carrier mobility; therefore, the TDCF can be used to follow the evolution of the charge carrier mobility. Furthermore, the field dependence of charge generation can be studied by changing the generation voltage while keeping the time delay short.

In this work, a new flip-field variant of the TDFC technique was introduced for the study of hybrid perovskite films. In this case, the generation and extraction voltages have opposite signs (Figure 3.5b). Thus, the photogenerated charge carriers initially drift in one direction and are extracted in the opposite direction after a certain time. This measurement provides information about spatial traps that hinder the extraction of the charge carriers.

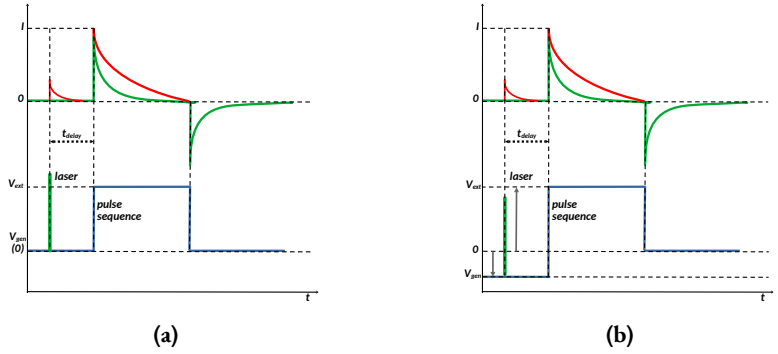

Figure 3.5: Conceptual representation of TDCF a) conventional b) flip-field measurement kinetics.

4 Results and Discussion

In this chapter an overview of the scientific publications **A**-**F** is given, which is divided into individual articles.

4.1 Overshoot Effect in Hybrid Perovskite Solar Cells

In the first article of this work (Paper **A**), electroluminescence (EL) spectroscopy was used to study charge carrier dynamics in hybrid perovskites solar cells under charge injection conditions. These processes are equally important for solar cells and LEDs because electrons and holes recombine in perovskite wether they are photogenerated (photoluminescence) or electrically injected (electroluminescence), so photovoltaic and electroluminescent efficiency are closely related.[157,158] Therefore, EL spectroscopy provides useful information about solar cell properties. It has been used to determine open-circuit voltage losses and some other photovoltaic parameters.[158–160]

First, the dynamics of PL, EL and current of solution-processed ($CsFAMAPb(I_xBr_{1-x})$) triple-cation perovskite solar cell under a DC voltage was investigated. The observed dynamics of the measured parameters on a slow time scale (seconds/minutes, Figure 4.1), shows remarkably different behaviour. The PL (Figure 4.1a) is only weakly voltage dependent, and shows a rapid partial drop during the first 20 s and then remains constant. On the other hand, the intensity of EL is very weak at first and then increases for a few minutes (Figure 4.1b). The electric current also increases, but faster, and is substantial from the beginning. To investigate this

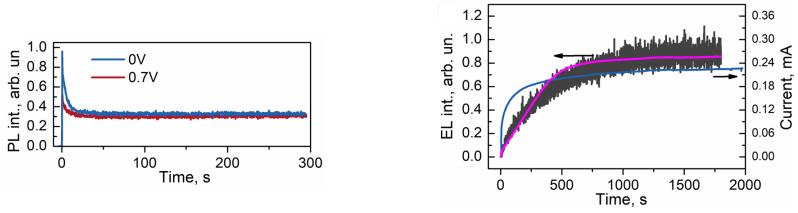

(a) (b)

Figure 4.1: a) PL intensity dynamics after starting optical excitation. Blue kinetics corresponds to the absence of external electric field, and the red one shows the corresponding dynamics when 0.7 V forward bias was applied. b) Experimental (dark gray) and simulated (magenta) EL intensity (left axis) and electric current (blue) kinetics (right axis) measured while applying 0.7 V forward bias.

EL behaviour, the fast dynamics of EL (microseconds) under pulsed voltage bias was studied. Figure 4.2a shows a typical time response of EL intensity and electric current density in a perovskite solar cell driven by a rectangular voltage pulse. After an initial capacitive peak, the current additionally decreased slightly during the voltage pulse. The appearance of EL was delayed by several microseconds, and its intensity gradually increased in contrast to the current response, followed by the strong short-duration spike (overshoot) observed immediately after the voltage was turned off. However, depending on the duration and amplitude of the applied voltage, the temporal profile of EL was also complex (Figure 4.2b, c). The delay time varied approximately inversely proportional to the applied voltage, with an additional delay of about 1 μs caused by the charging of the geometric capacitor, which delayed the voltage growth on the sample.

When the charge transmitted through the sample was held constant while the duration and voltage of electric pulse were changed (Figure 4.2b), the maximum EL intensity at the end of the electric pulse (10–30 μs) was almost identical before the overshoot. This indicates that the intensity of EL is determined by the transmitted charge rather than the applied voltage. However, at higher voltages, the EL kinetics showed a qualitatively different behaviour: after reaching its maximum, the intensity of EL partially decreased again (Figure 4.2c). As mentioned earlier, termination

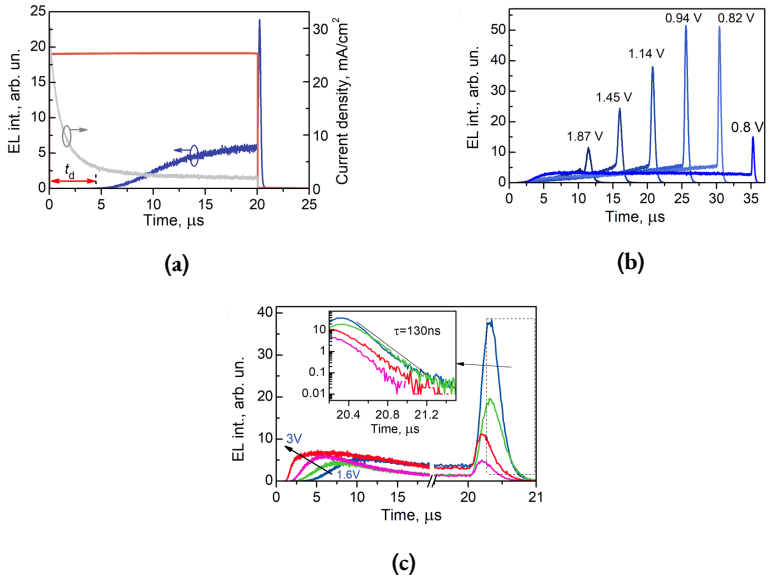

Figure 4.2: a) Current density kinetics (gray, right axis) after the application of 20 µs duration and 1.3 V rectangular voltage pulse (red) and EL kinetics measured at 770 nm (blue, left axis). b) EL transients, measured at identical transmitted charge density per electrical pulse of 80 nC/cm^2, but different pulse durations and voltages. c) EL transients created by 20 µs 1.6, 1.9, 2.2, and 3 V pulses. The inset shows the decay of the EL pulse.

of the voltage pulse triggered an abrupt increase in intensity of EL (Figure 4.2). This EL peak showed a strong and non-monotonic dependence on the parameters of the applied electrical pulses. At a constant electrical pulse duration of 20 µs, the peak decreased with voltage but increased again at high voltages (Figure 4.2c). A similar non-monotonic dependence was also observed by changing the duration of the electrical pulse and its amplitude at a constant transmitted charge (Figure 4.2b). Short high-voltage pulses produced only a weak peak that increased with pulse duration, but long and low voltage pulses again produced a weaker peak.

A model that can explain the EL evolution in perovskite solar cells on both slow (seconds/minutes) and fast (microseconds) time scales is shown schematically in Figure 4.3. It links the dynamics of free charge carriers to the redistribution of ions in

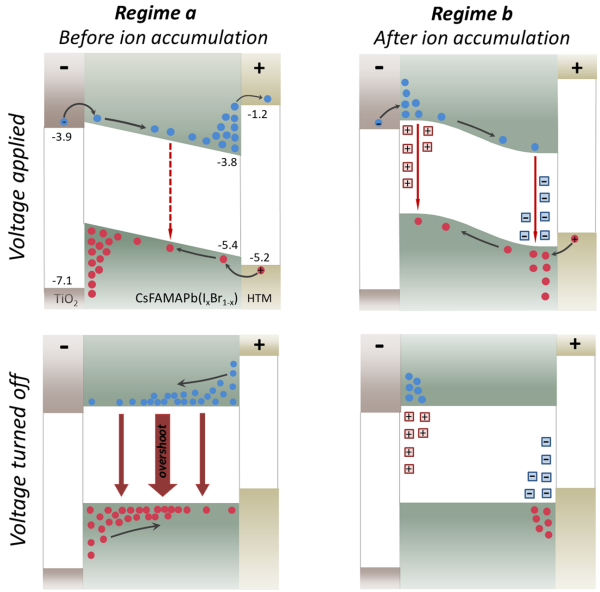

Figure 4.3: Model for the electroluminescence overshoot pulse formation. Left-hand-side graphs show device operation in regime a), taking place before accumulation of ions, and right-hand-side graphs represents operation in regime b), achieved after ion accumulation on the perovskite layer edges. Blue and red circles show distributions of electrons and holes, respectively, while red and blue squares represent distributions of corresponding ions. Red lines show radiative carrier recombination. Numbers in the top left graph indicate energies of the valence and conduction band edges.

the perovskite layer. Two performance regimes of the device can be distinguished: a) before the redistribution of mobile ions and b) after the device has been exposed to the external electric field for some time, resulting in observable ion redistribution within the perovskite. In regime a), electrons and holes are injected across small barriers of TiO_2 and Spiro – MeOTAD, drift through the perovskite, and accumulate near interfaces with charge carrier transport layers due to high extraction barriers. In regime a), electrons and holes are injected across small barriers of TiO_2 and Spiro – MeOTAD, drift through the perovskite layer, and accumulate near interfaces with charge carrier transport layers due to high extraction barriers. A very weak EL signal is observed in this regime, limited by two factors: 1) weak recombi-

nation of charge carriers as they drift through the layer of accumulated charges of opposite sign, and 2) even weaker recombination in the perovskite bulk due to the very small overlap between the distributions of accumulated electrons and holes. The accumulation of charge carriers near perovskite interfaces may be limited by surface recombination[161] and/or permeation through the energy barriers at high voltages. Termination of the applied voltage pulse eliminates the electric field, (or even reverses it for a short time), resulting in a mixing of the spatial distribution of electrons and holes by diffusion, leading to an increase in luminescence intensity observed as the overshoot effect. In contrast, the redistributed mobile ions in regime b) form the p-i-n structure with high hole and electron densities near the interfaces of the transport layers. The injected electrons and holes drift rapidly through the perovskite layer toward the opposing electrodes until they reach regions doped with opposite charge carriers. There they recombine rapidly, causing the strong EL signal. Due to the fast recombination, the injected electrons and holes in regime b) do not accumulate in the perovskite layer, so the overshoot effect does not occur.

These observations led to **the first statement of the thesis**: the accumulation of charge carriers in the perovskite layer under forward voltage causes the electroluminescence overshoot effect, while the ion redistribution induced by the electric field minimizes the accumulation of charge carriers and the overshoot effect in perovskite solar cells.

4.2 Importance of Balaced Injection Current in PeLEDs

In the second article of this work (Paper **B**), previously described implementation of the transient EL spectroscopy was used to investigate a phenomenon known as efficiency roll-off in hybrid perovskite LEDs.[162] Despite the rapid advances in PeLEDs, the EQE tends to decrease at high current density (J). The current density corresponding to a 50 % drop in EQE (J_0) is in the range of ≈ 10–100 mA/cm^2 for many PeLEDs, and such a drop is undesirable when targeting high brightness applications or ultimately injection lasing. Several mechanisms have been proposed to explain the EQE roll-off at high current densities, notably Auger recombination,[163,164] Joule heating, and charge imbalance.[165] For example, using pulsed driving, Kim et. al demonstrated that PeLEDs can sustain J up to 150 A/cm^2 without signs of Auger recombination.[165] They attributed the observed EQE roll-off to Joule heating combined with unbalanced charge injection into the device. Joule heating increases the local temperature of the device, which increases the dissociation rate of the excitons, and it can affect the charge transport properties of the organic layers.[166] It is important to notice, that balancing the charge injection resulted in significantly lower roll-

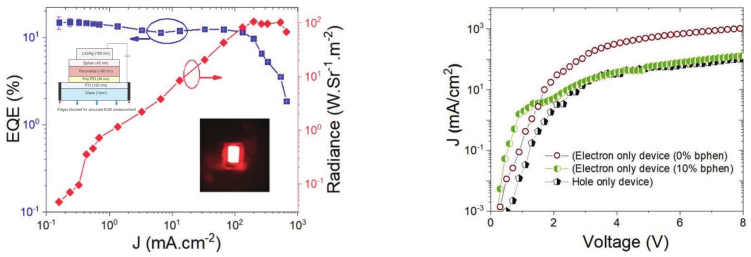

(a) **(b)**

Figure 4.4: (a) EQE and radiance of a champion (in terms of operating current range) PeLED employing 2D/3D perovskite and 10 % Alq_3-doped bphen. Schematic in the inset present various material layers and their thickness used in fabrication for PeLEDs. Photo in the inset shows a bright device operating at 50 mA/cm^2. (b) Unipolar devices to quantify only one type of current flowing through the device for study the charge balancing effect.

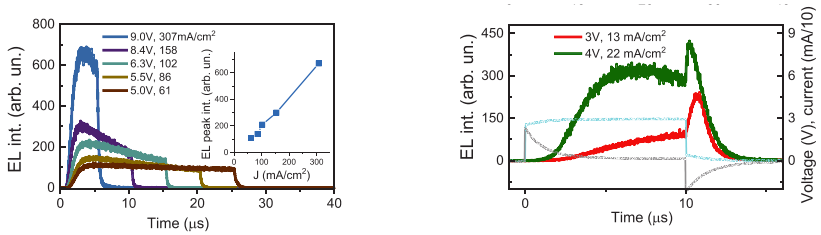

(a) (b)

Figure 4.5: Electroluminescence transients of 2D/3D PeLEDs with pristine bphen as ETL obtained by pulsed driving (20 kHz voltage pulses). a) The duration of the pump pulse and the voltage were varied, keeping the average current the same. The inset in a) shows the dependence of the peak EL intensity on the current density during the pump pulse. b) The pump pulses had a fixed width of 10 µs. Cyan and gray lines show voltage and current pulses, respectively. All transients were obtained more than 5 minutes after the pump pulse train was turned on.

off in organic LEDs (OLEDs)[162] and quantum dot LEDs[167] at high J. For a device operated under unbalanced charge injection conditions, the excess charge could leak through the device, reducing its EQE.[168] The excess carrier concentration may also annihilate singlet excitons.[162]

To thoroughly investigate the balance between charge injection/and transport in Pe-LEDs and its influence on EQE roll-off, improved PeLED devices were fabricated. Stoichiometric tuning of the 2D/3D perovskite films resulted in high EQE, indicating dominant radiative recombination at $J \approx 0.1\text{-}1\,\mathrm{mA/cm^2}$. Systematic control of charge injection into the emitting layer minimized the EQE roll-off up to $J \geq 200\,\mathrm{mA/cm^2}$, and the optimized devices maintained EQE $\approx 10\,\%$ up to $J = 200\,\mathrm{mA/cm^2}$ (Figure 4.4).

A model explaining the importance of charge balance at high current densities was constructed from pulsed bias transient electroluminescence measurements. Figure 4.5 shows EL transients for 2D/3D PeLEDs with pristine bphen as ETL, induced by periodic 20 kHz electrical pulses of varying duration from 5 to 25 µs. During these measurements, the average current was kept identical by adjusting the

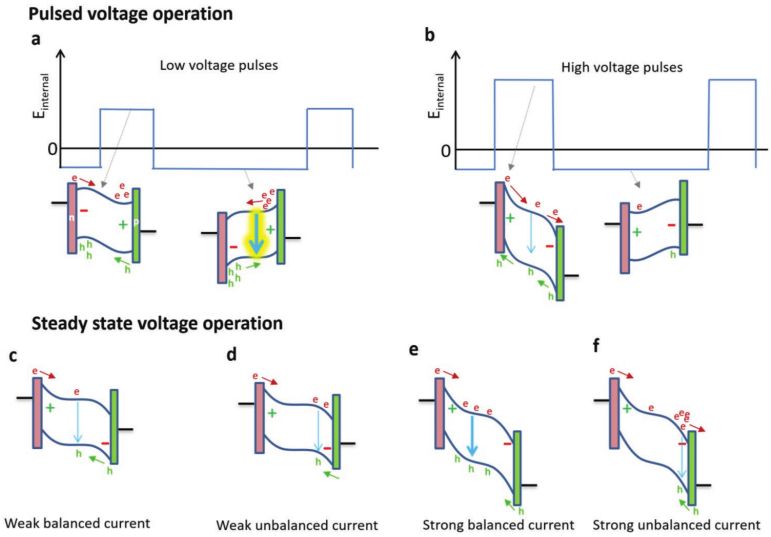

Figure 4.6: Top panel a) and b) show driving of PeLEDs by periodic pulses. At low applied pulse bias, accumulation of positive (+) and negative (−) ions and/or vacancies is determined by the built-in field (negative $E_{internal}$) by screening it during intervals between voltage pulses. The pulse action creates potential pockets at the opposing interfaces, leading to separation and accumulation of electrons and holes. Once the electrical pulse is terminated, electrons and holes move and mix causing fast recombination and an EL overshoot (Figure 4.5b). High-voltage pulses generate opposite ion distribution and a potential shape that facilitates carrier leakage rather than accumulation and, thus, no overshoot. After a high-voltage pulse, potential pockets for electrons and holes are formed (at built-in electric field) which cause carrier accumulation at zero applied voltage. Bottom panel c)–f) show PeLEDs operation at steady-state applied voltage at various current regimes when ions always cause electric field screening. c) and d) show PeLED performance at low voltage and weak current when carriers efficiently recombine; e) and f) illustrate electron accumulation next to positive electrode and leakage.

pulse voltage, which also ensured identical charge injection during the voltage pulse. This condition was important because otherwise the results varied greatly depending on the pulse duration and voltage. It is assumed that this condition helps to ensure that the spatial distribution of mobile ions remains the same. As shown by the inset in Figure 4.5, the intensity of the EL peak increases linearly with current,

indicating no efficiency roll-off for a pulse current density of at least 300 mA/cm^2. The EL transients (Figure 4.5), however, show that the intensity of EL decreases on a time scale of tens of microseconds. Figure 4.5b shows the EL transients obtained when the average current was reduced by lower voltage pulses. The transients show complex EL dynamics. The short EL spike reported earlier (overshoot effect) is also evident in the PeLEDs. In hybrid perovskite devices, mobile ions can redistribute during the application of an external voltage. This phenomena can explain the difference observed between the dynamics of EL at higher voltages (Figure 4.5a) and lower voltages (Figure 4.5b), as shown in the schematic diagram in Figure 4.6. The shape of the electric potentials across the perovskite layer is determined by the applied voltage, the built-in electric field, and the distribution of mobile ions. The ions move relatively slowly (on a time scale of minutes), so their distribution can be expected to remain unchanged throughout the measurement period, i.e., during the pulse action and the intervals between pulses, which are determined by the average electric field generated by the electric pulse and the built-in field (short circuit) between pulses which are in opposite directions. At low voltage and short duration of the electric pulses, the built-in field dominates and creates an ion distribution profile that shields the built-in field between the electric pulses and creates potential pockets during the action of the voltage pulses, as shown in Figure 4.6a. The injected charge carriers, which avoided recombination when passing through the perovskite layer, accumulate in these potential pockets but mix when the electric pulse is removed. This leads to rapid recombination of the charge carriers, which can be observed as EL overshoot. At high pulse voltages (Figure 4.6b), the pulses and ions redistribute accordingly. They produce strong potential drops at the interfaces, resulting in a rapid drift of the injected charge carriers and their escape to the opposite electrode. This prevents the accumulation of charge carriers, which leads to the absence of an overshoot effect in the intervals between voltage pulses, which in turn leads to the accumulation of charge carriers that neutralize the ionic charge. This explains the dynamics of EL during the voltage pulse shown in Figure 4.5a. The pulsed dynamics of EL demonstrates the importance of the spatial car-

rier distribution for PeLED operation and allows schematic plots to be drawn for the steady state PeLED performance in different regimes (Figure 4.6c-f). The ion distribution is determined by the average field. In steady-state mode, the external field dominates over the built-in field and causes field screening effect in the centre of the perovskite layer (Figure 4.6c). The charge carriers recombine efficiently in a flat potential region (Figure 4.6c, e). In the case of an unbalanced, stronger electron current, the recombination region shifts toward the hole-injecting electrode (Figure 4.6d). In the case of a strong and unbalanced current, the recombination region shifts strongly toward the positive electrode. The recombination cannot prevent the accumulation of electrons and their leakage to the positive electrode, which reduces the efficiency of PeLED performance.

These results led to **the second statement of the thesis:** an unfavorable space charge distribution leads to a roll-off of the external quantum efficiency in hybrid perovskite light-emitting diodes, which can be avoided by a balanced injection current.

4.3 Multiphase Performance Dynamics of PeLEDs

In the third article of this work (Paper **C**), ionic motion in PeLEDs was investigated, since many problems such as performance hysteresis,[149,169] variations in EL EQE and PL efficiency[170,171] are related to ion movement under electrical stress. The performance hysteresis in perovskite solar cells has been extensively studied and attributed to the changes in perovskite transport layer interfaces or to the movement of mobile ions.[140,172–174] Ion motion in metal halide perovskites is a very complex and poorly understood phenome-non. In general, all the constituents of metal halide perovskites - halides, lead, and organic cations - can form vacancies, interstitials, and anti-sites, that can be mobile and act as charge carrier traps.[140,175,176] On the other hand, theoretical evaluations show that only a few of them form deep traps that act as nonradiative recombination centers,[175] while shallow traps have a negligible effect on trap-assisted recombination.[177] In lifetime measurements of PeLEDs, it is consistently observed that various PeLED stacks improve over a period of minutes to hours before they begin to degrade.[170,178–180] The persistent improvement in EQE of PeLED under applied positive voltage (so-called stressing regime) was explained by the movement of mobile excess iodine ions filling vacancies and decreasing the concentration of iodine interstitials, thus acting as deep carrier traps.[170,180]. Consequently, PeLEDs exhibit complex performance dynamics over a wide timescale range, which has been commonly attributed to ionic motion. However, the reported time scales, the intensity of the observed changes, and their association with specific types of ions are highly variable, suggesting that this issue requires further attention.

First, the EL and current dynamics of a PeLED based on $MAPbI_3$ perovskite were studied upon abrupt application of the pump voltage. After the first application of a constant voltage to the PeLED, only for a few minutes, a significant growth of EL intensity and electric current was observed. Figure 4.7a shows the kinetics of normalized EL intensity and current growth at room temperature after application of 2 V. Immediately after the voltage was applied, the EL intensity was very weak

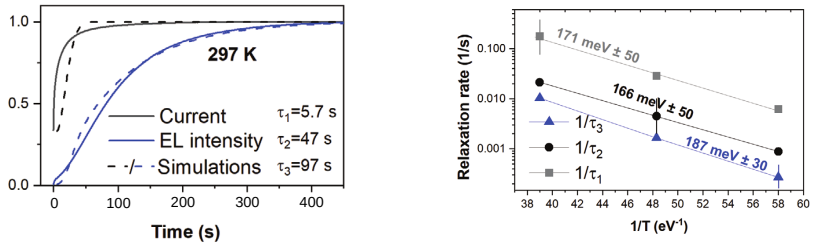

Figure 4.7: EL and current dynamics in pristine PeLEDs under first-time application of 2 V. a) Normalised EL (blue lines) and current (black lines) growth kinetics, measured (solid lines) and simulated (dashed lines, see below for discussion) b) Arrhenius plot for the slow EL growth time constant τ_3 (blue), fast current growth time constant τ_1 (grey line), and slow current growth time constant τ_2 (black).

but increased and reached a plateau after a few minutes at room temperature (know as stressing effect[170]). The electric current was nonvanishing from the beginning and then increased 3–5 times, but the growth rate was much faster than that of EL. The initial current was almost constant during tens of ms and produced almost no EL during this time. It should be noted that the delayed growth of EL cannot be explained by the charging of the sample capacitance, since according to the properties of the device RC this process should occur on a time scale of several μs, i.e., about 10^4 times faster. Therefore, the initial absence of EL suggests that either a) the initial current is generated by the injection of only one type of charge carrier, which then escapes to the opposite electrode and does not generate EL, or b) EL is not present due to rapid non-radiative recombination. The EL starts to grow after about 100 ms, and up to about 10 s it grows simultaneously with the current. Nevertheless, the intensity of EL remains low during the first ≈10 s. The faster growth starts only when the current almost stabilizes, suggesting that the later growth process is not related to carrier injection. Following previous works it is natural to relate the observed processes to the motion of ions in the hybrid perovskite. The kinetics of the current growth can be fitted quite well (dashed black line in Figure 4.7a) with the bi-exponential rise functions. The EL kinetics was successfully fitted (dashed

blue line in Figure 4.7a) by using the same time constants τ_1, τ_2 and adding an additional delayed, slow-saturating growth component (for details on the fitting, see Paper **C**). Figure 4.7b shows the determined activation energies E_a of the mobile ions from the Arrhenius equation 4.1

$$k_i = k_{i_0} \exp\left(-\frac{E_a^i}{k_B T}\right) \tag{4.1}$$

where $k_i = \tau_i^{-1}$, k_B Boltzmann constat and T is the absolute temperature. The Arrhenius plot yields surprisingly identical activation energies of about 175 meV for all three processes, strongly suggesting that they all have the same physical origin, i.e., are related to the same type of ions. According to the theoretical studies, iodine interstitials and vacancies have the lowest activation energies, ranging from 80 meV to over 800 meV in various publications.[137,140,176,181] Very similar activation energy values (E_a = (137 ± 28) meV and (190 ± 50) meV) have been determined experimentally from the light soaking-induced PL enhancement and attributed to the motion and annihilation of iodide interstitials and vacancies.[182,183] The attribution of the observed dynamics to iodine species is consistent with other publications claiming that iodide defects are particularly important in optoelectronic devices because they can move easily when an electric field is applied.[137,182,184,185] According to Dong et. al, the movement of the negatively charged iodine interstitials I^- occurs on a time scale of tens of seconds.[186] A similar conclusion that the redistribution of iodide defects causes reversible variations in current and EL intensity on a time scale of seconds was also recently suggested by the analysis of performance hysteresis of $FAPbI_3$ PeLEDs.[169]. Samples under investigation were prepared under iodine-rich conditions from a solution containing 20 mol % excess PMAI (benyzlammonium iodide), suggesting that iodide interstitials inside the crystallites or iodine ions at the crystallite boundaries should be the dominant defects.[175,185] Although the role of other types of charged mobile species cannot be completely ruled out, all evidence suggests that the I^- ions are responsible for the observed PeLED performance dynamics.

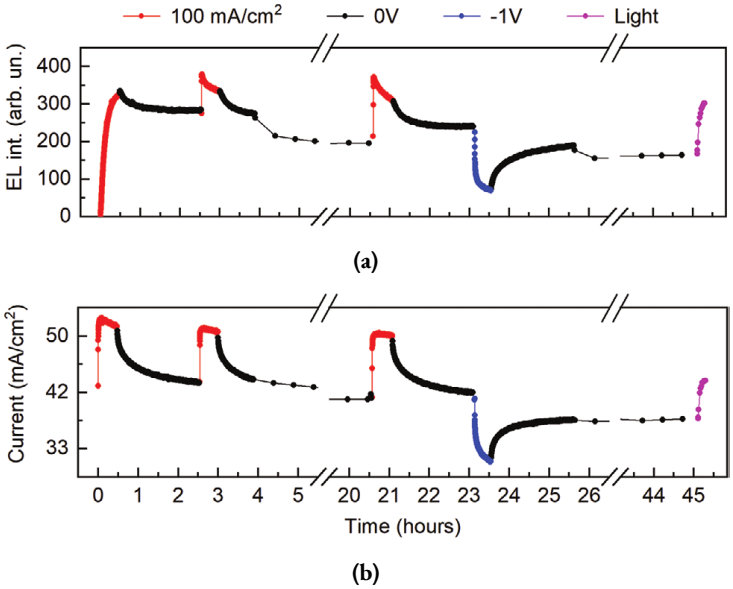

Figure 4.8: Stressing-induced processes monitored by pump pulse trains. a) EL intensity and b) current dynamics monitored by short positive voltage pulses of 1.45 V, during following types of stress and relaxation: stressing by 100 mA/cm^2 current (red dots); relaxation at zero applied voltage (black dots); stressing by negative −1 V voltage (blue dots); light soaking at 0 V voltage (magenta dots).

To obtain information about the stressing characteristics, an investigation technique was developed to decouple the monitoring of the PeLED parameters from the stressing effects. To stress the device, 100 mA/cm^2 current density was applied (the voltage was approximately 1.7 V) for different time intervals, and after each stressing interval, the PeLED status was monitored with a series of square pulses with an amplitude of 1.45 V and a duration of 5 µs, followed by a 30 µs rest period for 30 ms. These short low-voltage monitoring pulses only slightly affected the performance of the PeLED. This study protocol made it possible to separate the stressing of the PeLED from the monitoring of its parameters. It also allowed to study the recovery of the PeLED performance after the stress current ended, as well as the effects of other influences such as negative voltage and light soaking effects. To obtain more

information about the state of the PeLED, the current and EL spectra were recorded simultaneously. Figure 4.8 shows the EL and current kinetics measured for the untreated sample at different time intervals after application of a positive (red dots), or negative (blue dots) voltage, during relaxation (0 V) (black dots), and under light ilumination at (1 sun intensity at 0 V) (magenta dots). The initial EL intensity of the unstressed sample was very weak. The growth of EL was 2–3 times slower than at a constant voltage of 2 V, obviously due to the weaker current generated by the lower stressing voltage of 1.7 V. In addition, the current-induced Joule heating at higher current densities increases the junction temperature,[187] which may accelerate the process due to its highly thermally activated nature. The current growth was less significant than when a constant voltage was applied, apparently due to the non-negligible influence of the monitoring pulses. After termination of the stressing voltage, both EL and the current gradually decreased. During several hours, the current decreased to the same value as it was before stressing, whereas the EL intensity decreased only by less than 20 %. Moreover, the decay rates of EL and the current kinetics were very similar. The second application of stressing voltage after 2.5 h and the third application after 22 h caused very rapid EL growth, even to a higher value than obtained during the first stressing session. Surprisingly, after this rapid initial increase, the EL intensity slowly decreased during the second and third stressing sessions, in contrast to the steady increase during the first session. The experimental data described above lead to the stressing scenario shown schematically in Figure 4.9. The intensity of EL is determined by three processes: rapid reversible EL growth consistent with bi-componential saturating current growth with time constants τ_1 and τ_2; slow persistent EL growth with time constant τ_3; and reversible EL decay. The time constants vary as a function of applied voltage and temperature. This model naturally explains the two striking differences observed during the first and subsequent stressing sessions, namely the greater EL intensity and its decay observed during the subsequent stressing sessions. During the first session, the reversible EL decay is compensated by the irreversible EL growth, which does not occur during the subsequent sessions.

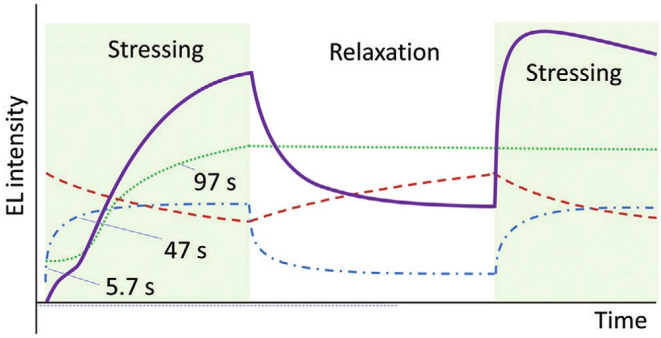

Figure 4.9: Major stressing-induced processes. EL development kinetics (solid magenta line), bi-exponential current growth causing rapid reversible EL growth component (dash-dotted blue line), slow irreversible EL growth component (dotted green line), and reversible EL decay (dashed red line). The numbers show time constants of various processes at room temperature at 2 V stress voltage obtained from exponential fitting

To gain deeper insight into the stressing dynamics and independently verify this proposed multicomponent scheme, the stressing-induced dynamics of several other PeLED parameters: EL wavelength, PL efficiency and its decay kinetics, sample capacitance, and electro-absorption (EA) were measured. Stressing-induced changes of these parameters are shown in Figure 4.10. The initial developement phase of EL lasts approximally 20 s at RT, during this time it was observed how other PeLED parameters change. Figure 4.10a shows the dynamics of PL intensity observed during sample stressing. The intensity of PL was measured at 0 V when stressing voltage was temporarily turned off. As can be seen in the inset of Figure 4.10a, the intensity of PL decreases slightly in the first ten seconds, i.e., during the initial development phase. Thereafter, it increases more than 2.5-fold during the slow irreversible EL growth phase. Termination of stressing voltage also leads to a rapid increase in PL intensity. Figure 4.10b shows the PL decay kinetics, revealing a biexponential decay. The kinetics were measured at 0 V after the sample was stressed for the indicated time interval. Comparing the PL decay kinetics before and after 15 s of applied stressing, we find that the fast stressing-induced PL intensity decay is mainly caused by a faster PL decay on a time scale of tens of ns. The PL decay for unstressed

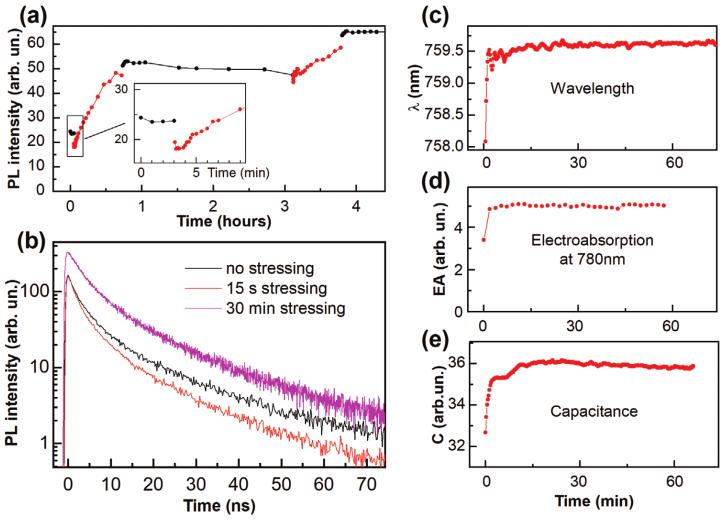

Figure 4.10: Changes of various PeLED parameters, induced by stressing with 100 mA/cm^2 current. a) PL intensity dependence on stressing time (red points) and relaxation at applied zero voltage (black points), b) PL decay kinetics in sample stressed for different time intervals, c) wavelength of the EL band maximum, d) EA at 780 nm, and e) capacitance kinetics during sample stressing.

samples has also been measured under variuos negative and positive voltages that do not reach the EL operating point. The applied voltage mainly alters the slow decay phase, apparently by changing the electric field within the perovskite layer and thus the charge carrier extraction. This means that the faster PL decay observed in the short-time stressed sample may also be caused by the change of the electric field within the perovskite film. This assumption is supported by the EA measurements (Figure 4.10d), which show an increase in the EA signal after short stressing. The EA signal is proportional to the square of the electric field strength, so changes in the EA signal should be considered indicative of the redistribution of electric field strength across the perovskite film thickness. Additional support is also provided by the capacitance measurements, which show an increase in capacitance during the fast stressing phase (Figure 4.10e), indicating that the electric field in the stressed sample is concentrated in the thinner perovskite layer. The initial fast stressing phase

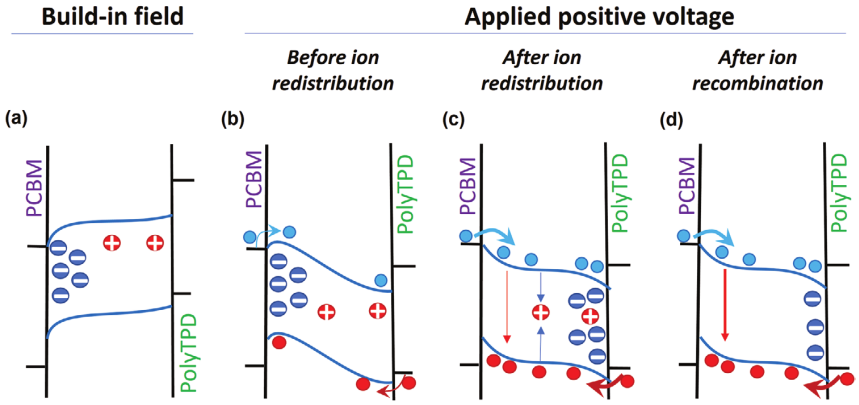

Figure 4.11: Schematic representation of potential surfaces and ion distributions at different phases of the PeLED stressing. a) Under built-in electric field, I^- ions (blue symbols) and vacancies V^+ (red symbols) accumulate next to PCBM and PolyTPD electrodes, respectively. b) Abrupt application of stressing voltage creates electric field potential with barriers for electron and hole injection, and results in only weak EL because of the spatial separation of electron and hole densities. c) Redistribution of I^- ions and vacancies (assumed to be less mobile) reduces barriers for both electrons an holes and also causes ion recombination. d) EL intensity increases when ion recombination eliminates majority of vacancies acting as recombination centers.

also changes the EL spectrum; the wavelength of the luminescence peak exhibits a slight red shift (Figure 4.10c). The shift in emission wavelength was attributed to the interference of EL radiation emitted toward the transparent electrode and reflected from the metal electrode: The red shift indicates that the recombination zone moves away from the interface with the electron transporting layer.[165,187] Thus, this is another indication that the fast stressing phase changes the distribution of the electric field and consequently the distribution of charge carriers within the perovskite layer. All the observations described above suggest that the fast phase is caused by ionic motion, which alters the electric field distribution within the perovskite layer.

All observed experimental data led to a qualitative model, which is shown schematically in Figure 4.11. At 0 V, different work functions of the electrodes generate an electric field in the perovskite layer that is opposite to the direction of the elec-

tric field during operation of the PeLED. This field accumulates negative mobile I^- ions adjacent to the PCBM electron transport layer, while positively charged vacancies accumulate near to the hole transport layer (PolyTPD). The accumulated ions partially or completely screen the electric field in the central part of the perovskite layer. The field screening would be assymetric, as shown in Figure 4.11a for the case of different concentrations of positive and negative ions. This potential shape indicates that the flat potential in the central part of the perovskite layer causes slow extraction of photogenerated charge carriers. Therefore, the untreated sample shows relatively weak PL quenching (as shown in Figure 4.10b) which is caused by the extraction of the charge carriers. Applying the stressing voltage does not immediately change the ion distribution, resulting in the initial potential shape as shown in Figure 4.11b. This potential shape creates additional barriers for charge carrier injection, while the additional barrier for hole injection of about 200 meV is caused by the difference between the work functions of the perovskite and the hole transporting layer. The barriers for electrons and holes are different, so the injection of one type of carrier can be partially or almost completely blocked, resulting in a very low EL. Subsequently, the applied stressing voltage causes the ions to drift away from the interfaces with the transport layers, reducing the barriers to carrier injection. The potential then takes the form shown in Figure 4.11c, allowing for efficient injection of both electrons and holes, and thus a more efficient EL. However, the role of positive and negative ions seems to be very different in the samples studied. This is because: a) identical activation energies obtained for different processes strongly suggest that one type of mobile ion strongly dominates, and b) the concentration of iodine interstitials in the iodine-rich samples is likely to be much greater than that of iodine vacancies. Figure 4.11 shows the dominant role of I^- ions. It should be noted that other processes that can change the current and thus the EL intensity cannot be completely excluded. For example, the applied voltage can cause changes in the contact resistance of the electrodes and thus carrier injection rates. However, changes in the intensity of the perovskite PL and the EL wavelength, which occur simultaneously with the current and EL growth suggest that all these processes are

interconnected and caused mainly by the processes in the perovskite layer. On the other hand, ion injection into the transport layers has been shown to be at least partially responsible for the PeLED EQE roll-off and degradation that occur at higher voltages and for longer times.[188,189]

Slow permanent EL growth. The slow stressing phase starts with a delay of about 25 s at RT after application of the stressing voltage. It results in a sharp increase in EL intensity while the current remains at the same level as in the preceding fast stressing phase. The slow stressing phase also causes an almost threefold permanent increase in the intensity of PL (Figure 4.10a). As can be seen in Figure 4.10b, the slow stressing phase increases the initial intensity of PL kinetics, slows its decay during the first 10 ns, but does not change the decay of PL on a time scale of $t >$ 10 ns (red and magenta curves obtained after 15 s and 30 min stressing). The PL kinetics at $t > 10$ ns is attributed to carrier extraction, so this process does not change during the slow stressing phase. On the other hand, the fast initial PL decay should be attributed to carrier trapping. Therefore, the growth of EL and PL during the slow stressing phase is therefore a manifestation of the enhanced efficiency of radiative recombination, apparently caused by the reduced nonradiative Shockley-Read-Hall recombination associated with carrier trapping. This conclusion is supported by the increased open-circuit voltage of the stressed PeLED operated as a solar cell, which is also indicative of the reduced non-radiative relaxation. This slow phase, as mentioned earlier, is characterized by the same activation energy as the fast phases, strongly suggesting that it is also related to the motion of the iodine ions.

A similar PL enhancement of $MAPbI_3$ perovskites induced only by optical soaking, is a well-known phenomenon. It has been explained by excitation-induced spatial redistribution and recombination of iodine interstitials and vacancies which act as recombination centers.[182,183] Such recombination is not possible in PeLEDs before their stressing because, according to the presented model, the built-in electric field concentrates the iodine ions and vacancies in narrow layers adjacent to the opposing transport layers so that they are spatially separated and cannot recombine. The applied stressing voltage pulls the ion populations toward each other, they mix,

as shown in Figure 4.11c, and begin to recombine. Thus, the delayed start of the slow permanent EL growth phase at about 25 s corresponds to the time required for the charged species to redistribute and mix in the perovskite layer. Recombination of the iodide defects takes about 10 min at RT and longer at lower temperatures. The rate of recombination of the iodide defects is proportional to the diffusivity of the more mobile species, so the rate of this process, as well as the processes due to ion redistribution, is characterized by the same activation energy. Recombination of the I^- interstitials and vacancies[182,183] permanently reduces the concentration of the recombination centers. At different ion and vacancy concentrations, the smaller species, in this case V^+, suffer relatively larger losses.

Reversible EL decay. This reversible process, observed as a partial decay of the intensity of EL during the repetitive device stressing (Figure 4.8) and shown by the red dashed line in the diagram of Figure 4.9, reduces the intensity of EL, but does not significantly change the current, PL, EL wavelength, and EA (Figures 4.8 and 4.10). This process shows a fast component of several minutes and a much slower decay on a time scale of hours. During the initial first-time stressing this decay is masked by the increase in EL described above. During repeated stressing, the rapid decay phase also competes with the EL growth, resulting in somewhat faster EL saturation compared to the current. Similar decay processes have been observed and studied in detail in previous publications:[180,187] the fast decay component has been attributed to heating of the sample by the current flow, while the slow component is related to the partially reversible degradation of the device, which is probably also related to ions.

Relaxation after stressing. Termination of the stress voltage leads to a simultaneous decay of the current and the EL intensity (Figure 4.8, black dots), as the restored built-in electric field pulls the ions back to their initial position, as in untreated sample, restoring the barriers to charge carrier injection. However, the initial state of untreated sample is not fully restored, since the trap density and the ion density irreversibly decrease, as described above. It should also be noted that the current and EL decrease much more slowly during relaxation than during re-

peated stressing, although both processes should be caused by the movement of I^- ions. According to the model of ion redistribution presented above, the processes of stressing and relaxation are not identical. First, because of the different electric field strengths and it's spatial distributions. The recombination of I^- with V^+ reduces the ion density and can also change the dynamics. Finally, the stressing and relaxation processes may also differ in that ion movement during PeLED stressing occurs in the presence of charge carriers, while no charge carriers are present during relaxation. It has been reported that ion diffusivity is enhanced by optical excitation, but the mechanism of this phenomenon remains unclear.[190] Thus, ion diffusivity may be enhanced by charge carriers, both photogenerated and injected, which accelerates ion motion during stressing.

Impact of negative voltage. Applying a negative voltage to the stressed sample after its relaxation at 0V resulted in an additional decay of EL intensity and current (Figure 4.8, blue dots). The enhancement of the internal electric field beyond the built-in value led to a stronger accumulation of ionic species and additionally increased the barriers for charge carrier injection. After termination of the negative voltage, current and EL intensity gradually recovered to the values characteristic of stressed samples at zero applied voltage (Figure 4.8). Application of negative voltage for a prolonged period showed additional slow EL decay and almost completely quenched the EL after 25 h. We hypothesize that a strong negative voltage applied over a long period of time causes a redistribution of less mobile ions, probably MA^+, which further increase the barriers to carrier injection. Subsequent application of a positive stressing voltage returned the device to the strong electroluminescent state.

Light soaking. The effect of light soaking on the intensities of PL and EL was also investigated by illuminating the PeLED with white light of 1 sun intensity. Surprisingly, no significant changes in PL intensity and its decay kinetics were observed in the pristine, unstressed sample.[182,183] However, light soaking increased the current of a non-stressed sample by about 20 % and doubled the intensity of EL, which, however, remained about ten times lower than after current stressing. Consequently, the influence of light soaking was similar to the influence of the fast-

stressing phase. Light soaking of the stressed sample also caused similar changes to additional current stressing, i.e., an increase in current and EL intensity, which later relaxed when light soaking was terminated.

The model presented above explains this unusual influence of light soaking in a similar way to perovskite solar cells, where the redistribution of ions or vacancies is driven by a photoinduced voltage that generates an additional electric field.[191] The optical excitation of PeLED generates an open circuit voltage as in solar cells. This reduces the built-in electric field similar to an applied positive voltage. The reduced internal electric field causes redistribution of iodine ions, reducing or eliminating barriers to carrier injection, resulting in an increase in current and EL.

These considerations led to **the third statement of the thesis:** electric field-induced redistribution of ions of a single type in the perovskite layer causes complex multiphase dynamics of electroluminescence and current in $MAPbI_3$ perovskite light-emitting diodes.

4.4 Electric Field-Induced Luminescence Quenching in PeLEDs

In the fourth article (submitted paper **F**) of this work, we used our implementation of the time-resolved photoluminescence measurement technique on different time scales to investigate the phenomenon of electric field-induced luminescence quenching (EFILQ) in $MAPbI_3$ based PeLEDs to directly observe the electronic processes in the perovskite. This is a very suitable technique to study PeLEDs, first because there is no carrier injection under reverse bias, and second because it not only studies the recombination of carriers, but also provides information about the carrier trap population, the influence of ionic motion, the extraction barriers for carriers, and the changes that occur in the active material during device operation.

First, the simple PL and EL relationship was examined. Figure 4.12a shows that the intensity of PL increases more than two times as the applied voltage is gradually increased from −2.5 V to +1.2 V. (The PL signal for forward voltages was measured directly on top of the EL signal and the pure PL intensity was obtained in this case by subtracting the EL from the total luminescence intensity) At higher forward voltages, the obtained PL intensity decreased slightly. The sharp increase in EL signal hindered the PL measurements at higher forward voltages. The determined voltage dependence of the PL intensity is quite expected. The PL intensity is highest at about +1.2 V, which roughly corresponds to the EL threshold voltage when the carrier injection is still insignificant, but the internal electric field is approximately compensated. The situation suddenly becomes more complicated when the applied voltage changes abruptly. Figure 4.12b shows the dynamics of PL, caused by abrupt voltage changes between +1 V (without exceeding the PeLED operating threshold) and −2 V. The intensity of PL changes in a very complex way, involving a combination of instantaneous (within the time resolution of less than a second), hundreds of seconds, and even much slower processes.

To investigate the fast PL modulation processes, a sinusoidally modulated voltage was applied. The PL modulation was performed with a 0.1 V AC voltage applied

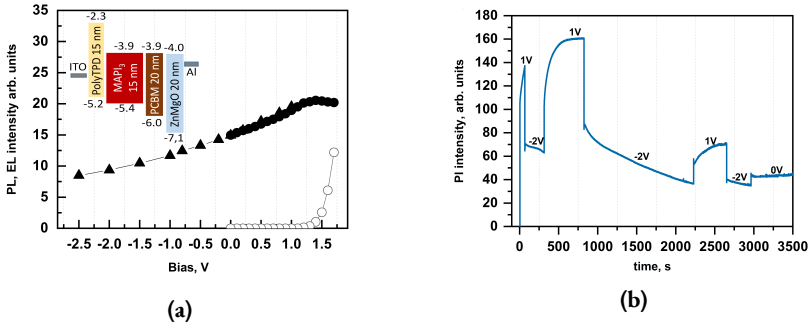

Figure 4.12: a) Dependence of $MAPbI_3$ PeLED photoluminescence (filled symbols) and electroluminescence (open symbols) intensity on applied voltage. Inset shows the geometric structure and schematic of the electronic energy levels of the studied PeLED b) PL intensity measured by abrupt variation of the applied voltage between −2 Vand +1 V.

along with a constant offset. Figure 4.13a shows the PL modulation intensity divided by average PL intensity as a function of voltage modulation frequency, which was varied in the range 0.1–10 kHz. The PL modulation intensity increases significantly with modulation frequency in the range of 0.1–1 kHz and stabilizes at about 9 kHz. Thus, this type of measurement is insensitive to the slow PL changes that occur on the time scale of seconds, indicating that the fast PL modulation occurs on the sub-millisecond or faster scale. Since photochemical processes can hardly occur that fast, the fast PL quenching has been attributed to electronic processes that change the carrier concentrations or their radiative recombination rate. The weaker PL quenching at lower frequencies suggests that some processes on a millisecond time scale appear to reduce PL quenching by reducing the electric field strength. Such processes are typically attributed to ionic motion.[140,175,176]

Figure 4.13b shows the dependence of the relative PL modulations (alternating PL intensity divided by average intensity) induced by a 0.1 V AC voltage on the offset voltage. Measurements were made at a frequency of 6 kHz, at which the screening of the electric field by moving ions should be negligible. The relative quenching is approximately constant at negative voltages, but increases almost twofold at about +1 V and decreases rapidly near the EL threshold voltage when, ideally, there is no

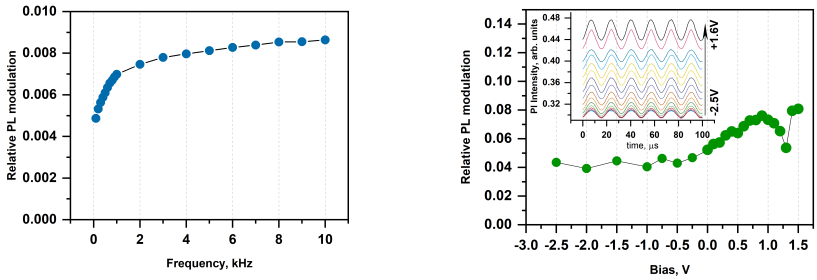

(a) (b)

Figure 4.13: a) Dependence of the relative PL modulation on the frequency of the sinusoidal 0.1 V voltage with a −1 V offset. b) Dependence of the relative PL modulation on the sinusoidal 0.1 V voltage on the voltage offset. The inset shows the modulated PL intensity at different offset voltages.

carrier extraction and no injection. A further increase in the offset voltage again causes a stronger luminescence modulation caused by the appearance of the EL signal. However, the abrupt drop in modulation confirms the conclusion drawn earlier that the PL intensity drop induced by an abrupt voltage change is actually caused by a direct PL quenching due to the electric field and not by a voltage-induced material change.

In addition, EFILQ properties were investigated with a periodic rectangular modulated voltage. The periodic modulation allowed to average the kinetics of PL and to track the dynamics of PL with high time resolution. Figure 4.14 shows the dynamics of PL when negative voltage pulses were applied relative to an offset voltage of +1 V. The offset of +1 V was chosen to avoid PL quenching due to carrier extraction and to ensure that the internal electric field was weak or absent; hereafter referred to as a compensating voltage. The negative voltage drop resulted in an immediate (within sub-millisecond time resolution) decrease in PL intensity, consistent with effective PL modulation by high frequency sinusoidal voltage. Figure 4.14b the voltage dependence of the initial relative PL quenching calculated as $\Delta PL_V/PL_0 = (PL_0 - PL_V)/PL_0$, where PL_0 is the PL intensity at compensating voltage of 1 V and PL_V is the PL intensity under the applied voltage pulse. The

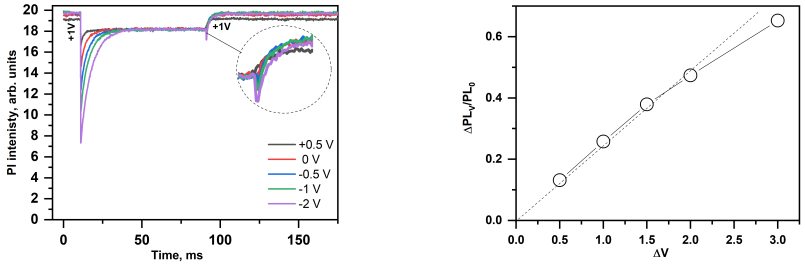

Figure 4.14: a) Photoluminescence dynamics induced by rectangular electric pulses measured at various negative pulse voltages with constant +1 V offset. The inset shows the magnified kinetics at the time of termination of the pulse. b) The dependence of the maximum PL quenching intensity on the voltage of the negative pulse.

initial relative PL quenching was approximately proportional to the voltage drop, and reached a slight saturation at large voltage drop values. The intensity of PL was quenched more than two times at the highest −3 V voltage used, and then partially recovered within a few milliseconds. This process can be attributed to a consequence of the redistribution of mobile ions which screens the applied electric field. Some unusual details of the dynamics of PL also deserve attention. First, the recovery rate of PL intensity after application of a negative voltage pulse depends strongly on the pulse voltage. The recovery takes about 5 ms after a voltage drop from +1 V to +0.5 V and more than 20 ms when the voltage drops to −2 V. Second, the intensity of PL after stabilisation is remarkably independent of the negative pulse voltage. Third, the intensity of PL drops again when the negative voltage is turned off and recovers with similar dynamics as observed when the negative pulse is applied, as shown by the inset in Figure 4.14a. Thus, the rapidly recovering PL drop occurs with both a negative and positive voltage jump.

The model shown in Figure 4.15 explains these details. The applied voltage of +1 V approximately compensates for the built-in voltage (Figure 4.15a) and completely suppresses the internal electric field and EFILQ. An applied negative voltage initially produces an approximately homogeneous electric field distribution in

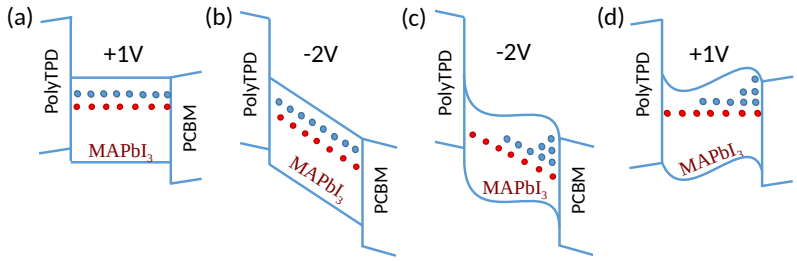

Figure 4.15: Model of the electronic levels of $MAPbI_3$ PeLED a) under constant 1.1 V voltage, b) immediately after voltage drop to reverse voltage, c) after screening of the electric field at reverse voltage, d) immediately after termination of the reverse voltage pulse.

the perovskite layer (linearly changing electric potential, as shown in Figure 4.15b), resulting in strong PL quenching. The redistribution of ions almost completely screens the electric field in most of the perovskite layer independent of the applied voltage (Figure 4.15c), leading to a partial recovery of PL to a level almost independent of the applied voltage. Moreover, the screening of the weak electric field requires only minor shifts of the ions and this process is fast and occurs within a few ms, as shown by the kinetics obtained at low pulse voltage (Figure 4.14a, curve +0.5 V). On the other hand, the screening of the strong electric field requires the accumulation of a large fraction of the available ions drifting over a long distance through the perovskite layer, so that the drift time increases to more than 20 ms at high applied voltages. PL quenching induced by the termination of the negative voltage pulse is also consistent with the proposed model. As Figure 4.15d shows, after the termination of the voltage pulse, the accumulated ions generate an electric field in the opposite direction, which also causes a separation of the electron and hole distributions and consequently triggers the PL quenching, which gradually recovers as the accumulated ions diffuse.

To obtain additional details about the electronic quenching mechanism, ultrafast PL kinetics were measured at DC or pulsed voltages. In addition, PL decay kinetics were measured at different times after application of the voltage pulse. Figure 4.16 shows the PL kinetics measured under DC and pulsed voltages. PL de-

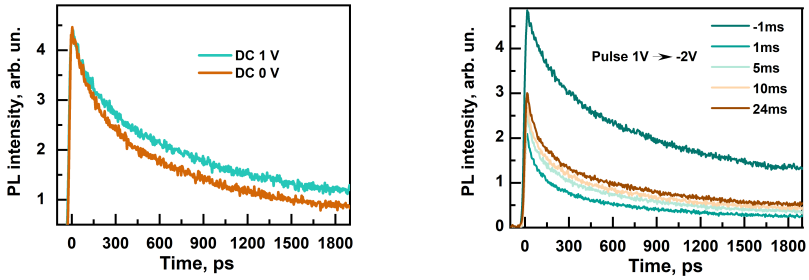

Figure 4.16: (a) Kinetics of transient photoluminescence measured at +1 V and 0 V DC. (b) PL kinetics under negative voltage pulses of 30 ms duration from 1 V offset to −2 V. Kinetics were measured at various delay times relative to the start of the voltage pulse. The curve at −1 ms were measured before the voltage pulse, i.e. at +1 V.

cay is slightly slower at +1 V constant (compensating) voltage than at 0 V, which is consistent with the PL intensity at steady state (Figure 4.12a). Figure 4.16b shows the kinetics measured at different times before and after application of rectangular negative pulse of −2 V, relatively to the compensating +1 V voltage. The kinetics measured 1 ms before the negative pulse is identical to those measured under constant +1 V voltage. However, the kinetics measured during the pulse action were sensitive to the timing of the optical pulse relative to the onset of the voltage pulse. In addition, comparison of Figures 4.12a and 4.12b shows that the pulsed voltage causes more significant changes in PL kinetics than the constant voltage. Importantly, the initial PL amplitude was independent of the constant applied voltage, but decreases when the pulsed voltage is applied. This difference is due to the structural and electronic quenching mechanisms that occur at constant and pulsed voltages, respectively. The structural changes lead to the appearance of additional PL quenching centers and only change the PL decay rate. On the other hand, the electronic mechanism, can reduce the recombination rate of the charge carriers very rapidly, thus affecting the initial amplitude. Comparison of the PL kinetics before and immediately after application of the negative pulse shows that the applied volt-

age causes an attenuation of the initial PL intensity and induces a faster decay during the first ≈500 ps, but the PL decay rate remains remarkably independent of the applied voltage in the 1000–2000 ps range. The kinetics measured at longer times after the application of voltage pulse shows both a weaker decrease of the initial PL intensity and a less significant acceleration of the PL decay rate, which is consistent with electric field screening. Consequently, we can clearly distinguish between instantaneous and gradual PL quenching phases, often referred to as amplitude and rate quenching. Rate quenching is consistent with the charge carrier extraction picture presented above. The field-induced acceleration of PL decay is an expression of charge carrier extraction and the redistribution of the electron and hole "clouds". Surprisingly, the electric field strongly accelerates the initial faster PL decay phase observed during the first hundreds of ps, while it does not change the second slower PL decay phase at times longer than 1 ns. The fast $MAPbI_3$ PL decay phase is usually attributed to carrier trapping.[95,192] This attribution leads to the logical conclusion that the electric field strongly accelerates the extraction of non-captured carriers, but only weakly changes the kinetics of the trapped carriers.

The instantaneous PL quenching phase deserves special attention. It is much faster than the carrier extraction and spatial redistribution processes described above. Therefore, it is more likely to be due to the reduced radiative recombination rate of excitons or geminate charge pairs. The studied perovskite film of PeLEDs consists of grains with a diameter of ≈10 nm. Under the influence of an electric field, the wave functions of electrons and holes within the single grain can be shifted in opposite direction, which decreases their radiative recombination rate. The carrier mobility within a single crystalline grain is expected to be much higher than the macroscopic mobility, which is reduced by intergranular junctions that create barriers to carrier movement.[193] Therefore, the carrier shift within the grain can be very rapid, causing the instantaneous PL quenching phase.

The results presented above lead to **the fourth statement of the thesis**: electric field-induced luminescence quenching in $MAPbI_3$ perovskites is determined by the

direct effect of the electric field on the charge carrier distributions and the influence on the spatial redistribution of ions in the perovskite layer.

4.5 Energy Barriers in Hybrid Perovskite Films

In the last article of this work (Paper **D**), the motion dynamics of charge carriers was investigated. Electrical contact measurement techniques: transient photocurrent and time-delayed collection field were used to study polycrystalline $MAPbI_3$ perovskite films deposited on interdigitated Pt electrodes (IDE). The chosen sample configuration provides the opportunity to study the lateral motion of photogenerated charge carriers in the perovskite film, which are not affected by the interfacial phenomena or additional layers usually present in sandwich-configuration devices such as solar cells or LEDs.

To investigate the physical processes in the perovskite, conventional transient photocurrent measurements were performed at different temperatures. Figure 4.17a shows the photocurrent kinetics measured at different temperatures. The initial photocurrent values show no clear dependence on temperature, suggesting that the generation of charge carriers and their initial mobility are temperature-independent. A similar temperature-independent charge carrier mobility during the first hundreds of ps was also reported for conjugated polymers[194] or a weak temperature dependence for hybrid perovskites.[195] A weak temperature dependence was observed for the photoluminescence decay of $MAPbI_3$. However, Figure 4.17a shows that the photocurrent decays much faster at lower temperatures. At low temperatures, higher photocurrent is also measured on a longer time scale (several µs). This is to be expected because fewer carriers are extracted when the photocurrent drops very quickly and therefore more carriers remain in the sample. The voltage dependence of the photocurrent kinetics shown in Figure 4.17b also differs qualitatively at 100 K from that at room temperature: the photocurrent decays faster and the slow photocurrent component almost disappears at low bias voltage. This behaviour indicates that charge carriers are quickly trapped at low temperatures, while a strong electric field gradually pulls the charge carriers out of the traps and maintains a weak photocurrent for several µs.

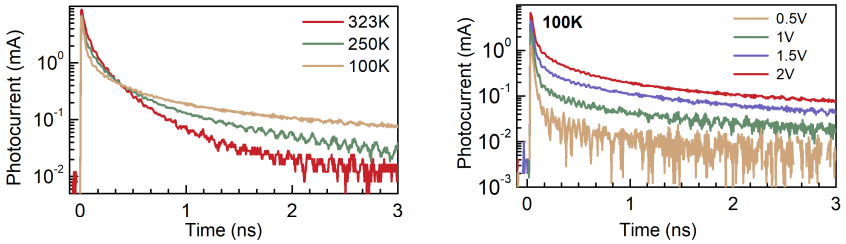

Figure 4.17: a) Photocurrent kinetics at different temperatures measured at 2 V applied voltage and 15 nJ/cm^2 excitation intensity, b) photocurrent kinetics at 100 K at different applied voltages.

To further investigate the decay of charge carrier density and mobility kinetics, the TDCF measurement technique was applied. Figure 4.18a, b shows the kinetics of charge carrier extraction at different extraction times at 323 K and 100 K and the insets show the kinetics of the cumulative current. At room temperature, both the initial and cumulative current decrease rapidly with delay time due to the rapid recombination of the charge carriers. The kinetics of the cumulative current clearly shows two extraction phases: the fast one, which lasts hundreds of ns, and the slow one, which lasts several µs. The fast extraction phase decreases rapidly at longer extraction delays and practically disappears at delays longer than 5 µs. While the slow phase remains constant for several µs, it gradually becomes dominant and decreases on a time scale of several tens of µs. It is plausible that the slow phase corresponds to the extraction of trapped charge carriers, which are only weakly affected by the recombination of the charge carriers and therefore survive for several tens of microseconds. The situation changes drastically at low temperatures (T = 100 K, Figure 4.18b).

The peaks of the photocurrent are sharper at low temperatures, which is consistent with the faster decay of the charge carrier mobility. More importantly, the peak intensity is less dependent on the delay time, indicating that, first, the recombination of charge carriers is significantly suppressed and, second, the mobility does not

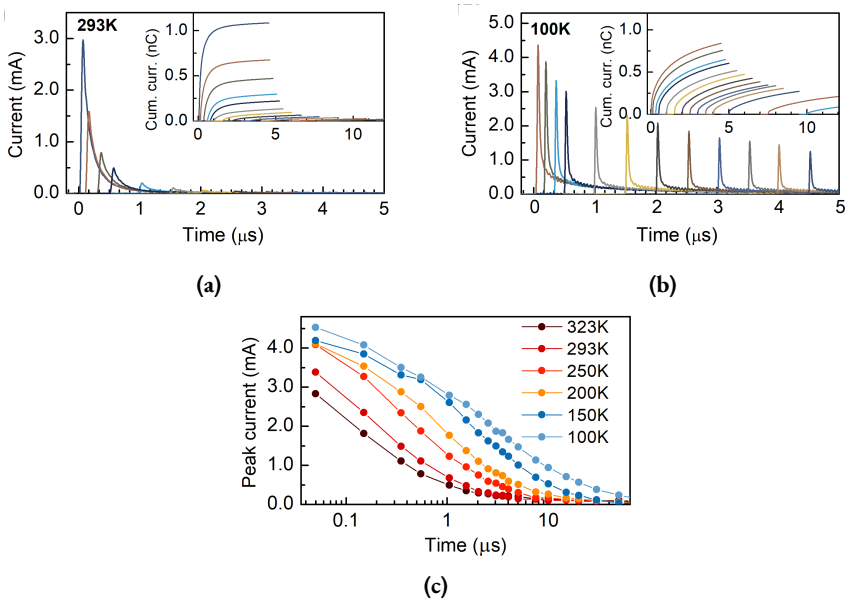

Figure 4.18: TDCF data obtained with 0 V pre-bias and 2 V extraction voltages at 15 nJ/cm^2 excitation intensity. Carrier extraction kinetics at different extraction pulse delays at a) 293 K and b) 100 K. Insets show the kinetics of cumulative current obtained by integrating the extraction kinetics. c) Dependence of peak extraction current values on extraction delay times at different temperatures.

significantly decrease during the waiting time at 100 K. The kinetics of the cumulative current also show that despite the strong initial current, only about 20–30 % of the charge carriers are extracted during the short, intense current pulse, while the dominant charge carrier extraction occurs on a time scale of several microseconds. All processes that determine the current kinetics, such as recombination, decrease in mobility and charge carrier extraction, are therefore relatively slow. From this information, the important question arises, what process could cause such a rapid drop in the extraction current? This discrepancy can be resolved by assuming that the charge carrier mobility does not change during the waiting time between carrier generation and the application of the electric extraction pulse, but decreases rapidly as soon as the electric field is applied. In other words, the charge carrier mo-

bility only starts to decrease when the charge carriers start to drift under the applied electric field. This behaviour suggests that the rapid drop in mobility is caused by energy barriers that impede carrier drift, rather than energy traps. This is to be expected in a perovskite material, which consists of small crystalline grains. At low temperatures, the charge carriers generated by light are confined in a single grain and their properties do not change with time. They also do not recombine when generated in different grains. When the electric field is applied, the charge carriers drift rapidly, but only over short distances until they reach the grain boundaries. Figure 4.18c, which plots the initial currents as functions of the delay time at different temperatures, shows that the survival time of the charge carriers gradually increases at lower temperatures. Since Shockley-Read-Hall (SRH) recombination dominates at the low excitation intensity used, the increasing carrier lifetime at low temperature should be due to the decreasing SRH recombination rate. This finding is consistent with the proposed barrier-controlled charge carrier movement. At low temperatures, charge carriers are trapped in individual perovskite grains and cannot reach trapped charge carriers in neighbouring grains.

To verify the mechanism of barrier-limited charge carrier extraction, a modified TDCF technique with field flipping was created. During optical excitation, different voltage pulses with different polarity and offset (pre-bias) were applied. Figure 4.19 shows the kinetics of the photocurrent measured with 2 V extraction voltage at different pre-bias voltages and different temperatures. A photocurrent peak was observed immediately after the optical excitation, which is determined by the charge carrier extraction with pre-bias voltage. Applying an extraction voltage of 2 V causes another peak to appear. The second peak is stronger when the pre-bias voltage and the extraction voltage have opposite polarity. This is particularly evident at a temperature of 100 K - the second peak is weak when the pre-bias and extraction voltage have the same polarity and becomes very strong when a high pre-bias with opposite polarity is used. This behavior confirms the character of spatially confined charge carrier motion at lower temperatures. Under the applied electric field, the charge carriers drift rapidly but only over short distances within the perovskite grains until

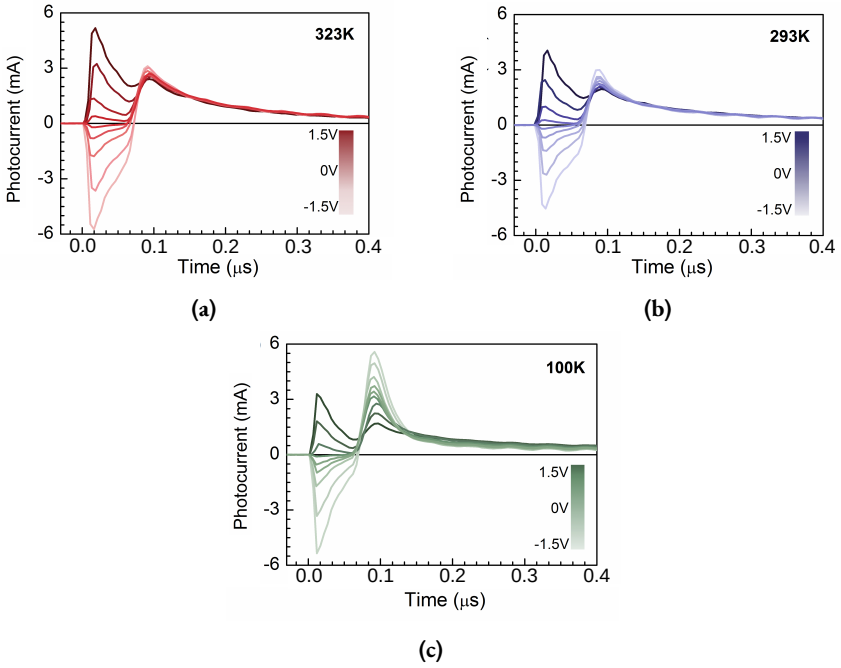

Figure 4.19: Photocurrent kinetics at three different temperatures obtained by modified TDCF measurements under 15 nJ/cm^2 excitation intensity when collection voltage of 2 V was applied 60 ns after optical excitation pulse, which was applied under different voltages and polarity pre-bias fields.

they reach the grain boundaries and cause a very rapid photocurrent decay. If the direction of the electric field is reversed, the charge carriers drift back to the opposite side of the perovskite grain and produce a strong current until they reach the boundaries again. Importantly, the strong second peak also shows that the charge carriers are not trapped in energy traps during the waiting period. As the temperature increases, this behavior becomes less pronounced; the intensity of the extraction peak becomes almost independent of the direction of the pre-bias at 323 K. At room temperature, the dependence of the extraction current on the pre-bias voltage is much less pronounced than at 100 K, but stronger than at 323 K. This indicates

that the charge carriers can overcome energy barriers at room temperature, but the influence of the barrier on the movement of the charge carriers is still significant.

These results led to **the fifth statement of the thesis:** there are potential barriers to lateral carrier movement in the polycrystalline hybrid perovskite films that impacts carrier mobility, diffusion and recombination rates.

5 Conclusions

1. Ion motion and spatial accumulation at the interfaces significantly affect the functional mechanism of hybrid perovskite solar cells under the charge injection condition, leading to two different working regimes a) before and b) after ion redistribution. The electroluminescence overshoot effect observed in regime a) could be of particular interest for the development of electrically pumped perovskite lasers.

2. Balanced electron and hole current leads to improved external quantum efficiency , EQE roll-off, and lifetime of 2D/3D perovskite light-emitting diodes. This is related to the spatial charge carrier distribution in the perovskite emission layer. If a balanced carrier transport/injection is ensured, the leakage of excess carriers through the device can be avoided up to high current densities. This is very important when targeting high brightness applications in perovskite light-emitting diodes.

3. Complex changes in electroluminescence and current in $MAPbI_3$ perovskite ba-sed light-emitting diodes occurring on different time scales are caused by the mig-ration of ions of a single type. The spatial redistribution of charged species along the perovskite layer thickness not only changes the shape of the electric potential and the barriers to charge carrier injection, but also acts as non-radiative recombination centers. A deeper understanding of the functional mechanism in perovskite light-emitting diodes could be of great importance for device optimization when it comes to high-efficiency devices.

4. Electric field-induced PL quenching in $MAPbI_3$ perovskites is determined by three processes: a) direct influence of electric field on charge carrier density and distribution in the perovskite layer (electronic part), b) electric field screening by mobile ions, and c) electric field-induced change in material structure. Structural changes are mainly responsible for EFILQ at constant voltage, while the electronic part causes immediate quenching of PL intensity when voltage pulses are applied. Two electronic quenching mechanisms are also distinguished: one for charge carrier separation in the individual perovskite crystal grains and one for the entire perovskite layer. The extraction of charge carriers from the perovskite layer and the spatial separation of electron and hole "clouds" cause PL variations on the order of tens and hundreds of picoseconds, while the instantaneous quenching is caused by the displacement of electrons and holes in the individual perovskite grains within a few ps. The electronic PL quenching part is strongly influenced by the screening of the electric field induced by the mobile ions and occurs within tens of milliseconds at room temperature. All the processes described should be taken into account when analyzing the performance of perovskite devices, as they cause the hysteresis in solar cells and the complex electroluminescence and current dynamics of perovskite light-emitting diodes.

5. The main processes controlling lateral carrier motion in polycrystalline $MAPbI_3$ perovskite films were determined using transient photocurrent and modified time-delayed collection field techniques together with temperature variations. Analysis of the obtained data showed that potential barriers in the grain boundaries, rather than carrier traps, are responsible for the rapid decrease in carrier mobility at low temperatures. Temperature-dependent measurements revealed that at room temperature and even at higher temperatures potential barriers still play an important role in determining charge carrier mobility, diffusion and recombination rates.The paradigm shift findings are of great importance for devices fabricated in lateral configurations, such as field-effect transistors, photodiodes, photodetectors, and lateral solar cells.

List of Publications

On the subject of the Thesis:

A. R. Gegevičius, M. Franckevičius, J. Chmeliov, W. Tress, and V. Gulbinas. "Electroluminescence Dynamics in Perovskite Solar Cells Reveals Giant Overshoot Effect". *The Journal of Physical Chemistry Letters* 10:8, 2019, p. 1779.

B. A. Fakharuddin, W. Qiu, G. Croes, A. Devižis, R. Gegevičius, A. Vakhnin, C. Rolin, J. Genoe, R. Gehlhaar, A. Kadashchuk, V. Gulbinas, and P. Heremans. "Reduced Efficiency Roll-Off and Improved Stability of Mixed 2D/3D Perovskite Light Emitting Diodes by Balancing Charge Injection". *Advanced Functional Materials* 29:37, 2019, p. 1904101.

C. J. Chmeliov, K. Elkhouly, R. Gegevičius, L. Jonušis, A. Devižis, A. Gelžinis, M. Franckevičius, I. Goldberg, J. Hofkens, P. Heremans, W. Qiu, and V. Gulbinas. "Ion Motion Determines Multiphase Performance Dynamics of Perovskite LEDs". *Advanced Optical Materials* 9:24, 2021, p. 2101560.

D. R. Jasiūnas*, R. Gegevičius*, M. Franckevičius, V. Jašinskas, and V. Gulbinas. "Energy Barriers Restrict Charge Carrier Motion in MAPI Perovskite Films". *Advanced Optical Materials* 8:16, 2020, p. 2000036.

E. R. Gegevičius, M. Franckevičius, and V. Gulbinas. "The Role of Grain Boundaries in Charge Carrier Dynamics in Polycrystalline Metal Halide Perovskites". *European Journal of Inorganic Chemistry* 2021:35, 2021, p. 3519.

*shared first authorship

F. R. Gegevičius, K. Elkhouly, M. Franckevičius, J. Chmeliov, R. Gehlhaar, W. Qiu, P. Heremans, and V. Gulbinas. "Electric Field-Induced Quenching of $MAPbI_3$ Photoluminescence in PeLED Architecture". *ACS Applied Materials & Interfaces*, 2023, under review.

Not included in the Thesis:

R. Gegevičius, M. Franckevičius, V. Pakštas, R. Augulis, and V. Gulbinas. "High-Speed, Sensitive Planar Perovskite Photodetector Based on Interdigitated Pt and Au Electrodes". *physica status solidi (a)* 215:7, 2018, p. 1700822.

R. Gegevičius, M. Treideris, V. Pakštas, M. Franckevičius, and V. Gulbinas. "Oxide Layer Enhances Photocurrent Gain of the Planar $MAPbI_3$ Photodetector". *Advanced Electronic Materials* 4:7, 2018, p. 1800114.

K. T. Cho, M. Cavazzini, K. Rakstys, S. Orlandi, S. Paek, M. Franckevičius, H. Kanda, R. Gegevičius, Q. V. Emmanuel, G. Pozzi, and M. K. Nazeeruddin. "Perovskite Solar Cells: 18% Efficiency Using Zn(II) and Cu(II) Octakis(diarylamine)phthalocyanines as Hole-Transporting Materials". *ACS Applied Energy Materials* 2:9, 2019, p. 6195.

S. Paek, C. Roldán-Carmona, K. T. Cho, M. Franckevičius, H. Kim, H. Kanda, N. Drigo, K. Lin, M. Pei, R. Gegevičius, H. J. Yun, H. Yang, P. A. Schouwink, C. Corminboeuf, A. M. Asiri, and M. K. Nazeeruddin. "Molecular Design and Operational Stability: Toward Stable 3D/2D Perovskite Interlayers". *Advanced Science* 7:19, 2020, p. 2001014.

R. Jasiūnas, R. Gegevičius, M. Franckevičius, N. Phung, A. Abate, and V. Gulbinas. "Suppression of Electron Trapping in $MAPbI_3$ Perovskite by Sr^{2+} Doping". *physica status solidi (RRL) – Rapid Research Letters* 14:11, 2020, p. 2000307.

N. Drigo, C. Roldan-Carmona, M. Franckevičius, K.-H. Lin, R. Gegevičius, H. Kim, P. A. Scho-uwink, A. A. Sutanto, S. Olthof, M. Sohail, K. Meerholz, V. Gulbinas, C. Corminboeuf, S. Paek, and M. K. Nazeeruddin. "Doped but Stable: Spirobisacridine Hole Transporting Materials for Hysteresis-Free and Stable Perovskite Solar Cells". en. *Journal of the American Chemical Society* 142:4, 2020, p. 1792.

R. Xia, Y. Xu, B. Chen, H. Kanda, M. Franckevičius, R. Gegevičius, S. Wang, Y. Chen, D. Chen, J. N. Ding, N. Yuan, Y. Zhao, C. Roldán Carmona, X. Zhang, P. Dyson, and M. K. Nazeeruddin. "Interfacial Passivation of Wide-bandgap Perovskite Solar Cells and Tandem Solar Cells". *Journal of Materials Chemistry A*, 2021, p. 21939.

S. Paek, S. B. Khan, M. Franckevičius, R. Gegevičius, O. A. Syzgantseva, M. A. Syzgantseva, S. Kinche, A. M. Asiri, C. Roldán-Carmona, and M. K. Nazeeruddin. "Cation optimization for burn-in loss-free perovskite solar devices". *Journal of Materials Chemistry A* 9:9, 2021, p. 5374.

G. Kavaliauskaitė, G. Kuksėnaitė, R. Gegevičius, V. Pakštas, A. Selskis, V. Strazdienė, A. Padarauskas, E. Orentas, V. Gulbinas, and M. Franckevičius. "S-Methylthiouronium Improves the Photostability of Methylammonium Lead Iodide Perovskites". *ACS Applied Energy Materials* 4:7, 2021, p. 6466.

Santrauka

Įvadas

Perovskitas – $CaTiO_3$ mineralas atrastas 1839 metais vokiečių mineralogo Gustav Rose Uralo kalnuose ir pavadintas mineralogo Lev Alekseyevich von Perovski garbei. Mineralai dėl susikaupusių priemaišų tamsiai rudi, o gryni – skaidrūs. Iškasamų mineralų kietumas 5.5–6, tankis nuo 3.98 iki 4.26 g/cm^3, o atspindžio koeficientas siekia 2.38. Perovskito pavadinimas šiuo metu naudojamas apibrėžti plačiai junginių klasei pasižyminčiai $CaTiO_3$ struktūra ir aprašoma ABX_3 struktūrine formule. Perovskito struktūros junginiai, plačiai sutinkami gamtoje. Vienas jų $(Fe, MG)SiO_3$ labiausiai paplitusi uoliena žemės plutoje sudaranti 38 % žemės masės. 1940 metais atradus $BaTiO_3$ dielektrines ir feroelektrinės savybės susidomėjimas perovskitais pradėjo augti. Neilgai trukus $BaTiO_3$ buvo pritaikytas elektronikos pramonėje gaminant kondensatorius ir elektromechaninius keitiklius, vėliau pradėtas taikyti ir netiesinėje optikoje, bei medicininiuose tyrimuose. Tyrinėjant $BaTiO_3$ kristalus ir siekiant pagerinti jų savybes buvo susintetina daugybė naujų perovskitinių junginių su įvairiausiomis fizikinėmis ir cheminėmis savybėmis. Vieni įdomiausi šios klasės junginių – hibridiniai perovskitai struktūroje apjungiantys mažą organinį katijoną ir neorganinį metalo halido anijoną. Pirmą kartą tokie junginiai aprašyti 1978 metais vokiečių mokslininko Dieter Weber. Vėliau 1990–2000 metais šiuos junginius buvo bandoma taikyti organinėje elektronikoje gaminant tranzistorius ir šviesą emituojančius diodus, tačiau tikrasis hibridinių perovskitų potencialas atsiskleidė tik 2009 metais, kada pirmą kartą jie buvo panaudoti saulės elementų gamyboje. Pirmojo $MAPbI_3$ perovskito saulės elemento efektyvumas siekė 3.8 %, po 4 metų jau 15 %,

o 2022 metais buvo pasiektas naujausias efektyvumo rekordas siekiantis 25.8 % taip priartėjant prie 31 % teorinio efektyvumo limito. Perovskitų technologija besivystydama tokiu greičiu, efektyvumu jau aplenkė ir CdTe saulės elementus, kurie užimą antrą vietą saulės elementų rinkoje. Taip pat hibridiniai perovskitai sėkmingai naudojami ir kitose optoelektronikos srityse: fototedektoriams, šviesos diodams ir fototranzistoriams gaminti. Kuriami perovskitiniai prietaisai efektyvumu nenusileidžia, o kai kur ir lenkia, klasikinių technologijų gaminius. Perovskitų sėkmę lėmė jų išskirtinės fizikinės savybės: draustinės juostos tarpas, sugerties koeficientas, krūvininkų judris – labai panašios į klasikinių neorganinių puslaidininkių, o tuo pačiu itin maža kristalinių defektų koncentracija ir galimybė lieti medžiagą tiesiogiai iš tirpalo – tipiškos organiniams puslaidininkiams. Tačiau gamtoje visos geros savybės turi savo kainą, ne išimtis ir hibridiniai perovskitai, susiduriantys su rimtais stabilumo ir atsikartojamumo iššūkiais.

Disertacijos tikslai

Nors hibridinių perovskitų taikymas optoelektronikoje ir susilaukė didžiulio dėmesio pastaraisiais metais, tačiau daugelis fundamentinių klausimų apie krūvininkų generaciją ištraukimą ir rekombinaciją, bei joninį judėjimą vis dar lieka neatsakyti. Tokios žinios leistų identifikuoti limituojančius veiksnius siekiant tolimesnio prietaisų efektyvumo, bei stabilumo parametrų gerinimo. Šio darbo tikslas buvo detaliau panagrinėti pagrindinius optoelektroninius procesus įvairių hibridinių perovskitų prietaisuose paruoštų skirtingose architektūrose. Fiksuoti, bei išanalizuoti joninį judėjimą hibridiniuose perovskituose ir identifikuoti jo daromą įtaką krūvininkų pernašai, bei optolektroninių prietaisų veikimui.

Disertacijos uždaviniai

- Įdiegti ir taikyti nestacionarios elektroliuminescencijos matavimo metodiką hibridiniams perovskitams tirti.

- Išanalizuoti elektroliuminescencijos kinetikas ir susieti jas su krūvininkų dinamikos vyksmais hibridinių perovskitų prietaisuose.
- Įdiegti ir pritaikyti kinetinius elektrinius ir optinius matavimo metodus jonų judėjimo hibridiniuose perovskituose tyrimui.
- Ištirti laisvųjų krūvininkų dinamikos procesus ir įvertinti joninio judėjimo įtaką krūvininkų rekombinacijai ir ištraukimui.

Ginamieji teiginiai

1. Krūvininkų kaupimasis perovskito sluoksnyje nulemia elektroliuminescencijos signalo antimpulsio atsiradimą, o elektrinio lauko sukeltas judrių jonų persiskisrtymas perovskito sluoksnyje šį efektą mažina.
2. Nepalankus erdvinio krūvio pasiskirstymas perovskitiniuose šviestukuose sukelia išorinio kvantinio našumo charakteristikos krytį, o elektronų ir skylių injekcijos srovės subalansavimas, leidžia šio efekto išvengti.
3. Elektrinio lauko sukeltas vienos rūšies jonų judėjimas perovskito sluoksnyje sukelia sudėtingą daugiakomponentę $MAPbI_3$ šviestuko elektroliuminescencijos ir srovės dinamiką.
4. Elektrinio lauko indukuotas fluorescencijos gesinimo mechanizmas $MAPbI_3$ perovskite priklauso nuo elektrinio lauko daromos įtakos krūvininkų pasiskirstymui ir jonų persiskirstymo perovskito sluoknsyje.
5. Lateraliniam krūvininkų judėjimui polikristalinėse hibridinių perovskitų plėvelėse egzistuoja energetiniai barjerai darantys įtaką, krūvininkų judriui, difuzijai ir rekombinacijai.

Naujumas ir aktualumas

- Pritaikyta nestacionariosios elektroliuminescencijos matavimo metodika yra jautri ir tinkama joninio judėjimo ir jų erdvinio pasiskirstymo tyrimams hibridinio perovskito optoelektroniniuose prietaisuose.
- Sukurta matavimo metodika, panaudojant įvairias elektrinių impulsų formas ir trukmes leidžianti tiesiogiai stebėti elektrinio lauko sukeltus pokyčius hidridinio perovskito sluoksnyje laikui bėgant.
- Pastebėtas elektroliuminescencijos signalo antimpulsio atsidarimas hibridinio perovskito saulės elementuose.
- Eksperimentiškai nustatyta jonų rūšis daranti pagrindinę įtaką hibridinių perovskitų šviestukų elektroliuminescencijos ir srovės dinamikai.
- Sukurti ir įdiegti klasikinių nestacionariųjų matavimų metodikų patobulinimai leido ištirti energetinių barjerų egzistavimą ir jų daromą įtaką krūvininkų judriui polikristalinėse hibridinių perovskitų plėvelėse.

Tyrimo metodikos

Be rutininių nuostoviosios sugerties ir fluorescencijos matavimų, didelis dėmesys buvo skiriamas naujų nestacionariųjų dinaminių metodų adaptavimui ir taikymui hibridinių perovskitų tyrimui. Darbe naudotos matavimo technikos: nestacionarioji fluorescencija (laike koreliuotų pavienių fotonų skaičiavimas) ir elektroliuminescencija, elektriniu lauku moduliuota fluorescencija, fotosrovių kinetikos, uždelstojo ištraukimo lauko bei apverstojo ištraukimo lauko variacijos. Laikiniai procesai, šiame darbe, buvo nagrinėjami pradedant pikosekundėmis ir baigiant dienomis.

Rezultatai ir aptarimas

Pirmajame pristatome darbe (publikacija **A**) buvo panaudotas nestacionariosios elektroliuminescencijos tyrimo metodas skirtas nagrinėti krūvininkų dinamikai hibridinio perovskito saulės elementuose, krūvio injekcijos sąlygomis. Darbe buvo parodyta, jog nestacionariosios elektroliuminescencijos spektroskopija, yra jautri ir tinkama joninio judėjimo hibridiniame perovskite stebėjimui ir tyrimui. Analizuojama elektroliuminescencijos signalo dinamika laiko skalėse nuo ms iki s atskleidė egzistuojantį elektroliuminescencijos signalo antimpulsį, atsirandanti po elektrinio impulso išsijungimo. Pasiūlytas veikimo mechanizmas aiškinantis tokio antimpulsio atsiradimo priežastis, joninio judėjimo įtaką lemiančią antimpulsio dinamikos pokyčius ir jo sąsaja su prietaiso veikimo charakteristikomis. Užregistruotas jonų judėjimas ir jų kaupimasis sluoksnių sandūrose, lemiantis skirtingus saulės elemento veikimo rėžimus.

Antrajame darbe (publikacija **B**) anksčiau pristatytas nestacionariosios elektroliuminescencijos tyrimo metodas buvo panaudotas 2D/3D architektūros hibridinio perovskito šviestukams tirti. Buvo siekiama išsiaiškinti kas lemia šviestuko išorinio kvantinio našumo charakteristikos krytį. Nustatytą, jog svarbiausią vaidmenį atlieka nesubalansuota elektronų ir skylių injekcijos srovė. Subalansavus srovę galima išvengti didelių srovės nuotėkių užtikrinant nekintančias išorinio kvantinio našumo vertes, net ir esant didelėms injekcijos įtampos vertėms. Darbe pristatytas detalus mechanizmas, aiškinantis šio efekto atsiradimo priežastis ir eigą, aptarti būdai ir galimybės tokio efekto išvengimui.

Trečiasis darbas (publikacija **C**) buvo skirtas tolimesniam hibridinio perovskito šviestukų tyrimui, pasinaudojat nestacionariais elektroliuminescencijos, fluorescencijos ir srovės matavimais buvo stebima šviestuko veikimo charakteristikų evoliuciją bėgant laikui. Sukurta ir pristatytą matavimo metodika leidžianti tiesiogiai stebėti elektrinio lauko sukeltus pokyčius perovskito sluoksnyje. Nustatyta, kad sudėtingą šviestuko elektroliuminescenciją ir srovės dinamiką nulemia joninis judėjimas perovskito sluoksnyje. Išanalizavus elektroliuminescencijos ir srovės procesų gyvavimo

trukmes, buvo įvertinta pagrindinių jonų aktyvacijos energija siekianti ≈175 mV, kuri atitinka jodido jonų energiją perovskito kristale.

Ketvirtasis darbas skitas fluorescencijos gesinimo elektriniu lauku tyrimui $MAPbI_3$ perovskito šviestukuose. Pristatytos matavimo metodikos leidžiančios tirti fluorescencijos gesinimo elektriniu lauku procesus nuo ps iki s tinkamos hibridiniams perovskitams tirti. Tyrimui panaudos skirtingos elektrinių impulsų laikinės charakteristikos ir formos leido įvertinti skirtingos prigimties procesus veikiančius skirtingose laiko skalėse. Nustatyti trys pagrindiniai procesai lemiantys elektriniu lauku indukuotos fluorescencijos gesinimą. Be tiesioginio elektrinio lauko įtakos krūvininkų tankiui ir jų pasiskirstymui, elektrinis laukas taip pat indukuoja ir judrių jonų persiskirstymą perovskito sluoksnyje, dėl ko atsiranda išorinio elektrinio lauko ekranavimas pasireiškiantis kaip fluorescencijos gesinimo signalo atsistatymas. Ultraspartieji fluorescencijos gesinimo elektriniu lauku matavimai atskleidė krūvininkų atsiskyrimo procesus vykstančius atskirame kristalo domene, o taip pat stebimas ir elektrinio lauko sukeltas krūvininkų ištraukimas į kontaktus. Darbe detaliai aprašomi gesinimo vyksmai ir aptariamas jų veikimo mechanizmas.

Penktajame darbe (publikacija **D**) panaudojus nestacionarios fotosrovės ir uždelstojo ištraukimo lauko matavimus, buvo tiriamas lateralinis krūvininkų judėjimas polikristalinėse $MAPbI_3$ perovskito plėvelėse. Stebima krūvininkų dinamika bėgant laikui, nuo sužadinimo iki jų ištraukimo į kontaktus, taip pat analizuojami ir krūvininkų rekombinacijos bei jų patekimo į gaudykles procesai. Darbe pristatyta modifikuota apverstojo ištraukimo lauko matavimo technika leidusi nustatyti egzistuojančius energetinius barjerus lateraliniam krūvininkų judėjimui hibridinių perovskitų plėvelėse. Temperatūrinės priklausomybės atskleidė, jog didžiausią įtaką, krūvininkų judriui energetiniai barjerai daro 100 K temperatūroje, tačiau reiškinys stebimas ir kambario ar aukštesnėje temperatūroje.

Išvados

1. Jonų judėjimas aktyviame perovskito sluoksnyje ir jų kaupimasis sandūrose daro įtaką hibridinio perovskito saulės elemento veikimo charakteristikoms krūvio injekcijos sąlygomis. Skiriami du veikimo rėžimai: a) iki ir b) po jonų persiskirstymo aktyviame sluoksnyje. Režime a) stebimas elektroliuminescencijos antimpulsis gali būti būti svarbus, siekiant sukurti elektriškai kaupinamą hibridinio perovskito lazerį.

2. Subalansuota elektronų ir skylių injekcijos srovė lemia didesnį išorinį kvantinį našumą ir geresnį stabilumą 2D/3D hibridinio perovskito šviestukuose. Tai siejama su erdviniu krūvininkų pasiskirstymu emisiniame sluoksnyje, užtikrinus injekcinės srovės balansą galima išvengti perteklinių krūvininkų kuriamo srovės nuotėkio, net esant didelėms injekcijos įtampos vertėms. Rezultatas reikšmingai svarbus kuriant didelio skaisčio hibridinio perovskito šviestukus.

3. Skirtingose laiko skalėse stebima sudėtinga elektroliuminescencijos ir srovės dinamika $MAPbI_3$ perovskito šviestukuose yra nulemta vienos rūšies jonų judėjimo perovskito sluoksnyje. Jonų sankaupos sandūros sluoksnyje kuria energetinius barjerus krūvininkų injekcijai, ir veikia kaip nespindulinės rekombinacijos centrai. Gilesnis veikimo mechanizmo supratimas, svarbus kuriamų prietaisų optimizavimui, siekiant našių ir stabilių hibridinio perovskito šviestukų realizavimo.

4. Elektrinio lauko sukeltas fluorescencijos gesinimas $MAPbI_3$ perovskituose priklauso nuo nuo trijų pagrindinių procesų: a) elektrinio lauko įtakos krūvininkų tankiui ir jų pasiskirstymui (elektroninė dalis) b) elektrinio lauko ekranavimo jonais, c) elektrinio lauko sukeltų pokyčių medžiagoje. Išskirti du elektroninės gesinimo dalies mechanizmai: sugeneruotų krūvininkų atsiskyrimas ir judėjimas 1) atskiram kristalite 2) visam perovskito sluoksnyje. Krūvininkų ištraukimo įtaka fluorescencijos gesinimui stebima 10–100 ps laiko skalėje, o krūvininkų atsiskyrimas atskiram kristalite įvyksta trumpiau nei per

kelias ps. Taip pat elektroninė fluorescencijos gesinimo dalis, stipriai priklauso nuo elektrinio lauko ekranavimo judriaisiais jonais, pasireiškiančio ms laiko skalėje. Aprašyti procesai – veiksniai sukeliantys stebimą srovės histerezę saulės elementuose ir sudėtingą elektroliuminescencijos ir srovės dinamiką šviestukuose, todėl svarbūs analizuojant hibridinių perovskitų optoelektroninius prietaisus.

5. Naudojat laikinius fotosrovės ir modifikuotą uždelstojo ištraukimo lauko, matavimo metodus, nustatyti pagrindiniai veiksniai darantys įtaka lateraliniam krūvininkų judėjimui $MAPbI_3$ perovskito polikristalinėse plėvelėse. Atskleisti energetiniai barjerai egzistuojantys kristalų grūdelių riboje – pagrindinis veiksnys lemiantis greitą krūvininkų judrio mažėjimą bėgant laikui. Rezultatai svarbūs kuriant ir analizuojant vertikalios architektūros hibridinių perovskitų optoelektroninius prietaisus: lauko fototranzistorius, fotodiodus, lateralinius fotodetektorius ir vertikalius saulės elementus.

Copies of publications

THE JOURNAL OF PHYSICAL CHEMISTRY Letters

Cite This: *J. Phys. Chem. Lett.* 2019, 10, 1779−1783

Letter

pubs.acs.org/JPCL

Electroluminescence Dynamics in Perovskite Solar Cells Reveals Giant Overshoot Effect

Rokas Gegevičius,[†] Marius Franckevičius,[*,†] Jevgenij Chmeliov,[†,‡] Wolfgang Tress,[§] and Vidmantas Gulbinas[†,‡]

[†]Department of Molecular Compound Physics, Center for Physical Sciences and Technology, Saulėtekio Avenue 3, LT-10257 Vilnius, Lithuania

[‡]Institute of Chemical Physics, Faculty of Physics, Vilnius University, Saulėtekio Avenue 9, LT-10222 Vilnius, Lithuania

[§]Laboratory of Photomolecular Science, ISIC, Swiss Federal Institute of Technology (EPFL), CH-1015 Lausanne, Switzerland

Supporting Information

ABSTRACT: High performance of both photovoltaic and electroluminescent devices requires low nonradiative recombination losses. In perovskites, such loses strongly depend on the carrier traps related to the mobile ions and vacancies, causing *I*−*V* hysteresis of solar cells and influencing the performance of other optoelectronic devices, such as photodetectors and LEDs. To address the dynamics of the mobile ions, here we investigate electroluminescence time evolution in perovskite solar cells under constant and pulsed voltage conditions. We propose a model, accounting for the spatial ion accumulation and explaining the complex electroluminescence dynamics both on fast (microseconds) and slow (seconds) time scales. We demonstrate the appearance of a high-intensity short electroluminescence peak (overshoot pulse) immediately after termination of the electrical pulse. The generation of a giant overshoot pulse suggests a simple way to achieve high pulsed luminescence intensity with a low current density, which opens new prospects toward optical gain and implementation of electrically pumped lasers.

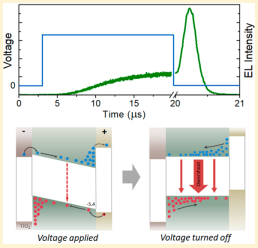

Dynamic processes in perovskites related to the carrier trap formation, migration, and accumulation, as well as formation and deactivation of nonradiative recombination channels, cause the well-known photocurrent hysteresis problem[1] and govern the time evolution of photo- and electroluminescence.[2] They depend in a complex way on the material chemical structure and morphology, as well as on experimental conditions, and therefore still remain weakly explored and understood. These processes are equally important for solar cells and LEDs; photovoltaic and electroluminescence efficiencies are closely interrelated.[3,4] Therefore, electroluminescence (EL) spectroscopy gives useful information about properties of solar cells. It has been employed to identify open-circuit voltage losses and some other photovoltaic parameters.[4−6] Here we demonstrate that transient electroluminescence is very sensitive to the ion accumulation and their spatial distribution and therefore is a powerful tool to address the ion dynamics and related electronic processes in solar cells and LEDs.

We studied the EL dynamics of solution-processed triple-cation perovskite solar cells ($CsFAMAPb(I_xBr_{1-x})$)[7] (see the Supporting Information for more detail) by applying either a constant or pulsed forward voltage. The observed current, EL, and photoluminescence (PL) dynamics on a slow time scale, presented in Figure 1, exhibit remarkably distinct behavior. The PL (Figure 1a) is weakly voltage-dependent, shows a fast partial decrease during the initial 20 s, and then remains constant. On the other hand, the EL intensity is initially very weak and increases for several minutes (Figure 1b). The electric current also increases, albeit faster, and is sizable from the very beginning.

Slow processes such as migration of ions or vacancies, carrier trapping, etc., taking place in perovskites during seconds and minutes, have been widely discussed.[8−11] Ion redistribution may affect nonradiative carrier recombination and charge carrier injection,[12,13] or even cause the formation of a *p*-*i*-*n* structure due to the accumulation of mobile ions next to perovskite/contact layer interfaces.[12] As demonstrated for light-emitting electrochemical cells, an increased conductivity of *p* and *n* layers may significantly affect carrier recombination by concentrating the electric field in the central undoped region.[14,15] Very weak initial EL can hardly be explained by the fast nonradiative recombination, because it would also result in weak PL. Therefore, initially weak EL yield may be due to injection of only one charge carrier type and/or reduced radiative recombination rate, caused by, for example, spatial separation of injected electrons and holes, which in turn may change in time during the formation of the *p*-*i*-*n* structure.

Received: March 4, 2019
Accepted: March 27, 2019
Published: March 28, 2019

DOI: 10.1021/acs.jpclett.9b00618
J. Phys. Chem. Lett. 2019, 10, 1779−1783

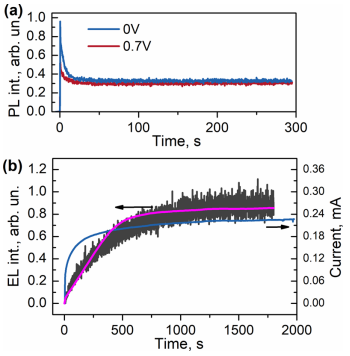

Figure 1. (a) PL intensity dynamics after starting optical excitation. Blue kinetics corresponds to the absence of external electric field, and the red one shows the corresponding dynamics when 0.7 V forward bias was applied. (b) Experimental (dark gray) and simulated (magenta) EL intensity (left axis) and electric current (blue) kinetics (right axis) measured while applying 0.7 V forward bias.

To clarify this EL behavior, we investigated the fast EL dynamics under pulsed voltage bias. To avoid uncertainties caused by the slow processes, these measurements were performed after more than 10 min following the application of periodic voltage pulses, when the slow response reached a steady state. Figure 2a presents a typical temporal response of the EL intensity and electric current density in a perovskite solar cell driven by a rectangular voltage pulse. After an initial capacitive current spike, the current additionally slightly decreased during the entire voltage pulse. The EL appearance was delayed by several microseconds, and its intensity, in contrast to the current behavior, gradually increased, followed by the strong short-lived spike (overshoot) observed immediately after the voltage was switched off. However, depending on the duration and amplitude of the applied voltage, the EL temporal profile was also more complex (see Figure 2b,c). The delay time (when EL exceeded measurement sensitivity) varies approximately inversely proportionally to the applied voltage, with an additional delay of about 1 μs (see Figure S3) caused by charging of the geometrical capacitor, retarding the voltage growth on the sample. The voltage-dependent delay is most likely caused by the accumulation of charge carriers inside the perovskite layer, as will be discussed below. However, other processes, such as the population of carrier traps or fast migration of ions, cannot be completely excluded. It should be mentioned that the overall EL dynamics including the overshoot signal is a fundamental property of perovskites because we observed it not only in the perovskite compositions shown here but also in perovskites of different compositions, including classical methylammonium lead iodide (MAPI) (see Figure S4) and quasi-two-dimensional perovskites. We have also studied perovskite devices protected from moisture and oxygen by sealing them with a polymer. Both sealed and unsealed devices behaved very similarly during the measurements. However, sample degradation was observed at high operation voltages.

When charge transmitted through the sample was kept constant while changing the electrical pulse duration and

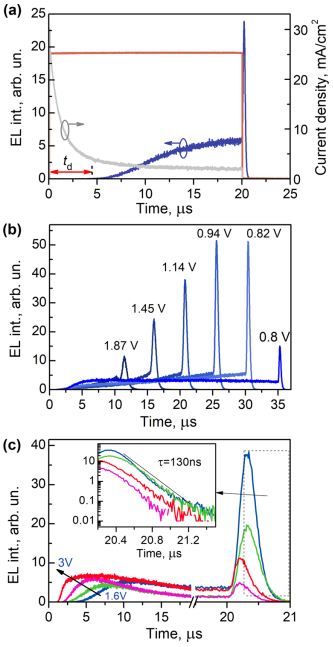

Figure 2. (a) Current density kinetics (gray, right axis) after the application of 20 μs duration and 1.3 V rectangular voltage pulse (red) and EL kinetics measured at 770 nm (blue, left axis). (b) EL transients, measured at identical transmitted charge density per electrical pulse of 80 nC/cm^2, but different pulse durations and voltages. (c) EL transients created by 20 μs 1.6, 1.9, 2.2, and 3 V pulses. The inset shows the decay of the EL pulse.

voltage (Figure 2b), the maximal EL intensity at the end of the electrical pulse (10−30 μs) prior the overshoot was almost identical. This suggests that the EL intensity is determined by the transmitted charge rather than the applied voltage. Meanwhile, at higher voltages, EL kinetics exhibited qualitatively different behavior: after reaching its maximum, the EL intensity then partly decayed again (Figure 2c).

As mentioned, the termination of the voltage pulse triggered an abrupt increase of the EL intensity (Figure 2). This EL peak showed a strong and nonmonotonic dependence on the parameters of the applied electrical pulses. At constant electrical pulse duration of 20 μs, the peak decreased with voltage but increased again at high voltages (Figures 2c and S3). A similar nonmonotonic dependence was also observed by changing the electrical pulse duration and its amplitude at a constant transmitted charge (Figure 2b). Short high-voltage pulses created only a weak peak, which increased with the pulse duration, but long and low-voltage pulses resulted in a weaker peak again. In addition, the peak, as well as the regular EL intensities, showed some still unclear variations depending on the sample treatment history. For instance, the strongest

DOI: 10.1021/acs.jpclett.9b00618
J. Phys. Chem. Lett. 2019, 10, 1779−1783

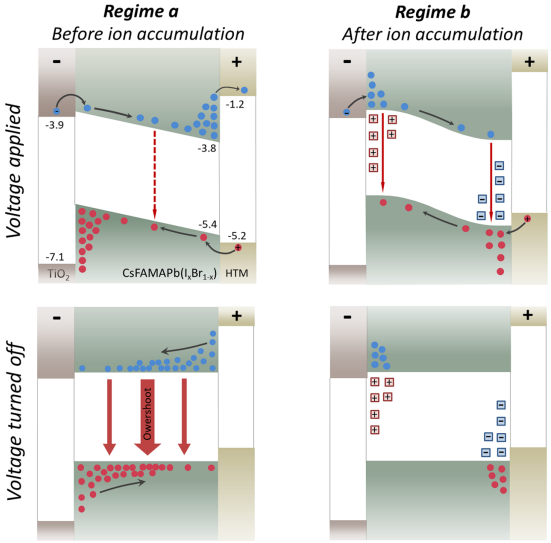

Figure 3. Model for the electroluminescence overshoot pulse formation. Left-hand-side graphs show device operation in regime a, taking place before accumulation of ions, and right-hand-side cartoons show operation in regime b, achieved after ion accumulation on the perovskite layer edges. Blue and red circles show distributions of electrons and holes, respectively, while red and blue squares represent distributions of corresponding ions. Red lines show radiative carrier recombination. Numbers in the top left graph indicate energies of the valence and conduction band edges.

peak exceeding regular EL intensity more than 30 times was obtained with 20 μs and 1.8 V pulses (see Figure S5).

We have also measured EL transients at constant applied voltage but different pulse durations (see Figure S6a,b). These results show that the overshoot can be obtained only with a certain set of the parameters. We attribute the influence of the pulse durations to the modifications of mobile ion distribution, as discussed below. Ion redistribution was suggested to be responsible for the observed current−voltage hysteresis of perovskite solar cells. Such hysteresis presented in Figure S7 indicates that ion migration plays an important role in the investigated devices as well.

The formation of a EL peak after termination of the voltage pulse has been previously observed in organic LEDs and is known as the electroluminescence overshoot (EO).[16−18] It was attributed either to the recombination of detrapped holes with electrons or to the redistribution of accumulated charge carriers. Although the basic EO formation mechanism in the perovskite solar cell may be similar as in organic LEDs, ion redistribution in the former plays an additional crucial role, making the EO properties much more complex. To relate free charge carrier dynamics and recombination with the ion redistribution, we propose a model that is schematically illustrated in Figure 3 and, as we show below, can explain the EL evolution in perovskite solar cells on both slow (seconds−minutes) and fast (microseconds) time scales. We distinguish two extreme device performance regimes: (a) before redistribution of mobile ions and (b) after the device is exposed to the external electric field for a longer time, resulting in notable ion redistribution within the perovskite layer.

In regime a, electrons and holes injected over small barriers from TiO_2 and Spiro-MeOTAD, respectively, drift through the perovskite layer and, facing high extraction barriers, accumulate close to the interfaces with carrier transport layers. In this regime, one would observe very weak EL signal that is limited by two factors: (i) weak charge carrier recombination while quickly drifting through the layer of the accumulated charges of the opposite sign and (ii) even weaker recombination in the perovskite bulk due to very small overlap between the distributions of the accumulated electrons and holes. Carrier accumulation next to perovskite interfaces is most likely limited by the surface recombination[19] and/or permeation through the energy barriers at high voltages. Termination of the applied voltage removes the electric field, or even inverts it for a short time, and causes mixing of electron and hole spatial distributions by diffusion, consequently increasing luminescence intensity observed as an overshoot effect. Alternatively, in regime b, redistributed mobile ions form the *p-i-n* structure with high hole and electron densities next to interfaces with TiO_2 and Spiro-MeOTAD layers, respectively. Injected electrons and holes quickly drift through the perovskite layer toward opposite electrodes until reaching regions doped with opposite charge carriers. Therein they rapidly recombine, causing the strong EL signal. Because of the fast recombination, injected electrons and holes do not accumulate inside the perovskite layer in regime b, and therefore the overshoot effect should be completely absent.

DOI: 10.1021/acs.jpclett.9b00618
J. Phys. Chem. Lett. 2019, 10, 1779−1783

The above-described experimental data correspond to the intermediate regime, when the doped regions are formed, but the doping level is not sufficient to completely prevent accumulation of the injected charge carriers. Application of low voltages results in weak ion redistribution and material doping; thus, the recombination of the injected carriers with the equilibrium carriers is relatively slow, which in turn allows significant carrier accumulation. Then the device's performance is similar to the regime a, enabling the formation of a strong overshoot pulse. On the other hand, application of higher voltage leads to more pronounced ion redistribution and, accordingly, a higher doping level. As a result, carrier recombination in the doped regions accelerates, causing stronger steady-state EL but minimizing accumulation of injected charge carriers and the overshoot pulse, as was indeed observed experimentally (Figure 2c).

The detailed mathematical description of this EL model is presented in the Supporting Information. Briefly, we have modeled time evolution of charge carrier concentration by means of the Einstein–Smoluchowski diffusion equation, additionally taking into account electron–hole recombination. We also assumed that some cations and anions are mobile on a time scale of tens of seconds, their initial densities being free parameters. Exposed to the external electric field, these mobile ions drift through the perovskite layer until their densities reach steady-state exponential distributions near the corresponding electrodes. For simplicity, we also assumed identical electron and hole properties. The carrier mobility used in our model was of 5 $cm^2 V^{-1} s^{-1}$, which is in the range of typically reported values of 1–100 $cm^2 V^{-1} s^{-1}$.[20−22] The used electron–hole radiative recombination rate of $\gamma = 3\ \mu m^3\ s^{-1}$ is close to the one reported in ref 5. The model also accounts for formation of the doped regions at the perovskite interfaces due to mentioned ion redistribution as well as charge carrier trapping into nonradiative traps, responsible for a PL decay with a time constant of 130 ns (see Figure S2b).

The modeled long-term (seconds to minutes) EL evolution is shown with magenta line in Figure 1b. The model reproduces the experimentally observed continuous EL growth from zero to the steady-state value. Calculated EL dynamics under pulsed excitation corresponding to the above-described experimental data are presented in Figure 4. The model quantitatively reproduces all observed EL dynamical properties: delayed EL growth, its partial decay on a microsecond time scale, and formation of the overshoot pulse. It also predicts an intensity decrease immediately after the voltage switch-off that was indeed experimentally observed at the highest voltage in Figure 2c, as well as the growth of the EO amplitude with the increase of voltage pulse durations under constant current density (Figures 2b and 4a) and its decrease at high voltages (Figures 2c and 4b). The total quantitative agreement between the modeled and experimental curves was not completely achieved. This is not surprising because the model is significantly simplified: we assumed identical properties of anions and cations, of electrons and holes, and did not account for such phenomena as material inhomogeneity, electric field screening, etc. Currently, we have little information about these processes; therefore, our approach was to keep the model simple, including as few free parameters as possible.

Nevertheless, our model explains the main EL dynamic features, which validates it and makes it useful for understanding and controlling both solar cell and LED performance.

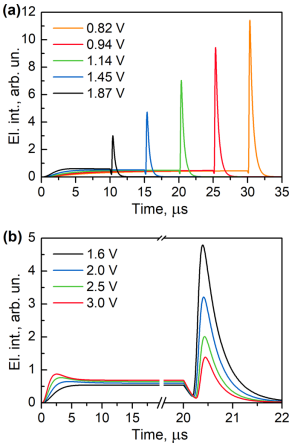

Figure 4. (a) Calculated EL transients at different pulse durations and voltages but identical transmitted charge density of 80 nC/cm^2 per electrical pulse. (b) EL kinetics, calculated for 20 μs pulses of different voltage (see Figure 2 for the corresponding experimental data).

Simulation results (presented in Figure S10) indicate that the overshoot pulse intensity might be further amplified by reducing the surface recombination rate as well as charge trapping.

The overshoot effect may be particularly interesting in the development of electrically pumped perovskite lasers. To date, only optically pumped perovskite lasers have been demonstrated.[23−26] Electrical pumping of perovskite or other solution-processed lasers would open new exciting possibilities for their application; however, their realization still meets serious difficulties. The high current density needed to achieve optical gain and the concomitant device heating are among the major limiting factors.[25,27] The giant overshoot effect, enabling high pulsed luminescence intensity with a low current density by accumulating charge carriers inside a perovskite layer may facilitate circumventing this problem. The overshoot effect resembles quality switching (Q-switching) in lasers, used to obtain high power short pulses with long pumping pulse. Further increase of overshoot pulse intensity may be achieved by developing perovskites with higher luminescence yield as well as by engineering of the device architecture permitting a higher density of accumulated charge carriers by minimizing the density of mobile ions or surface recombination.

■ ASSOCIATED CONTENT

Supporting Information

The Supporting Information is available free of charge on the ACS Publications website at DOI: 10.1021/acs.jpclett.9b00618.

Description of experimental methods (PDF)

■ AUTHOR INFORMATION

Corresponding Author

*E-mail: marius.franckevicius@ftmc.lt.

DOI: 10.1021/acs.jpclett.9b00618
J. Phys. Chem. Lett. 2019, 10, 1779−1783

The Journal of Physical Chemistry Letters Letter

ORCID

Marius Franckevičius: 0000-0001-8020-7201
Jevgenij Chmeliov: 0000-0002-7591-1373
Wolfgang Tress: 0000-0002-4010-239X

Notes

The authors declare no competing financial interest.

■ ACKNOWLEDGMENTS

R.G., M.F., and V.G. acknowledge funding from the European Social Fund according to the activity "Improvement of researchers' qualification by implementing world-class R&D projects" of Measure No. 09.3.3-LMT-K-712-01-0031.

■ REFERENCES

(1) Lee, J. W.; Kim, S. G.; Bae, S. H.; Lee, D. K.; Lin, O.; Yang, Y.; Park, N. G. *Nano Lett.* **2017**, *17*, 4270.
(2) Chirvony, V. S.; Martínez-Pastor, J. P. *J. Phys. Chem. Lett.* **2018**, *9* (17), 4955.
(3) Miller, O. D.; Yablonovitch, E.; Kurtz, S. R. *Photovoltaics, IEEE J.* **2012**, *2*, 303.
(4) Tress, W.; Marinova, N.; Inganäs, O.; Nazeeruddin, M. K.; Zakeeruddin, S. M.; Graetzel, M. *Adv. Energy Mater.* **2015**, *5*, 1400812.
(5) Bi, D.; Tress, W.; Dar, M. I.; Gao, P.; Luo, J.; Renevier, C.; Schenk, K.; Abate, A.; Giordano, F.; Correa Baena, J. P.; Decoppet, J. D.; Zakeeruddin, S. M.; Nazeeruddin, M. K.; Grätzel, M.; Hagfeldt, A. *Sci. Adv.* **2016**, *2*, No. e1501170.
(6) Hameiri, Z.; Soufiani, A. M.; Juhl, M. K.; Jiang, L.; Huang, F.; Cheng, Y.; Kampwerth, H.; Weber, J. W.; Green, M. A.; Trupke, T. *Prog. Photovoltaics* **2015**, *23*, 1697.
(7) Saliba, M.; Matsui, T.; Seo, J. Y.; Domanski, K.; Correa-Baena, J. P.; Nazeeruddin, M. K.; Zakeeruddin, S. M.; Tress, W.; Abate, A.; Hagfeldt, A.; et al. *Energy Environ. Sci.* **2016**, *9*, 1989.
(8) Meloni, S.; Moehl, T.; Tress, W.; Franckevičius, M.; Saliba, M.; Lee, Y. H.; Gao, P.; Nazeeruddin, M. K.; Zakeeruddin, S. M.; Rothlisberger, U.; et al. *Nat. Commun.* **2016**, *7*, 10334.
(9) Tress, W.; Yavari, M.; Domanski, K.; Yadav, P.; Niesen, B.; Correa-Baena, J.-P.; Hagfeldt, A.; Gratzel, M. *Energy Environ. Sci.* **2018**, *11*, 151.
(10) Yuan, Y.; Huang, J. *Acc. Chem. Res.* **2016**, *49*, 286.
(11) Shan, X.; Li, J.; Chen, M.; Geske, T.; Bade, S. G. R.; Yu, Z. *J. Phys. Chem. Lett.* **2017**, *8*, 2412.
(12) Deng, Y.; Xiao, Z.; Huang, J. *Adv. Energy Mater.* **2015**, *5*, 1500721.
(13) Sherkar, T. S.; Momblona, C.; Gil-Escrig, L.; Ávila, J.; Sessolo, M.; Bolink, H. J.; Koster, L. J. A. *ACS Energy Lett.* **2017**, *2*, 1214.
(14) Devižis, A.; Jenatsch, S.; Diethelm, M.; Gulbinas, V.; Nüesch, F. A.; Hany, R. *ACS Photonics* **2018**, *5*, 3124.
(15) Jenatsch, S.; Wang, L.; Bulloni, M.; Véron, A. C.; Ruhstaller, B.; Altazin, S.; Nüesch, F.; Hany, R. *ACS Appl. Mater. Interfaces* **2016**, *8*, 6554.
(16) Lupton, J. M.; Nikitenko, V. R.; Samuel, I. D. W.; Bässler, H. *J. Appl. Phys.* **2001**, *89*, 311.
(17) Nikitenko, V. R.; Arkhipov, V. I.; Tak, Y. H.; Pommerehne, J.; Bässler, H.; Hörhold, H. H. *J. Appl. Phys.* **1997**, *81*, 7514.
(18) Chandra, V. K.; Tiwari, M.; Chandra, B. P.; Ramrakhiani, M. *Synth. Met.* **2011**, *161*, 460.
(19) Lopez-Varo, P.; Jiménez-Tejada, J. A.; García-Rosell, M.; Ravishankar, S.; Garcia-Belmonte, G.; Bisquert, J.; Almora, O. *Adv. Energy Mater.* **2018**, *8*, 1702772.
(20) Ponseca, C. S.; Savenije, T. J.; Abdellah, M.; Zheng, K.; Yartsev, A.; Pascher, T.; Harlang, T.; Chabera, P.; Pullerits, T.; Stepanov, A.; et al. *J. Am. Chem. Soc.* **2014**, *136*, 5189.
(21) Motta, C.; El-Mellouhi, F.; Sanvito, S. *Sci. Rep.* **2015**, *5*, 12746.
(22) Wehrenfennig, C.; Eperon, G. E.; Johnston, M. B.; Snaith, H. J.; Herz, L. M. *Adv. Mater.* **2014**, *26*, 1584.
(23) Harwell, J. R.; Whitworth, G. L.; Turnbull, G. A.; Samuel, I. D. W. *Sci. Rep.* **2017**, *7*, 11727.
(24) Zhu, H.; Fu, Y.; Meng, F.; Wu, X.; Gong, Z.; Ding, Q.; Gustafsson, M. V.; Trinh, M. T.; Jin, S.; Zhu, X. Y. *Nat. Mater.* **2015**, *14*, 636.
(25) Jia, Y.; Kerner, R. A.; Grede, A. J.; Rand, B. P.; Giebink, N. C. *Nat. Photonics* **2017**, *11*, 784.
(26) Wang, K.; Sun, W.; Li, J.; Gu, Z.; Xiao, S.; Song, Q. *ACS Photonics* **2016**, *3*, 1125.
(27) Sutherland, B. R.; Sargent, E. H. Perovskite Photonic Sources. *Nat. Photonics* **2016**, *10*, 295.

DOI: 10.1021/acs.jpclett.9b00618
J. Phys. Chem. Lett. 2019, 10, 1779−1783

FULL PAPER

Perovskite LEDs

ADVANCED FUNCTIONAL MATERIALS

www.afm-journal.de

Reduced Efficiency Roll-Off and Improved Stability of Mixed 2D/3D Perovskite Light Emitting Diodes by Balancing Charge Injection

Azhar Fakharuddin, Weiming Qiu, Guillaume Croes, Andrius Devižis, Rokas Gegevičius, Alexander Vakhnin, Cedric Rolin, Jan Genoe, Robert Gehlhaar, Andrey Kadashchuk, Vidmantas Gulbinas,* and Paul Heremans**

Perovskite light emitting diodes (PeLEDs) have reached external quantum efficiencies (EQEs) over 21%. Their EQE, however, drops at increasing current densities (J) and their lifetime is still limited to just a few hours. The mechanisms leading to EQE roll-off and device instability require thorough investigation. Here, improvement in EQE, EQE roll-off, and lifetime of PeLEDs is demonstrated by tuning the balance of electron/hole transport into a mixed 2D/3D perovskite emissive layer. The mixed 2D/3D perovskite layer induces exciton confinement and beneficially influences the electron/hole distribution inside the perovskite layer. By tuning the electron injection to match the hole injection in such active layer, a nearly flat EQE for J = 0.1–200 mA cm^{-2}, a reduced EQE roll-off until J = 250 mA cm^{-2}, and a half-lifetime of ≈47 h at J = 10 mA cm^{-2} is reached. A model is also proposed to explain these improvements that account for the spatial electron/hole distributions.

1. Introduction

Solution processed organometallic hybrid perovskites have emerged as a successful material for a range of optoelectronic devices, such as light emitting diodes (LEDs), lasers, and photodetectors.[1] The remarkable progress of these devices is mainly made via controlling the defect states responsible for nonradiative recombination. This resulted in a photoluminescence quantum efficiency (PLQE) >70% in perovskite thin films.[2,3] Several methods have been shown to allow the external quantum efficiency (EQE) of perovskite LEDs (PeLEDs) to reach up to 21%: by using nanocrystals;[4,5] by employing hybrid perovskite materials with 2D/3D crystal structure[6,7] to confine charge carriers spatially; by using 2D/3D perovskite passivated with an insulating polymer;[8] by anion exchange in colloidal quantum dot films leading to a low trap-state density.[9] Despite the rapid progress made in PeLEDs, the EQE tends to drop at high current density (J), a phenomenon known as efficiency roll-off.[10] The current density corresponding to 50% EQE drop (J_0) for many PeLEDs is in the range ≈10–100 mA cm^{-2}.[5,6,8,11] Such roll-off is undesirable when targeting high-brightness applications or ultimately injection lasing.

Various mechanisms have been proposed to explain the EQE roll-off at high current densities, in particular Auger recombination,[12,13] Joule heating, and charge imbalance.[14] For example, Zou et al.[13] suggested that the EQE roll-off is caused by luminescence quenching due to nonradiative Auger recombination, which was suppressed by tuning the width of quantum wells in 2D/3D perovskite employing a multiple quantum well structure. Kim et al.[14] demonstrated via pulsed driving that PeLEDs could withstand J up to 150 A cm^{-2} with no sign of Auger recombination. They assigned the observed EQE roll-off to Joule heating combined with imbalanced charge injection into the device. Joule heating increases the local temperature of the device, thereby enhancing the exciton dissociation rate, and it may affect charge transport properties of organic layers.[15] Balancing the charge injection resulted in significantly reduced roll-off in organic LEDs (OLEDs)[10] and quantum dot LEDs[16] at high J. The role of such balance, however, still remains unexplored for PeLEDs. For a device operating in imbalanced charge injection conditions, the surplus charge could leak through the

Dr. A. Fakharuddin, Dr. W. Qiu, G. Croes, Dr. C. Rolin, Prof. J. Genoe, Dr. R. Gehlhaar, Prof. A. Kadashchuk, Prof. P. Heremans
IMEC
Kapeldreef 75, 3001 Leuven, Belgium
E-mail: azhar.fakhar.uddin@imec.be; Paul.heremans@imec.be
Dr. A. Fakharuddin, Dr. W. Qiu, G. Croes, Prof. J. Genoe, Prof. P. Heremans
Department of Electrical Engineering
KU Leuven
Kasteelpark Arenberg, 3001 Leuven, Belgium
Dr. A. Devižis, R. Gegevičius, Prof. V. Gulbinas
Center for Physical Sciences and Technology
Sauletekio av. 3, LT-10257 Vilnius, Lithuania
E-mail: Vidmantas.gulbinas@ftmc.lt
Dr. A. Vakhnin, Prof. A. Kadashchuk
Institute of Physics
National Academy of Sciences of Ukraine
Prospect Nauky 46, 03028 Kyiv, Ukraine
The ORCID identification number(s) for the author(s) of this article can be found under https://doi.org/10.1002/adfm.201904101.

DOI: 10.1002/adfm.201904101

ADVANCED SCIENCE NEWS
www.advancedsciencenews.com

ADVANCED FUNCTIONAL MATERIALS
www.afm-journal.de

device, thus reducing its EQE.[17] The excess carrier concentration may also annihilate singlet excitons.[10] Notably, in OLEDs, charge balance also determines where the excitons are formed and their concentration. In OLEDs, an exciton density spread across the emitter thickness is preferred over excitons concentrated close to an interface, as this causes exciton–exciton annihilation.[10] A thorough investigation of the charge injection/transport balance in PeLEDs and its influence on EQE roll-off is therefore required. We also note negligible roll-off in a report[3] where EQE of ≈20.7% is demonstrated via reduced light-trapping. But no detail is provided to explain the low EQE roll-off.

In PeLEDs, the peak EQE usually occurs at very low current density ($J \leq 10^{-1}$ mA cm^{-2}).[8,18] These devices are, however, characterized by a significant roll-off that kicks in at a modest current density of $J_0 \approx 10$ mA cm^{-2}. Some reports show an EQE roll-off at higher current density $J_0 \approx 100$ mA cm^{-2} (and beyond), and in those cases, the peak EQE is at higher J (10–30 mA cm^{-2}),[3,13] suggesting that in these devices, a significant trap-mediated recombination competes with radiative recombination. A device that combines high EQE at low J and reduced roll-off at high current density is yet to be realized. Furthermore, little is known regarding the mechanisms leading to degradation of PeLEDs. A lifetime of a few hours at $J \approx 1$ A cm^{-2} was recently reported using hybrid 2D/3D perovskite,[19] which suggests that such materials can intrinsically withstand high J.

In the present study, we improve device performance at low as well as high J in PeLEDs employing quasi-2D perovskite (BA-incorporating $MAPb(I/Br)_3$, BA = *n*-butylammonium) which we refer to as mixed 2D/3D perovskite. Stoichiometric tuning of 2D/3D perovskite films leads to a high EQE, suggesting dominant radiative recombination, at $J \approx 0.1$–1 mA cm^{-2}, whereas systematic control over the charge injection into the emissive layer (together with optimized stoichiometry) minimizes EQE roll-off up to $J \geq 200$ mA cm^{-2}. We show a peak EQE of 16.7 ± 1% at 0.4 mA cm^{-2} for the champion device. The optimized devices maintain EQE ≈10% up to $J = 200$ mA cm^{-2}. Additionally, these optimized devices show a T_{50} (lifetime defined as the operation time at which luminescence drops by half) of several tens of hours (for a best device $T_{50} \approx 47$ h at 10 mA cm^{-2} and $T_{50} \approx 12$ h at 100 mA cm^{-2}), which is about the benchmark stability values reported for PeLEDs at these current densities.[3,8] Extensive spectroscopy measurements of the optimized perovskite films and devices suggest that these improvements stem from three effects combined in a single device: 1) the optimized stoichiometry of 2D/3D perovskites, which leads to exciton confinement and beneficial confinement of charge carriers in 3D domains in the mixed 2D/3D emissive layers; 2) the control over spatial electron/hole distribution in the perovskite semiconductor; 3) the balanced charge injection in the optimized device stack.

2. Results and Discussion

2.1. Performance of Perovskite Light Emitting Diodes Based on 2D/3D and 3D Perovskite

We first optimize the performance of 2D/3D PeLEDs by tuning the perovskite stoichiometry in an LED architecture shown in **Figure 1**a. A 3D perovskite $MAPb(I/Br)_3$ is used as reference. Its stoichiometry is systematically tuned toward 2D/3D perovskite via incorporation of the large cation BA. The BA concentration was varied from 0% to 60% (see the Experimental Section and Table S2 in the Supporting Information) in the precursor solution containing PbI_2. X-ray diffraction, UV–vis absorption, and photoluminescence investigations (Figures S1–S3, Supporting Information) unambiguously assert the mixed presence of 3D and 2D domains in these layers. The diodes further comprise 4,7-Diphenyl-1,10-phenanthroline (bphen) and poly(4-butylphenyl-diphenyl-amine), poly-TPD as electron and hole transport layer, respectively.

The 2D/3D perovskite emissive layer is a dense pinhole-free thin film (≈80 nm, Figure S2b, Supporting Information), slightly thinner than a reference 3D film (≈100 nm, Figure S2c, Supporting Information). We optimized the thickness of transport/injecting layers via optical simulations (Figure S4, Supporting Information) in order to maximize performance of our PeLEDs. The detailed device performance of PeLEDs as a function of different BAI concentrations (0–60%) is provided in Table S3 in the Supporting Information. The optimum concentration of 50% BAI in the 2D/3D perovskite films results in the highest best and average EQE, and therefore, in our further experiments, we only use this optimized stoichiometry of 2D/3D perovskite. We note that the electroluminescence (EL) emission peak and EQE stabilize after several minutes (Figures S5 and S6, Supporting Information), and, throughout the study, we only report stabilized EQE values.

We further optimized device performance by systematically doping the bphen electron transport layer (ETL) with a small molecule Alq_3 (Tris(8-hydroxy-quinolinato)aluminum) to alter electron transport/injection into the PeLEDs (as will be elaborated in the latter sections). Figure 1c shows EQE dependency of PeLEDs upon ETL doping. The PeLEDs employing Alq_3-doped bphen as ETL, particularly using higher doping concentrations, demonstrate a flat EQE for a wide range of applied bias (injection current). This contrasts with devices with pristine bphen that show significant EQE roll-off. For example, the EQE_{max} for PeLED with pristine bphen drops by 72% at 6.5 V ($J = 161$ mA cm^{-2}), whereas the EQE_{max} of devices with 10% and 20% doped bphen show only ≤20% EQE drop, up to 7 V ($J = 112$ and 73 mA cm^{-2} for 10% and 20% Alq_3-doped bphen, respectively). A statistical analysis made for over 150 devices from 12 different batches, shown in Figure 1d, supports the fact that Alq_3-doped bphen increases the highest as well as the average EQE of PeLEDs. The highest (average) EQE of PeLEDs made using 2D/3D perovskite films increases from 9.9% (av. 5.3%) with pristine bphen to 10.5% (av. 7.9%), 12.5% (av. 8.9%), 16.8% (av. 12.7%), and 11.1% (av. 7.1%) when the bphen ETL is doped with 2%, 5%, 10%, and 20% Alq_3, respectively. The 3D counterparts showed significantly lower EQE (Figure S8, Supporting Information).

Next, we analyze the EQE performance over a wide range of injection current density ($J \approx 0.05$–660 mA cm^{-2}), well beyond the roll-off current densities (between 10–50 mA cm^{-2}[5,6,8,11]) reported in literature. We only choose PeLEDs with pristine (0%) and 10% doped bphen as ETL, both for 2D/3D and 3D PeLEDs (**Figure 2**a). A significant roll-off is observed for 3D PeLEDs. The peak EQE of 1.2% at 13 mA cm^{-2} for 3D PeLEDs

ADVANCED SCIENCE NEWS
www.advancedsciencenews.com

ADVANCED FUNCTIONAL MATERIALS
www.afm-journal.de

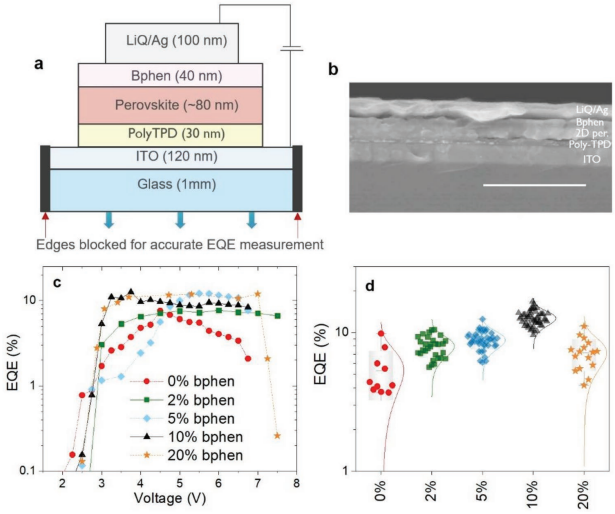

Figure 1. a) Schematic showing various material layers for PeLEDs and their thickness. The edges of LEDs are covered such that no light from the edges can contribute to EQE.[20] b) Cross-section of a complete PeLED employing 2D/3D perovskite. Scale bar: 500 nm. The lower panel shows the symbols used to plot EQE versus voltage plot in c). The various percentages refer to the concentration of Alq_3 in bphen ETL. Statistics made for over 150 PeLEDs with different bphen doping levels are shown in (d). The EQE (stabilized) is measured at J, 1–20 mA cm^{-2} (as will be discussed in subsequent section, the EQE remains nearly flat for $J \approx 10^{-1}$–10^{2} mA cm^{-2}).

(0% bphen) drops by more than two orders in magnitude at 66 mA cm^{-2}. This improves slightly when 10% doped bphen is used as ETL with a device that demonstrates EQE of 4.26% and 2.26% at 66 and 100 mA cm^{-2} (corresponding to ≈42% and 69% drop in the peak EQE). These results show that the efficiency roll-off is significantly affected by charge transport/injection into the device. A similar and even more pronounced trend is observed for 2D/3D perovskite-based LEDs: The peak EQE for the 2D/3D PeLEDs with pristine bphen ETL drops from 8.1% at $J = 13$ mA cm^{-2} by almost an order of magnitude at $J \approx 100$ mA cm^{-2} and the devices completely degraded at $J \geq 200$ mA cm^{-2}. For the same perovskite emissive layer, however, the LED performance greatly improves when bphen doped with 10% Alq_3 is used as ETL. The peak EQE of ≈13.8% drops only by ≈26% at 100 mA cm^{-2} (EQE 10.8%) and an EQE of 4.1% is recorded for $J = 200$ mA cm^{-2}.

The champion device (in terms of EQE roll-off) employing ITO/poly-TPD/2D/3D.Per/10% bphen/Liq/Ag showed a nearly flat EQE for $J = 0.2$–150 mA cm^{-2} (peak EQE of 15%) with negligible roll-off (EQE of 9.7% at 200 mA cm^{-2}). The J_0, defined as the current density at which the EQE drops to 50%, was ≈250 mA cm^{-2} and the device still showed EQE of 1.9% at $J = 660$ mA cm^{-2}. The champion device (in terms of the highest EQE) showed an EQE of 16.7 ± 1% at $J = 0.4$ mA cm^{-2} with negligible roll-off at higher J (Figure S10, Supporting Information). To show the performance reproducibility of this best-performing device structure, we also report the average EQE of nine devices made from different batches measured at J up to 660 mA cm^{-2} (Figure 2c). The EQE trend is similar for all devices (flat EQE over a wide J). We also note EQE ≈12.2% at 100 mA cm^{-2} in the best device, which is among the highest reported values at such J employing organic–inorganic hybrid perovskites.[8,9,13,21] Contrary to the widespread literature reporting a substantial efficiency roll-off for 2D/3D PeLEDs, typically at $J \approx 10$–50 mA cm^{-2},[5,6,8,11,22] and even at lower J for 3D PeLEDs,[22] our 2D/3D PeLEDs showed only a minor EQE drop for J up to 200 mA cm^{-2} (≈50 mA cm^{-2} for 3D PeLEDs).

2.2. Lifetime Measurements of Mixed 2D/3D PeLEDs

In order to investigate the stability of our PeLEDs, we first carried out lifetime measurements at a constant $J \approx 13$ mA cm^{-2}. The lifetime measurements in Figure 2d reveal that for both 2D/3D and 3D perovskite emissive layers, the alteration of the ETL brings about a great improvement in lifetime. Clearly, the device stability is more strongly correlated to charge injection and transport into the device than with the initial EQE. For example, 2D/3D PeLEDs with pristine bphen (0%) as an ETL have a high initial EQE, but under continuous J stress, the EQE

ADVANCED SCIENCE NEWS
www.advancedsciencenews.com

ADVANCED FUNCTIONAL MATERIALS
www.afm-journal.de

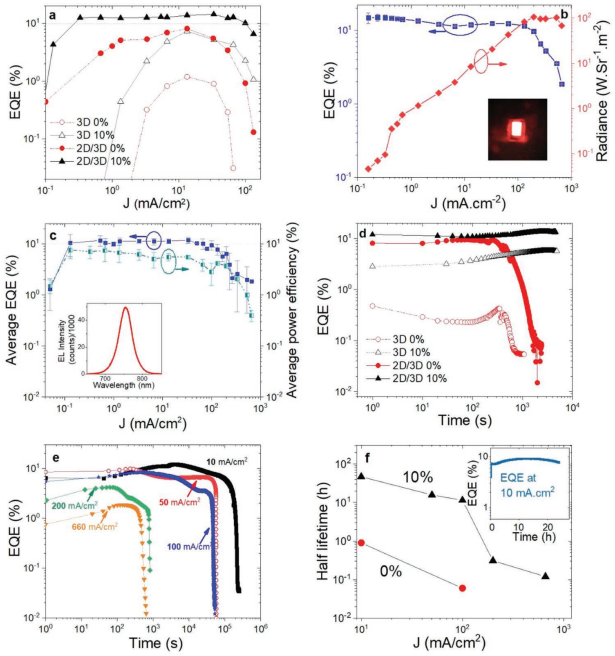

Figure 2. a) Current density (*J*) versus EQE plots of PeLEDs employing 3D and 2D/3D perovskites as emitter layer. 0% and 10% correspond to pristine bphen (0%) and 10% Alq_3-doped bphen as ETL. b) EQE and radiance of a champion (in terms of operating current range) PeLED employing 2D/3D perovskite and 10% Alq_3-doped bphen. Photo in the inset shows a bright device operating at 50 mA cm^{-2}. c) Average EQE and power efficiency of eight best performing PeLEDs for a reliable comparison of data. Inset of (c) shows a typical EL spectrum of an optimized 2D/3D PeLEDs recorded at J = 50 mA cm^{-2} ($\lambda_{emission}$ = 755 nm, full width at half maxima (FWHM) = 41 nm). d) Stability of PeLEDs shown in (a) at a constant J = 13 mA cm^{-2}. e) Stability of champion PeLEDs employing 2D/3D perovskite and 10% Alq_3-doped bphen as ETL as a function of J. f) Half-lifetime (T_{50}) of all four types of PeLEDs as a function of J. Inset shows EQE measured at a constant J = 10 mA cm^{-2}. The device shows T_{85} of 14.2 h (with respect to peak EQE which was reached after 10.8 h after the start of the measurement). For details, refer to Figure S9 in the Supporting Information.

rapidly drops to near zero within 20 min. On the contrary, the 3D and 2D/3D PeLEDs (3D PeLED start at significantly lower EQE) with 10% doped bphen as ETL show no drop in EQE even after 90 min at the same J. These findings emphasize the importance of charge injection balance into the PeLEDs, just as in organic LEDs and quantum-dot LEDs.[10,23]

We also measured lifetime of PeLEDs at continuous J (10–660 mA cm^{-2}) as shown in Figure 2e for the champion 2D/3D perovskite with 10% Alq_3-doped bphen. We note a rise in EQE for the initial few minutes, which we attribute to ion migration and halide redistribution.[24] Furthermore, the EL emission peak red-shifts during this stabilization time, after which it remains stable throughout the measurement (see Figure S5 in the Supporting Information for details). From the half-lifetime (T_{50}) plot of PeLEDs with different compositions (Figure 2f), we note a direct correlation between J and T_{50}. Clearly, the doping of the ETL with 10% Alq_3 improves the lifetime substantially, regardless of the emissive layer and the injected current. For example, the T_{50} for 2D/3D PeLEDs improved from 0.8 h (for 0% bphen) to ≈47 h (10% bphen) in a best device at J = 10 mA cm^{-2}. Such lifetime value is among the longest reported so far for PeLEDs, which typically display lifetimes of several minutes to only a few hours, at lower injection current values.[8,22] Note that a T_{50} up to 96 h has recently been reported at 100 mA cm^{-2} (EQE 3.85%).[19] This excellent performance results from the use of a new large cation 3-bromobenzylammonium iodide to form the 2D perovskite and of different injecting contacts.

The doped ETL with 10% Alq_3-doped bphen yields remarkable improvements in EQE, roll-off, and stability, particularly in

ADVANCED SCIENCE NEWS
www.advancedsciencenews.com

ADVANCED FUNCTIONAL MATERIALS
www.afm-journal.de

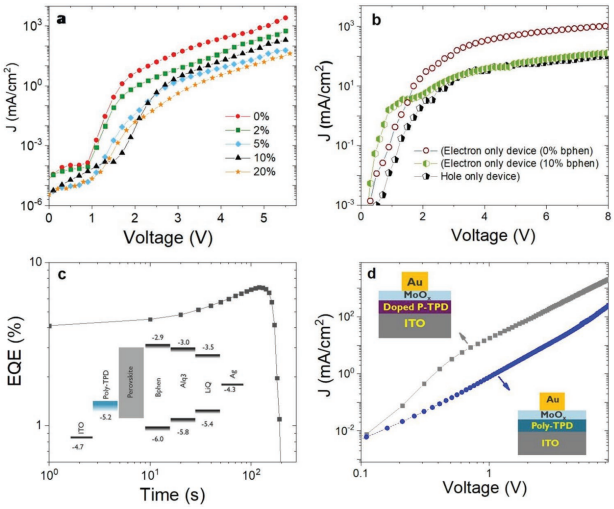

Figure 3. a) Current–voltage curves of PeLEDs employing 2D/3D perovskite as a function of doping of ETL. b) Unipolar devices to quantify only one type of current flowing through the device. c) EQE of PeLEDs employing F6TCNNQ as HTL while the rest of device configuration remains the same. For details of inset (c), refer to Figure S13 in the Supporting Information. d) HODs employing poly-TPD and 2% F6TCNNQ-doped poly-TPD as hole transport layer, a thin layer of MoO_x (5 nm), and 80 nm thick Au layer.

the devices employing 2D/3D perovskite emissive layers. Surprisingly the doping of bphen with Alq_3 diminishes the electron transport characteristics. Indeed, the current–voltage curves in **Figure 3**a 2D/3D PeLEDs suggest that the systematic doping of bphen with Alq_3 increases the resistivity of the ETL. We explain this observation by noting that the lowest unoccupied molecular orbital (LUMO) of the Alq_3 is energetically lower than that of bphen (Figure 3c).[25] Therefore, Alq_3 molecules form shallow electron traps in the bphen matrix. These extrinsic traps increase the energy disorder in the matrix because the energy width of the resulting hopping site gets effectively broader, which hinder electron hopping reducing thus the overall electron mobility.[26] To experimentally validate these assumptions, we fabricated single-layer devices that allow only one type of charge carrier to pass through the device.[5,27] The electron-only device (EOD) consists of ITO/ZnO/PEIE/2D3D. perovskite/bhpen(0%,10%)/LiQ/Ag (PEIE is polyethylenimine ethoxylated) whereas the architecture of the hole-only device (HOD) is ITO/poly-TPD/2D3D.perovskite/poly-TPD/MoO_3/Au. Thickness of all the layers in single carrier devices resembles those in PeLEDs. The measured *J–V* curves (Figure 3b) demonstrate that the electron current in EOD employing 10% doped bphen drops by almost a factor of 10 in comparison with that employing pristine bphen. As a result, it matches better with the hole current passing through the HOD. Pristine bphen has a reported electron mobility ($\mu_e \approx 5 \times 10^{-4}$ cm^2 V^{-1} s^{-1})[28] that is fivefold the hole mobility reported for poly-TPD ($\mu_h \approx 1 \times 10^4$ cm^2 V^{-1} s^{-1}).[29] By doping bphen with 10% Alq_3, we reduce the electron transport and establish a better electron/hole balance. Note that this direct comparison between currents in EOD and HOD may be affected by differences in the properties of perovskite layers grown on different charge selective contacts.[30] We note however, that their morphologies revealed by atomic force microscopy (AFM) in Figures S1 and S11 in the Supporting Information are very similar.

In order to confirm that charge balance leads to high EQE and long lifetime in PeLEDs employing poly-TPD as HTL and 10% doped bphen as ETL, we doped poly-TPD with a small molecule 2,2′-(perfluoro-naphthalene-2,6-diylidene)dimalononitrile (F6TCNNQ).[31] The EQE of the PeLEDs employing 2% F6TCNNQ-doped poly-TPD as HTL and 10% Alq_3-doped bphen as ETL dropped to ≈7%. Also, their half lifetime dropped to around 3 min at 10 mA cm^{-2} (Figure 3c). We attribute this to a higher hole current in the doped HTL, as revealed by the *J–V* curves of HODs employing poly-TPD and 2% F6TCNNQ-doped poly-TPD in Figure 3d. A comparison of single carrier complete devices further shows a dominant hole current in PeLEDs when poly-TPD is doped with 2% F6TCNNQ (Figure S14, Supporting Information). We rule out any difference in perovskite morphology grown on top of 2% F6TCNNQ-doped poly-TPD solution processed thin film (Figure S15, Supporting Information). We further reveal the importance of charge balance by employing 2% F6TCNNQ-doped poly-TPD HTL together with pristine bphen ETL in PeLEDs. The half lifetime

of these devices increases significantly from ≈3 min (when 10% doped bphen is used as ETL, Figure 3c) to beyond 75 min (Figure S16, Supporting Information). These results clearly show that the excess charges (holes in Figure 3c and electrons in Figure 2d) reduce the EQE and the operational lifetime. This could be explained by the fact that the dominant charge carrier can follow a direct path through the device without contributing to radiative recombination. The unbalance of charges in both cases contributes to device degradation and EQE roll-off. The PeLEDs with 10% Alq_3-doped bphen and poly-TPD show better tuned e/h balance over a wide range of current densities, correlated with better stability and reduced EQE roll-off. A higher doping concentration (20% Alq_3) in the bphen ETL further reduces electron mobility (Figure 2a) so that the hole current starts to dominate in the device. This results in reduced EQE and higher EQE roll-off. Nonetheless, the fact that 2D/3D PeLEDs with 10% doped bphen show the highest EQE, reduced EQE roll-off, and significantly enhanced stability compared to their 3D counterparts suggests that the unique flat EQE curve (Figure 2a) also originates partly due to the intrinsic properties of 2D/3D perovskite (as will be elaborated in discussion section below).

2.3. Origin of Flat EQE over a Wide Range of Injection Current Density in 2D/3D PeLEDs

Contrary to many reports where the EQE typically drops by orders of magnitude with increasing current density,[5,6,8,11,22] our optimized 2D/3D PeLEDs show nearly flat EQE over a wide current range. To get more information about the physical processes related to the above-described 2D/3D PeLED functional properties, we performed transient absorption (TA) and thermally stimulated luminescence (TSL) investigations of both types of perovskite films and transient electroluminescence measurements of 2D/3D PeLEDs under device pumping by periodic voltage pulses.

TA spectroscopy reveals remarkable differences in the behavior of the excited states of 2D/3D and 3D perovskites (**Figure 4**). This data gives evidence for exciton confinement in the 2D/3D perovskite film. Figure 4a–d shows excitation intensity dependent TA plots for both perovskite films. Both 3D and 2D/3D samples exhibit bleaching of the ground state (GS) absorption at the absorption band edge at ≈700 and ≈580 nm, respectively. In contrast to 3D film (Figure 4e), the GS absorption recovery in 2D/3D film is much faster and independent of excitation intensity (Figure 4f).

The most prominent phenomenological peculiarity of the 2D/3D perovskite is the presence of a broad bleaching band below the bandgap in the 610–720 nm region. This band appears gradually during 1–2 ps (see bleaching kinetics at 650 nm in Figure 4g), simultaneously with the partial regeneration of the GS absorption of the 2D phase at 580 nm (Figure 4g). We attribute this long wavelength bleaching to the filling by lower-bandgap 3D phase domains in the 2D/3D film that act as traps for carriers and are crucial for the electroluminescent properties of devices. The energy distance between the 2D bandgap and this bleaching band implies trap energies being broadly distributed between several tens and more than 300 meV.

The presence of moderately deep traps for charge carriers in 2D/3D perovskite films have been directly confirmed by means of low-temperature TSL measurements (see **Figure 5**a). TSL measurements indicate explicitly the occurrence of charge carrier trapping and provide insights into charge trap density distribution in semiconducting materials.[32] Noteworthy is

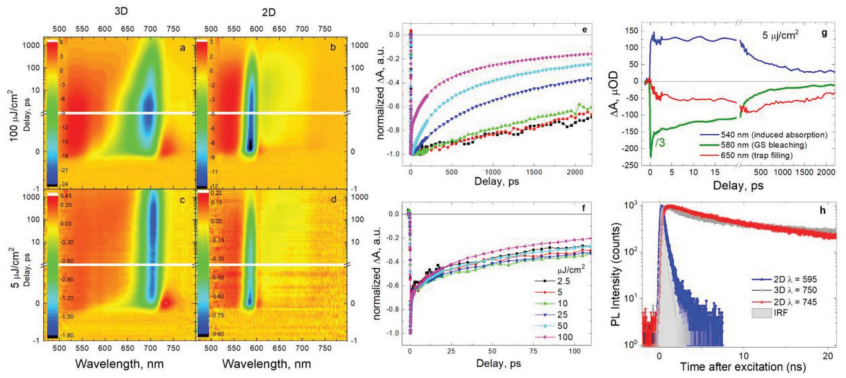

Figure 4. 3D plots of the transient absorption data for 3D perovskite film. a) 100 μJ cm^{-2} (high excitation intensity); c) 5 μJ cm^{-2} (low excitation intensity); 2D/3D perovskite film. b) 100 μJ cm^{-2} and d) 5 μJ cm^{-2}. e) Decay of the ground state bleaching of 3D perovskite film (700 nm band) and f) 2D/3D perovskite film (580 nm) at different excitation intensities. g) Kinetics of the induced absorption (540 nm), ground state bleaching of 2D/3D perovskite (580 nm), and bleaching below the bandgap of the 2D/3D perovskite attributed to the filling of the trap states (650 nm). For clarity, the 580 nm kinetic is divided by the factor of 3. h) Time-resolved photoluminescence decay kinetics (excited at 470 nm) of the 3D and 2D/3D perovskite films.

ADVANCED SCIENCE NEWS
www.advancedsciencenews.com

ADVANCED FUNCTIONAL MATERIALS
www.afm-journal.de

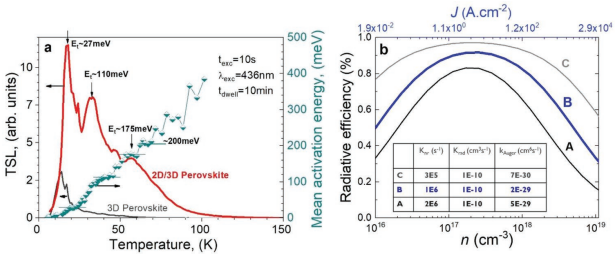

Figure 5. a) TSL measurements of 3D and 2D/3D perovskite films showing trap-density distribution measured at low temperature. The TSL curves were recorded in a linear heating regime after excitation with 436 nm light for 10 s at 4.2 K, and the mean activation energies were estimated by fractional TSL technique. b) Calculated internal quantum efficiency versus charge carrier density. The parameters used for calculation are in the inset of the figure. The current density J for the B (blue line) is shown on the top axis. A typical film thickness of PeLEDs, e.g., d = 60 nm is employed. Typical 300 K value of k_{NR} = 1(±0.5)E6 s^{-1}, k_{rad} = 1E–10 cm^3 s^{-1}, and k_{rad} are adapted from literature.[34] k_{Auger} is estimated k_{Auger} = 2E–29 cm^6 s^{-1} from experiments (k_{Auger} = 2–8E–29 cm^6 s^{-1})[35] and theory (k_{Auger} = 3–30 cm^6 s^{-1}).[36,37]

the different trap concentration and trap distribution profile of the two types of perovskites. 3D perovskite films showed a relatively weak TSL observed only at very low temperatures below ≈70 K (TSL curve maximum at ≈15 K) implying the presence of just shallow trap states. In contrast, the TSL signal for 2D/3D perovskites was significantly stronger, detectable to the temperature as high as ≈130 K (Figure 5a) and featuring additional TSL bands at ≈35, 45, and 60 K. It should be noted that since TSL excitation has been performed at very low temperature, any ion migration leading to photoinduced trap formation ("light-soaking" effect) is suppressed at T_{exc} = 4.2 K, and therefore, plays no role in our TSL measurements. This is also supported by observed invariability of the measured TSL curve shapes upon different light exposure times ranging from 10 s to several tens of minutes. Average trap depths evaluated by the fractional TSL technique are also presented in Figure 5a and show a very broad distribution of trap depths ranging from a few meV to more than 300 meV in 2D/3D perovskite films. This proves univocally that the specific structure of the mixed 2D/3D hybrid perovskite films gives rise to creation of moderately deep charge traps, as opposed to the 3D films. This agrees nicely with results of transient absorption measurements in 2D/3D films (Figure 4a–d) and corroborates the assignment of the broad bleaching band observed below the bandgap to trapping of the charge carriers. We attribute these traps to the minor inclusions of 3D phase domains, which drain photogenerated charges from the 2D phase.[33] Transient absorption investigations suggest that one type of the charge carriers is captured significantly faster than the other. This process is reflected by the partial recovery of the 2D phase absorption during first few picoseconds, when one type of charge carriers is transferred to the 3D phase, causing simultaneous bleaching of the 3D phase absorption (Figure 4g). As charge carriers of another type still reside within the 2D phase, the charges of opposite signs are spatially separated, preventing bimolecular recombination. That explains why the TA dynamics in the 2D/3D film is virtually insensitive to the excitation intensity (Figure 4f), in sharp contrast to the 3D film (Figure 4e).

After several hundreds of picoseconds, bleaching of both 3D and 2D absorptions decay simultaneously when charge carriers of one type are also captured by 3D domains and they recombine. This picture is also validated from the EL and PL spectrum and kinetics, where the emission comes dominantly from the 3D phase. The 2D emission decays very rapidly when one type of charge carriers is trapped by 3D domains (Figure 4h). While slowly decaying 3D fluorescence reflects capture of another charge carrier type and their recombination. Comparison of the PL and TA kinetics also provides clear evidence that 3D domains rapidly trap one type of charge carriers rather than excitons; exciton trapping would cause simultaneous decay of the 2D PL and of its absorption bleaching. When both types of charge carriers are trapped in a 3D domain, they recombine via exciton state. The exciton experiences spatial confinement within the 3D domain volume. Fast trapping of one charge carrier type has a strong influence on the PeLED performance as it disables carrier recombination not only in the 2D phase, but also on nonradiative recombination centers present in the 2D/3D film. Although the presence of nonradiative traps in some 3D domains cannot be excluded, they play only a marginal role because carrier migration between separated 3D domains is strongly restricted and carriers captured by trap-free domains can hardly reach a nonradiative trap. The trap-assisted nonradiative recombination is expected to be particularly important at low PeLED driving current when charge carrier densities are low, consequently carrier lifetimes are long because of slow bimolecular recombination (proportional to $n \cdot p$), and carriers have a high probability to be trapped by nonradiative recombination centers. Consequently, fast trapping of one carrier type by 3D domains in 2D/3D perovskite explains not only higher EQE of 2D/3D PeLEDs, but also their more effective performance at low current densities.

The origin of high EQE can be further explained by solving the rate equation of charge carrier density ($G = k_{NR} \cdot n + k_{rad} \cdot n^2 + k_{Auger} \cdot n^3$, where the generation rate, $G = J/(q \cdot d)$, d is the film thickness, and q is elementary charge) for the reported values of k_{NR}, k_{rad}, and k_{Auger}. Figure 5b suggests that

radiative recombination competes with trap-assisted recombination at low carrier densities ($n \leq 5 \times 10^{16}$ cm^{-3}) and with Auger recombination at high current and carrier densities (e.g., $n \geq 10^{18}$ cm^{-3}). It also highlights two important arguments. First, a high internal quantum efficiency (IQE (EQE)) at low J is only possible when radiative recombination dominates over nonradiative recombination. In our experiments, we achieve this by optimized stoichiometry in mixed-2D/3D perovskite films as we elaborated above. Furthermore, the efficiency roll-off that we moved from <100 to >200 mA cm^{-2} by balancing charge injection is likely still not limited by Auger recombination in our experiments. Indeed, Auger recombination is expected to only kick in at significantly higher current densities of the order of 100 A cm^{-2}. This corroborates experimental findings of Kim et al.[14] who found no signs of Auger recombination for a current density of up to 150 A cm^{-2}.

2.4. Pulsed Driving to Explain PeLEDs Operation

We will now discuss the EL kinetics for 2D/3D PeLEDs under pulsed voltage driving, which enables us to develop a PeLED operation model explaining the importance of charge balancing at high current densities. **Figure 6** shows EL transients for 2D/3D PeLEDs with pristine bphen as ETL induced by periodic 20 kHz electrical pulses of different durations, ranging from 5 to 25 µs. During these measurements, average current was kept identical by adjusting the pulse voltage, which also ensured identical charge transmitted during the voltage pulse. This condition was essential, because the results otherwise varied strongly depending on the pulse duration or voltage. We predict that this condition helps us to keep identical spatial distribution of mobile ions, as we will discuss below. Importantly, as the inset in Figure 6 shows, the intensity of the EL peak linearly increases with the current, indicating no efficiency roll-off for pulse current density up to at least 300 mA cm^{-2}. The EL transients (Figure 6), however, show that the EL intensity drops down on a tens of microsecond time scale.

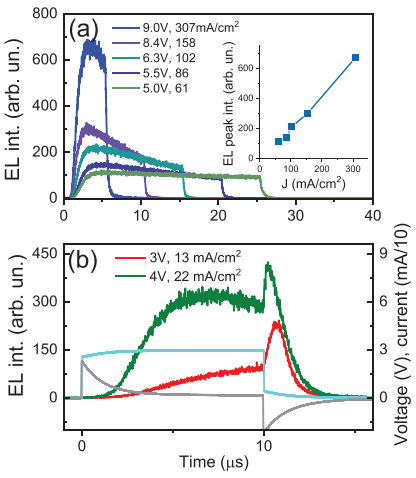

Figure 6. Electroluminescence transients of 2D/3D PeLEDs with pristine bphen as ETL obtained via pulsed driving (20 kHz voltage pulses). a) Pumping pulse duration and voltage were varied by keeping identical average current. Inset in (a) shows dependence of the peak EL intensity on the current density during the pump pulse action. b) Pumping pulses were of fixed 10 µs duration. Cyan and gray lines show voltage and current pulses, respectively. All transients were obtained more than 5 min after driving pulse train was switched on.

Figure 6b shows EL transients obtained when the average current was reduced using lower voltage pulses. The transients show complex EL dynamics. The most unusual feature is a short EL peak after termination of the voltage pulse, known as an overshoot effect first reported for some OLEDs.[38] We explain it by assuming that the electron and hole distributions are spatially separated during the electrical pulse action, and mix upon release of the voltage pulse, thus producing an EL peak.[39] In perovskite devices, also mobile ions can redistribute during application of a voltage at the electrodes. They can explain the difference between EL dynamics at large voltages (Figure 6a) and small voltages (Figure 6b), as we illustrate in the schematic in **Figure 7**.

Shapes of electrical potentials across the perovskite layer are determined by applied voltage, built-in electric field, and distribution of mobile ions. Ions move relatively slowly (minutes time scale), therefore we assume that their distributions remain unchanged during the total period including pulse action and intervals between pulses, determined by the average of electric fields created by electric pulses and built-in field between pulses (short circuit), which are of opposite directions. At low voltage and short durations of electrical pulses, the built-in field dominates, creating an ion distribution profile that screens the built-in field between electrical pulses and creates potential pockets during the voltage pulse action, as shown in Figure 7a. Injected charge carriers, which avoided recombination by passing through the perovskite layer, accumulate in these potential pockets, but mix when the electrical pulse is removed. This causes fast carrier recombination observed as EL overshoot. At high pulse voltages (Figure 7b), the average field has the polarity determined by the applied pulses, and ions redistribute accordingly. They create strong potential drops at the interfaces that cause fast drift of injected carriers and their leakage to the opposite electrode, preventing carrier accumulation and formation of the overshoot pulse upon release of the voltage pulse. Potential pockets in this case may be formed during intervals between voltage pulses, causing accumulation of carriers that neutralize ion charge. This explains the EL dynamics during the voltage pulse action shown in Figure 6a.

The pulsed EL dynamics point at the importance of the spatial charge carrier distributions for the operation of PeLEDs and enable to draw schematic pictures for steady state PeLED performance in different regimes, which are presented in Figure 7c–f. Ion distribution is determined by the average field. In case of steady-state operation, the external field dominates over the built-in field and causes a field screening in the center

ADVANCED SCIENCE NEWS
www.advancedsciencenews.com

ADVANCED FUNCTIONAL MATERIALS
www.afm-journal.de

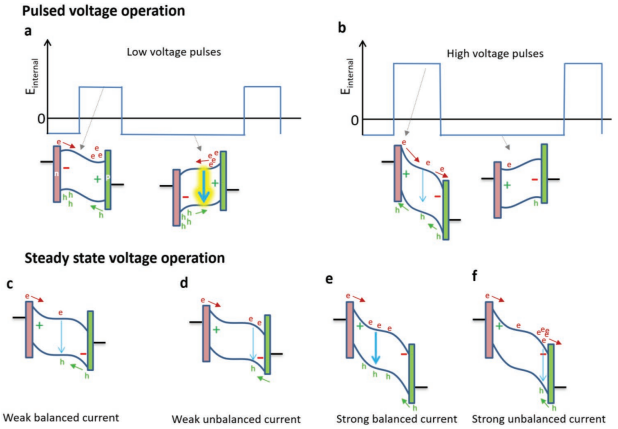

Figure 7. Top panel (a) and (b) show driving of PeLEDs by periodic pulses. At low applied pulse bias, accumulation of positive (+) and negative (–) ions and/or vacancies is determined by the built-in field (negative $E_{internal}$) by screening it during intervals between voltage pulses. The pulse action creates potential pockets at the opposing interfaces, leading to separation and accumulation of electrons and holes. Once the electrical pulse is terminated, electrons and holes move and mix causing fast recombination and an EL overshoot (Figure 6b). High-voltage pulses generate opposite ion distribution and a potential shape that facilitates carrier leakage rather than accumulation and, thus, no overshoot. After a high-voltage pulse, potential pockets for electrons and holes are formed (at built-in electric field) which cause carrier accumulation at zero applied voltage. Bottom panel (c)–(f) show PeLEDs operation at steady-state applied voltage at various current regimes when ions always cause electric field screening. (c) and (d) show PeLED performance at low voltage and weak current when carriers efficiently recombine; (e) and (f) illustrate performance at high voltage and strong current. Unbalanced strong current causes electron accumulation next to positive electrode and leakage.

of the perovskite layer (Figure 7c). Charge carriers efficiently recombine in a flat potential region (Figure 7c,e). In case of unbalanced stronger electron current, the recombination region shifts toward the hole-injecting electrode (Figure 7d). In case of strong and unbalanced current, the recombination region strongly shifts toward positive electrode, and recombination cannot prevent electron accumulation and their leaking to the positively biased electrode, which reduces the PeLED performance efficiency.

Although this model is significantly simplified and some of its aspects remain hypothetical, it qualitatively explains basic properties of PeLED performance at pulsed and steady driving voltages as they are observed. Together with the peculiarities of carrier dynamics in 2D/3D perovskites revealed by transient absorption it helps to understand main EL loss channels and gives explanation for the unprecedented wide range of the optimized 2D/3D PeLED performance.

3. Conclusions

We have demonstrated improvements in external quantum efficiency, EQE roll-off, and lifetime of perovskite light emitting diodes by tuning the electron and hole transport into the perovskite emissive layer as well as the stoichiometry of perovskite film. We compare 3D perovskite, $MAPb(I/Br)_3$, and a mixed 2D/3D perovskite structure formed by incorporation of large cations.

To explain the high EQE at low current densities (J) in our optimized 2D/3D PeLEDs, we show, by transient absorption and photoluminescence spectroscopy, exciton confinement and beneficial charge trapping in 3D domains of 2D/3D perovskite films, which reduces carrier loss to nonradiative recombination.

To maintain high EQE at high J, it appears that it is important to balance electron and hole injection. The nature of the perovskite film is also of large importance, as we note significant roll-off in 3D PeLEDs even with balanced charges. In the optimized 2D/3D PeLEDs, charge balancing improves EQE and EQE roll-off, appearing only at $J = 250$ mA cm^{-2} (for 50% EQE drop).

To explain this result, we analyze electroluminescence transients. They point at importance of the spatial charge carrier distribution in the perovskite emissive layer. When balanced charge carrier transport/injection is provided, excess carriers leakage through the device can be avoided up to high current densities.

Finally, we also note that excess carrier concentration, both electron and holes, heavily degrade device lifetime. In PeLEDs employing optimized 2D/3D stoichiometry, the half lifetime reaches a remarkable of ≈47 h at $J = 10$ mA cm^{-2} for optimized charge balance.

Our optimized PeLEDs with optimum charge injection balance into the emissive layer as well as optimized stoichiometry of perovskite film have an EQE of ≈16.7 ± 1% at $J = 0.4$ mA cm^{-2}, significantly reduced EQE roll-off (EQE 12.2% at 100 mA cm^{-2}), and a remarkable half lifetime ≈12 h at $J = 100$ mA cm^{-2} (T_{85} of 14.2 h at 10 mA cm^{-2}).

4. Experimental Section

Materials: Lead iodide (TCI), methyl ammonium iodide, methylammonium bromide and iso-Butylammonium iodide (Greatcell), 4,7-Diphenyl-1,10-phenanthroline (Lumtec Taiwan), Tris-(8-hydroxyquinoline)aluminum (Alq$_3$, Sigma-Aldrich), and poly-TPD (1-Materials) were used without any further purification. All the solvents were purchased from Sigma-Aldrich.

Device Fabrication: The devices were made on pixelated prepatterned ITO substrates. The substrates were cleaned with Extran soap water, distilled water, acetone, and IPA via sonication (10 min each). Subsequently, the substrates were exposed to oxygen plasma (200 W) for 7 min. Poly[*N*,*N*′-bis(4-butylphenyl)-*N*,*N*′-bis(phenyl)-benzidine] also called poly-TPD (6 mg mL^{-1} in chlorobenzene) was spin coated on ITO substrates (1000 rpm for 30 s: acc. 5000 rpm) and annealed at 150 °C for 20 min to form HTL. The poly-TPD films were exposed to O_2 plasma (1–2 s) to improve wetting properties. The perovskite film was deposited in a single step. At first, a warm solution (kept at 50 °C) containing 0.3 M PbI_2 and different molar ratios of BAI (Table S1, Supporting Information) dissolved in a mixture of DMF and DMSO (1 mL DMF, 21.6 [L DMSO) was spin coated (3000 rpm for 30 s; acc. 3000 rpm). Next to it, a solution containing different molar ratios of MAI and MABr (Table S2, Supporting Information) was dropped on the spinning substrates (2000 rpm for 30 s; acc. 3000 rpm). Perovskite film formation was completed by annealing it at 80 °C for 20 min. A 40 nm thick ETL (bphen and 2%, 5%, 10%, and 20% Alq$_3$-doped bphen) was deposited via evaporation (pressure < 4E−7 mbar). For doped bphen ETL, at first, 20 nm of pristine bphen was deposited followed by another 20 nm of bphen:Alq$_3$. The doping ratio was controlled via coevaporation rates of the two small molecules. LiQ (2 nm) was evaporated to form an electron injection layer. Ag (100 nm) was used as metal back contact that defined the active area of the devices (0.0204 cm^2).

Fabrication of Single Carrier Devices: Electron-only devices employed an architecture ZnO/PEIE/perovskite/bphen(0%,10%)/LiQ/Ag. ZnO was spin coated from a solution of zinc acetate dehydrate in ethanol (3000 rpm for 30 s) followed by annealing at 250 °C for 10 min. PEIE dilution in 2-methoxyethanal (0.2 wt%) was spin-coated at 2000 rpm and annealed at 100 °C for 10 min. Both ZnO and PEIE were processed in air. Prior to spin coating perovskite, PEIE film were spin coated with DMF to wash away excess PEIE. For hole-only device, poly-TPD or 2% F6TCNNQ-doped poly-TPD were used as HTL. MoO_x was deposited via evaporation at <4E−7 mbar and Au (80 nm) was used as a metal contact. For HOD employing poly-TPD on both sides, the deposition of poly-TPD on top of the perovskite layer followed same spinning parameter as before, however, the annealing temperature was reduced to 80 °C (10 min) in order to avoid degradation of perovskite layer at higher temperature.

Morphological, Structural, and Optical Characterizations: Morphology of the films was characterized via atomic force microscopy (Bruker) and SEM (FEI Nova 200). Crystallinity of the perovskite films was investigated via X-ray diffractometer (Panalytical X'Pert Pro).

Photoluminescence: Photoluminescence was recorded with Edinburgh-F900 (Edinburgh Instruments) fluorometer. Time-correlated single photon counting (TCSPC) was the time-resolved technique used to obtain kinetic traces of the photoluminescence decay. 100 or 10 ns time window was used with 4096 bin channels. A picosecond-pulsed diode laser EPL-470 (Edinburgh Instruments) emitting ≈100 ps pulses (2 MHz repetition frequency) at 470 nm wavelength was used as an excitation source. The data of time-resolved fluorescence experiments were processed and analyzed using F900 software (Edinburgh Instruments).

Transient Absorption Spectroscopy of Perovskite Films: The transient absorption setup was based on the amplified femtosecond laser Pharos 10-600-PP laser (Light Conversion Ltd.), operating at fundamental wavelength of 1032 nm, repetition rate of 200 kHz, and pulse width of <250 fs. The measurements were performed at repetition rate of 200/42 = 4.762 kHz frequency achieved by using the pulse picker. The collinear optical parametric amplifier Orpheus PO15F2L (Light Conversion Ltd.) was used to obtain 515 nm wavelength pulses for sample excitation. Excitation was modulated at 4.762/6 = 0.794 kHz frequency by mechanical chopper synchronized to the output of the pulse picker. As a probe, pulses were used, spectrally broadened by means of continuum generation in the sapphire crystal. The detection equipment consisted of Andor-Shamrock SR-500i-B1-R spectrometer (Andor Technology, 150 lines mm^{-1} diffraction grating) equipped with Andor-Newton (Andor Technology) DU970 CCD camera (1600 × 200 pixels). The reading of the camera was synchronized with the chopper.

Thermally Stimulated Luminescence of Perovskite Films: TSL is the phenomenon of luminescent emission after removal of excitation under conditions of increasing temperature. Generally, in the TSL method, the trapping states are first populated by photogeneration of charge carriers, usually at low temperatures (in this case $T_{exc} = 4.2$ K) in order to prevent a fast escape. The trapped charge carriers after certain dwell time (t_{dwell}) after terminating the excitation are released by heating up the sample with a linear temperature ramp, and the luminescence due to radiative recombination is recorded as a function of temperature. In the present study, TSL measurements were carried out over a temperature range from 4.2 to 330 K using an optical temperature-regulating helium cryostat. Perovskite samples were cooled down to 4.2 K and irradiated with $\lambda_{exc} = 436$ nm light (cw-excitation) selected by appropriate sets of cut-off filter from a high-pressure mercury lamp. In these experiments, rather short excitation time = 10 s was used, in order to prevent any possible photoinduced changes in perovskite crystal structure. Measurements were done as follows: First, after terminating the photoexcitation, the samples were kept in dark at a constant temperature $T = 4.2$ K during a certain dwell time (t_{dwell} = 10 min in these experiments) in order to allow all isothermal emission processes, like exciton emission and isothermal charge recombination, to decay to negligible level. Note that immediately after photoexcitation at 4.2 K, an intensive emission was observed from the perovskite films—called in literature as "long isothermal afterglow." The afterglow decay kinetics (typically hyperbolic decay kinetics) were measured at very long delay times from 1 to 10^3 s after switching off the excitation (integration time 1 s) with the same equipment as was used for TSL measurements, but under the condition of constant temperature (not presented here). Second, after the afterglow signal drops to sufficiently low level, TSL measurements were started upon heating the sample, i.e., emission from perovskite samples was measured which was stimulated by linearly increasing temperature from 5 to 300 K. All measurements were done in the dark—no light excitation during TSL heating run. TSL arises due to recombination of thermally liberated charge carriers which were trapped on some sort of trapping states at low temperature and one normally measures TSL emission intensity versus temperature. Note that with TSL method, traps were detected only for one sort of charge carriers—for the most mobile charge carrier which were expected to be trapped on shallower states. As soon as the shallower trapped carrier was thermally released, they recombined with deeper trapped carriers of the opposite sign, and therefore the latter could no longer be detected at higher temperatures. The measured TSL curve was a rather exact replica of the in-gap trap states for one sort of charge carriers—TSL intensity was proportional to the density of occupied trap states and that trap depth could be measured using so-called fractional-TSL measurements.

The fractional heating TSL technique (also called the fractional glow technique), originally proposed by Gobrecht and Hofmann[40] is an extension of the initial rise method and is based on cycling the sample

with a large number of small temperature oscillations superimposed on a uniform heating ramp. The main reason for applying this method was that the usual quantitative evaluation of the TSL glow curves is very inaccurate, or even impossible, if the traps are continuously distributed in energy or if there are several types of traps with discrete but very close lying activation energies. In this case, the glow peaks fuse together, and individual glow maxima may not be discernable. The mean activation energy $\langle E \rangle$ was determined during each temperature cycle with a temperature change, ΔT, as[41]

$$\langle E \rangle(T) = -\frac{d\left[\ln I(T)\right]}{d\left(1/kT\right)}; \text{at } \_\beta = \text{const}, \ \_\Delta T \ll T, \ \_n \ll n_{\text{tot}} \tag{1}$$

where $I(T)$ is the intensity of the TSL, T is the temperature, and k is the Boltzmann constant. Here, n is the number of charge carriers released during each temperature cycle and n_{tot} s the total number of carriers trapped by the same sort of traps. These conditions determine the so-called "initial rise method" which is actually the basis for Equation (1). Since a temperature oscillation, ΔT, is usually much less than mean value of T, the E could be assumed as equal to $E(T)$, the activation energy of traps emptied at the temperature T. A trap distribution function, $H(E)$, can be determined in arbitrary units as[41]

$$H(E) \propto \frac{I(E)}{d\langle E \rangle / dT} \tag{2}$$

where $I(E)$ is TSL after converting the temperature scale to the energy scale by means of empirically accessible $\langle E \rangle(T)$ dependence obtained by Equation (1). As one can see from Equation (2), in the case when $\langle E \rangle(T)$ is a linear function, the TSL intensity dependence $I(T)$ is an exact replica of trap density-of-states distribution function.[32]

Measurement of External Quantum Efficiency, Efficiency Roll-Off, and Device Lifetime: The EQE of the PeLEDs was measured in glovebox (see the Supporting Information for EQE calculation details) and an integrating sphere. The photocurrent (I_{photon}) was measured by a Newport 818-SL-L Silicon photodetector and the spectral data was acquired via a Flame Spectrometer by Ocean Optics. Current–voltage (J–V) measurements were performed by an Agilent 4155C Semiconductor Parameter Analyzer. All the device measurements were carried out at room temperature and unencapsulated. As a time-evolution of EQE was noted, only stabilized value was reported here. This was particularly important while reporting EQE roll-off. For each applied current, only the stabilized value was reported for comparison. The lifetime measurements were measured at a fixed injection current and the data were recorded periodically every 20–30 s.

Pulsed Driving of PeLEDs and Electroluminescence Transient Measurements: EL transients were recorded by using time-correlated single photon counting Edinburg Instruments spectrometer combined with pulsed voltage generator. Electrical pulses, instead of optical excitation, were used to excite luminescence. This technique enabled high sensitivity together with sub-nanosecond time-resolution.

Optical Simulation of PeLEDs: The optical constants of the materials in the PeLEDs were derived from multiple angle ellipsometry measurements using an RC2 Ellipsometer (J.A. Woollam Co.). Resulting optical material properties were used in transfer matrix modeling of the thin film optics of the stack.

Supporting Information

Supporting Information is available from the Wiley Online Library or from the author.

Acknowledgements

A.F. and W.Q. contributed equally to this work. The authors acknowledge funding from the European Research Council under the European Horizon 2020 Programme/ERC grant agreement no 835133 (ULTRA-LUX). W.Q. would like to thank the financial support of the postdoctoral fellowship grant (12Z4618N) from FWO. This research was also supported by the VW Foundation, by bilateral Lithuanian-Ukrainian cooperation project no. M/72-2018, and by the National Academy of Science of Ukraine (Project No. VC/202). A.F. carried out the device fabrication and characterization and wrote the first draft of the manuscript. W.Q. started the project, optimized perovskite recipe, and developed the idea of ETL doping. G.C. assisted in device fabrication and optimization. A.D., R.G., and V.G. performed ultrafast spectroscopy and pulsed EL measurements. R.G. carried out electromagnetic simulation and ellipsometry measurements. A.V. and A.K. carried out TSL measurements. C.R., J.G., and P.H. involved in discussion on data analysis. All the authors participated in manuscript revisions and proof reading. P.H. led the project.

Conflict of Interest

The authors declare no conflict of interest.

Keywords

charge injection, EQE roll-off, LEDs lifetime, perovskite light emission, perovskite optoelectronics

Received: May 22, 2019
Revised: June 30, 2019
Published online:

[1] a) B. R. Sutherland, E. H. Sargent, *Nat. Photonics* **2016**, *10*, 295; b) F. P. García de Arquer, A. Armin, P. Meredith, E. H. Sargent, *Nat. Rev. Mater.* **2017**, *2*, 16100; c) A. Fakharuddin, U. Shabbir, W. Qiu, T. Iqbal, M. Sultan, P. Heremans, L. Schmidt-Mende, *Adv. Mater.* **2019**, *338*, 1807095.

[2] M. Ban, Y. Zou, J. P. H. Rivett, Y. Yang, T. H. Thomas, Y. Tan, T. Song, X. Gao, D. Credington, F. Deschler, S. Henning, S. Baoquan, *Nat. Commun.* **2018**, *9*, 3892.

[3] Y. Cao, N. Wang, H. Tian, J. Guo, Y. Wei, H. Chen, Y. Miao, W. Zou, K. Pan, Y. He, H. Cao, Y. Ke, M. Xu, Y. Wang, M. Yang, K. Du, Z. Fu, D. Kong, D. Dai, Y. Jin, G. Li, H. Li, Q. Peng, J. Wang, W. Huang, *Nature* **2018**, *562*, 249.

[4] a) H. Cho, S.-H. Jeong, M.-H. Park, Y.-H. Kim, C. Wolf, C.-L. Lee, J. H. Heo, A. Sadhanala, N. Myoung, S. Yoo, S. H. Im, R. H. Friend, T.-W. Lee, *Science* **2015**, *350*, 1222; b) Z. Xiao, R. A. Kerner, L. Zhao, N. L. Tran, K. M. Lee, T.-W. Koh, G. D. Scholes, B. P. Rand, *Nat. Photonics* **2017**, *11*, 108.

[5] F. Yan, J. Xing, G. Xing, L. Quan, S. T. Tan, J. Zhao, R. Su, L. Zhang, S. Chen, Y. Zhao, A. Huan, E. H. Sargent, Q. Xiong, H. V. Demir, *Nano Lett.* **2018**, *18*, 3157.

[6] X. Yang, X. Zhang, J. Deng, Z. Chu, Q. Jiang, J. Meng, P. Wang, L. Zhang, Z. Yin, J. You, *Nat. Commun.* **2018**, *9*, 570.

[7] X. Y. Chin, A. Perumal, A. Bruno, N. Yantara, S. A. Veldhuis, L. Martinez-Sarti, B. Chandran, V. Chirvony, A. S.-Z. Lo, J. So, C. Soci, M. Gratzel, H. J. Bolink, N. Mathews, S. G. Mhaisalkar, *Energy Environ. Sci.* **2018**, *11*, 1770.

[8] B. Zhao, S. Bai, V. Kim, R. Lamboll, R. Shivanna, F. Auras, J. M. Richter, L. Yang, L. Dai, M. Alsari, X.-J. She, L. Liang, J. Zhang, S. Lilliu, P. Gao, H. J. Snaith, J. Wang, N. C. Greenham, R. H. Friend, D. Di, *Nat. Photonics* **2018**, *12*, 783.

[9] T. Chiba, Y. Hayashi, H. Ebe, K. Hoshi, J. Sato, S. Sato, Y.-J. Pu, S. Ohisa, J. Kido, *Nat. Photonics* **2018**, *12*, 681.

[10] C. Murawski, K. Leo, M. C. Gather, *Adv. Mater.* **2013**, *25*, 6801.
[11] a) Y. Shang, G. Li, W. Liu, Z. Ning, *Adv. Funct. Mater.* **2018**, *28*, 1801193; b) M. Lu, X. Zhang, X. Bai, H. Wu, X. Shen, Y. Zhang, W. Zhang, W. Zheng, H. Song, W. W. Yu, A. L. Rogach, *ACS Energy Lett.* **2018**, *3*, 1571.
[12] M. Yang, N. Wang, S. Zhang, W. Zou, Y. He, Y. Wei, M. Xu, J. Wang, W. Huang, *J. Phys. Chem. Lett.* **2018**, *9*, 2038.
[13] W. Zou, R. Li, S. Zhang, Y. Liu, N. Wang, Y. Cao, Y. Miao, M. Xu, Q. Guo, D. Di, L. Zhang, C. Yi, F. Gao, R. H. Friend, J. Wang, W. Huang, *Nat. Commun.* **2018**, *9*, 608.
[14] K. Kim, L. Zhao, J. S. Price, A. J. Grede, K. Roh, A. N. Brigeman, M. Lopez, B. P. Rand, N. C. Giebink, *Nat. Commun.* **2018**, *9*, 4893.
[15] P. Tyagi, L. I. Giri, S. Tuli, R. Srivastava, *J. Appl. Phys.* **2014**, *115*, 034518.
[16] X. Dai, Z. Zhang, Y. Jin, Y. Niu, H. Cao, X. Liang, L. Chen, J. Wang, X. Peng, *Nature* **2014**, *515*, 96.
[17] M.-H. Kim, M. F. Schubert, Q. Dai, J. K. Kim, E. F. Schubert, J. Piprek, Y. Park, *Appl. Phys. Lett.* **2007**, *91*, 183507.
[18] M. K. Gangishetty, S. Hou, Q. Quan, D. N. Congreve, *Adv. Mater.* **2018**, *30*, 1706226.
[19] R. Yang, R. Li, Y. Cao, Y. Wei, Y. Miao, W. L. Tan, X. Jiao, H. Chen, L. Zhang, Q. Chen, H. Zhang, W. Zou, Y. Wang, M. Yang, C. Yi, N. Wang, F. Gao, C. R. McNeill, T. Qin, J. Wang, W. Huang, *Adv. Mater.* **2018**, *30*, 1804771.
[20] S. R. Forrest, D. D. C. Bradley, M. E. Thompson, *Adv. Mater.* **2003**, *15*, 1043.
[21] a) C. Wu, T. Wu, Y. Yang, J. A. McLeod, Y. Wang, Y. Zou, T. Zhai, J. Li, M. Ban, T. Song, X. Gao, S. Duhm, H. Sirringhaus, B. Sun, *ACS Nano* **2019**, *12*, 1645; b) W. Xu, Q. Hu, S. Bai, C. Bao, Y. Miao, Z. Yuan, T. Borzda, A. J. Barker, E. Tyukalova, Z. Hu, M. Kawecki, H. Wang, Z. Yan, X. Liu, X. Shi, K. Uvdal, M. Fahlman, W. Zhang, M. Duchamp, J.-M. Liu, A. Petrozza, J. Wang, L.-M. Liu, W. Huang, F. Gao, *Nat. Photonics* **2019**, *13*, 418.
[22] H. Cho, Y.-H. Kim, C. Wolf, H.-D. Lee, T.-W. Lee, *Adv. Mater.* **2018**, *30*, 1704587.
[23] a) C. Adachi, M. A. Baldo, M. E. Thompson, S. R. Forrest, *J. Appl. Phys.* **2001**, *90*, 5048; b) J. Lim, Y.-S. Park, K. Wu, H. J. Yun, V. I. Klimov, *Nano Lett.* **2018**, *18*, 6645.
[24] a) M. De Bastiani, G. Dell'Erba, M. Gandini, V. D'Innocenzo, S. Neutzner, A. R. S. Kandada, G. Grancini, M. Binda, M. Prato, J. M. Ball, M. Caironi, A. Petrozza, *Adv. Energy Mater.* **2016**, *6*, 1501453. b) D. W. deQuilettes, W. Zhang, V. M. Burlakov, D. J. Graham, T. Leijtens, A. Osherov, V. Bulović, H. J. Snaith, D. S. Ginger, S. D. Stranks, *Nat. Commun.* **2016**, *7*, 11683; c) K. K. Wong, A. Fakharuddin, P. Ehrenreich, T. Deckert, M. Abdi-Jalebi, R. H. Friend, L. Schmidt-Mende, *J. Phys. Chem. C* **2018**, *122*, 10691.
[25] B. Liu, L. Wang, H. Gu, H. Sun, H. V. Demir, *Adv. Opt. Mater.* **2018**, *6*, 1800220.
[26] I. I. Fishchuk, A. K. Kadashchuk, A. Vakhnin, Y. Korosko, H. Bässler, B. Souharce, U. Scherf, *Phys. Rev. B* **2006**, *73*, 115210.
[27] H. Shen, W. Cao, N. T. Shewmon, C. Yang, L. S. Li, J. Xue, *Nano Lett.* **2015**, *15*, 1211.
[28] M. Redecker, D. D. C. Bradley, M. Inbasekaran, W. W. Wu, E. P. Woo, *Adv. Mater.* **1999**, *11*, 241.
[29] M. W. Thesen, B. Höfer, M. Debeaux, S. Janietz, A. Wedel, A. Köhler, H.-H. Johannes, H. Krueger, *J. Polym. Sci., Part A: Polym. Chem.* **2010**, *48*, 3417.
[30] S. Olthof, K. Meerholz, *Sci. Rep.* **2017**, *7*, 40267.
[31] B. Lüssem, M. L. Tietze, H. Kleemann, C. Hoßbach, J. W. Bartha, A. Zakhidov, K. Leo, *Nat. Commun.* **2013**, *4*, 2775.
[32] A. Kadashchuk, Y. Skryshevskii, A. Vakhnin, N. Ostapenko, V. I. Arkhipov, E. V. Emelianova, H. Bässler, *Phys. Rev. B* **2001**, *63*, 115205.
[33] M. Yuan, L. N. Quan, R. Comin, G. Walters, R. Sabatini, O. Voznyy, S. Hoogland, Y. Zhao, E. M. Beauregard, P. Kanjanaboos, Z. Lu, D. H. Kim, E. H. Sargent, *Nat. Nanotechnol.* **2016**, *11*, 872.
[34] M. B. Johnston, L. M. Herz, *Acc. Chem. Res.* **2016**, *49*, 146.
[35] a) R. L. Milot, G. E. Eperon, H. J. Snaith, M. B. Johnston, L. M. Herz, *Adv. Funct. Mater.* **2015**, *25*, 6218; b) L. M. Herz, *Annu. Rev. Phys. Chem.* **2016**, *67*, 65; c) F. Staub, H. Hempel, J.-C. Hebig, J. Mock, U. W. Paetzold, U. Rau, T. Unold, T. Kirchartz, *Phys. Rev. Appl.* **2016**, *6*, 044017.
[36] A. Haug, D. Kerkhoff, W. Lochmann, *Phys. Status Solidi B* **1978**, *89*, 357.
[37] J. Even, L. Pedesseau, C. Katan, M. Kepenekian, J.-S. Lauret, D. Sapori, E. Deleporte, *J. Phys. Chem. C* **2015**, *119*, 10161.
[38] V. R. Nikitenko, V. I. Arkhipov, Y.-H. Tak, J. Pommerehne, H. Bässler, H.-H. Hörhold, *J. Appl. Phys.* **1997**, *81*, 7514.
[39] R. Gegevičius, M. Franckevičius, J. Chmeliov, W. Tress, V. Gulbinas, *J. Phys. Chem. Lett.* **2019**, *10*, 1779.
[40] H. Gobrecht, D. Hofmann, *J. Phys. Chem. Solids* **1966**, *27*, 509.
[41] I. A. Tale, *Phys. Status Solidi A* **1981**, *66*, 65.

RESEARCH ARTICLE

ADVANCED OPTICAL MATERIALS
www.advopticalmat.de

Ion Motion Determines Multiphase Performance Dynamics of Perovskite LEDs

Jevgenij Chmeliov, Karim Elkhouly, Rokas Gegevičius, Lukas Jonušis, Andrius Devižis, Andrius Gelžinis, Marius Franckevičius, Iakov Goldberg, Johan Hofkens, Paul Heremans, Weiming Qiu, and Vidmantas Gulbinas**

Perovskite light-emitting diodes (PeLEDs) currently reach up to about 20% external quantum efficiency (EQE) and are becoming a promising technology for display and lighting applications. Still, many issues regarding their performance remain unresolved, particularly those related to stability, operation in non-stationary regimes, and efficiency roll-off at high current densities. Here, some of those issues in PeLEDs based on $MAPbI_3$ perovskite are addressed. The authors analyze the electroluminescence (EL) and current dynamics after the first-time voltage application and after application of sequences of voltage pulses, at different temperatures. Analysis of the results suggests that the complex dynamics observed on time scales from sub-seconds to minutes and hours can be explained by the spatial redistribution of mobile species, most likely iodine interstitials, characterized by ≈175 meV activation energy. This redistribution alters the carrier injection, spatial electric field, and charge carrier density distributions as well as density of nonradiative recombination centers within the perovskite layer. Mathematical modeling of the ion motion and related processes enabled to reproduce the EL and current dynamics and to disentangle complex sequence of processes governing the PeLED operation.

1. Introduction

Perovskite light-emitting diodes (PeLEDs) are a promising technology for development of wavelength-tunable, large-area, solution-processed, flexible light sources.[1–6] These devices have already demonstrated external quantum efficiencies (EQE) exceeding 20%.[4–6] However, many problems still remain unsolved, limiting the widespread usage of PeLEDs. One of them, inherent to all perovskite devices, is the short-term and long-term stability. PeLEDs also suffer from efficiency roll-off limiting their brightness.[7–10] Another issue, particularly important for the high-speed device operation, is the occurrence of hysteresis[1,11] and variations of the electroluminescence (EL) EQE and photoluminescence (PL) efficiency[3,12] under electrical stress.

The performance hysteresis in perovskite solar cells was widely investigated and was attributed to the changes of perovskite-transport layer interfaces or to the motion of mobile ions.[13–16] Ion motion in metal-halide perovskites is a very complex and still poorly understood phenomenon. Generally, all constituents of metal halide perovskites—halides, lead, and organic cations—may form vacancies, interstitials, and anti-sites, which may be mobile and act as carrier traps.[16–18] On the other hand, theoretical evaluations show that only few of them form deep traps acting as non-radiative recombination centers,[17] while shallow traps have a negligible effect on a trap-assisted recombination.[19]

In lifetime measurements of PeLEDs, it is constantly observed that different PeLED stacks improve over a timeframe of minutes to hours, then they start to degrade.[3,20–22] Persistent enhancement of the EQE of PeLED, under applied positive voltage (so-called stressing regime), has been explained by the motion of the mobile excess iodide ions that fill vacancies and reduce

J. Chmeliov, R. Gegevičius, L. Jonušis, A. Devižis, A. Gelžinis, M. Franckevičius, V. Gulbinas
Department of Molecular Compound Physics
Center for Physical Sciences and Technology
Saulėtekio Avenue 3, Vilnius LT-10257, Lithuania
E-mail: vidmantas.gulbinas@ftmc.lt
J. Chmeliov, A. Gelžinis, V. Gulbinas
Institute of Chemical Physics
Faculty of Physics
Vilnius University
Saulėtekio Avenue 9, Vilnius LT-10222, Lithuania
The ORCID identification number(s) for the author(s) of this article can be found under https://doi.org/10.1002/adom.202101560.
K. Elkhouly, I. Goldberg, P. Heremans, W. Qiu
Imec
Kapeldreef 75, Leuven 3001, Belgium
E-mail: Weiming.Qiu@imec.be
K. Elkhouly, I. Goldberg, P. Heremans
Department of Electrical Engineering
KU Leuven
Kasteelpark Arenberg
Leuven 3001, Belgium
J. Hofkens, W. Qiu
Department of Chemistry
KU Leuven
Celestijnenlaan 200F, Leuven 3001, Belgium

DOI: 10.1002/adom.202101560

ADVANCED SCIENCE NEWS
www.advancedsciencenews.com

ADVANCED OPTICAL MATERIALS
www.advopticalmat.de

concentration of iodine interstitials, acting as deep carrier traps.[3,22] Similar gradual performance enhancement under positive bias voltage was also reported for perovskite solar cells and was likewise attributed to the motion and recombination of ions and vacancies.[23] On the other hand, Wang et al. observed reversible changes of the EQE of PeLED and also ascribed them to the motion of iodine ions.[2] Recently, Cheng et al. reported that diffusion of organic cations from the perovskite to the electron-transporting layer is responsible for the EQE roll-off.[24] Leijtens. et al. attributed reversible changes, observed on a time scale of several minutes, to the motion of methylammonium cations (MA^+).[25,26] The PeLED operation was also reported to show a fast dynamics occurring on time scales of milliseconds to seconds.[22,27] In case of PeLEDs pumped by short electrical pulses, time-averaged pumping history was shown to change the device performance.[28]

Consequently, PeLEDs show complex performance dynamics on a wide timescale range, which was typically attributed to the ion motion. However, the reported time scales, intensities of the observed changes, and their attribution to some particular kinds of ions are very different. And still poorly understood. Overall, the underlying physical mechanisms of the ion motion-induced variations in device performance still remain far from clear.

Herein, we report a detailed study of the ion motion that causes both persistent and reversible changes of the PeLED performance, taking place on time scales ranging from milliseconds to hours. Temperature dependencies revealed identical activation energies for all these processes occurring on different time scales. We suggest a mechanism explaining the majority of the observed changes by motion of a single type of charged defects and their recombination with "counter" defects acting as recombination centers. The validity of our model is supported by numerical simulations.

2. Experimental Results and Discussion

2.1. EL and Current Dynamics

We first investigated the EL and current dynamics of a PeLED based on $MAPbI_3$ perovskite under abrupt application of the pump voltage. The device structure and the corresponding energy level diagram are presented in **Figure 1**. Description of the PeLED fabrication procedures can be found in the experimental section, while Figure S2, Supporting Information, gives IV characteristics and voltage dependence of EL EQE of the device stabilized after 30 min operation.

We have shown in our previous work that the use of PCBM/ZnMgO electron injection layer significantly improves the device stability.[29] The PeLEDs have little variation in device performance and lifetimes. The transient dynamics are highly reproducible across multiple devices, which ensures the reliable and reproducible measurements in this study.

After abrupt first-time application of a constant voltage to the PeLED, just for several minutes, we observe a significant growth of the EL intensity and electric current. **Figure 2**a presents normalized EL intensity and current growth kinetics at different device temperatures after application of 2 V voltage. Since the first-time voltage application can be studied only once, curves at different temperatures were measured for different devices formed on the same substrate.

Immediately after the voltage was applied, the EL intensity was very weak, but it increased and reached a plateau after several minutes at room temperature and after more than 1 h at 200 K. Similar behavior of PeLEDs has been reported before[3] and was denoted as stressing. The electrical current was non-vanishing from the very beginning and then increased 3–5 times, but the growth rate was significantly faster than that of EL. Figure 2b shows the current and EL kinetics at 297 K on a logarithmic time scale, more clearly demonstrating the initial growth dynamics. The initial current was almost constant during tens of milliseconds and created almost no EL during this time. It should be noted that the delayed growth of the EL cannot be explained by the charging of the sample capacitance since this process, according to the device RC characteristics, should take place on a timescale of several microseconds, that is, about 10^4 times faster. Therefore, the initial absence of EL suggests that either a) the initial current is created by injection of only one type of charge carriers, which then leak to the opposite electrode creating no EL, or b) EL is absent because of fast nonradiative recombination. The EL starts to grow after

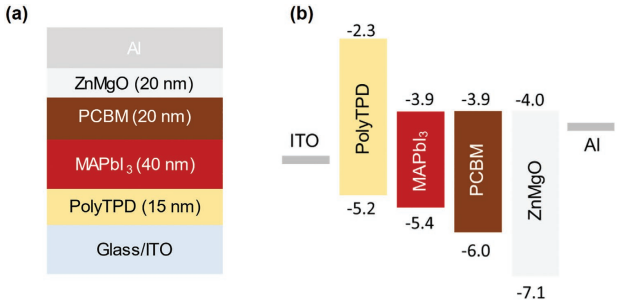

Figure 1. a) The PeLED structure and b) corresponding energy level diagram. Numbers in (b) represent conductance and valence band boundary energies in eV.

ADVANCED SCIENCE NEWS
www.advancedsciencenews.com

ADVANCED OPTICAL MATERIALS
www.advopticalmat.de

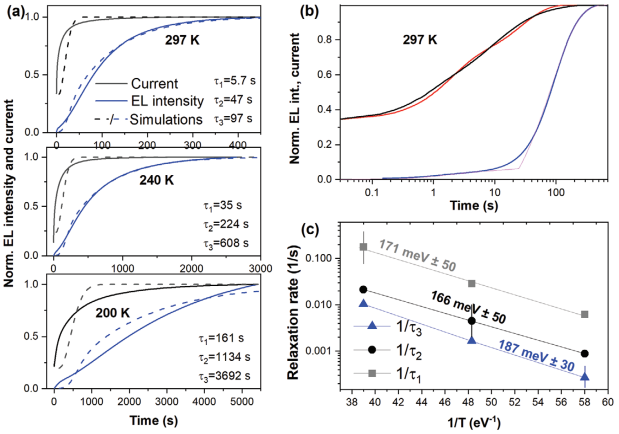

Figure 2. EL and current dynamics at different temperatures in pristine PeLEDs under first-time application of 2 V voltage. a) Normalised EL (blue lines) and current (black lines) growth kinetics, measured (solid lines) and simulated (dashed lines, see below for discussion) at three different temperatures (kinetics at different temperatures are measured for different samples, formed on the same substrate). b) Current and EL kinetics at room temperature on a logarithmic time scale (black and blue lines, respectively), red and magenta lines show approximations by Equations (1) and (2) respectively. c) Arrhenius plot for the slow EL growth time constant τ_3 (blue), fast current growth time constant τ_1 (grey line), and slow current growth time constant τ_2 (black).

about 100 ms, and up to about 10 s, it grows simultaneously with current. Nevertheless, the EL intensity remains low during the initial ≈10 s. Faster growth starts only when current almost stabilizes, which suggests that the later growth process is not related to the carrier injection.

The current growth kinetics can be reasonably well (see red line in Figure 2b) fitted with the bi-exponential rise functions as:

$$I(t) = I_0 + a_1\left[1-\exp\left(-t/\tau_1\right)\right] + a_2\left[1-\exp\left(-t/\tau_2\right)\right] \quad (1)$$

resulting in time constants of $\tau_1 = 1.7$ and $\tau_2 = 25$ s at room temperature (RT). We have also successfully fitted the EL kinetics (magenta line in Figure 2b) using the same time constants τ_1, τ_2 and correspondingly modified coefficients a_1 and a_2 and additional delayed slow saturating growth component:

$$\mathrm{EL}(t) = a_1'\left[1-\exp\left(-t/\tau_1\right)\right] + a_2'\left[1-\exp\left(-t/\tau_2\right)\right] + b\left[1-\exp\left(-(t-\Delta t)/\tau_3\right)\right] \quad (2)$$

Here we consider that the third component equals zero while $t < \Delta t$. The best fit gives $\Delta t = 25$ s and $\tau_3 = 97$ s. These fitting results show that the weak EL intensity during initial several tens of seconds is proportional to the growing current part, while the strongly increasing EL phase starts after delay of about 25 s. Similar fitting has been also performed for the lower temperature data. The obtained time constants are listed in Figure 2a.

Following earlier publications discussed in the Introduction, it is natural to attribute the observed processes to the motion of ions. We presented the time constants, obtained from the EL and current rise kinetics at different temperatures (Figure 2a), in Arrhenius coordinates (see Figure 2c), which enabled us to evaluate activation energies E_a^i of ions, responsible for different processes:

$$k_i = k_{i0}\exp\left(-\frac{E_a^i}{k_B T}\right) \quad (3)$$

where $k_i = \tau_i^{-1}$, k_B is Boltzmann constant and T is the absolute temperature. The Arrhenius plot yields surprisingly identical, within the experimental accuracy, activation energies of about 175 meV for all three processes, strongly suggesting that they all have the same physical origin, that is, they are related to the same type of ion motion.

There is a large diversity in literature regarding mobile ions. According to the theoretical studies, iodine interstitials and vacancies have the lowest motion activation energies, ranging in different publications from about 80 meV to more than 800 meV.[16,18,30,31] Very similar activation energy values (E_a = 137 ± 28 meV and 190 ± 50 meV) as obtained by us have been evaluated experimentally from the light soaking-induced PL enhancement and attributed to the motion and annihilation of iodine interstitials and vacancies.[32,33] Similar motion activation energies have been also reported for another halide Br^- ions.[34–36] It should be noted, that motion of other ions has been also considered. For example, Liu et al. observed lateral

ADVANCED SCIENCE NEWS
www.advancedsciencenews.com

ADVANCED OPTICAL MATERIALS
www.advopticalmat.de

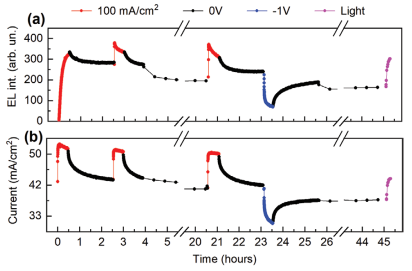

Figure 3. Stressing-induced processes monitored by pump pulse trains. a) EL intensity and b) current dynamics monitored by short positive voltage pulses of 1.45 V, during following types of stress and relaxation: stressing by 100 mA cm^{-2} current (red points); relaxation at zero applied voltage (black points); stressing by negative −1 V voltage (blue points); light soaking at 0 V voltage (magenta points).

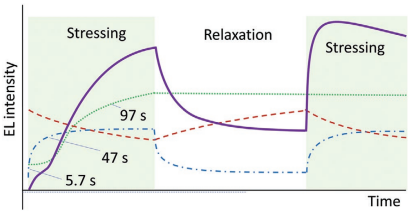

Figure 4. Major stressing-induced processes. EL development kinetics (solid magenta line), bi-exponential current growth causing fast reversible EL growth component (dash-dotted blue line), slow irreversible EL growth component (dotted green line), and reversible EL decay (dashed red line). The numbers show time constants of various processes at room temperature at 2 V stress voltage obtained from exponential fitting.

drift of MA^+ ions during tens of seconds on a surprisingly large, more than tens of micrometers distances.[37] However, the reported activation energies for migration of MA^+ and Pb^+ ions typically exceed 500 meV. Attribution of the observed dynamics to iodine species is consistent with other publications claiming that iodine defects are particularly important in optoelectronic devices since they can easily move under application of electric field.[30,32,38,39] According to Dong et al., motion of negatively charged iodine interstitials I^- takes place on a timescale of tens of seconds.[34] A similar conclusion that redistribution of iodine defects causes reversible variations of current and EL intensity on a timescale of seconds has been also recently suggested by analyzing performance hysteresis of $FAPbI_3$ PeLEDs.[11] According to Buin et al., positively charged iodine vacancies V_i^+ should be the most mobile charged iodine defects.[17] However, our samples were prepared under iodine-rich conditions from solution with 20 mol% excess PMAI (benyzlammonium iodide), which suggests that iodine interstitials inside the bulk of crystallites or iodine ions at the crystallite boundaries should be dominating defects.[17,18] Although we cannot completely exclude role of other kinds of charged mobile species, iodine interstitials I^- seem to be the most likely mobile species mainly responsible for the observed PeLED performance dynamics.

To get more information about the stressing properties, we have modified our investigation technique to decouple monitoring of the PeLED parameters from the stressing impact. For stressing, we applied 100 mA cm^{-2} current density (voltage was about 1.7 V) for different time intervals and after each stressing interval, we monitored the PeLED status by using a series of rectangular pulses of 1.45 V in amplitude and 5 µs in duration, applied with 30 µs period for 30 ms (see Figure S1, Supporting Information, for time sequence of electrical pulses). These short low-voltage monitoring pulses only weakly affected the PeLED performance. Such investigation protocol enabled us to separate the PeLED stressing and monitoring of its parameters. It also enabled us to investigate the recovery of the PeLED performance after the stressing current was terminated, as well as the effect of other impacts such as negative voltage and light soaking. To get more information about the PeLED status, we have also simultaneously monitored current and the EL spectrum. Similarly, we have also monitored stressing-induced changes of the perovskite electroabsorption (EA), sample capacitance, PL intensity, and its decay kinetics.

Figure 3 shows the EL and current kinetics, measured for the fresh sample affected at different time intervals by positive (red points), or negative (blue points) voltage, during relaxation at zero applied voltage (black points), as well as under light soaking by 1 sun intensity light at 0 V (magenta points). Similar to the case of continuous stressing (Figure 2a), the initial EL intensity of the non-stressed sample was very weak. The EL growth was 2–3 times slower than observed with 2 V steady-state voltage, which was apparently caused by the weaker current created by lower stressing voltage of 1.7 V. Moreover, current-induced Joule heating at higher current densities increases the junction temperature,[29] which can accelerate the process due to its highly thermally activated nature. The current growth was less significant than under application of constant voltage, apparently because of non-negligible impact of monitoring pulses.

After termination of the stressing voltage, both EL and current gradually decreased. During several hours, the current decreased to the same value as it was before stressing, while the EL intensity decreased only by less than 20%. Moreover, the decay rates of both EL and current kinetics were very similar. Second application of the stressing voltage after 2.5 h and the third application after 22 h caused very fast EL growth even to a higher value than the value reached during the first stressing session. Surprisingly, after this fast initial rise, the EL intensity slowly decreased during the second and third stressing sessions, unlike the steady increase during the first session.

The above-described experimental data lead to the stressing scenario schematically presented in **Figure 4**. We suggest that the EL intensity is determined by three processes: fast reversible EL growth congruous with the bi-componential saturating current growth with time constants τ_1 and τ_2; slow persistent EL growth with time constant τ_3; and reversible EL decay. The time constants vary depending on the applied voltage and temperature. This model naturally explains the two striking differences

ADVANCED SCIENCE NEWS
www.advancedsciencenews.com

ADVANCED OPTICAL MATERIALS
www.advopticalmat.de

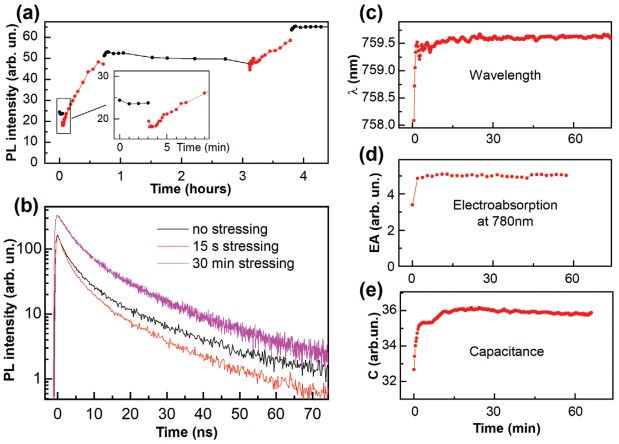

Figure 5. Changes of various PeLED parameters, induced by stressing with 100 mA cm^{-2} current. a) PL intensity dependence on stressing time (red points) and relaxation at applied zero voltage (black points), b) PL decay kinetics in sample stressed for different time intervals, c) wavelength of the EL band maximum, d) EA at 780 nm, and e) capacitance kinetics during sample stressing.

observed during the first and subsequent stressing sessions, that is, larger EL intensity and its decay observed during subsequent stressing sections. During the first section, the reversible EL decay is compensated by the persistence EL growth, which does not take place during subsequent sections.

To get more insight into the stressing dynamics and independently verify this proposed multi-component scheme, we have additionally measured stressing-induced dynamics of several other PeLED parameters: EL wavelength, PL efficiency and its decay kinetics, sample capacitance, and EA. Stressing-induced changes of these parameters are presented in **Figure 5**. Below we discuss these data sequentially by analyzing the stressing-induced processes presented in Figure 4.

2.2. Stressing-Induced Processes

Fast reversible current and EL growth. As shown in Figure 2b, the initial evolution phase, expressed as growth of current together with emergence and initial development of EL, continues for about 20 s at RT. We will consider how other PeLED parameters change during this time. Figure 5a shows the PL intensity dynamics monitored during the sample stressing. The PL intensity was measured at zero applied voltage when stressing voltage was temporarily switched off. As shown in the inset in Figure 5a, the PL intensity slightly drops down during initial tens of seconds, that is, during the initial evolution phase. Afterward, it increases more than 2.5 times during the slow irreversible EL growth phase discussed below. Termination of the stress voltage causes a fast PL intensity increase again.

Figure 5b shows the PL decay kinetics, which reveals a bi-exponential decay. The kinetics were measured at zero applied voltage after stressing the sample for the indicated time intervals. Comparing PL decay kinetics before and after 15 s stressing, we observe that the fast stressing-induced PL intensity drop is mainly caused by faster PL decay on a timescale of tens of ns. We have also measured the PL decays for non-stressed sample under applied different negative and positive voltages not reaching EL operation threshold. These kinetics are presented in Figure S3, Supporting Information. The applied voltage mainly changes the slow decay phase, apparently by varying electric field inside the perovskite layer and, thus carrier extraction. It implies that the faster PL decay observed for the shortly stressed sample may also be caused by the modification of the electric field within the perovskite film. This assumption is supported by the EA measurements (see Figure 5d), which show an increase of the EA signal after a short-time stressing. The EA signal is proportional to the square of the electric field strength, therefore changes of the EA signal shall be considered as an indication of the redistribution of the electric field strength over perovskite layer thickness. Additional support is also provided by the capacitance measurements that demonstrate capacitance increase during the fast stressing phase (see Figure 5e), indicating that the electric field in the stressed sample concentrates in thinner perovskite layer. The initial fast stressing phase also changes the EL spectrum; the luminescence peak wavelength exhibits a slight red shift (Figure 5c). The shift in emission wavelength was attributed to the interference of EL radiation emitted towards transparent electrode and that reflected from the metal electrode: the red shift indicates that the recombination zone moves away from the interface

ADVANCED SCIENCE NEWS
www.advancedsciencenews.com

ADVANCED OPTICAL MATERIALS
www.advopticalmat.de

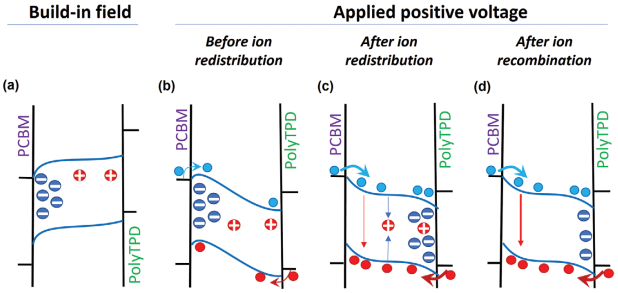

Figure 6. Schematic representation of potential surfaces and ion distributions at different phases of the PeLED stressing. a) Under built-in electric field, I^- ions (blue symbols) and vacancies V^+ (red symbols) accumulate next to PCBM and PolyTPD electrodes, respectively. b) Abrupt application of stressing voltage creates electric field potential with barriers for electron and hole injection, and results in only weak EL because of the spatial separation of electron and hole densities. c) Redistribution of I^- ions and vacancies (assumed to be less mobile) reduces barriers for both electrons and holes and also causes ion recombination. d) EL intensity increases when ion recombination eliminates majority of vacancies acting as recombination centers.

with the electron transporting layer.[28,29] Thus, this is another indication that the fast stressing phase changes the electric field distribution and consequently also the distribution of charge carriers inside the perovskite layer.

All the above-discussed observations are consistent with conclusion that the fast phase is caused by the ion motion, which changes the electric field distribution within the perovskite layer. Although this conclusion is quite expected, the experimental data described above also give important information enabling us to consider the shape of the electric potential and its modifications during stressing, which leads to the changes of carrier injection and recombination. We suggest the qualitative model schematically presented in **Figure 6**. At zero applied voltage, different work functions of electrodes create built-in electric field inside the perovskite layer of opposite direction than electric field in operating PeLED. This field accumulates negative mobile I^- ions next to the PCBM electron transport layer, while positive ions accumulate next to the hole transporting layer. The accumulated ions partly or completely screen the electric field in the central part of the perovskite layer. The field screening would be non-symmetrical, as shown in Figure 6a in case of different concentrations of positive and negative ions. This potential shape suggests that the flat potential in the central perovskite layer part causes slow extraction of photogenerated charge carriers, therefore pristine sample exhibits relatively weak PL quenching (as shown in Figure 5b) caused by the carrier extraction.

Application of the stressing voltage does not change the ion distribution instantaneously, therefore the initial shape of the potential becomes as shown in Figure 6b. This potential shape creates additional barriers for the carrier injection, while additional barrier for the hole injection of about 200 meV is created by the difference between work functions of perovskite and hole transporting material PolyTPD (see Figure 1). The barriers for electrons and holes are different, therefore injection of one type of charge carriers may be partly or almost completely blocked causing very low EL.

Subsequently, applied stressing voltage causes a drift of ions away from the interfaces with the transporting layers, thus reducing the barriers for the carrier injection. Finally, ions change their positions causing reduction of injection barriers. The potential shape becomes as shown in Figure 6c, enabling efficient injection of both electrons and holes and, thus, more efficient EL. However, the roles of positive and negative ions seem to be significantly different in our samples. This is because: a) identical activation energies obtained for different processes strongly suggest that one kind of mobile ions strongly dominates and b) concentration of iodine interstitials in our iodine-rich samples is expected to be much larger than that of iodine vacancies. Figure 6 accounts for the dominating role of I^- ions. It should be noted, that we cannot also completely rule out some other processes that may change the current and, thus, the EL intensity. For example, applied voltage may cause changes in the contact resistance of electrodes and, thus, carrier injection rates. However, the above-described changes of the perovskite PL intensity and EL wavelength taking place simultaneously with the current and EL growth suggest all these processes are interrelated mainly caused by the processes in perovskite layer. On the other hand, ion injection into transport layers was demonstrated to be at least partly responsible for the PeLED EQE roll-off and degradation taking place at higher voltages and longer times.[24,40]

Slow permanent EL growth. As shown in Figure 2b, the slow (tens of minutes) stressing phase starts with a delay of about 25 s at RT after application of the stressing voltage and causes major enhancement of the EL intensity, while current remains at the same level as reached during the previous fast stressing phase. The slow stressing phase also causes almost threefold permanent enhancement of the PL intensity (Figure 5a). As shown in Figure 5b, the slow stressing phase increases the initial intensity of the PL kinetics, slackens its decay during initial 10 ns, but does not change the PL decay on a $t > 10$ ns time scale (compare red and magenta curves obtained after 15 s and 30 min stressing). We attributed the PL kinetics at $t > 10$ ns to

the carrier extraction, thus this process does not change during the slow stressing phase. On the other hand, the fast initial PL decay should be attributed to the carrier trapping. Therefore, EL and PL growth during the slow stressing phase is a manifestation of the enhanced radiative recombination efficiency, apparently caused by the reduced non-radiative Shockley–Read–Hall recombination related to the carrier trapping. This conclusion is supported by the increased open circuit voltage of the stressed PeLED operating as solar cell (see Figure S4, Supporting Information, for IV curves under artificial solar illumination), which is also an indication of the reduced nonradiative relaxation. This slow phase, as was discussed, is characterized by the same activation energy as the fast phases, strongly suggesting that it is also related to the motion of iodine ions.

Similar PL enhancement of $MAPbI_3$ perovskites, only induced by optical soaking, is a well-known phenomenon. It was explained by excitation-induced spatial redistribution and recombination of iodine interstitials and vacancies,[32,33] which act as recombination centers. Such recombination is not possible in PeLEDs before their stressing because, according to our model, the built-in electric field concentrates iodine ions and vacancies in narrow layers next to the opposite transport layers, thus they are spatially separated and cannot recombine. Applied stressing voltage drags ion populations towards each other, they mix, as shown in Figure 6c, and start to recombine. Thus, the delayed start of the slow permanent EL growth phase at about 25 s corresponds to the time needed for charged species to redistribute across the perovskite layer and mix together. Recombination of the iodine defects lasts for about 10 min at RT and longer at lower temperatures. The recombination rate of iodine defects is proportional to the diffusivity of more mobile species, therefore the rate of this process as well as processes attributed to the ion redistribution is characterized by the same activation energy. Recombination of the iodine interstitials and vacancies permanently reduces concentration of recombination centers. In case of different ion and vacancy concentrations, the minor species, in our case V^+, suffer relatively larger losses.

Reversible EL decay. This reversible process observed as partial decay of the EL intensity during the repeatable device stressing (Figure 3) and presented by the red line in diagram in Figure 4 reduces the EL intensity, but does not change significantly the current, PL, EL wavelength, and EA (Figures 3 and 5). This process reveals a fast component of several minutes and a much slower decay on a time scale of hours. During the first-time stressing this decay process is masked by EL increase discussed above. During the repeatable stressing, the fast decrease phase also competes with the EL growth causing slightly faster EL saturation in comparison with the current. Similar decay processes have been observed and investigated in detail in previous publications.[22,29] The fast decay component has been attributed to the sample heating due to current flow, while the slow component is related to the partly reversible device degradation, probably also related to ions.

Relaxation after stressing. Termination of the stress voltage causes simultaneous decay of the current and EL intensity (Figure 3 black points), because recreated built-in electric field drags ions back to their initial positions as in pristine sample, thus recreating barriers for the carrier injection. However, the initial state of pristine sample does not recover completely because of the irreversible reduction of the trap and ion densities, as discussed above. It should be also noted that the current and EL decays during relaxation are much slower than their growth during repeatable stressing, although both processes are expected to be caused by the motion of I^- ions. According to the above-presented ion redistribution model, the stressing and relaxation processes shall not be identical. First, because of different electric field strengths and its spatial distributions. Recombination of I^- with V^+, reduces the ion density and may also change the dynamics. Finally, the stressing and relaxation processes may also be different because ion motion during the PeLED stressing takes place in the presence of charge carriers, while charge carriers are absent during relaxation. Ion diffusivity has been reported being enhanced by optical excitation, however, the mechanism of this phenomenon remains vague.[41] Thus, ion diffusivity may be enhanced by charge carriers, both photogenerated and injected, which makes ion motion faster during stressing.

Impact of negative voltage. Application of the negative voltage to the stressed sample after its relaxation at zero voltage caused additional decay of the EL intensity and current (see Figure 3, blue points). Reinforcement of the internal electric field above the built-in value caused stronger accumulation of ionic species and additionally increased barriers for the carrier injection. After termination of the negative voltage, current and EL intensity gradually recover to the values characteristic of stressed samples at zero applied voltage (see Figure 3).

Application of the negative voltage for a long time interval revealed an additional slow EL decay and almost completely quenched the EL after 25 h (see Figure S5, Supporting Information). We speculate that strong negative voltage applied for a long time may cause redistribution of less mobile ions, probably MA^+, which additionally increase barriers for the carrier injection. Subsequent application of a positive stressing voltage returned the device to the strongly electroluminescent state again.

Light soaking. We have also attempted to investigate the influence of light soaking on the PL and EL intensities by illuminating the PeLED with 1 sun intensity light, similarly as was used in Ref. [32,33]. Surprisingly, no significant changes in the PL intensity and its decay kinetics were observed in pristine non-stressed samples (see Figure S6c, Supporting Information). The light soaking, however, increased the current of a non-stressed sample by about 20% and approximately doubled the EL intensity (see Figure S6a,b, Supporting Information), which, however, remained about tenfold lower than after current-stressing. Consequently, the influence of the light soaking was similar to the one produced by the fast-stressing phase. The light soaking of the stressed sample also caused similar changes as additional current stressing, that is, increased the current and EL intensity, which later relaxed again when the light soaking was terminated.

Our above-presented model explains this unusual influence of light soaking in a similar way as was proposed for perovskite solar cells, where redistribution of ions or vacancies was suggested to be driven by photoinduced voltage creating additional electric field.[42] Optical excitation of PeLED generates an open circuit voltage like in solar cells. Consequently, it reduces the built-in electric field similar to an applied positive voltage. The

ADVANCED SCIENCE NEWS
www.advancedsciencenews.com

ADVANCED OPTICAL MATERIALS
www.advopticalmat.de

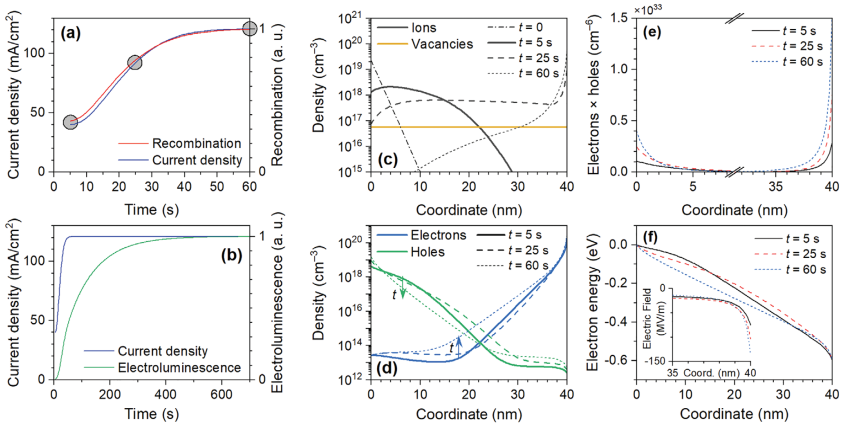

Figure 7. Simulated perovskite stressing dynamics. a) Time dependence of the current density $j(t)$ (blue line, left axis), and spatial overlap of the electron and hole densities $\int n(x,t)p(x,t)dx$ determining recombination rate (red line, right axis) during the initial fast stressing phase. b) Dynamics of the current density and EL intensity during the slow stressing phase. c) Ion densities within the perovskite layer (0 and 40 nm coordinates correspond to the interfaces with PCBM and PolyTPD respectively), calculated at different delay times, shown with shaded circles in panel a (black lines). Density of immobile ion vacancies remained constant (yellow line). d) Calculated densities of electrons (blue lines) and holes (green lines) at the same delay times. e) Distributions of the spatial overlap of carrier densities $n(x, t) \cdot p(x, t)$, calculated at the same delay times. f) Calculated electrostatic energy of the electron in the perovskite layer at the same delay times, the inset shows electric field strength next to Poly TPD layer. In panels (c–f), point $x = 0$ corresponds to the interface with the electron transporting layer.

reduced internal electric field causes redistribution of iodine ions resulting in the reduction or complete disappearance of barriers for the carrier injection, and, as a consequence, increase in current and EL.

3. Numerical Modeling of the Stressing-Induced Processes

To further verify the suggested stressing mechanism, we have modeled the ion redistribution processes and related PeLED performance dynamics. The model is described in Supporting Information and is based on the Einstein–Smoluchowski diffusion–reaction equations. Briefly, we set the initial ion density to follow exponential spatial distribution (see dash-dotted line in **Figure 7**c), corresponding to zero applied voltage, when the electric field inside perovskite is determined by the built-in voltage. Next, we calculated the electric field potential immediately after a positive PeLED pumping voltage was applied. Assuming that carrier transport layers are inexhaustible carrier sources, considering that mobility of charge carriers is several orders of magnitude larger than that of mobile ions, and accounting for the charge carrier recombination and their drift in the electric field produced by the externally applied voltage and internal distribution of ions and carriers themselves, we calculated the resulting stationary distribution of electrons and holes in perovskite layer as well as their current density. Assuming that small variations in ion density do not significantly change the distribution of the net electric field in the perovskite, we then propagated ion dynamics for a short time interval, recalculated stationary distributions of charge carriers, and iteratively repeated the cycle. As a result, we obtained not only the gradual ion redistribution in the net electric field created by applied voltage, ions, and charge carriers but also the effect of this redistribution onto the electric current and spatial densities of the electrons and holes. During these calculations, we accounted for carrier recombination without distinguishing between radiative and nonradiative parts assuming just a constant bimolecular recombination rate. For the sake of simplicity, we considered motion of only negative iodine ions, which, as was discussed, likely are dominating players. Since the very initial stage of ion migration might be influenced by other effects not explicitly accounted for in this model (e.g., initial ion distribution might be not strictly exponential, pronounced overlap of high-density distributions of ions and holes might indirectly influence ion mobility, etc.), in the discussion below we focus on the modeling results following the initial 5-s transitional period at room temperature and correspondingly longer period at lower temperature when ion diffusion is slower.

As already mentioned, our model directly gives time dependence of the current density on a time scale of seconds, and, finally, we calculate the EL intensity as follows. We assume that the EL intensity is proportional to the spatial overlap of the electron, $n(x)$, and hole, $p(x)$, densities multiplied by efficiency of radiative recombination, $\xi(t)$, which changes due to the current stressing:

$$\mathrm{EL}(t) \propto \xi(t) \cdot \int n(x,t)\, p(x,t)\, \mathrm{d}x \tag{4}$$

Here, the integral is taken across the perovskite layer. For simplicity, we also assume that the current stressing rate is proportional to the current density, thus the efficiency of the radiative recombination equals to:

$$\xi(t) = 1 - \exp\left(-k_{\mathrm{str}}\, j(t)\, t\right) \tag{5}$$

where $j(t)$ is current density and k_{str} is the stressing rate constant.

The model contains several variable parameters. Some of them such as carrier mobilities, bimolecular recombination rate, ion density, were chosen based on literature data, others evaluated from the sample structure and geometry, remaining are free parameters varied to achieve a reasonable agreement with the experimental data. The parameter values used in our calculations are listed in Table S1, Supporting Information.

Figures a shows current and recombination rate dynamics during the initial fast stressing phase, evaluated for optimal parameter values, while Figure 7b shows also an EL dynamics on a longer time scale. The latter was calculated according to Equation (5). For comparison with experimental data, the evaluated current and EL dynamics at different temperatures are also presented with dashed lines in Figure 2a. A reasonable agreement with experimental data has been obtained except for the very initial times. Processes at lower temperatures were calculated just assuming that the ion mobility decreases with temperature as described by Equation (3) with activation energy E_a = 181 meV, which is close to the activation energies determined from Figure 2c.

Our inability to reproduce the very initial dynamics indicates that some additional fast processes take place, which was not included in the model. In our calculations, we consider that the ion mobility is constant. In case of the disordered material, however, the initial ion motion may be significantly faster than determined by their mobility at longer times, as was observed for carrier motion in disordered organic semiconductors.[43] Such dispersional ion motion would cause much faster initial current growth, and its slower saturation at longer times, as observed experimentally. The fast initial electric field redistribution may also be caused by the presence of the slow component of the dielectric permittivity, which could be present in perovskites due to ferroelectric polarization.[44] We cannot also completely exclude that our attribution of the observed processes to the motion of iodine interstitials is incorrect. Some evaluations suggest dynamics during tens and hundreds of seconds may be caused by motion of MA of Pb defects, while motion of iodine defects should be much faster.[16] Thus, motion of iodine defects may be responsible for the dynamics during sub-seconds and several initial seconds. However, so far we do not have arguments in favor of one or another process.

Figures 7c,d show spatial distributions of mobile negative and immobile positive ions as well as electrons and holes, calculated at three time moments: 1) immediately after application of positive voltage, 2) in the intermediate stage of ion redistribution phase, and 3) after the complete ion redistribution. Figures 7f,e also show distributions of electron energy and product of electron and hole densities determining carrier recombination rate and, thus, EL intensity. The initial ion distribution is determined by the built-in electric field corresponding to about 1.2 V built-in voltage created by the differences between work functions of transport layers and electrodes. Correspondingly, applied positive voltage of 2 V in the ideal case creates potential difference on the perovskite layer equal to 0.8 V. However, apparently a fraction of the applied voltage drops on transport layers, therefore we consider potential difference across perovskite layer being of 0.6 V under applied 2 V voltage. Immediately after voltage application, the initial ion distribution creates a potential energy surface for electrons exhibiting a flat zone close to the negative electrode, which limits the electron injection. On the other hand, the hole injection is limited by the barrier of about 200 meV originating from the difference between HOMO levels of PolyTPD and $MAPbI_3$. This barrier narrows when electrons and negative iodine ions accumulate next to the PolyTPD layer and create strong electric field as shown in inset in Figure 7f, enabling faster hole injection by tunneling, hence increase of the hole density at the positive electrode (point x = 40 nm). Consequently, when iodine ions redistribute and gradually accumulate next to PolyTPD layer, both electron and hole injection rates increase which in turn lead to the increase in carrier density and recombination rate.

As shown in Figure 7e, the carrier recombination takes place close to the perovskite layer surfaces where charge carriers accumulate. Before the ion redistribution, stronger carrier recombination takes place close to the negative Al electrode. Later on, due to ion diffusion, recombination intensifies along the positive ITO electrode, which is in agreement with the observed red shift of the EL wavelength (see Figure 5c), indicating shift of the recombination zone away from the metal electrode.[28,29]Concentration of the electric field in a thin layer (inset in Figure 7f) shall lead to increase in the EA signal and in sample capacitance, in agreement with the experimental data (see Figures 5d,e).

Even though the used calculations simplify some of the processes taking place in real PeLEDs, they quite closely reproduce the current and EL dynamics and also qualitatively explain changes of the PL wavelength, EA, and capacitance taking place during the PeLED stressing. Depending on the PeLED structure and properties of the perovskites used, processes in other PeLEDs may be significantly different. Figure S8, Supporting Information, shows how the current and EL dynamics change under variation of some model parameters. Quantitative similarity retains by changing carrier mobility, ion density by orders of magnitude, but significantly changes depending on the applied potential difference across perovskite layer. Consequently, our investigations suggest major principles enabling to understand and predict the PeLED operation dynamics, which is an important step in their further development.

4. Conclusions

EL intensity and current of $MAPbI_3$ PeLED show complex growth kinetics after application of constant pump voltage. The initial EL intensity of pristine sample is very weak and grows hundreds of times on time scales of milliseconds to tens of

minutes. Subsequent application of voltage after the device "rests" for tens of minutes or hours creates a much stronger initial EL, which additionally grows by tens of percent during seconds. We analyzed the EL growth processes by using several investigation techniques that enabled us to investigate changes of EL intensity, current, and EL spectrum taking place during current stressing, relaxation after stressing, application of negative voltage or light soaking. Analysis of the experimental results together with mathematical modeling revealed that the complex changes taking place on several very different time scales are caused by the motion of ions characterized by activation energies of about 175 meV. Our experimental results and literature data suggest that negative iodine ions play a dominating role. Spatial redistribution of ions along the perovskite layer thickness changes shape of electric potential, barriers for carrier injection, and also causes of their recombination with iodine interstitials acting as nonradiative recombination centers.

We believe that the obtained deeper understanding of the processes taking place in operating PeLEDs will be important for their optimization directed to more efficient performance, particularly in dynamic regimes.

5. Experimental Section

Device Fabrication: Fabrication of the PeLEDs was described elsewhere.[22] Briefly, PolyTPD was spin coated on the precleaned ITO substrates at 4000 rpm for 40 s and then anneal at 150 °C for 20 min, followed by treating with O_2 plasma for 6 s at a power of 100 W to improve surface wettability. Afterward, $MAPbI_3$ with 20 mol% extra benzylammonium iodide was deposited on PolyTPD in N2 filled glove box, using an antisolvent method. Then, PCBM solution in chlorobenzene was deposited at 3000 rpm, followed by depositing ZnMgO nanoparticles in ethanol at 4000 rpm. The devices were finished by thermal evaporation of 100 nm Al. The device area was defined by the shadow mask and was 0.125 cm^2 with dimensions of 2.5 mm × 5 mm.

Investigation Techniques: EL and current dynamics under application of steady state voltage were measured using Keithley 2604B dual channel SMUs. The sample was mounted in vacuum in a JANIS vpf-100 liquid nitrogen cryostat, where the sample temperature was controlled using a Lakeshore 335 temperature controller. A Silicon photodiode 818-SL from Newport was used to monitor the EL signal. The sampling rate was set to 100 ms for both channels. The experiment starts by applying a DC voltage to the PeLED, while the current and EL dynamics were simultaneously monitored using the two SMUs.

Pulsed stressing measurements were performed according to protocol presented in Supporting Information. Briefly, the sample was stressed by 100 mA cm^{-2} current for variable time durations and subsequently EL intensity, current, and mean EL wavelength were measured by switching-of the stressing voltage and applying a train of short electrical probing pulses. The voltage was applied by using arbitrary function generator Tektronix AFG3101 and current was measured with Agilent Technologies DS05054A oscilloscope using 50 Ω input. EL intensity and spectrum were measured with AvaSpec-HS1024 × 58/122 fiber optic spectrometer (Avantes). The same procedure was used to investigate the light soaking impact, only in this case, 1 sunlight intensity was applied instead of stressing current. During investigations of the relaxation processes, the sample, between probing pulses, was kept at zero voltage in dark.

PL, EA, and capacitance were investigated by using the same stressing protocol, but measurements were performed at zero applied voltage. Capacitance measurements were performed by using the same setup by applying sinusoidal voltage and measuring alternative current passing through the device. The relative capacitance changes were evaluated from the current amplitude and phase shift.

EA measurements were performed as described in Ref. [45]. The EA signal was measured by comparing absorption spectra at positive and negative 1 V voltages. The positive 1 V voltage compensated the built-in voltage, thus the net potential difference across the perovskite layer was close to zero. While at –1 V applied voltage the potential difference was about 2 V.

Time-resolved PL measurements were performed by the Edinburgh Instruments Time Correlated Single Photon Counting (TCSPC) spectrometer. Picosecond pulsed diode laser EPL-470 emitting 72 ps pulses at 470 nm with the repetition rate of 500 kHz (interval 2 µs) was used for the sample excitation.

Supporting Information

Supporting Information is available from the Wiley Online Library or from the author.

Acknowledgements

K.E. contributed equally to the work as the first author. The authors acknowledge funding from the European Research Council (ERC) under the European Union's Horizon 2020 research and innovation programme (grant agreement No 835133, ULTRA-LUX) and funding from European Regional Development Fund (project No 01.2.2-LMT-K-718-03-0048) under grant agreement with the Research Council of Lithuania (LMTLT). W.Q. would like to thank the financial support of the postdoctoral fellowship grant from FWO.

Conflict of Interest

The authors declare no conflict of interest.

Data Availability Statement

The data that supports the findings of this study are available in the supplementary material of this article.

Keywords

dynamic operation, electroluminescence, ion migration, light-emitting diodes, perovskites

Received: July 29, 2021
Revised: September 3, 2021
Published online:

[1] Z.-K. Tan, R. S. Moghaddam, M. L. Lai, P. Docampo, R. Higler, F. Deschler, M. Price, A. Sadhanala, L. M. Pazos, D. Credgington, F. Hanusch, T. Bein, H. J. Snaith, R. H. Friend, *Nat. Nanotechnol.* **2014**, *9*, 687.
[2] J. Wang, N. Wang, Y. Jin, J. Si, Z.-K. Tan, H. Du, L. Cheng, X. Dai, S. Bai, H. He, Z. Ye, M. L. Lai, R. H. Friend, W. Huang, *Adv. Mater.* **2015**, *27*, 2311.
[3] L. Zhao, J. Gao, Y. L. Lin, Y.-W. Yeh, K. M. Lee, N. Yao, Y.-L. Loo, B. P. Rand, *Adv. Mater.* **2017**, *29*, 1605317.

[4] Y. Cao, N. Wang, H. Tian, J. Guo, Y. Wei, H. Chen, Y. Miao, W. Zou, K. Pan, Y. He, H. Cao, Y. Ke, M. Xu, Y. Wang, M. Yang, K. Du, Z. Fu, D. Kong, D. Dai, Y. Jin, G. Li, H. Li, Q. Peng, J. Wang, W. Huang, *Nature* **2018**, *562*, 249.
[5] W. Xu, Q. Hu, S. Bai, C. Bao, Y. Miao, Z. Yuan, T. Borzda, A. J. Barker, E. Tyukalova, Z. Hu, M. Kawecki, H. Wang, Z. Yan, X. Liu, X. Shi, K. Uvdal, M. Fahlman, W. Zhang, M. Duchamp, J.-M. Liu, A. Petrozza, J. Wang, L.-M. Liu, W. Huang, F. Gao, *Nat. Photonics* **2019**, *13*, 418.
[6] T. Chiba, Y. Hayashi, H. Ebe, K. Hoshi, J. Sato, S. Sato, Y.-J. Pu, S. Ohisa, J. Kido, *Nat. Photonics* **2018**, *12*, 681.
[7] C. Murawski, K. Leo, M. C. Gather, *Adv. Mater.* **2013**, *25*, 6801.
[8] M. Yang, N. Wang, S. Zhang, W. Zou, Y. He, Y. Wei, M. Xu, J. Wang, W. Huang, *J. Phys. Chem. Lett.* **2018**, *9*, 2038.
[9] W. Zou, R. Li, S. Zhang, Y. Liu, N. Wang, Y. Cao, Y. Miao, M. Xu, Q. Guo, D. Di, L. Zhang, C. Yi, F. Gao, R. H. Friend, J. Wang, W. Huang, *Nat. Commun.* **2018**, *9*, 608.
[10] A. Fakharuddin, W. Qiu, G. Croes, A. Devižis, R. Gegevičius, A. Vakhnin, C. Rolin, J. Genoe, R. Gehlhaar, A. Kadashchuk, V. Gulbinas, P. Heremans, *Adv. Funct. Mater.* **2019**, *29*, 1904101.
[11] H. Wang, Z. Chen, J. Hu, H. Yu, C. Kuang, J. Qin, X. Liu, Y. Lu, M. Fahlman, L. Hou, X. Liu, F. Gao, *Adv. Funct. Mater.* **2021**, *31*, 2007596.
[12] R. Gegevičius, M. Franckevičius, J. Chmeliov, W. Tress, V. Gulbinas, *J. Phys. Chem. Lett.* **2019**, *10*, 1779.
[13] H. J. Snaith, A. Abate, J. M. Ball, G. E. Eperon, T. Leijtens, N. K. Noel, S. D. Stranks, J. T.-W. Wang, K. Wojciechowski, W. Zhang, *J. Phys. Chem. Lett.* **2014**, *5*, 1511.
[14] H.-W. Chen, N. Sakai, M. Ikegami, T. Miyasaka, *J. Phys. Chem. Lett.* **2015**, *6*, 164.
[15] W. Tress, N. Marinova, T. Moehl, S. M. Zakeeruddin, M. K. Nazeeruddin, M. Grätzel, *Energy Environ. Sci.* **2015**, *8*, 995.
[16] J. M. Azpiroz, E. Mosconi, J. Bisquert, F. De Angelis, *Energy Environ. Sci.* **2015**, *8*, 2118.
[17] A. Buin, P. Pietsch, J. Xu, O. Voznyy, A. H. Ip, R. Comin, E. H. Sargent, *Nano Lett.*. **2014**, *14*, 6281.
[18] W.-J. Yin, T. Shi, Y. Yan, *Appl. Phys. Lett.* **2014**, *104*, 063903.
[19] E. Aydin, M. Bastiani, S. Wolf, *Adv. Mater.* **2019**, *31*, 1900428.
[20] Y. Shang, Y. Liao, Q. Wei, Z. Wang, B. Xiang, Y. Ke, W. Liu, Z. Ning, *Sci. Adv.* **2019**, *5*, eaaw8072.
[21] J. H. Warby, B. Wenger, A. J. Ramadan, R. D. J. Oliver, H. C. Sansom, A. R. Marshall, H. J. Snaith, *ACS Nano* **2020**, *14*, 8855.
[22] K. Elkhouly, R. Gehlhaar, J. Genoe, P. Heremans, W. Qiu, *Adv. Optical Mater.* **2020**, *8*, 2000941.
[23] J. Wu, Y. Li, S. Tan, B. Yu, H. Li, Y. Li, J. Shi, H. Wu, Y. Luo, D. Li, Q. Meng, *ACS Appl. Mater. Interfaces* **2020**, *12*, 27258.
[24] T. Cheng, G. Tumen-Ulzii, D. Klotz, S. Watanabe, T. Matsushima, C. Adachi, *ACS Appl. Mater. Interfaces* **2020**, *12*, 33004.
[25] T. Leijtens, E. T. Hoke, G. Grancini, D. J. Slotcavage, G. E. Eperon, J. M. Ball, M. De Bastiani, A. R. Bowring, N. Martino, K. Wojciechowski, M. D. McGehee, H. J. Snaith, A. Petrozza, *Adv. Energy Mater.* **2015**, *5*, 1500962.
[26] Y. Yuan, J. Chae, Y. Shao, Q. Wang, Z. Xiao, A. Centrone, J. Huang, *Adv. Energy Mater.* **2015**, *5*, 1500615.
[27] X.-K. Liu, W. Xu, S. Bai, Y. Jin, J. Wang, R. H. Friend, F. Gao, *Nat. Mater.* **2021**, *20*, 10.
[28] H. Kim, L. Zhao, J. S. Price, A. J. Grede, K. Roh, A. N. Brigeman, M. Lopez, B. P. Rand, N. C. Giebink, *Nat. Commun.* **2018**, *9*, 4893.
[29] K. Elkhouly, I. Goldberg, H. Boyen, A. Franquet, V. Spampinato, T. Ke, R. Gehlhaar, J. Genoe, J. Hofkens, P. Heremans, W. Qiu, *Adv. Optical Mater.* **2021**, 2100586.
[30] C. Eames, J. M. Frost, P. R. F. Barnes, B. C. O'Regan, A. Walsh, M. S. Islam, *Nat. Commun.* **2015**, *6*, 7497.
[31] J. Haruyama, K. Sodeyama, L. Han, Y. Tateyama, *J. Am. Chem. Soc.* **2015**, *137*, 10048.
[32] E. Mosconi, D. Meggiolaro, H. J. Snaith, S. D. Stranks, F. De Angelis, *Energy Environ. Sci.* **2016**, *9*, 3180.
[33] D. W. deQuilettes, W. Zhang, V. M. Burlakov, D. J. Graham, T. Leijtens, A. Osherov, V. Bulović, H. J. Snaith, D. S. Ginger, S. D. Stranks, *Nat. Commun.* **2016**, *7*, 11683.
[34] Q. Dong, J. Mendes, L. Lei, D. Seyitliyev, L. Zhu, S. He, K. Gundogdu, F. So, *ACS Appl. Mater. Interfaces* **2020**, *12*, 48845.
[35] S. Meloni, T. Moehl, W. Tress, M. Franckevičius, M. Saliba, Y. H. Lee, P. Gao, M. K. Nazeeruddin, S. M. Zakeeruddin, U. Rothlisberger, M. Graetzel, *Nat. Commun.* **2016**, *7*, 10334.
[36] A. Oranskaia, J. Yin, O. M. Bakr, J.-L. Brédas, O. F. Mohammed, *J. Phys. Chem. Lett.* **2018**, *9*, 5474.
[37] Y. Liu, A. V. Ievlev, N. Borodinov, M. Lorenz, K. Xiao, M. Ahmadi, B. Hu, S. V. Kalinin, O. S. Ovchinnikova, *Adv. Funct. Mater.* **2021**, *31*, 2008777.
[38] C. Li, A. Guerrero, S. Huettner, J. Bisquert, *Nat. Commun.* **2018**, *9*, 5113.
[39] H. Jin, E. Debroye, M. Keshavarz, I. G. Scheblykin, M. B. J. Roeffaers, J. Hofkens, J. A. Steele, *Mater. Horiz.* **2020**, *7*, 397.
[40] Y. Guo, S. Apergi, N. Li, M. Chen, C. Yin, Z. Yuan, F. Gao, F. Xie, G. Brocks, S. Tao, N. Zhao, *Nat. Commun.* **2021**, *12*, 644.
[41] Y.-C. Zhao, W.-K. Zhou, X. Zhou, K.-H. Liu, D.-P. Yu, Q. Zhao, *Light: Sci. Appl.* **2017**, *6*, e16243.
[42] Y. Deng, Z. Xiao, J. Huang, *Adv. Energy Mater.* **2015**, *5*, 1500721.
[43] V. Gulbinas, *Lith. J. Phys.* **2020**, *60*, 1.
[44] B. Chen, M. Yang, S. Priya, K. Zhu, *J. Phys. Chem. Lett.* **2016**, *7*, 905.
[45] R. Jasiūnas, H. Zhang, J. Yuan, X. Zhou, D. Qian, Y. Zou, A. Devižis, J. Šulskus, F. Gao, V. Gulbinas, *J. Phys. Chem. C* **2020**, *124*, 21283.

FULL PAPER

ADVANCED OPTICAL MATERIALS
www.advopticalmat.de

Energy Barriers Restrict Charge Carrier Motion in MAPI Perovskite Films

Rokas Jasiūnas, Rokas Gegevičius, Marius Franckevičius, Vidmantas Jašinskas, and Vidmantas Gulbinas*

Understanding of charge trapping processes in halide perovskites is vital to further improve performance of perovskite optoelectronic devices such as solar cells, photodetectors, and LEDs. In this work, transient photocurrent, time-delayed collection field and transient fluorescence techniques along with numerical simulations are combined to address charge carrier trapping processes during their lateral motion in prototypical methylammonium lead iodide perovskite films formed on interdigitated electrodes. Carrier mobility decreases on hundreds of ns timescale, and its rate depends on the motion character—it is faster when charge carriers drift in the electric field and slower when the motion is caused by diffusion only. This difference becomes particularly evident at low temperatures. Based on the time-delayed collection field data and carrier motion modelling results, it is demonstrated that the rapid mobility decay at low temperatures is mainly caused by the energy barriers, most likely formed at crystallite boundaries. Even though these barriers are surmountable at room temperature, they still play a major role in determining carrier mobility and diffusion rates. Suggested concept of the potential barriers moves beyond the conventional understanding of carrier mobility, diffusion, and recombination processes in hybrid perovskites.

1. Introduction

Hybrid perovskite materials have witnessed immense development in a range of optoelectronic devices, for example, efficient solar cells,[1] bright tunable LEDs,[2] fast and sensitive photodetectors,[3] and beyond. The success is primarily due to exceptional optoelectronic properties of hybrid perovskites such as low charge carrier recombination rates which are responsible for impressive diffusion lengths,[4] tunable bandgap and large optical absorption coefficient.[5,6] During recent years, the knowledge about fundamental processes in perovskite materials has greatly expanded; however, many aspects of charge carrier transport are still poorly understood and demand a more in-depth investigation. These include charge carrier trapping and mobility, which are critical when it comes to device performance[7] and stability.[8]

The popular belief is that lead halide perovskites have lower carrier trap densities than other low-temperature solution-processed semiconductors.[9] However, carrier trapping processes strongly affect carrier motion and play a vital role in solar cell performance at solar fluences.[10,11] Though the extensive time-resolved photoluminescence and terahertz spectroscopy studies were conducted to reveal the nature of trap states in hybrid perovskites, clear evidence on how they affect charge carrier mobility is still lacking.

Recent literature data reports a wide distribution of mobility values in hybrid perovskite materials, ranging from tens to ≈100 $cm^2 V^{-1} s^{-1}$ for single crystals and from 10^{-4} to more than 10 $cm^2 V^{-1} s^{-1}$ for polycrystalline films.[12–19] Typically, high-frequency THz measurements give higher values than, for example, time-of-flight (TOF) or space-charge limited current (SCLC) techniques.[19] Mobility investigations are often performed in complete solar cells where additional transport layers may complicate accurate data evaluation.[19] Another related, but still unresolved question is how to understand the relation between carrier mobility and bi-molecular recombination rate, because recombination rate in some perovskites is several orders of magnitude lower than that evaluated from mobility values on a base of Langevin relation.[14]

Typically, solution processed hybrid perovskite films are polycrystalline composed of the crystalline grains. Grain boundaries are considered to play an important role in carrier motion and recombination. It is typically believed that grain boundaries create trap states for charge carriers. Carrier trapping reduces their mobility and causes Shockley–Read–Hole recombination. On the other hand, there are few papers that account the existence of energy barriers at the grain boundaries,[20–22] but their influence on the carrier mobility remains completely unexplored.

In this work, we addressed carrier motion dynamics in classical $MAPbI_3$ (MAPI) perovskite films deposited on Pt

R. Jasiūnas, R. Gegevičius, Dr. M. Franckevičius, V. Jašinskas, Prof. V. Gulbinas
Department of Molecular Compound Physics
Center for Physical Sciences and Technology
Saulėtekio Avenue 3, Vilnius LT-10257, Lithuania
E-mail: marius.franckevicius@ftmc.lt
Prof. V. Gulbinas
Institute of Chemical Physics
Faculty of Physics
Vilnius University
Saulėtekio Avenue 9, Vilnius LT-10222, Lithuania
The ORCID identification number(s) for the author(s) of this article can be found under https://doi.org/10.1002/adom.202000036.

DOI: 10.1002/adom.202000036

ADVANCED SCIENCE NEWS
www.advancedsciencenews.com

ADVANCED OPTICAL MATERIALS
www.advopticalmat.de

interdigitated electrodes (IDE). Selected sample configuration provides a possibility to probe the lateral motion of photogenerated carriers in perovskite film, being unaffected or weakly affected by the interface phenomena, or additional layers, which are usually present in sandwich-type devices such as solar cells or LEDs. By combining conventional transient photocurrent, transient photoluminescence and time-delayed collection field techniques we monitor carrier motion at different temperatures and demonstrate that carrier mobility at low temperatures is mainly determined by energy barriers, most likely formed by not perfect intergrain connections. At room temperature, barrier influence on carrier mobility is less significant, however carrier motion hampering is still observable. Similar behavior was also obtained for triple cation $Cs_{0.05}MA_{0.15}FA_{0.8}PbI_{2.55}Br_{0.45}$ (CsFAMA) perovskites, suggesting that existence of energy barriers is independent on perovskite composition and is inherent to this material class.

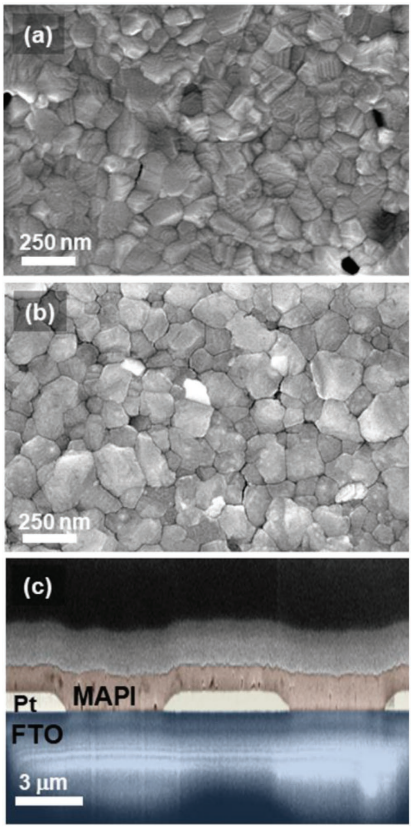

Figure 1. Top view scanning electron microscope (SEM) images of a) MAPI and b) CsFAMA. c) The cross-sectional SEM image demonstrates lateral configurations of the perovskite films deposited on IDE.

2. Results and Discussion

2.1. Charge Carrier Extraction, Recombination, and Trapping

At first, we will consider transient photocurrent kinetics measured for the MAPI perovskite films deposited on Pt interdigitated electrodes. Scanning electron microscope images of the samples are presented in **Figure 1**a,b. Measurements were performed at different experimental conditions to distinguish between carrier recombination, extraction and trapping processes. According to the energy level positions, Pt establishes the junction barrier for injection of both carrier types into $MAPbI_3$ layer. No barrier should be for the carrier extraction, or if some barriers are still formed, their influence on photocurrent shall be only marginal in the case of pulsed excitation. Moreover, as it was demonstrated in ref. [10] and confirmed by our investigations (see Section S4, Supporting Information), electron currents are significantly lower than those of holes, because of the fast electron trapping, which additionally suppress possible influence of the Schottky barrier. On the other hand, electron trapping may significantly impact carrier recombination by Shockley–Read–Hole (SRH) process. Transient photocurrent created by a short light pulse may be formally expressed as

$$j(t) = e[n_e(t)\mu_e(t) + n_h(t)\mu_h(t)]F \quad (1)$$

where e is the electron charge, F is the electric field strength, $n_{e,h}(t)$ and $\mu_{e,h}(t)$ are time-dependent densities of photogenerated electrons and holes and their mobilities, respectively. Carrier trapping is one of the processes that change the densities of mobile carriers. However, precise accounting for the carrier trapping is a difficult task since deep carrier trapping reduces the carrier density, while shallow trapping reduces their mobility. We do not have sufficient information about these processes; moreover, such separation depends on temperature and on the considered time scale. Therefore, in the following analysis, we regard total carrier concentrations, including the trapped carriers, while carrier trapping is accounted by considering carrier mobilities averaged over free and trapped carriers. We can additionally simplify this expression by introducing effective carrier mobility averaged over electrons and holes and considering total carrier density $n = n_e + n_h$. Then photocurrent may be expressed as

$$j(t) = en(t)\mu_{ef}(t)F \quad (2)$$

Kinetics of the carrier concentration may be expressed as

$$\frac{dn}{dt} = -\frac{j(t)}{de} - kn - \gamma(t)n^2 \quad (3)$$

where d is the distance between electrodes, k is the linear SRH carrier recombination rate, and $\gamma(t)$ is bimolecular

ADVANCED SCIENCE NEWS
www.advancedsciencenews.com

ADVANCED OPTICAL MATERIALS
www.advopticalmat.de

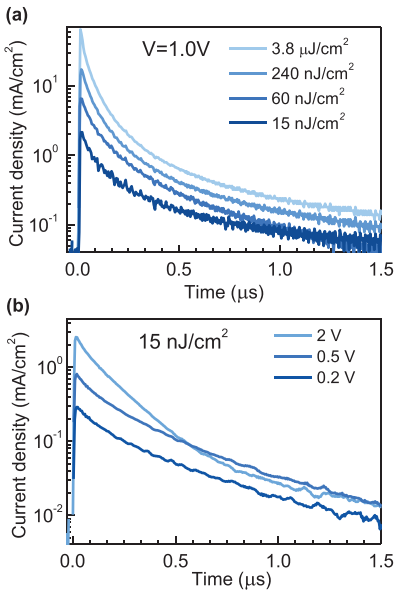

Figure 2. Transient photocurrent kinetics a) at different excitation intensities under 1 V applied voltage and b) at constant excitation intensity of 15 nJ cm^{-2} but different applied voltages.

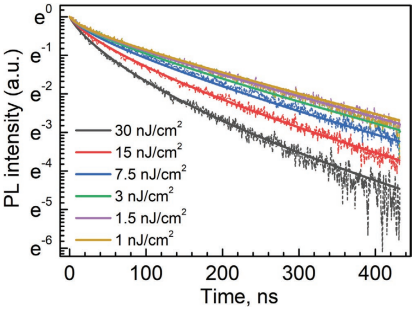

Figure 3. Photoluminescence kinetics of MAPI perovskite at different excitation intensities. $\lambda_{ex} = 470$ nm. Dotted lines represent experimental results, and solid lines show modelling results.

recombination rate. By considering carrier recombination, we ignore inhomogeneous spatial carrier distributions. Spatial separation of electrons and holes moving to opposite directions is accounted into the time-dependent recombination rate.

Charge carriers concentrations decrease due to their recombination and extraction to electrodes. Bimolecular recombination and extraction processes depend on carrier concentrations and drift rates, respectively. Thus, we can change these rates by changing the excitation intensity and bias voltage. In this way, we can reach condition where one or both these processes may be suppressed and neglected. **Figure 2**a,b shows such dependencies. At the two lowest excitation intensities, the shape of the photocurrent kinetics only weakly depends on the excitation intensity (Figure 2a). Therefore, we consider that shape of these kinetics curves is only marginally affected by the bimolecular recombination. Likewise, the identical shape of the photocurrent kinetics at 0.2 and 0.5 V applied voltages indicates that carrier extraction is also insignificant at these voltages.

Consequently, the photocurrent decay at the lowest excitation intensity and 0.2 V bias voltage should be mainly caused by the linear SRH recombination and/or decreasing charge carrier mobility, later of which, according to our approach, also accounts for carrier trapping. It should also be noted, that the initial photocurrent does not scale linearly with the excitation intensity, as Figure S4b (Supporting Information) presented in the Supporting Information shows, the initial photocurrent almost saturates at the highest excitation intensities. It indicates the existence of an additional fast nonlinear recombination phase, which at high excitation intensities reduces carrier density faster than the time resolution of our measurements. To address this rapid decay phase, we have investigated photoluminescence (PL) kinetics with a better time resolution. **Figure 3** shows the PL kinetics measured at different excitation intensities. At low excitation intensities, the PL intensity at longer times decays exponentially with the time constant of 180 ns. It reveals a recombination phase in tens of nanoseconds, which is not observed in photocurrent measurements due to insufficient time resolution. PL intensity may be expressed as a product of free electron and hole densities PL $\approx n(t)p(t)$. We have modelled the PL kinetics considering that electron and hole densities decrease as

$$\frac{dn}{dt} = -nk(t) - \gamma np \tag{4}$$

$$\frac{dp}{dt} = -\gamma np \tag{5}$$

Here $k(t)$, for the sake of simplicity, expresses the linear free-electron decay rate caused by their trapping, thermal detrapping and SRH recombination, γ is bimolecular recombination rate. Spatial carrier separation shall be absent in PL measurements performed without electric field, therefore bimolecular recombination rate γ here is considered as constant. It should be noted that the carrier decay rate obtained from PL investigations perfectly explains the saturation of the photocurrent peak (the modelling details and results are presented in Section S3, Supporting Information). The modelling gives the bimolecular recombination rate equal to $\gamma = 2.2 \times 10^{-9}$ cm^3 s^{-1}, which is similar to that reported in ref. [10], but significantly higher than the values reported in later publications.[6,23,24] The difference may

ADVANCED SCIENCE NEWS
www.advancedsciencenews.com

ADVANCED OPTICAL MATERIALS
www.advopticalmat.de

be at least partly caused by the specific sample configuration where metal electrodes suppress photon recycling, which otherwise significantly reduces the external recombination rate.[25,26] Noteworthy, that the linear PL decay rate was shorter for the films prepared on electrode comb than on conventional glass substrate, which should also be attributed to the suppressed photon recycling.

According to the photoluminescence kinetics, carrier decay rate at the lowest excitation intensity used in transient photocurrent measurements is weakly affected by the bimolecular recombination. It should be noted, that at the identical excitation intensity and low applied voltages the photocurrent decays two times slower than photoluminescence. It could be due to the different influence of the carrier trapping on photocurrent and PL. Trapping of one sign of carriers completely decimates luminescence while regarding photocurrent it only reduces the mobility of one sign of carriers.

To get more information about the physical processes, we additionally performed transient photocurrent measurements at different temperatures. **Figure 4**a shows the photocurrent kinetics at several different temperatures. The initial photocurrent value shows no clear dependence on temperature, indicating that the carrier generation, as well as their initial mobility, are temperature-independent. Similar temperature-independent carrier mobility during initial hundreds of ps was also reported for conjugated polymers,[27] or weak temperature dependence for hybrid perovskites.[15] Weak temperature dependence was observed for the MAPI photoluminescence decay.[28] Figure 4a, however, shows that the photocurrent drops much faster at low temperatures. We also note a higher photocurrent at a longer time scale (several µs) at low temperatures. This should be expected since less charge carriers are extracted when photocurrent decays very rapidly, therefore more carriers remain in the sample. Voltage dependence of the photocurrent kinetics shown in Figure 4b also becomes qualitatively different at 100 K than at room temperature: the photocurrent decays more rapidly, and the slow photocurrent component almost vanishes at low bias voltage. This behavior suggests that charge carriers are rapidly trapped at low temperatures, while strong electric field gradually withdraws carriers from traps and keeps a weak photocurrent during several µs.

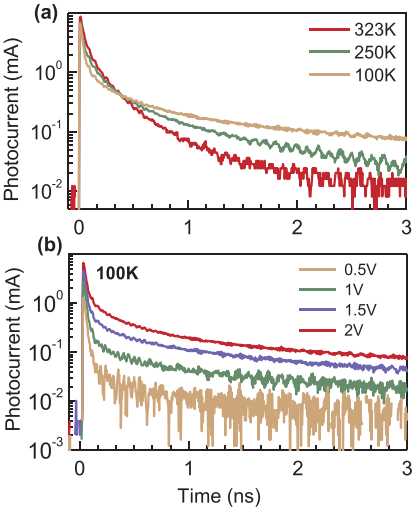

Figure 4. a) Photocurrent kinetics at different temperatures measured at 2 V applied voltage and 15 nJ cm^{-2} excitation intensity, b) photocurrent kinetics at 100 K at different applied voltages.

2.2. Time-Delayed Collection Field Investigations

Time-delayed collection field (TDCF) technique provides additional information about carrier density decay and mobility kinetics. In the simplest implementation of this technique, sample excitation is performed at zero voltage, while extraction voltage is applied after a variable delay (see **Figure 5** for the time chart of the TDCF measurements). Dependence of the total extracted charge (cumulated current) on the delay time between optical excitation and application of extraction voltage represents charge carrier density decrease at zero bias voltage. On the other hand, initial photocurrent corresponds to the product of carrier density and their mobility; therefore, it is possible to track evolution of the initial carrier mobility. **Figure 6**a,b shows carrier extraction kinetics at different extraction times at 323 and 100 K temperatures and the inserts show the kinetics of the cumulated current. At room temperature, both initial and cumulated currents rapidly decrease with the delay time because of the rapid carrier recombination. Kinetics of the cumulated current clearly shows two extraction phases: the fast, lasting for hundreds of ns, and the slow, lasting for several µs. The fast extraction phase rapidly decreases at longer extraction delays and practically disappears at delays longer than 5 µs. While the slow phase remains constant during several µs, therefore gradually becomes dominant, and decays on a time scale of tens of µs. It is reasonable to state that the slow phase corresponds to the extraction of trapped charge carriers, which are weakly affected by the carrier recombination, therefore, survive for tens of microseconds.

Situation drastically changes at low temperatures ($T = 100$ K, see Figure 6b). Photocurrent peaks are sharper at low temperature in agreement with the faster carrier mobility decay. More

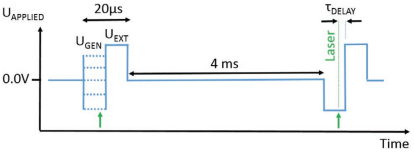

Figure 5. Time chart of the TDCF measurements. Conventional TDFC measurements correspond to $U_{gen} = 0$, while flipped field measurements were performed at $U_{gen} < 0$.

ADVANCED SCIENCE NEWS
www.advancedsciencenews.com

ADVANCED OPTICAL MATERIALS
www.advopticalmat.de

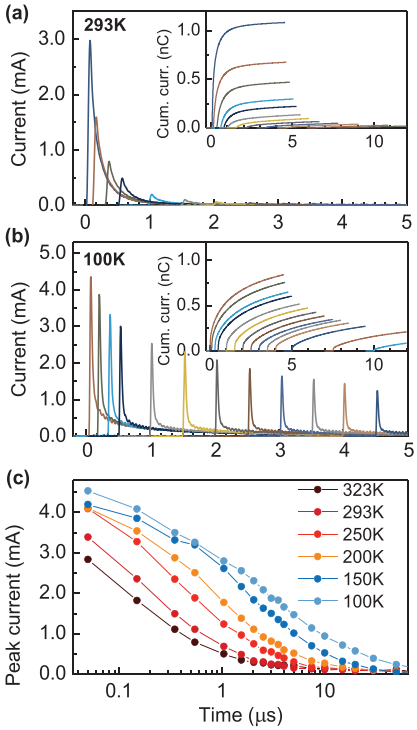

Figure 6. TDCF data obtained with 0 V pre-bias and 2 V and extraction voltages at 15 nJ cm^{-2} excitation intensity. a,b) Carrier extraction kinetics at different extraction pulse delays at 100 and 293 K temperatures. Inserts show the kinetics of cumulated current obtained by integrating the extraction kinetics. c) Dependence of peak extraction current values on extraction delay times at different temperatures.

importantly, peak intensity is less dependent on delay time, indicating that, firstly, the carrier recombination is significantly suppressed, and secondly, mobility does not drop considerably during the waiting time at $T = 100$ K. Kinetics of the cumulated current also shows that despite the strong initial current, only about 20–30% of charge carriers are extracted during the short, intense current pulse; while dominating carrier extraction takes place on a several microseconds time scale. Thus, all processes determining current kinetics such as recombination, mobility decrease and carrier extraction are relatively slow. From this information, an important question arises as which process could cause such a fast extraction current decay? We can resolve this discrepancy by assuming that carrier mobility does not change during waiting time between the carrier generation and application of the electrical extraction pulse, but rapidly decreases once the electric field is applied. In other words, carrier mobility starts to decrease only when charge carriers start to drift under the applied electric field. This behavior suggests that fast mobility decay is caused by energy barriers, which hinder carrier drift, rather than by energy traps. This is expected for the perovskite material composed of small crystalline grains. At low temperature, photogenerated charge carriers are confined within a single grain, and their properties do not change with time, they also do not recombine if they are created within different grains. Under the application of the electric field, charge carriers rapidly drift, but only short distances until they reach the grain boundaries. Figure 4c presenting initial currents as functions of the delay time at different temperatures shows that carrier survival time gradually increases at lower temperatures. Since SRH recombination dominated at the used low excitation intensity, the increasing carrier lifetime at low temperature should be attributed to the decreasing SRH recombination rate. This finding is in agreement with the proposed barrier controlled carrier motion–charge carriers at low temperatures are confined within single perovskite grains and cannot reach trapped carriers at neighboring grains.

To additionally verify the barrier-limited carrier extraction mechanism, we have employed a modified TDCF technique with field flipping as described earlier in ref. [29]. We applied an electrical voltage of variable strength and polarity during the optical excitation and waiting time (pre-bias voltage). **Figure 7** shows the photocurrent kinetics measured with 2 V extraction voltage at various pre-bias voltages and different temperatures. We observe a photocurrent peak immediately after optical excitation determined by the carrier extraction using pre-bias voltage. Application of 2 V extraction voltage causes the appearance of another peak. The second peak is stronger when the pre-bias and extraction voltages are of opposite polarities. This is particularly clear at 100 K temperature–the second peak is weak when the pre-bias and extraction voltages are of the same polarity, and becomes very strong when a high pre-bias voltage of opposite polarity is used. This behavior confirms the spatially confined carrier motion character at lower temperatures. Under the applied electric field, charge carriers rapidly drift, but only for short distances inside perovskite grains until they reach the grain boundaries causing very fast photocurrent decay. When we flip the electric field direction, carriers drift back to the opposite side of the perovskite grain, creating strong current until they reach boundaries again. Importantly, the strong second peak also shows that the carriers are not trapped inside energy traps during the waiting time. By increasing temperature, this behavior becomes less expressed; the intensity of the extraction peak becomes almost independent of the direction of the pre-bias voltage at 323 K. At room temperature, the dependence of the extraction current on the pre-bias voltage is much less pronounced than at 100 K, but stronger than at 323 K. This indicates that charge carriers can surmount energy barriers at room temperature, but the barrier influence on the carrier motion is still significant. We have also performed identical investigations at 150, 200, and 250 K. These data are available in the Supporting Information. The carrier extraction character changes gradually by changing temperature, without

ADVANCED SCIENCE NEWS
www.advancedsciencenews.com

ADVANCED OPTICAL MATERIALS
www.advopticalmat.de

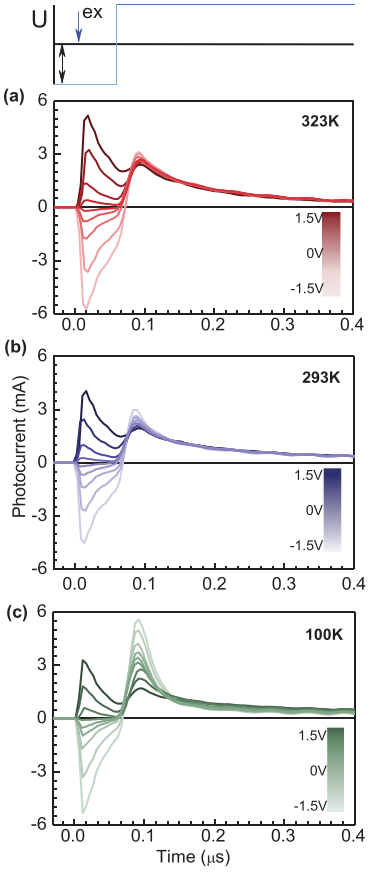

Figure 7. Photocurrent kinetics at three different temperatures obtained by modified TDCF measurements under 15 nJ cm^{-2} excitation intensity when collection voltage of 2 V was applied 60 ns after optical excitation pulse, which was applied under different voltages and polarity pre-bias fields.

more expresses changes by passing 160 K temperature of the tetragonal to orthorhombic phase transition present in MAPI.

We have performed similar TDCF measurements for the state of the art triple cation CsFAMA perovskites and have observed very similar trends in photocurrent kinetics (see Figure S9, Supporting Information). These results confirm that the existence of energy barriers is inherent to perovskite films of polycrystalline structure regardless of their composition.

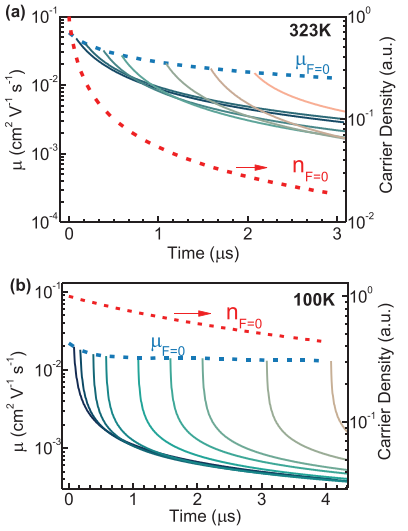

Figure 8. Modelled charge carrier density and their mobility kinetics at a) 323 K and b) 100 K temperatures. Dashed lines show charge carrier density (red) and their mobility (blue) kinetics at zero applied voltage. Solid lines show mobility kinetics after delayed application of collection voltage.

We have modelled the TDCF extraction kinetics measured at zero pre-bias voltage presented in **Figure 8** (the modelling quality is presented in Figure S10, Supporting Information). We numerically solved Equations (2) and (3). Experimental peak current values presented in Figure 6 supported information on the carrier decay at zero applied voltage, i.e., term $kn + \gamma(t)n^2$, while shapes of carrier extraction curves were mainly determined by the time dependence of the carrier mobility. Figure 8 shows the kinetics of major undergoing processes obtained from the modelling results. At 323 K, carrier recombination at a given excitation intensity reduces the carrier density ≈10 times during the first microsecond (red dashed line in Figure 8a). At the same time, the carrier mobility decreases about twice due to carrier trapping at zero applied field (blue line), nevertheless, it additionally decreases few times more due to energy barriers when the charge carriers start to drift under the applied electrical field. The obtained carrier mobility is below 10^{-1} cm^2 V^{-1} s^{-1}. Similar low mobility values were reported for polycrystalline MAPI films.[12–18]

At 100 K temperature and zero applied voltage (Figure 8b), carrier recombination is much slower along with slower mobility decay. Thus, the current under applied electric field decreases mainly due to the presence of barriers, which reduce carrier mobility more than 10 times during hundreds of nanoseconds.

As Figure 1 shows, the scanning electron microscopy (SEM) images of the perovskite films clearly reveal the grain structure.

ADVANCED SCIENCE NEWS
www.advancedsciencenews.com

ADVANCED OPTICAL MATERIALS
www.advopticalmat.de

The grain sizes range from tens to more than a hundred nanometers. Consequently, we can consider that the average barrier-free carrier drift distances are approximately half of this length. Integrated carrier extraction kinetics at low temperature shows that nearly 10% of charge is extracted during the fast extraction phase. Assuming that the extracted charge is proportional to the average carrier drift distance and that extraction of all charge corresponds to the average carrier drift equal to the half of the distance between electrodes (2.5 µm), we obtained barrier-free drift distances of 250 nm, which are slightly larger than the grain sizes. Therefore, it is more likely that not all intergrain interfaces form potential barriers. Charge carriers can probably pass several grains before being trapped by a high energy barrier.

The carrier extraction kinetics is closely identical in the 100–200 K temperature range (see Figure 3b and Figure S8, Supporting Information) indicating that the barriers are too high to be surmounted. Therefore the weak long-lasting photocurrent component shouldn't be attributed to the thermally stimulated processes such as carrier jumps over the potential barriers. The relative contribution of this component increases at the strong electric field indicating the possibility of electric field-assisted carrier tunnelling.

Thus, our results show that barriers play determining role in reducing carrier mobility at low temperatures. However, as follows from Figure 7b, their role at room temperature is also substantial. The presence of barriers explains orders of magnitude lower mobility values obtained for polycrystalline perovskite films than for single crystals and also very low mobility obtained for the lateral carrier motion.

3. Conclusions

Combination of the transient photocurrent and time-delayed collection field techniques along with temperature variation and numerical simulations enabled us to resolve and characterize the main processes determining lateral carrier motion in MAPI hybrid perovskite films. The initial carrier mobility remains insensitive to the temperature, while its decay becomes much faster at 100 K. TDCF investigations showed that potential barriers rather than traps mainly determine the rapid mobility decrease. At room and even elevated temperatures, potential barriers still play an essential role in determining the carrier mobility, diffusion and recombination rate.

Described perovskite properties and charge carrier behavior correspond to the lateral carrier motion. These novel insights are of great importance for devices produced in lateral configurations such as field-effect transistors, lateral photodiodes, photodetectors, and recently suggested lateral solar cells.[29,30] Considering vertical, sandwich-type devices, like typical solar cells or LEDs, where interelectrode distances are comparable with grain sizes, the role of potential barriers is less straightforward. They probably play a less important role for the carrier extraction. Nevertheless, their significance for the recombination processes, governed by diffusion (including in lateral directions) cannot be excluded. Also, they are responsible for the reduced carrier recombination rate compared with carrier mobility,[14] which is a highly important feature enabling high-efficiency solar cell performance.

4. Experimental Section

Substrate: Devices were prepared on commercial Pt interdigitated electrode arrays (ED-IDE3-Pl, Micrux Technologies) with the total area of 9.6 mm^2 formed by 150 nm thick Pt electrodes of 5 µm width and 5 µm interelectrode distances.

Samples: Single-step spin-coating technique,[3] was used for the device preparation. The $CH_3NH_3PbI_3$ perovskite stock solution was prepared by mixing lead iodide (PbI_2) and methylamonium iodide (MAI) in DMSO. The molar ratio of PbI_2:MAI was 1:1. The spin coating was performed with a two-step program: first step, 1000 rpm for 10 s with a ramp of 200 rpm s^{-1}, and second step, 5000 rpm for 30 s with a ramp of 2000 rpm s^{-1}. After sample was heated at 100 °C for 10 min on a hotplate and yielded about 400 nm thick perovskite layer.

Photoluminescence Lifetime Measurements: Photoluminescence decay kinetics were measured using the Edinburgh Instruments time-correlated single photon counting (TCSPC) fluorescence spectrometer F900. The picosecond pulsed diode laser EPL-470 emitting 72 ps pulses at 470 nm with the repetition rate of 500 kHz (interval 2 µs) was used for the sample excitation. The time resolution of the setup was about several hundreds of picoseconds by applying apparatus function deconvolution.

Transient Photocurrent and TDFC Measurements: Transient photocurrent and time delayed collection field investigations were performed with an Agilent Technologies DS05054A oscilloscope using 50 Ω input resistor and a Tektronix AFG 3101 function generator. In order to minimize electric field induced ionic movement very short electrical pulses (10 µs in TPC and 20 µs in TDCF) were used, each followed by 2–4 ms relaxation time at zero applied field. Samples were excited by radiation of the optical parametric amplifier Topas-C (Light Conversion Ltd.) pumped by femtosecond Ti:sapphire laser Integra-C from Quantronix Inc. generating 130 fs duration pulses at 430 Hz repetition rate. Collinear optical parametric amplifier TOPAS-C was used for the generation of the excitation pulse emitting at 500 nm.

Supporting Information

Supporting Information is available from the Wiley Online Library or from the author.

Acknowledgements

R.J. and R.G. contributed equally to this work. Authors acknowledge funding from the European Social Fund according to the activity "Improvement of researchers" qualification by implementing world-class R&D projects' of Measure No. 09.3.3-LMT-K-712-01-0031. The authors thank Dr. Azhar Fakharuddin for valuable discussion.

Conflict of Interest

The authors declare no conflict of interest.

Keywords

energy barriers, hybrid perovskites, mobility, photoluminescence, time-delayed collection field

Received: January 3, 2020
Revised: April 28, 2020
Published online:

[1] M. A. Green, Y. Hishikawa, E. D. Dunlop, D. H. Levi, J. Hohl-Ebinger, M. Yoshita, A. W. Y. Ho-Baillie, *Prog. Photovoltaics* **2019**, *27*, 3.

[2] B. Zhao, S. Bai, V. Kim, R. Lamboll, R. Shivanna, F. Auras, J. M. Richter, L. Yang, L. Dai, M. Alsari, X. J. She, L. Liang, J. Zhang, S. Lilliu, P. Gao, H. J. Snaith, J. Wang, N. C. Greenham, R. H. Friend, D. Di, *Nat. Photonics* **2018**, *12*, 783.
[3] R. Gegevičius, M. Franckevičius, V. Pakštas, R. Augulis, V. Gulbinas, *Phys. Status Solidi A* **2018**, *215*, 1700822.
[4] Y. Chen, H. T. Yi, X. Wu, R. Haroldson, Y. N. Gartstein, Y. I. Rodionov, K. S. Tikhonov, A. Zakhidov, X. Y. Zhu, V. Podzorov, *Nat. Commun.* **2016**, *7*, 12253.
[5] J. H. Noh, S. H. Im, J. H. Heo, T. N. Mandal, S. Il Seok, *Nano Lett.* **2013**, *13*, 1764.
[6] E. T. Hoke, D. J. Slotcavage, E. R. Dohner, A. R. Bowring, H. I. Karunadasa, M. D. McGehee, *Chem. Sci.* **2015**, *6*, 613.
[7] J. M. Ball, A. Petrozza, *Nat. Energy* **2016**, *1*, 16149.
[8] S. G. Motti, D. Meggiolaro, A. J. Barker, E. Mosconi, C. A. R. Perini, J. M. Ball, M. Gandini, M. Kim, F. De Angelis, A. Petrozza, *Nat. Photonics* **2019**, *13*, 532.
[9] D. Shi, V. Adinolfi, R. Comin, M. Yuan, E. Alarousu, A. Buin, Y. Chen, S. Hoogland, A. Rothenberger, K. Katsiev, Y. Losovyj, X. Zhang, P. A. Dowben, O. F. Mohammed, E. H. Sargent, O. M. Bakr, *Science* **2015**, *347*, 519.
[10] T. Leijtens, G. E. Eperon, A. J. Barker, G. Grancini, W. Zhang, J. M. Ball, A. R. S. Kandada, H. J. Snaith, A. Petrozza, *Energy Environ. Sci.* **2016**, *9*, 3472.
[11] S. D. Stranks, V. M. Burlakov, T. Leijtens, J. M. Ball, A. Goriely, H. J. Snaith, *Phys. Rev. Appl.* **2014**, *2*, 034007.
[12] T. M. Brenner, D. A. Egger, L. Kronik, G. Hodes, D. Cahen, *Nat. Rev. Mater.* **2016**, *1*, 15007.
[13] C. C. Stoumpos, C. D. Malliakas, M. G. Kanatzidis, *Inorg. Chem.* **2013**, *52*, 9019.
[14] C. Wehrenfennig, G. E. Eperon, M. B. Johnston, H. J. Snaith, L. M. Herz, *Adv. Mater.* **2014**, *26*, 1584.
[15] B. Maynard, Q. Long, E. A. Schiff, M. Yang, K. Zhu, R. Kottokkaran, H. Abbas, V. L. Dalal, *Appl. Phys. Lett.* **2016**, *108*, 173505.
[16] N. Ahn, D. Y. Son, I. H. Jang, S. M. Kang, M. Choi, N. G. Park, *J. Am. Chem. Soc.* **2015**, *137*, 8696.
[17] Y. Chen, J. Peng, D. Su, X. Chen, Z. Liang, *ACS Appl. Mater. Interfaces* **2015**, *7*, 4471.
[18] C. S. Ponseca, P. Chábera, J. Uhlig, P. Persson, V. Sundström, *Chem. Rev.* **2017**, *117*, 10940.
[19] L. M. Herz, *ACS Energy Lett.* **2017**, *2*, 1539.
[20] D. Cahen, G. Hodes, Y. Rosenwaks, K. Gartsman, S. Mukhopadhyay, A. Henning, S. Kirmayer, E. Edri, *Nano Lett.* **2014**, *14*, 1000.
[21] J. S. Yun, A. Ho-baillie, S. Huang, S. H. Woo, Y. Heo, J. Seidel, F. Huang, Y. Cheng, M. A. Green, *J. Phys. Chem. Lett.* **2015**, *6*, 875.
[22] J.-J. Li, J.-Y. Ma, Q.-Q. Ge, J.-S. Hu, D. Wang, L.-J. Wan, *ACS Appl. Mater. Interfaces* **2015**, *7*, 28518.
[23] M. B. Johnston, L. M. Herz, *Acc. Chem. Res.* **2016**, *49*, 146.
[24] F. Staub, H. Hempel, J. C. Hebig, J. Mock, U. W. Paetzold, U. Rau, T. Unold, T. Kirchartz, *Phys. Rev. Appl.* **2016**, *6*, 044017.
[25] J. M. Richter, M. Abdi-Jalebi, A. Sadhanala, M. Tabachnyk, J. P. H. Rivett, L. M. Pazos-Outón, K. C. Gödel, M. Price, F. Deschler, R. H. Friend, *Nat. Commun.* **2016**, *7*, 13941.
[26] L. M. Pazos-Outón, M. Szumilo, R. Lamboll, J. M. Richter, M. Crespo-Quesada, M. Abdi-Jalebi, H. J. Beeson, M. Vrućinić, M. Alsari, H. J. Snaith, B. Ehrler, R. H. Friend, F. Deschler, *Science* **2016**, *351*, 1430.
[27] A. Devizis, K. Meerholz, D. Hertel, V. Gulbinas, *Phys. Rev. B* **2010**, *82*, 155204.
[28] R. Augulis, M. Franckevičius, V. Abramavičius, D. Abramavičius, S. M. Zakeeruddin, M. Grätzel, V. Gulbinas, *Adv. Energy Mater.* **2017**, *7*, 1700405.
[29] R. Jasiūnas, A. Melianas, Y. Xia, N. Felekidis, V. Gulbinas, M. Kemerink, *Adv. Electron. Mater.* **2018**, *4*, 1800144.
[30] Y. Yuan, T. Li, Q. Wang, J. Xing, A. Gruverman, J. Huang, *Sci. Adv.* **2017**, *3*, 1602164.

EurJIC
European Journal of Inorganic Chemistry

Minireviews
doi.org/10.1002/ejic.202100360

Check for updates
European Chemical Societies Publishing

The Role of Grain Boundaries in Charge Carrier Dynamics in Polycrystalline Metal Halide Perovskites

Rokas Gegevičius,[a] Marius Franckevičius,*[a] and Vidmantas Gulbinas[a]

Boundaries of perovskite grains forming polycrystalline films are the most sensitive place for the formation of the defect states and accumulation of impurities. The intra-bandgap states located at the boundaries forming traps for charge carriers are commonly discussed as causing nonradiative carrier recombination and reducing carrier mobility. Grain boundaries (GB) may also disturb carrier motion by creating scattering centres and barriers, however, their role was less frequently considered. On the other hand, grain boundaries may also facilitate the splitting of exciton states and the generation of free charge carriers. Consequently, the grain boundaries are responsible or affect a wide range of perovskite properties and processes strongly influencing the performance of perovskite-based optoelectronic devices. Nevertheless, abundant literature data related to the properties of grain boundaries and their influence are highly controversial. In this minireview, we discuss the most importnat literature data related to the structure and properties of grain boundaries and their role in device performance.

1. Introduction

Unprecedented success in the development of perovskite solar cells also stimulated attempts to apply metal halide perovskite for other devices, such as light-emitting diodes or light detectors. Significant achievements were reported in these areas as well. Although it is possible to grow perovskite crystals with dimensions up to several centimeters, however, the application of single crystals is less attractive, because single crystal-based devices shall compete with a much more mature classical semiconductor technology. Perovskites are manly attractive due to the possibility to form thin films using relatively simple and cheap solution-based technology. It enables the fabrication of large-area devices particularly important for solar cells, displays and lighting applications. Therefore, by application areas and fabrication technologies, perovskites should be considered as competitors for organic electronics. However, the physical properties of organic materials and perovskites are significantly different. Technologically, it is relatively easy to fabricate fine, homogeneous amorphous organic films. On the other hand, perovskites are crystalline materials, and the fabrication of fine polycrystalline films is a challenging task very sensitive to formation technologies. Moreover, this task is even contradictive, since smaller surface roughness, lower pinhole probability is easier achievable with smaller crystallites, however then perovskite partly loses advantages of crystalline material.

The crystallinity of perovskites causes the formation of delocalized charge carrier wavefunctions and, thus, high carrier mobility, which in single crystals reaches values up to about 1000 cm^2/Vs, typical for classical crystalline semiconductors. Carrier mobility is a very important parameter of all electronic materials, and relatively high mobility values are partly responsible for the great success of the perovskites. However, the mobility drastically decreases in polycrystalline films. Delocalized states break at grain boundaries (GBs) and localized states with different energies are formed. At least three factors may be responsible for the mobility decrease: a) carrier traps created in the bulk of crystallites and at their surfaces, b) potential barriers for the motion of carriers created by the GBs, c) uneven energy landscape. Moreover, the mobility in such heterogeneous materials becomes a "bad" parameter, which depends on the carrier drift or diffusion distance, time, measurement technique. Therefore, actual mobilities may be different in different devices. For example, actual carrier mobility in tens of nanometres thick film of perovskite LED, containing single crystallites stretching over the total film thickness may be very different from actual mobilities in hundreds of nanometres thick solar cell films composed of crystallites stacked on top of each other, or particularly in devices with lateral carrier motion such as lateral photodetectors or field effect-transistors. GBs in the latter case may play a major role in carrier motion.

GBs are also considered as the most likely places for the formation of defect states, which may act as carrier traps or scattering centres. Indeed, it is commonly believed that most of the imperfections in solution-processed perovskite films are mainly located at the GBs[1,2] since trap densities in solution-processed polycrystalline $MAPbI_3$ perovskite films (10^{16}–10^{17} cm^{-3}) is much higher compared to the single crystals (10^{9}–10^{10} cm^{-3}).[2–4] Charge carriers may be trapped reaching GBs and even recombine through the Shockley-Read-Hall (SRH) mechanism. On the other hand, charge carrier energies on localized boundary positions may be higher, thus boundaries may create barriers for one or both types of carriers. Consequently, GBs may be important by determining or at least influencing several core processes in perovskite-based devices: nonradiative carrier

[a] R. Gegevičius, Dr. M. Franckevičius, Prof. V. Gulbinas
Department of Molecular Compound Physics
Center for Physical Sciences and Technology
Saulėtekio ave. 3, LT-10257 Vilnius, Lithuania
E-mail: marius.franckevicius@ftmc.lt

Part of the joint "Perovskite Materials and Devices" Special Collection with ChemPlusChem.

EurJIC
European Journal of Inorganic Chemistry

Minireviews
doi.org/10.1002/ejic.202100360

Chemistry Europe
European Chemical Societies Publishing

recombination, radiative carrier recombination, carrier diffusion and drift.

In this minireview, we discuss experimental and theoretical data reported in the literature related to the chemical and physical properties of perovskite grain boundaries, formation of boundary-related electronic states and discuss their role in carrier mobility, diffusion and recombination as well as their influence on the device performance. We mainly focuss on metal halide perovskites used as active materials is solar cells, near IR detectors and PeLEDs. We do not touch quasy-two-dimensional perovskite structures, which have very distinctive properties.

2. Chemical structure and physical properties of the grain boundaries

Metal halide perovskites are ionic compounds with a high ionic character of the constitutive bonds and low formation energies. The lack of stoichiometric compositions at the surfaces of perovskite grains and the sublimation of organic molecules during the thermal annealing of the film makes these interfaces as a storage for both impurities and structural defects that accumulate there from the grain during growth and presents a more complicated chemical environment. Figure 1a and Figure 1b respectively show SEM and TEM images of the perovskite films revealing GBs[5] and Figure 1b demonstrates simulated structures of pristine $MAPbI_3$ and its GB.[6]

The sublimation of organic molecules and halides in the preparation process can leave uncoordinated ions such as Pb^{2+} or I^- at the perovskite grain boundaries. The uncoordinated ions depending on their nature can accept electrons or donate free electron pair for dative bond formation. Various other point defects, such as methylammonium (MA) or I vacancies, Pb or I clusters, Pb–I antisite defects, can induce additional structural

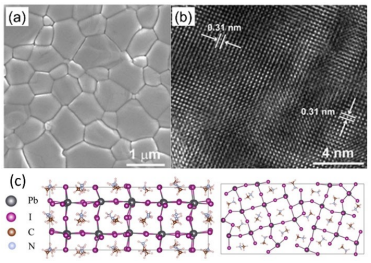

Figure 1. Experimental SEM (a) and TEM (b) pictures of $MAPbI_3$ thin film revealing grain boundaries and (c) simulated structure of pristine $MAPbI_3$ and its GB. Reproduced from Xiao et al.[5] and Wang et al.[6] Copyright (2019), with permission from the American Chemical Society.

disorder which opens a possibility for unpaired valence electrons to exist at the surface, considered as dangling bonds. Additionally, these unpaired electrons can form non-covalent wrong bonds, like cation-cation or anion-anion bonds, that are electrically active and can induce disorder.[7] The defect state energies may be located within conduction or valence bands, as well as within the energy bandgap. In the former case, the defects form carrier scattering centres, while in the latter case they act as traps for charge carriers.

In the computational study of GBs of $MAPbI_3$, Shan and Saidi demonstrated that most of the point defects segregate from the bulk to the GB region under all synthesis conditions.[8] Such segregation in some cases may be even useful since it reduces the amount of impurity in the crystallite leading to increased film quality.[9] Defects that are stable in the bulk

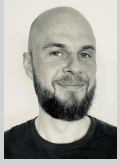

Rokas Gegevičius is currently a PhD student at prof. Vidmantas Gulbinas group at Center for Physical Sciences and Technolgy, where his main focus is on charge carrier transfer mechanisms in hybrid perovskite optoelectronic devices. He obtained his MSc. Degree in Physics with honors from Vilnius University and was awarded by Lithuanian Academy of Science for the best student scientific work in 2018.

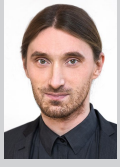

Dr. Marius Franckevičius received his PhD in 2011 from Vilnius University. He spent one year in Ecole Polytechnique Fédérale de Lausanne (EPFL) as a postdoctoral researcher in the Laboratory of Photonic and Interfaces. Currently, he is a Senior Research Scientist at the Center for Physical Sciences and Technology (FTMC) in Vilnius. His research interests are mainly focused on fabrication and physical characterization of thin film optoelectronic devices.

Prof. Vidmantas Gulbinas graduated from Vilnius University faculty of physics in 1980. Later worked in Instutute of Physics in Vilnius and received his Ph.D. in experimental physics in 1988. Currently he leads the department of Molecular Compounds Physics of the Center for Physical Sciences and Technolgy in Vilnius, Lithuania and is professor of Vilnius University. His main research activities are on development of ultrafast spectroscopic techniques and investigation of ultrafast optically induced processes in molecular solutions, aggregates and solids. Currently, he mainly concentrates on exciton and charge carrier dynamics in organic and hybrid photoconductors including perovskites and in their devices. He is coauthor of more than 180 papers.

EurJIC
European Journal of Inorganic Chemistry

Minireviews
doi.org/10.1002/ejic.202100360

Chemistry Europe
European Chemical Societies Publishing

normally have low formation energies in the GB region also. Some defects which are unstable in the bulk, such as MA_i and Pb_i, become stabilized in the GB region. Under I^- rich synthesis conditions, two detrimental defects MA_i and Pb_i have low formation energies respectively in the bulk and Σ5-(210) GB regions. MA_i is also a metastable defect in the bulk under moderate synthesis conditions. Both of these defects create trap states deep within bandgap and, thus, can act as SRH non-radiative recombination centres that can harm the performance of the devices. Other deep-level defects in polycrystalline $MAPbI_3$ were confirmed not to be energetically favourable.[8] Recently, Motti et al. have made similar conclusions that defects with low formation energies such as V_{MA} and V_I, create only shallow energy levels, while some defects with higher formation energies such as halide interstitials I_i and Br_i, and Pb vacancies contribute to deep energy levels in the bandgap.[10]

Yin et al.[11] investigated the impact of structural disorders at GBs on electronic quality of perovskite materials and concluded that Pb–Pb wrong bonds in both Σ3-(111) and Σ5-(310) GBs do not form subgap states due to relatively large distance between two Pb^{2+} cations. However, the wrong bonds in GBs still may form shallow defect states. Unpaired electrons may lead to unstructured crystallites, which distort crystal lattice varying from small distortion points to a completely broken surface of a crystallite.[11] Yan's group also argues that GBs in $MAPbI_3$ perovskite do not create deep midgap levels and GB-induced defect state in Σ5-(310) is close to the valence band maximum, and, thus, acts as a shallow trap.[12,13] This was also confirmed that GB defects have little to no effect on the band structure in all-inorganic perovskites as well.[14] Additionally, Wang et al.[7] performed time-domain ab Initio NAMD simulation of the non-radiative electron-hole recombination in $MAPbI_3$ with a Σ5-(310) GB and found that $MAPbI_3$ perovskite, due to the relatively soft structure, can rearrange and heal unsaturated chemical bonds created in GB regions, thus it does not necessarily accelerate charge carrier recombination. This study also confirmed that most of the defects in the GBs create only shallow trap states and charges can escape from these traps back to delocalized bands and continue long-distance transport. Charge separation by shallow traps was also suggested to be responsible for slow charge carrier recombination in perovskite.[6] All these segregated native point defects near grain boundary may also become electrically charged forming an electrostatic potential barrier for carrier transport between two crystallites, thus significantly reducing their effective mobility as well as photocurrent in the devices.[15,16] On the other hand, Liu et al., based on density functional theory, estimated that charged grain walls may reduce the bandgap by 20–40%, while uncharged walls have no substantial impact on the bandgap.[9]

3. Effective methods to control the defects in perovskite films

Uncoordinated ions present at the surfaces of perovskite grains may be at least partly passivated using simple Lewis acid-base chemistry. Lewis base interacts with uncoordinated Pb^{2+} or Pb clusters by donating an electron pair and forming a new dative bond. Fullerene derivatives like C_{60}, PCBM, ICBM may act as Lewis acids. For example, it was demonstrated that PCBM can be a highly effective passivation agent acting on uncoordinated I^- and antisite PbI^{3-} and can passivate both shallow and deep traps.[17] Other important Levis acids such as IPFP, TPFP or ICBA were also reported as efficient trap passivation compounds.[18,19] Some organic molecules with heteroatoms, like nitrogen or sulphur, also act as Lewis bases and can passivate perovskite defects. It was demonstrated that phenylethylammonium PEA^+ is exceptionally good for suppressing trap induced recombination at the surface and grain boundaries.[20] Some other organic molecules, such as derivatives of pyridine, thiophene and some amines, were demonstrated to be able to reduce nonradiative recombination and greatly improve charge carrier lifetimes.[21,22] Due to the charged nature of perovskite defects, ionic compounds can also be successfully used for passivation. Some metal ions, like sodium Na^+ potassium K^+, copper Cu^+, silver Ag^+, and rubidium Rb^+, can significantly reduce the defect density in the GBs interacting with anionic defects, such as uncoordinated I^-, antisite PbI_3^-, and MA^+ vacancies.[23] Chloride Cl^- and iodide I^- were shown to be effective as anionic passivation agents also.[24] Zwitterions - molecules that have both positive and negative charges - were also proved to be effective passivators. Zwitterions like L-α-phosphatidylcholine, choline chloride, choline iodide were active towards anionic Pb–I antisites and cationic Pb clusters and were capable to simultaneously passivate negatively and positively charged ionic defects.[25] There are also reports that controlled exposure of perovskites to oxygen and moisture during their manufacturing process leads to a reduction of specific trap states.[26,27] Another way of thinking to suppress the negative effects of grain boundaries is to enlarge perovskite grains. In polycrystalline films, the grain sizes depend on the crystallization rate. An effective method to control the crystallization rate is to perform thermal annealing under a solvent vapour atmosphere.[28] PbI_2 and MAI/FAI are highly soluble in DMF/DMSO leading to longer diffusion distance in wet solutions, providing slower crystallization and enlarged grain sizes up to 1 and 5 μm for $MAPbI_3$ and $FAPbI_3$ respectively.[29,30] Solvent annealed devices exhibit longer carrier lifetimes suggesting reduced defect concentrations. Pyridine, mentioned earlier as Lewis base passivator, was also used during the annealing process, resulting in $MAPbI_3$ films with a grain size up to 5 μm.[31] On the other hand, the solution-based hot-casting technique proved to be more efficient to fabricate high-quality films with millimetre-scale grains. The perovskite films made by this method exhibit significantly reduced defect concentrations and improved charge carrier mobility.[32]

To get a better grasp on all available passivation techniques and their acting mechanisms available for metal halide perovskites, we refer to very informative and thorough reviews given by Bo Chen et al.[33] and Wang et al.[34]

EurJIC
European Journal of Inorganic Chemistry

Minireviews
doi.org/10.1002/ejic.202100360

Chemistry Europe
European Chemical Societies Publishing

4. Electronic properties of grain boundaries and their role in carrier recombination

Polycrystalline solution-processed perovskite films often posess low photoluminescence (PL) quantum efficiencies (PLQE), of about tens of percent only. However, the PLQE, as well as PL lifetimes strongly vary depending on perovskite composition, fabrication procedures and postfabrication treatment enabling to reach PLQE of lead halide perovskites approaching 100%.[35–37] It indicates that intrinsic (unpassivated) perovskite films have significant nonradiative recombination losses, which are mainly caused by the Schocley-Read-Hall process when one of the carriers is trapped at the defect site and eventually recombines with the opposite carrier. These properties indicate that solution-processed perovskite films tend to posess high density of defect sites, which are typically straightforwardly attributed to the GBs, surfaces and interfaces,[35,38] athouth conventional PL spectroscopy gives only indirect evidences for this attribution.

Photoluminescence lifetime microscopy is a more powerfull tool to visualize and address electronic properties of GBs. Indeed, the GBs typically appeared as dark regions in the images (see Figure 2a), however interpretation of this information is controversial. deQuilettes et. al.[39] interpreted that 65% lower PL intensity at the GBs as an indication of higher defect concentration and stronger non-radiative recombination at GBs. These conclusions were in line with the above-discussed accumulation of impurities and structural defects at GBs. However, experiments with time-resolved photoluminescence imaging provided more controversial information and its interpretation. Tian et al. reported that the local carrier lifetimes are uniform across GBs and interior.[40] Later, Yang et al. also observed that PL lifetimes at GBs are similar or even longer than in the grain interior (see Figure 2a), and attributed the reduced PL intensity to the carrier diffusion away from the GBs forming a potential barrier.[41] Ciesielski et al. came to a similar conclusion based on the observation that areas close to the GBs showed more intense luminescence and slower initial PL decay because of the carrier reflection from GBs.[42] Yun et al.[43] performed photocurrent mapping of $MAPbI_3$ film by using c-AFM and observed higher current collection near GBs (see Figure 2b), which was attributed to more efficient carrier separation and transport along the GBs, and to downward band bending.

A more direct experimental information on the electrical properties of GBs was obtained by using the Kelvin probe force microscopy (KPFM). By measuring contact potential difference (CPD) across the grain boundaries, Edri et al. observed an upward band banding by about 40 meV suggesting that the grain boundaries created a small potential barrier.[44] Chen et al. attributed the band banding to the presence of PbI_3 at the grain surfaces, which form during the film annealing. They argue that PbI_3 having a large bandgap forms type I heterojunction with perovskite grain bulk creating a barrier both for electrons and holes.[33] On the other hand, KPFM investigations performed by Li et al. revealed the downward band bending at

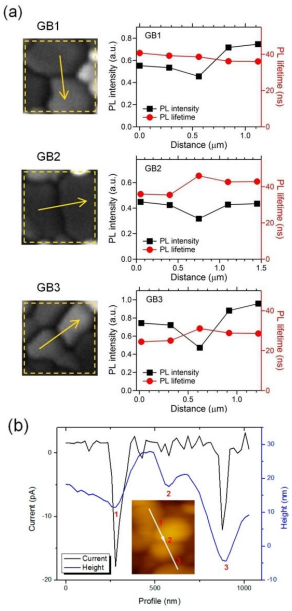

Figure 2. (a) Dark grain boundaries of $MAPbI_3$ in PL measurements and boundary potential obtained by Kelvin probe and (b) conductive-AFM height line profiles (blue) and current at illumination (black) measured for $MAPbI_3$ film. Reproduced from Yun et al.[42] Copyright (2015), with permission from the American Chemical Society and Yang et al.[41] Copyright (2017), with permission from The Royal Chemical Society.

GBs suggesting that GBs attract electrons while creating a barrier for holes.[45] Consequently, KPFM investigations suggest the formation of barriers at GBs for both or one type of charge carriers, however, they are controversial regarding the carrier type. Concerning the role of the GBs in the nonradiative carrier recombination, the contradictive literature data may be also considered as an indication that the properties of GBs may be significantly different depending e.g. if the GBs represent only structural defects, probably creating extended two-dimensional barriers, or they also contain some impurities forming localized trap states.

5. Carrier mobility and diffusion

Conceptions of charge carrier transport in semiconducting materials have been formulated at the end of the 20th century

EurJIC
European Journal of Inorganic Chemistry

Minireviews
doi.org/10.1002/ejic.202100360

Chemistry Europe
European Chemical Societies Publishing

mainly based on investigations of silicon. Electron mobility in bulk silicon reaches about 1400 cm^2/Vs at room temperature,[46] and decreases with temperature.[47] Such temperature dependence was attributed to the carrier scattering by impurities and phonons. Although carrier mobility in single-crystalline $MAPbI_3$ perovskite is somewhat lower, it also decreases with temperature[48] as in conventional semiconductors. Biewald et al. have recently reported that the mobility within a thin film measured in individual large crystal grains of $MAPbI_3$ decreases with temperature as $\mu \propto T^{(-1.8\pm0.1)}$ for tetragonal phase, which was attributed to the carrier scattering by lattice fluctuations and optical phonons.[49] Consequently, these properties show that charge carriers in crystalline single perovskite grains may be considered as delocalized quasi-particles characterized by wave-like motion. According to Sung et al., their motion during the initial 20 fs after photogeneration may be considered as ballistic propagation of coherent wavepackets.[50] Reported room temperature mobility values for single crystals of $MAPbI_3$ range from tens[49,51,58] to more than a hundred[48,53] of cm^2/Vs. Carrier mobility and diffusion coefficient for crystalline semiconductors are considered being interrelated by Einstein relation, thus diffusion coefficient ranges between about 0.1 and several cm^2/s. Despite these relatively modest diffusion coefficient values, very large carrier diffusion length extending hundreds of μm were reported[52,54] attributing them to very long carrier lifetimes reaching hundreds of microseconds at low excitation intensities.

Carrier motion in polycrystalline perovskites is more controversial. The complexity is caused by the interplay of two processes: carrier motion inside monocrystalline perovskite grains and crossing grain boundaries. Such motion character, typical for all polycrystalline semiconductors, has been widely investigated for polycrystalline silicon, which showed increased carrier mobility with temperature indicating thermally activated transport[15,55] Although the morphology of polycrystalline perovskites closely resembles that of classical polycrystalline semiconductors, conceptual understanding and theoretical description of their transport properties still lag far behind. Experimental investigations reported lower carrier mobilities in polycrystalline perovskites in comparison with single crystals, however, this difference is not so clear, mainly because of a very broad distribution of reported values. For example, reported mobilities for $MAPbI_3$ are distributed between less than 10^{-3} and more than 10 cm^2/Vs. Importantly, in contrast with polysilicon, the majority of investigations of the solution-processed polycrystalline perovskite films showed decreasing mobility with temperature[56–59] indicating a band-like transport, like in single crystals. On the other hand, increasing with temperature carrier mobility was also reported[60,61] suggesting thermally activated hopping character, like in polysilicon.

The reported tremendous differences in carrier mobilities and their motion character in perovskites may be partly caused by the differences between polycrystalline samples. Grain sizes and properties of the grain boundaries may significantly vary depending on preparation and treatment conditions. Investigation technique is another and probably even more important factor. Different techniques evaluate carrier mobility by probing different aspects of carrier motion. The most obvious cause of these differences is the difference between the so-coaled microscopic and macroscopic mobilities. Some techniques like Thz wave attenuation probe carrier motion at short distances, perhaps in some cases inside single grains, therefore the obtained mobility values may be close to those obtained for single crystals. While other techniques, like time-of-flight (TOF) or charge extraction by linearly increasing voltage (CELIV) probe carrier transport at much longer distances when carriers meet GBs and their motion is mainly determined by the boundary-crossing time rather than by intragrain mobility. These problems have been comprehensively discussed in the recent review by Peng et al.[62] They demonstrated a clear correlation between reported mobility value and probing time-scale of the used investigation technique. For example, the mobility values reported for $MAPbI_xCl_{3-x}$ films decrease from tens to 10^{-3}–10^{-4} cm^2/Vs when the probing time-scale increases from sub-picoseconds to nanoseconds. This, although, indirect information points to the importance of carrier traps and barriers, however is insufficient to make a decision, which of them plays a decisive role.

Important information about the role of GBs in carrier transport has been obtained using photoluminescence microscopy with spatial resolution better than the perovskite grain size. These investigations revealed a very strong variation between PL intensities of different perovskite grains.[39–42,49,63] These results evidenced restricted charge carrier diffusion between grains indicating that majority of charge carriers remain confined inside grains where they were generated, and their PL intensities are determined by nonradiative recombination processes inside individual grains. Confocal microscopy allowing spatially separated excitation and PL detection revealed absence or only weak PL intensity outside directly excited grain, which was considered as an evidence that no diffusive transport occurs across grain boundaries,[41,42] or grain boundaries exhibit limited and varying opacity to carrier transport depending on their connectivity.[39]

Since PL intensity is proportional to the product of the electron and hole densities, the reduced PL intensity outside directly excited grain may be caused by the reduced density of both or only one type of charge carriers. Thus, they provide no information if grain boundaries create barriers for one or both types of carriers. Snaider et al. attempted to fill this information gap by using transient absorption microscopy (TAM).[64] In contrast to PL microscopy, which probes only radiative carrier recombination, TAM probes the presence of all charge carriers. They concluded that the grain boundaries in polycrystalline $MAPbI_3$ films only slow down the carrier transport, still allowing carrier diffusion over multiple grains during several nanoseconds. Therefore, grain boundaries only twice reduce the carrier diffusion rate in films with micrometer size grains. Combining information provided by TAM and above described PL microscopy investigations revealing much lower grain boundary transmittance, we may conclude that grain boundaries create different barriers for different charge carrier types, therefore one type of charge carriers diffuse easier through the

EurJIC
European Journal of Inorganic Chemistry

Minireviews
doi.org/10.1002/ejic.202100360

Chemistry Europe
European Chemical Societies Publishing

grain boundaries, however producing no PL in perovskite area separated by GB.

We have recently addressed the boundary transmittance by using a modified time-delayed collection field technique.[16] The perovskite film was formed on the interdigitated comb of electrodes with an interelectrode distance of 5 μm. The perovskite film was excited by a short optical pulse under applied voltage. Charge carriers drifted with decreasing average speed because a fraction of charge carriers were stopped by reaching intergrain barriers. After a variable delay time, a voltage direction was flipped to the opposite and, as Figure 3 shows, a current pulse was observed again because suspended carriers started to move freely to the opposite direction. The opposite current pulse was only weak at room temperature indicating that only a small fraction of charge carriers have been "collected" by barriers in agreement with the conclusion of Snaider et al. that GBs only reduce carrier diffusion rate.[65] However, at a reduced temperature of 100 K, the initial photocurrent decayed rapidly and the amplitude of the opposite pulse almost reached that of the current pulse observed initially after photoexcitation. It indicated that the movement of the majority of photogenerated charge carriers of both types was suppressed by intergrain barriers. Another very important finding of these investigations is that the charge carriers were not trapped at the grain boundaries.

6. Effects of grain boundaries on the performance of solar cells, detectors, and LEDs

The debate on the role of grain boundaries in polycrystalline perovskite solar cells is still ongoing in the scientific community,[7,65] where both positive[66] and negative[67] effects in optoelectronic devices have been demonstrated. Nonradiative recombination is one of the main charge carrier loss channels that limits the performance parameters of the perovskite-based optoelectronic devices. Therefore high PLQY and long PL lifetimes are oftern considered as an indicator of the perovskite quality.[35] Thus, the efforts on reducing defect density towards obtaining high-performance perovskite devices has been an important research subject.[68]

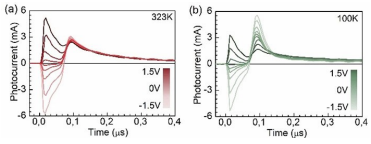

Figure 3. Transient photocurrent kinetics obtained at different temperatures using TDCF technique with flipped collection voltage for the $MAPbI_3$ film formed at interdigitate electrodes. The sample was optically excited at variable pre-bias voltages and a collection voltage of 2 V was applied 60 ns after the optical excitation pulse. Reproduced from Jasiūnas et al.[16]

Some studies reported that the GBs are beneficial for the efficient charge carrier separation, collection and local current flow,[43,69,70] which should be valuable for the perovskite-based devices. On the other hand, other studies conclude that GBs are detrimental, because contribute to nonradiative recombination losses and reduce device performance parameters.[63,71,72] The passivation of GBs is one of the most widely used strategies to reduce charge carrier loss channels essential for high-performance devices, especially open-circuit voltage.[73–78] Apart from grain passivation, alternative approaches were suggested to tune the grain sizes and to reduce the role of grain boundaries.[32,79,80] Regardless of the used strategy, the high-quality perovskite layers with increased grain sizes and reduced defect density at the GBs are a prerequisite for the high-performance solar cells and photodetectors.[68] The typical average grain sizes of polycrystalline perovskite materials used for solar cell applications vary from hundreds of nanometres to several millimetres. Nie et al.[32] noticed an obvious increase in V_{oc} from 0.4 V to 0.94 V and in fill factor from 0.4 to 0.83 with increasing grain size up to millimetre scale. This improvement was attributed to the reduced defect-assisted recombination, where recombination losses were suppressed from 40% for low-grain devices to only 5% for devices containing large grains. A more recent study by Yang et al.[71] showed that GdF3–aminobutanol-assisted Ostwald ripening used for the formation of perovskite films improved the quality of perovskite films mainly due to enlargement of the crystal grains and reduced density of vacancies. The treated perovskite films had higher PL efficiency and slightly blue-shifted spectra, which is mainly due to suppressed trap-assisted non-radiative recombination. The improved perovskite quality resulted in an increase in the power conversion efficiency of the solar cells from 18.1% to 21.21%.[71] Similar experimental evidence was also reported for $CsPbI_2Br$ perovskite solar cells.[81] The authors found that the quality of the perovskite layer depends on the temperature of the substrate used for the film deposition. The hot casting resulted in compact and pinhole-free perovskite films with large grain sizes and significantly reduced nonradiative recombination. As a consequence, hot-casted $CsPbI_2Br$ perovskite-based solar cells exhibited dramatically increased performance, mainly due to low nonradiative recombination. Recently Chen et. al.[82] demonstrated that application of the gas pumping method instead of antisolvent method enables formation of perrovskite layers without horizontal GBs. They suggest that the single grains extending through the entire layer thickness enable better carrier collection efficiency and, thus better device efficiency and reproducibility.

The large grains with low density of grain boundaries are also beneficial for perovskite photodetectors.[83,84] The conventional perovskite-based photodetectors typically employ either lateral (planar) or vertical geometries. In the vertical type devices, the interelectrode distance is small, thus vertical charge carrier transport is mainly limited by contact layers. Due to preferential orientation of grain boundaries,[85,86] this configuration enables devices with high-performance parameters especially response time and high sensitivity. In the lateral configuration devices, the spacing between electrodes is orders

EurJIC
European Journal of Inorganic Chemistry

Minireviews
doi.org/10.1002/ejic.202100360

Chemistry Europe
European Chemical Societies Publishing

of magnitude larger than in vertical ones, thus due to large travel distances, the carriers additionally experience strong scattering at the GBs thereby limiting their diffusion and increasing recombination probability. We have recently demonstrated that by improving the quality of perovskite film, it is possible to achieve photodetector of planar configuration with a response time below 1 ms, and high responsivity of 8.1 A/W.[87] More recently, Hasan et al. has demonstrated that the responsivity of the lateral photoconductors can achieve up to 79.4 A/W.[88] This achievement is mainly due to application meniscus-guided blade coating technique enabling to to grow thin films of oriented high-quality crystals possessing a low concentration of GBs, reduced density of recombination centres and lower lateral resistance compared to spin-coated polycrystalline films. While photodetectors based on perovskite single crystals, thus possessing no GBs, demonstrate additional orders of magnitude improvement of the sensitivity and speed parameters.[89,90]

Though the long charge carrier diffusion lengths for both electrons and holes are of great importance for perovskite solar cells and photodetectors, it is, however, undesirable for perovskite LEDs giving rise to low PLQYs, the criterion which is important for high-efficiency LEDs.[91] Thus, the strategies associated with the grain size increase are appropriate only for perovskite solar cells and photodetectors. On the contrary, to achieve high-performance LEDs, the perovskite surface should be smooth and composed of nanometer-sized small grains.[92–94] The small grains ensure spatial confinement of the electron-hole pairs and having increased exciton binding energies suppresses non-geminate recombination.[92,95] It has been demonstrated that perovskite films composed of small nanocrystals can achieve internal photoluminescence quantum yields up to 90% which is necessary for high-performance LEDs.[96,97] Back in 2015 Chao et al. reported green perovskite LEDs with an external quantum efficiency (EQE) of 8.53% composed of around 100 nm-sized $MAPbBr_3$ perovskite nanograins.[98] Whereas two years later, Xiao et al. presented $MAPbI_3$ and $MAPbBr_3$ based perovskite LEDs with nanocrystal sizes approaching 10 nm and film roughness of less than 1 nm that operated with EQE of 10.4 and 9.3%, respectively.[93] These studies reveal a clear correlation between crystal size decrease and performance parameters of LEDs. On the other hand, the grains should not be too small because the enlarged surface area of the grain boundaries may serve as emission quenching centres. To avoid defect induced PL quenching and to improve device performance, the passivation of perovskite films with various additives or self-passivation is performed.[99,100] Very recently Kim et all. simultaneously resolved both challenges using a one-dopant alloying strategy.[97] They found that the introduction of a small amount of guanidinium into conventional formamidinium-based perovskite nanocrystals leads to the formation of smaller perovskite nanocrystals with a higher degree of confinement. Additionally, they used a surface-stabilizing agent namely 1,3,5-tris(bromomethyl)-2,4,6-triethylbenzene which promotes the removal of the residual surface defects. Both strategies thus allowed to reduce defect density both inside the nanocrystal and on the surface which resulted in an increase in radiative recombination and PLQY above 90%. These improvements resulted in currently the world's highest EQE of 23.4% and current efficiency of 108 cd/A for green perovskite light-emitting diodes.

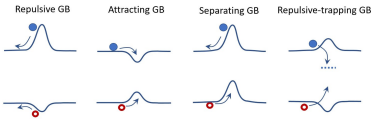

Figure 4. Major types of GBs discussed in the literature.

7. Summary

The abundant literature data devoted to the analysis of properties of perovskite grain boundaries may be roughly summarised by Figure 4 illustrating four major suggested GB types.

Spatially extended two-dimensional repulsive or attracting GBs may be formed if the intergrain matter has significantly wider or narower bandgap respectively than the intragrain perovskite. The narrower bandgap and, thus formation of attracting GB seem to be less likely. Separating GBs may be formed when the bandgap is similar but the absolute energy levels energies differ. Deffects, ions or impurities may create localized trap states indide the spatially extended potentials causing formation of trapping GBs.

The literature data so far gives no unambigous arguments in favour of one or another type. However, repulsive-trapping GBs seem to mach slightly better than other types for the literature data. On the other hand, it cannot be also excluded that all models may be valid depending on perovskite-type, fabrication and passivation procedures. Investigations directed towards unambiguous confirmation or rejection of some of GB types would be very helpful for a better understanding of the perovskite properties. While eleboration of the of the perovskite fabrication and posttreatment techniques enabling to control formation and properties of GB remain of the crutial importance in development of more efficient and stabile devices.

Acknowledgements

The authors acknowledge Lithuanian Research Council under grant agreement 01.2.2-LMT-K-718-03-0048.

Conflict of Interest

The authors declare no conflict of interest.

EurJIC
European Journal of Inorganic Chemistry

Minireviews
doi.org/10.1002/ejic.202100360

Chemistry Europe
European Chemical Societies Publishing

Keywords: Carrier mobility · Grain boundaries · Perovskite light-emitting diodes · Perovskite phases · Perovskite solar cells · Photophysics

[1] M.-S. Lee, S. Sarwar, S. Park, U. Asmat, D. T. Thuy, C. Han, S. Ahn, I. Jeong, S. Hong, *Sustain. Energy Fuels* **2020**, *4*, 3318–3325.
[2] Z. Ni, C. Bao, Y. Liu, Q. Jiang, W.-Q. Wu, S. Chen, X. Dai, B. Chen, B. Hartweg, Z. Yu, Z. Holman, J. Huang, *Science* **2020**, *367*, 1352–1358.
[3] C. Ran, J. Xu, W. Gao, C. Huang, S. Dou, *Chem. Soc. Rev.* **2018**, *47*, 4581–4610.
[4] H. Jin, *Mater. Horiz.* **2020**, *14*.
[5] M. Xiao, F. Huang, W. Huang, Y. Dkhissi, Y. Zhu, J. Etheridge, A. Gray-Weale, U. Bach, Y.-B. Cheng, L. Spiccia, *Angew. Chem. Int. Ed.* **2014**, *53*, 9898–9903; *Angew. Chem.* **2014**, *126*, 10056–10061.
[6] Y. Wang, W.-H. Fang, R. Long, O. V. Prezhdo, *J. Phys. Chem. Lett.* **2019**, *10*, 1617–1623.
[7] J.-W. Lee, S.-H. Bae, N. De Marco, Y.-T. Hsieh, Z. Dai, Y. Yang, *Mater. Today* **2018**, *7*, 149–160.
[8] W. Shan, W. A. Saidi, *J. Phys. Chem. Lett.* **2017**, *8*, 5935–5942.
[9] S. Liu, F. Zheng, N. Z. Koocher, H. Takenaka, F. Wang, A. M. Rappe, *J. Phys. Chem. Lett.* **2015**, *6*, 693–699.
[10] S. G. Motti, D. Meggiolaro, S. Martani, R. Sorrentino, A. J. Barker, F. De Angelis, A. Petrozza, *Adv. Mater.* **2019**, *31*, 1901183.
[11] S. M. Iftiquar, J. Yi, *Mater. Sci. Semicond. Process.* **2018**, *79*, 46–52.
[12] W.-J. Yin, T. Shi, Y. Yan, *Adv. Mater.* **2014**, *26*, 4653–4658.
[13] W.-J. Yin, T. Shi, Y. Yan, *J. Phys. Chem. C* **2015**, *119*, 5253–5264.
[14] Y. Guo, Q. Wang, W. A. Saidi, *J. Phys. Chem. C* **2017**, *121*, 1715–1722.
[15] J. Y. W. Seto, *J. Appl. Phys.* **1975**, *46*, 5247–5254.
[16] R. Jasiūnas, R. Gegevičius, M. Franckevičius, V. Jašinskas, V. Gulbinas, *Adv. Opt. Mater.* **2020**, *8*, 2000036.
[17] Y. Shao, Z. Xiao, C. Bi, Y. Yuan, J. Huang, *Nat. Commun.* **2014**, *5*, 5784.
[18] X. Qiu, Y. Liu, W. Li, Y. Hu, *Nanoscale* **2020**, *12*, 22425–22451.
[19] Z. Yang, J. Dou, S. Kou, J. Dang, Y. Ji, G. Yang, W.-Q. Wu, D.-B. Kuang, M. Wang, *Adv. Funct. Mater.* **2020**, *30*, 1910710.
[20] D. S. Lee, J. S. Yun, J. Kim, A. M. Soufiani, S. Chen, Y. Cho, X. Deng, J. Seidel, S. Lim, S. Huang, A. W. Y. Ho-Baillie, *ACS Energy Lett.* **2018**, *3*, 647–654.
[21] N. K. Noel, A. Abate, S. D. Stranks, E. S. Parrott, V. M. Burlakov, A. Goriely, H. J. Snaith, *ACS Nano* **2014**, *8*, 9815–9821.
[22] T. Y. Wen, S. Yang, P. F. Liu, L. J. Tang, H. W. Qiao, X. Chen, X. H. Yang, Y. Hou, H. G. Yang, *Adv. Energy Mater.* **2018**, *8*, 1703143.
[23] C. Bi, X. Zheng, B. Chen, H. Wei, J. Huang, *ACS Energy Lett.* **2017**, *2*, 1400–1406.
[24] V. L. Pool, A. Gold-Parker, M. D. McGehee, M. F. Toney, *Chem. Mater.* **2015**, *27*, 7240–7243.
[25] X. Zheng, B. Chen, J. Dai, Y. Fang, Y. Bai, Y. Lin, H. Wei, X. C. Zeng, J. Huang, *Nat. Energy* **2017**, *2*, 17102.
[26] H.-H. Fang, S. Adjokatse, H. Wei, J. Yang, G. R. Blake, J. Huang, J. Even, M. A. Loi, *Sci. Adv.* **2016**, *2*, e1600534.
[27] D. Meggiolaro, E. Mosconi, F. De Angelis, *ACS Energy Lett.* **2017**, *2*, 2794–2798.
[28] C. Liu, Y.-B. Cheng, Z. Ge, *Chem. Soc. Rev.* **2020**, *49*, 1653–1687.
[29] Z. Xiao, Q. Dong, C. Bi, Y. Shao, Y. Yuan, J. Huang, *Adv. Mater.* **2014**, *26*, 6503–6509.
[30] S. K. Yadavalli, Y. Zhou, N. P. Padture, *ACS Energy Lett.* **2018**, *3*, 63–64.
[31] B. Wang, K. Y. Wong, S. Yang, T. Chen, *J. Mater. Chem. A* **2016**, *4*, 3806–3812.
[32] W. Nie, H. Tsai, R. Asadpour, J.-C. Blancon, A. J. Neukirch, G. Gupta, J. J. Crochet, M. Chhowalla, S. Tretiak, M. A. Alam, H.-L. Wang, A. D. Mohite, *Science* **2015**, *347*, 522–525.
[33] B. Chen, P. N. Rudd, S. Yang, Y. Yuan, J. Huang, *Chem. Soc. Rev.* **2019**, *48*, 3842–3867.
[34] F. Wang, S. Bai, W. Tress, A. Hagfeldt, F. Gao, *npj Flex. Electron.* **2018**, *2*, 22.
[35] I. L. Braly, D. W. deQuilettes, L. M. Pazos-Outón, S. Burke, M. E. Ziffer, D. S. Ginger, H. W. Hillhouse, *Nat. Photonics* **2018**, *12*, 355–361.
[36] J. M. Richter, M. Abdi-Jalebi, A. Sadhanala, M. Tabachnyk, J. P. H. Rivett, L. M. Pazos-Outón, K. C. Gödel, M. Price, F. Deschler, R. H. Friend, *Nat. Commun.* **2016**, *7*, 13941.
[37] S. D. Stranks, V. M. Burlakov, T. Leijtens, J. M. Ball, A. Goriely, H. J. Snaith, *Phys. Rev. Appl.* **2014**, *2*, 034007.
[38] T. S. Sherkar, C. Momblona, L. Gil-Escrig, J. Ávila, M. Sessolo, H. J. Bolink, L. J. A. Koster, *ACS Energy Lett.* **2017**, *2*, 1214–1222.
[39] D. W. deQuilettes, S. Jariwala, S. Burke, M. E. Ziffer, J. T.-W. Wang, H. J. Snaith, D. S. Ginger, *ACS Nano* **2017**, *11*, 11488–11496.
[40] W. Tian, R. Cui, J. Leng, J. Liu, Y. Li, C. Zhao, J. Zhang, W. Deng, T. Lian, S. Jin, *Angew. Chem. Int. Ed.* **2016**, *55*, 13067–13071; *Angew. Chem.* **2016**, *128*, 13261–13265.
[41] M. Yang, Y. Zeng, Z. Li, D. H. Kim, C.-S. Jiang, J. van de Lagemaat, K. Zhu, *Phys. Chem. Chem. Phys.* **2017**, *19*, 5043–5050.
[42] R. Ciesielski, F. Schäfer, N. F. Hartmann, N. Giesbrecht, T. Bein, P. Docampo, A. Hartschuh, *ACS Appl. Mater. Interfaces* **2018**, *10*, 7974–7981.
[43] J. S. Yun, A. Ho-Baillie, S. Huang, S. H. Woo, Y. Heo, J. Seidel, F. Huang, Y.-B. Cheng, M. A. Green, *J. Phys. Chem. Lett.* **2015**, *6*, 875–880.
[44] E. Edri, S. Kirmayer, A. Henning, S. Mukhopadhyay, K. Gartsman, Y. Rosenwaks, G. Hodes, D. Cahen, *Nano Lett.* **2014**, *14*, 1000–1004.
[45] J.-J. Li, J.-Y. Ma, Q.-Q. Ge, J.-S. Hu, D. Wang, L.-J. Wan, *ACS Appl. Mater. Interfaces* **2015**, *7*, 28518–28523.
[46] F. Mousty, P. Ostoja, L. Passari, *J. Appl. Phys.* **1974**, *45*, 4576–4580.
[47] S. S. Li, W. R. Thurber, *Solid-State Electron.* **1977**, *20*, 609–616.
[48] S. Shrestha, G. J. Matt, A. Osvet, D. Niesner, R. Hock, C. J. Brabec, *J. Phys. Chem. C* **2018**, *122*, 5935–5939.
[49] A. Biewald, N. Giesbrecht, T. Bein, P. Docampo, A. Hartschuh, R. Ciesielski, *ACS Appl. Mater. Interfaces* **2019**, *11*, 20838–20844.
[50] J. Sung, P. Kukura, A. Rao, in *Women Renew. Energy WIRE* (Eds.: M. Lira-Cantu, Z. H. Kafafi), SPIE, San Diego, United States, **2019**, p. 6.
[51] M. I. Saidaminov, A. L. Abdelhady, B. Murali, E. Alarousu, V. M. Burlakov, W. Peng, I. Dursun, L. Wang, Y. He, G. Maculan, A. Goriely, T. Wu, O. F. Mohammed, O. M. Bakr, *Nat. Commun.* **2015**, *6*, 7586.
[52] Q. Dong, Y. Fang, Y. Shao, P. Mulligan, J. Qiu, L. Cao, J. Huang, *Science* **2015**, *347*, 967–970.
[53] D. A. Valverde-Chávez, C. S. Ponseca, C. C. Stoumpos, A. Yartsev, M. G. Kanatzidis, V. Sundström, D. G. Cooke, *Energy Environ. Sci.* **2015**, *8*, 3700–3707.
[54] Y. Bi, E. M. Hutter, Y. Fang, Q. Dong, J. Huang, T. J. Savenije, *J. Phys. Chem. Lett.* **2016**, *7*, 923–928.
[55] G. Baccarani, B. Riccò, G. Spadini, *J. Appl. Phys.* **1978**, *49*, 5565–5570.
[56] T. J. Savenije, C. S. Ponseca, L. Kunneman, M. Abdellah, K. Zheng, Y. Tian, Q. Zhu, S. E. Canton, I. G. Scheblykin, T. Pullerits, A. Yartsev, V. Sundström, *J. Phys. Chem. Lett.* **2014**, *5*, 2189–2194.
[57] R. L. Milot, G. E. Eperon, H. J. Snaith, M. B. Johnston, L. M. Herz, *Adv. Funct. Mater.* **2015**, *25*, 6218–6227.
[58] R. T. Ginting, E.-S. Jung, M.-K. Jeon, W.-Y. Jin, M. Song, J.-W. Kang, *Nano Energy* **2016**, *27*, 569–576.
[59] X. Y. Chin, D. Cortecchia, J. Yin, A. Bruno, C. Soci, *Nat. Commun.* **2015**, *6*, 7383.
[60] X. Zhang, S. Bi, J. Zhou, S. You, H. Zhou, Y. Zhang, Z. Tang, *J. Mater. Chem. C* **2017**, *5*, 9376–9382.
[61] J. Peng, Y. Sun, Y. Chen, Y. Yao, Z. Liang, *ACS Energy Lett.* **2016**, *1*, 1000–1006.
[62] J. Peng, Y. Chen, K. Zheng, T. Pullerits, Z. Liang, *Chem. Soc. Rev.* **2017**, *46*, 5714–5729.
[63] D. W. de Quilettes, S. M. Vorpahl, S. D. Stranks, H. Nagaoka, G. E. Eperon, M. E. Ziffer, H. J. Snaith, D. S. Ginger, *Science* **2015**, *348*, 683–686.
[64] J. M. Snaider, Z. Guo, T. Wang, M. Yang, L. Yuan, K. Zhu, L. Huang, *ACS Energy Lett.* **2018**, *3*, 1402–1408.
[65] A.-F. Castro-Méndez, J. Hidalgo, J.-P. Correa-Baena, *Adv. Energy Mater.* **2019**, 10.
[66] I. Visoly-Fisher, S. R. Cohen, K. Gartsman, A. Ruzin, D. Cahen, *Adv. Funct. Mater.* **2006**, *16*, 649–660.
[67] Y. Yan, W.-J. Yin, Y. Wu, T. Shi, N. R. Paudel, C. Li, J. Poplawsky, Z. Wang, J. Moseley, H. Guthrey, H. Moutinho, S. J. Pennycook, M. M. Al-Jassim, *J. Appl. Phys.* **2015**, *117*, 112807.
[68] H. Choi, K. Choi, Y. Choi, T. Kim, S. Lim, T. Park, *Small Methods* **2020**, *4*, 1900569.
[69] T. Du, C. H. Burgess, J. Kim, J. Zhang, J. R. Durrant, M. A. McLachlan, *Sustain. Energy Fuels* **2017**, *1*, 119–126.
[70] R. Long, J. Liu, O. V. Prezhdo, *J. Am. Chem. Soc.* **2016**, *138*, 3884–3890.
[71] Y. Yang, J. Wu, X. Wang, Q. Guo, X. Liu, W. Sun, Y. Wei, Y. Huang, Z. Lan, M. Huang, J. Lin, H. Chen, Z. Wei, *Adv. Mater.* **2020**, *32*, 1904347.
[72] G. W. P. Adhyaksa, S. Brittman, H. Åboliņš, A. Lof, X. Li, J. D. Keelor, Y. Luo, T. Duevski, R. M. A. Heeren, S. R. Ellis, D. P. Fenning, E. C. Garnett, *Adv. Mater.* **2018**, *30*, 1804792.
[73] Z. Li, F. Wang, C. Liu, F. Gao, L. Shen, W. Guo, *J. Mater. Chem. A* **2019**, *7*, 22359–22365.

EurJIC
European Journal of Inorganic Chemistry

Minireviews
doi.org/10.1002/ejic.202100360

Chemistry Europe
European Chemical Societies Publishing

[74] S. Chen, Q. Pan, J. Li, C. Zhao, X. Guo, Y. Zhao, T. Jiu, *Sci. China Mater.* **2020**, *63*, 2465–2476.
[75] Y. Zhang, S. Chen, H. Chen, G. Zhang, M. Zhao, C. Zhao, W. Guo, W. Ji, Z. Shi, T. Jiu, *J. Mater. Chem. C* **2020**, *8*, 5894–5903.
[76] W. Liu, N. Liu, S. Ji, H. Hua, Y. Ma, R. Hu, J. Zhang, L. Chu, X. Li, W. Huang, *Nano-Micro Lett.* **2020**, *12*, 119.
[77] Q. An, F. Paulus, D. Becker-Koch, C. Cho, Q. Sun, A. Weu, S. Bitton, N. Tessler, Y. Vaynzof, *Matter* **2021**, 5259023852100758.
[78] Q. Jiang, Y. Zhao, X. Zhang, X. Yang, Y. Chen, Z. Chu, Q. Ye, X. Li, Z. Yin, J. You, *Nat. Photonics* **2019**, *13*, 460–466.
[79] I. J. Park, S. Seo, M. A. Park, S. Lee, D. H. Kim, K. Zhu, H. Shin, J. Y. Kim, *ACS Appl. Mater. Interfaces* **2017**, *9*, 41898–41905.
[80] M. Nukunudompanich, G. Budiutama, K. Suzuki, K. Hasegawa, M. Ihara, *CrystEngComm* **2020**, *22*, 2718–2727.
[81] Z. Wang, X. Liu, Y. Lin, Y. Liao, Q. Wei, H. Chen, J. Qiu, Y. Chen, Y. Zheng, *J. Mater. Chem. A* **2019**, *7*, 2773–2779.
[82] J. Chen, X. Xu, X. Tang, T. Jiang, Z. Chen, L. Ye, Y. Tian, X. Chen, T. Liu, Y. Su, H. Zhu, D. Di, L. Li, Y. M. Yang, *J. Phys. Chem. Lett.* **2021**, *12*, 5580–5586.
[83] Z. Gao, Y. Zheng, G. Huang, G. Yang, X. Yu, J. Yu, *Micromachines* **2020**, *11*, 1090.
[84] C. Li, Y. Ma, Y. Xiao, L. Shen, L. Ding, *InfoMat* **2020**, *2*, 1247–1256.
[85] J. Song, Y. Zhou, N. P. Padture, B. D. Huey, *Nat. Commun.* **2020**, *11*, 3308.
[86] L. McGovern, I. Koschany, G. Grimaldi, L. A. Muscarella, B. Ehrler, *J. Phys. Chem. Lett.* **2021**, *12*, 2423–2428.
[87] R. Gegevičius, M. Franckevičius, V. Pakštas, R. Augulis, V. Gulbinas, *Phys. Status Solidi A* **2018**, *215*, 1700822.
[88] M. M. Hasan, C. Clegg, M. Manning, A. El Ghanam, C. Su, M. D. Harding, C. Bennett, I. G. Hill, G. I. Koleilat, *ACS Photonics* **2020**, *7*, 57–67.
[89] B. Yang, F. Zhang, J. Chen, S. Yang, X. Xia, T. Pullerits, W. Deng, K. Han, *Adv. Mater.* **2017**, *29*, 1703758.
[90] Z. Yang, Y. Deng, X. Zhang, S. Wang, H. Chen, S. Yang, J. Khurgin, N. X. Fang, X. Zhang, R. Ma, *Adv. Mater.* **2018**, *30*, 1704333.
[91] L.-P. Cheng, J.-S. Huang, Y. Shen, G.-P. Li, X.-K. Liu, W. Li, Y.-H. Wang, Y.-Q. Li, Y. Jiang, F. Gao, C.-S. Lee, J.-X. Tang, *Adv. Opt. Mater.* **2019**, *7*, 1801534.
[92] J. C. Yu, D. B. Kim, E. D. Jung, B. R. Lee, M. H. Song, *Nanoscale* **2016**, *8*, 7036–7042.
[93] Z. Xiao, R. A. Kerner, L. Zhao, N. L. Tran, K. M. Lee, T.-W. Koh, G. D. Scholes, B. P. Rand, *Nat. Photonics* **2017**, *11*, 108–115.
[94] S. Chu, W. Chen, Z. Fang, X. Xiao, Y. Liu, J. Chen, J. Huang, Z. Xiao, *Nat. Commun.* **2021**, *12*, 147.
[95] K. Zheng, Q. Zhu, M. Abdellah, M. E. Messing, W. Zhang, A. Generalov, Y. Niu, L. Ribaud, S. E. Canton, T. Pullerits, *J. Phys. Chem. Lett.* **2015**, *6*, 2969–2975.
[96] L. Protesescu, S. Yakunin, M. I. Bodnarchuk, F. Krieg, R. Caputo, C. H. Hendon, R. X. Yang, A. Walsh, M. V. Kovalenko, *Nano Lett.* **2015**, *15*, 3692–3696.
[97] Y.-H. Kim, S. Kim, A. Kakekhani, J. Park, J. Park, Y.-H. Lee, H. Xu, S. Nagane, R. B. Wexler, D.-H. Kim, S. H. Jo, L. Martínez-Sarti, P. Tan, A. Sadhanala, G.-S. Park, Y.-W. Kim, B. Hu, H. J. Bolink, S. Yoo, R. H. Friend, A. M. Rappe, T.-W. Lee, *Nat. Photonics* **2021**, *15*, 148–155.
[98] H. Cho, S.-H. Jeong, M.-H. Park, Y.-H. Kim, C. Wolf, C.-L. Lee, J. H. Heo, A. Sadhanala, N. Myoung, S. Yoo, S. H. Im, R. H. Friend, T.-W. Lee, *Science* **2015**, *350*, 1222–1225.
[99] Y.-C. Ye, Y. Li, Y. Tian, X.-Y. Cai, Y. Shen, K.-C. Shen, X. Gao, F. Song, W. Wang, J.-X. Tang, *Nanoscale* **2021**, *13*, 340–348.
[100] J. Qin, J. Zhang, Y. Bai, S. Ma, M. Wang, H. Xu, M. Loyd, Y. Zhan, X. Hou, B. Hu, *iScience* **2019**, *19*, 378–387.

Manuscript received: April 29, 2021
Revised manuscript received: June 29, 2021
Accepted manuscript online: July 1, 2021

Acronyms

2D	Two-dimensional
3D	Three-dimensional
AC	Alternating current
Alq3	8-Hydroxyquinoline aluminum salt
AMF	Atomic force microscopy
bphen	4,7-Diphenyl-1,10-phenanthroline
CELIV	Charge extraction by linearly increasing voltage
DBR	Distributed Bragg reflector
DC	Direct current
DFT	Density functional theory
DSCS	Dye-sentisized solar cells
EA	Electroabsorption
EDX	Energy dispersive X-ray spectroscopy
EFILQ	Electric field-induced luminescence quenching
EL	Electroluminescence
EQE	External quantuam efficency
ETL	Electron transporting layer
FA	Formamidinium
FTIR	Fourier transform infrared spectroscopy
HOIP	Hybrid Organic-Inorganic Perovskite
HOMO	Highest occupied molecular orbital
HTL	Hole transporting layer
IDE	Interdigitated electrode

LED	Light Emmiting Diode
LED	Organic Light Emmiting Diode
LO	Longitudinal optical
LUMO	Lowest unoccupied molecular orbital
MA	Mythylammonium
MWC	microwave conductivity
NW	Nanowire
PCBM	Phenyl-C61-butyric acid methyl ester
PCE	Power conversion efficiancy
PeLED	Perovskite Light Emmiting Diode
PhC	Photo-conductivity
PL	Photoluminescence
PLQ	Photoluminescence quenching
PLQY	Photoluminescence quantum yield
PMAI	benyzlammonium iodide
PolyTPD	Poly(4-butylphenyldiphenylamine)
PSC	Perovskite solar cells
PTIR	Photothermally induced resonance microscopy
QD	Quantum dot
SCLS	Space Charge Limited Current
TA	Transient absorption
TAM	Transient absorption microscopy
TCSPC	Time-correlated single photon counting
TDFC	Time-delayed collection field
TOF	Time-of-flight
TPC	Transient Photo-current
TRPL	Transient photoluminescence spectroscopy
TRTS	Time-resolved THz spectroscopy
XRD	X-ray diffraction

Bibliography

1. D. Weber. "$CH_3NH_3PbX_3$, ein Pb(II)-System mit kubischer Perowskitstruktur / $CH_3NH_3PbX_3$, a Pb(II)-System with Cubic Perovskite Structure". *Zeitschrift für Na-turforschung B* 33:12, 1, 1978, p. 1443.
DOI: 10.1515/znb-1978-1214.

2. K. Chondroudis and D. B. Mitzi. "Electroluminescence from an Organic–Inorganic Perovskite Incorporating a Quaterthiophene Dye within Lead Halide Perovskite Layers". *Chemistry of Materials* 11:11, 1999, p. 3028.
DOI: 10.1021/cm990561t.

3. D. Mitzi, C. Dimitrakopoulos, J. Rosner, D. Medeiros, Z. Xu, and C. Noyan. "Hybrid Field-Effect Transistor Based on a Low-Temperature Melt-Processed Channel Layer". *Advanced Materials* 14:23, 2002, p. 1772.
DOI: 10.1002/1521-4095(20021203)14:23<1772::AID-ADMA1772>3.0.CO;2-Y.

4. A. Kojima, K. Teshima, Y. Shirai, and T. Miyasaka. "Organometal Halide Perovskites as Visible-Light Sensitizers for Photovoltaic Cells". *Journal of the American Chemical Society* 131:17, 2009, p. 6050.
DOI: 10.1021/ja809598r.

5. J. Burschka, N. Pellet, S.-J. Moon, R. Humphry-Baker, P. Gao, M. K. Nazeeruddin, and M. Grätzel. "Sequential deposition as a route to high-performance perovskite-sensitized solar cells". *Nature* 499:7458, 2013, p. 316.
DOI: 10.1038/nature12340.

6. H. Min, D. Y. Lee, J. Kim, G. Kim, K. S. Lee, J. Kim, M. J. Paik, Y. K. Kim, K. S. Kim, M. G. Kim, T. J. Shin, and S. Il Seok. "Perovskite solar cells with atomically coherent interlayers on SnO_2 electrodes". *Nature* 598:7881, 2021, p. 444.
DOI: 10.1038/s41586-021-03964-8.

7. S. Rühle. "Tabulated values of the Shockley–Queisser limit for single junction solar cells". *Solar Energy* 130, 2016, p. 139.
DOI: 10.1016/j.solener.2016.02.015.

8. R. Gegevičius, M. Franckevičius, V. Pakštas, R. Augulis, and V. Gulbinas. "High-Speed, Sensitive Planar Perovskite Photodetector Based on Interdigitated Pt and Au Electrodes". *physica status solidi (a)* 215:7, 2018, p. 1700822.
DOI: 10.1002/pssa.201700822.

9. S. Shrestha, R. Fischer, G. J. Matt, P. Feldner, T. Michel, A. Osvet, I. Levchuk, B. Merle, S. Golkar, H. Chen, S. F. Tedde, O. Schmidt, R. Hock, M. Rührig, M. Göken, W. Heiss, G. Anton, and C. J. Brabec. "High-performance direct conversion X-ray detectors based on sintered hybrid lead triiodide perovskite wafers". *Nature Photonics* 11:7, 2017, p. 436.
DOI: 10.1038/nphoton.2017.94.

10. A. Fakharuddin, W. Qiu, G. Croes, A. Devižis, R. Gegevičius, A. Vakhnin, C. Rolin, J. Genoe, R. Gehlhaar, A. Kadashchuk, V. Gulbinas, and P. Heremans. "Reduced Efficiency Roll-Off and Improved Stability of Mixed 2D/3D Perovskite Light Emitting Diodes by Balancing Charge Injection". *Advanced Functional Materials* 29:37, 2019, p. 1904101.
DOI: 10.1002/adfm.201904101.

11. R. Brenes, D. Guo, A. Osherov, N. K. Noel, C. Eames, E. M. Hutter, S. K. Pathak, F. Niroui, R. H. Friend, M. S. Islam, H. J. Snaith, V. Bulović, T. J. Savenije, and S. D. Stranks. "Metal Halide Perovskite Polycrystalline Films Exhibiting Properties of Single Crystals". *Joule* 1:1, 2017, p. 155.
DOI: 10.1016/j.joule.2017.08.006.

12. T. Leijtens, G. E. Eperon, N. K. Noel, S. N. Habisreutinger, A. Petrozza, and H. J. Snaith. "Stability of Metal Halide Perovskite Solar Cells". *Advanced Energy Materials* 5:20, 2015, p. 1500963.
DOI: 10.1002/aenm.201500963.

13. V. M. Goldschmidt. "Die Gesetze der Krystallochemie". *Die Naturwissenschaften* 14:21, 1926, p. 477.
DOI: 10.1007/BF01507527.

14. J. A. Brehm, J. W. Bennett, M. R. Schoenberg, I. Grinberg, and A. M. Rappe. "The structural diversity of ABS_3 d^0 electronic configuration for the B-cation". *The Journal of Chemical Physics* 140:22, 14, 2014, p. 224703.
DOI: 10.1063/1.4879659.

15. D. B. Mitzi and K. Liang. "Preparation and Properties of $(C_4H_9NH_3)_2EuI_4$: A Luminescent Organic Inorganic Perovskite with a Divalent Rare Earth Metal Halide Framework". *Chemistry of Materials* 9:12, 1, 1997, p. 2990.
DOI: 10.1021/cm970352d.

16. J. Grimm, J. F. Suyver, E. Beurer, G. Carver, and H. U. Güdel. "Light-Emission and Excited-State Dynamics in Tm^{2+} Doped $CsCaCl_3$, $CsCaBr_3$, and $CsCaI_3$". *The Journal of Physical Chemistry B* 110:5, 1, 2006, p. 2093.
DOI: 10.1021/jp055930p.

17. H.-J. Seifert and D. Haberhauer. "Über die Systeme Alkalimetallbromid/Calciumbromid". *Zeitschrift für anorganische und allgemeine Chemie* 491:1, 1982, p. 301.
DOI: 10.1002/zaac.19824910139.

18. A. Horowitz, M. Amit, J. Makovsky, L. Dor, and Z. Kalman. "Structure types and phase transformations in KMnCl3 and TlMnCl3". *Journal of Solid State Chemistry* 43:2, 1982, p. 107.
DOI: 10.1016/0022-4596(82)90220-1.

19. G. Kieslich, S. Sun, and A. K. Cheetham. "Solid-state principles applied to organic inorganic perovskites: new tricks for an old dog". *Chem. Sci.* 5:12, 2014, p. 4712.
DOI: 10.1039/C4SC02211D.

20. B. Saparov and D. B. Mitzi. "Organic–Inorganic Perovskites: Structural Versatility for Functional Materials Design". *Chemical Reviews* 116:7, 13, 2016, p. 4558.
DOI: 10.1021/acs.chemrev.5b00715.

21. W. Li, Z. Wang, F. Deschler, S. Gao, R. H. Friend, and A. K. Cheetham. "Chemically diverse and multifunctional hybrid organic–inorganic perovskites". *Nature Reviews Materials* 2:3, 7, 2017, p. 16099.
DOI: 10.1038/natrevmats.2016.99.

22. D. A. Egger, A. M. Rappe, and L. Kronik. "Hybrid Organic-Inorganic Perovskites on the Move". *Accounts of Chemical Research* 49:3, 2016, p. 573.
DOI: 10.1021/acs.accounts.5b00540.

23. C. C. Stoumpos and M. G. Kanatzidis. "The Renaissance of Halide Perovskites and Their Evolution as Emerging Semiconductors". *Accounts of Chemical Research* 48:10, 20, 2015, p. 2791.
DOI: 10.1021/acs.accounts.5b00229.

24. K. T. Butler. "The chemical forces underlying octahedral tilting in halide perovskites". *Journal of Materials Chemistry C* 6:44, 2018, p. 12045.
DOI: 10.1039/C8TC02976H.

25. M. H. Du. "Efficient carrier transport in halide perovskites: theoretical perspectives". *Journal of Materials Chemistry A* 2:24, 2014, p. 9091.
DOI: 10.1039/C4TA01198H.

26. F. Brivio, J. M. Frost, J. M. Skelton, A. J. Jackson, O. J. Weber, M. T. Weller, A. R. Goñi, A. M. Leguy, P. R. F. Barnes, and A. Walsh. "Lattice dynamics and vibrational spectra of the orthorhombic, tetragonal, and cubic phases of methylammonium lead iodide". *Physical Review B* 92:14, 16, 2015, p. 144308.
DOI: 10.1103/PhysRevB.92.144308.

27. D. A. Egger and L. Kronik. "Role of Dispersive Interactions in Determining Structural Properties of Organic–Inorganic Halide Perovskites: Insights from First-Principles Calculations". *The Journal of Physical Chemistry Letters* 5:15, 7, 2014, p. 2728.
DOI: 10.1021/jz5012934.

28. E. Menéndez-Proupin, P. Palacios, P. Wahnón, and J. C. Conesa. "Self-consistent relativistic band structure of the $CH_3NH_3PbI_3$ perovskite". *Physical Review B* 90:4, 24, 2014, p. 045207.
DOI: 10.1103/PhysRevB.90.045207.

29. T. M. Brenner, D. A. Egger, L. Kronik, G. Hodes, and D. Cahen. "Hybrid organic inorganic perovskites: low-cost semiconductors with intriguing charge transport properties". *Nature Reviews Materials* 1:1, 11, 2016, p. 15007.
DOI: 10.1038/natrevmats.2015.7.

30. *Physics of Ferroelectrics: A Modern Perspective*. Vol. 105. Topics in Applied Physics. Sprin-ger Berlin Heidelberg, Berlin, Heidelberg, 2007.
DOI: 10.1007/978-3-540-34591-6.

31. Y. Lee, D. B. Mitzi, P. W. Barnes, and T. Vogt. "Pressure-induced phase transitions and templating effect in three-dimensional organic-inorganic hybrid perovskites". *Physical Review B* 68:2, 29, 2003, p. 020103.
DOI: 10.1103/PhysRevB.68.020103.

32. F. Brivio, A. B. Walker, and A. Walsh. "Structural and electronic properties of hybrid perovskites for high-efficiency thin-film photovoltaics from first-principles". *APL Materials* 1:4, 2013, p. 042111.
DOI: 10.1063/1.4824147.

33. C. Quarti, E. Mosconi, and F. De Angelis. "Interplay of Orientational Order and Electronic Structure in Methylammonium Lead Iodide: Implications for Solar Cell Operation". *Chemistry of Materials* 26:22, 25, 2014, p. 6557.
DOI: 10.1021/cm5032046.

34. C. Quarti, E. Mosconi, J. M. Ball, V. D'Innocenzo, C. Tao, S. Pathak, H. J. Snaith, A. Petrozza, and F. De Angelis. "Structural and optical properties of methylammonium lead iodide across the tetragonal to cubic phase transition: implications for perovskite solar cells". *Energy & Environmental Science* 9:1, 2016, p. 155.
DOI: 10.1039/C5EE02925B.

35. C. C. Stoumpos, C. D. Malliakas, and M. G. Kanatzidis. "Semiconducting Tin and Lead Iodide Perovskites with Organic Cations: Phase Transitions, High Mobilities, and Near-Infrared Photoluminescent Properties". *Inorganic Chemistry* 52:15, 2013, p. 9019.
DOI: 10.1021/ic401215x.

36. N. J. Jeon, J. H. Noh, Y. C. Kim, W. S. Yang, S. Ryu, and S. I. Seok. "Solvent engineering for high-performance inorganic–organic hybrid perovskite solar cells". *Nature Materials* 13:9, 2014, p. 897.
DOI: 10.1038/nmat4014.

37. Q. Dong, Y. Fang, Y. Shao, P. Mulligan, J. Qiu, L. Cao, and J. Huang. "Electron hole diffusion lengths > 175 μm in solution grown $CH_3NH_3PbI_3$ single crystals". *Science* 347:6225, 2015, p. 967.
DOI: 10.1126/science.aaa5760.

38. D. Shi, V. Adinolfi, R. Comin, M. Yuan, E. Alarousu, A. Buin, Y. Chen, S. Hoogland, A. Rothenberger, K. Katsiev, Y. Losovyj, X. Zhang, P. A. Dowben, O. F. Mohammed, E. H. Sargent, and O. M. Bakr. "Low trap-state density and long carrier diffusion in organolead trihalide perovskite single crystals". *Science* 347:6221, 2015, p. 519.
DOI: 10.1126/science.aaa2725.

39. A. M. A. Leguy, J. M. Frost, A. P. McMahon, V. G. Sakai, W. Kockelmann, C. Law, X. Li, F. Foglia, A. Walsh, B. C. O'Regan, J. Nelson, J. T. Cabral, and P. R. F. Barnes. "The dynamics of methylammonium ions in hybrid organic–inorganic perovskite solar cells". *Nature Communications* 6:1, 2015, p. 7124.
DOI: 10.1038/ncomms8124.

40. C. Motta, F. El-Mellouhi, S. Kais, N. Tabet, F. Alharbi, and S. Sanvito. "Revealing the role of organic cations in hybrid halide perovskite $CH_3NH_3PbI_3$". *Nature Communications* 6:1, 2015, p. 7026.
DOI: 10.1038/ncomms8026.

41. R. Gottesman, E. Haltzi, L. Gouda, S. Tirosh, Y. Bouhadana, A. Zaban, E. Mosconi, and F. De Angelis. "Extremely Slow Photoconductivity Response of $CH_3NH_3PbI_3$ Perovskites Suggesting Structural Changes under Working Conditions". *The Journal of Physical Chemistry Letters* 5:15, 2014, p. 2662.
DOI: 10.1021/jz501373f.

42. A. Mattoni, A. Filippetti, M. I. Saba, and P. Delugas. "Methylammonium Rotational Dynamics in Lead Halide Perovskite by Classical Molecular Dynamics: The Role of Temperature". *The Journal of Physical Chemistry C* 119:30, 2015, p. 17421.
DOI: 10.1021/acs.jpcc.5b04283.

43. A. A. Bakulin, O. Selig, H. J. Bakker, Y. L. Rezus, C. Müller, T. Glaser, R. Lovrincic, Z. Sun, Z. Chen, A. Walsh, J. M. Frost, and T. L. C. Jansen. "Real-Time Observation of Organic Cation Reorientation in Methylammonium Lead Iodide Perovskites". *The Journal of Physical Chemistry Letters* 6:18, 2015, p. 3663.
DOI: 10.1021/acs.jpclett.5b01555.

44. I. P. Swainson, C. Stock, S. F. Parker, L. Van Eijck, M. Russina, and J. W. Taylor. "From soft harmonic phonons to fast relaxational dynamics in $CH_3NH_3PbBr_3$". *Physical Review B* 92:10, 2015, p. 100303.
DOI: 10.1103/PhysRevB.92.100303.

45. Y. Zhou, F. Huang, Y.-B. Cheng, and A. Gray-Weale. "Photovoltaic performance and the energy landscape of $CH_3NH_3PbI_3$". *Physical Chemistry Chemical Physics* 17:35, 2015, p. 22604.
DOI: 10.1039/C5CP03352G.

46. J. L. Knutson, J. D. Martin, and D. B. Mitzi. "Tuning the Band Gap in Hybrid Tin Iodide Perovskite Semiconductors Using Structural Templating". *Inorganic Chemistry* 44:13, 2005, p. 4699.
DOI: 10.1021/ic050244q.

47. A. Stroppa, C. Quarti, F. De Angelis, and S. Picozzi. "Ferroelectric Polarization of $CH_3NH_3PbI_3$: A Detailed Study Based on Density Functional Theory and Symmetry Mode Analysis". *The Journal of Physical Chemistry Letters* 6:12, 2015, p. 2223.
DOI: 10.1021/acs.jpclett.5b00542.

48. J. M. Frost, K. T. Butler, F. Brivio, C. H. Hendon, M. van Schilfgaarde, and A. Walsh. "Atomistic Origins of High-Performance in Hybrid Halide Perovskite Solar Cells". *Nano Letters* 14:5, 2014, p. 2584.
DOI: 10.1021/nl500390f.

49. J. M. Frost, K. T. Butler, and A. Walsh. "Molecular ferroelectric contributions to anomalous hysteresis in hybrid perovskite solar cells". *APL Materials* 2:8, 2014, p. 081506.
DOI: 10.1063/1.4890246.

50. S. Liu, F. Zheng, N. Z. Koocher, H. Takenaka, F. Wang, and A. M. Rappe. "Ferroelectric Domain Wall Induced Band Gap Reduction and Charge Separation in Organometal Halide Perovskites". *The Journal of Physical Chemistry Letters* 6:4, 2015, p. 693.
DOI: 10.1021/jz502666j.

51. J. Ma and L.-W. Wang. "Nanoscale Charge Localization Induced by Random Orientations of Organic Molecules in Hybrid Perovskite $CH_3NH_3PbI_3$". *Nano Letters* 15:1, 2015, p. 248.
DOI: 10.1021/nl503494y.

52. M. Kepenekian, R. Robles, C. Katan, D. Sapori, L. Pedesseau, and J. Even. "Rashba and Dresselhaus Effects in Hybrid Organic–Inorganic Perovskites: From Basics to Devices". *ACS Nano* 9:12, 2015, p. 11557.
DOI: 10.1021/acsnano.5b04409.

53. M. Pope, C. E. Swenberg, M. Pope, and C. E. Swenberg. *Electronic Processes in Organic Crystals and Polymers*. Second Edition, Second Edition. Monographs on the Physics and Chemistry of Materials. Oxford University Press, Oxford, New York, 1999.

54. M. Liu, M. B. Johnston, and H. J. Snaith. "Efficient planar heterojunction perovskite solar cells by vapour deposition". *Nature* 501:7467, 2013, p. 395.
DOI: 10.1038/nature12509.

55. T. J. Savenije, C. S. Ponseca, L. Kunneman, M. Abdellah, K. Zheng, Y. Tian, Q. Zhu, S. E. Canton, I. G. Scheblykin, T. Pullerits, A. Yartsev, and V. Sundström. "Thermally Activated Exciton Dissociation and Recombination Control the Carrier Dynamics in Organometal Halide Perovskite". *The Journal of Physical Chemistry Letters* 5:13, 2014, p. 2189.
DOI: 10.1021/jz500858a.

56. L. Q. Phuong, Y. Nakaike, A. Wakamiya, and Y. Kanemitsu. "Free Excitons and Exciton–Phonon Coupling in $CH_3NH_3PbI_3$ Single Crystals Revealed by Photocurrent and Photoluminescence Measurements at Low Temperatures". *The Journal of Physical Chemistry Letters* 7:23, 2016, p. 4905.
DOI: 10.1021/acs.jpclett.6b02432.

57. Y. Yang, D. P. Ostrowski, R. M. France, K. Zhu, J. van de Lagemaat, J. M. Luther, and M. C. Beard. "Observation of a hot-phonon bottleneck in lead-iodide perovskites". *Nature Photonics* 10:1, 2016, p. 53.
DOI: 10.1038/nphoton.2015.213.

58. Q. Zhu, K. Zheng, M. Abdellah, A. Generalov, D. Haase, S. Carlson, Y. Niu, J. Heimdal, A. Engdahl, M. E. Messing, T. Pullerits, and S. E. Canton. "Correlating structure and electronic band-edge properties in organolead halide perovskites nanoparticles". *Physical Chemistry Chemical Physics* 18:22, 2016, p. 14933.
DOI: 10.1039/C6CP01843B.

59. M. Hirasawa, T. Ishihara, T. Goto, K. Uchida, and N. Miura. "Magnetoabsorption of the lowest exciton in perovskite-type compound (CH3NH3)PbI3". *Physica B: Condensed Matter* 201, 1994, p. 427.
DOI: 10.1016/0921-4526(94)91130-4.

60. A. Miyata, A. Mitioglu, P. Plochocka, O. Portugall, J. T.-W. Wang, S. D. Stranks, H. J. Snaith, and R. J. Nicholas. "Direct measurement of the exciton binding energy and effective masses for charge carriers in
organic inorganic trihalide perovskites". *Nature Physics* 11:7, 2015, p. 582.
DOI: 10.1038/nphys3357.

61. H. Zhu, K. Miyata, Y. Fu, J. Wang, P. P. Joshi, D. Niesner, K. W. Williams, S. Jin, and X.-Y. Zhu. "Screening in crystalline liquids protects energetic carriers in hybrid perovskites". *Science* 353:6306, 2016, p. 1409.
DOI: 10.1126/science.aaf9570.

62. S. Arrhenius. "Über die Dissociationswärme und den Einfluss der Temperatur auf den Dissociationsgrad der Elektrolyte". *Zeitschrift für Physikalische Chemie* 4U:1, 1889, p. 96.
DOI: 10.1515/zpch-1889-0408.

63. S. Sun, T. Salim, N. Mathews, M. Duchamp, C. Boothroyd, G. Xing, T. C. Sum, and Y. M. Lam. "The origin of high efficiency in low-temperature solution-processable bilayer organometal halide hybrid solar cells". *Energy Environ. Sci.* 7:1, 2014, p. 399.
DOI: 10.1039/C3EE43161D.

64. I. B. Koutselas, L Ducasse, and G. C. Papavassiliou. "Electronic properties of three- and low-dimensional semiconducting materials with Pb halide and Sn halide units". *Journal of Physics: Condensed Matter* 8:32, 1996, p. 5953.
DOI: 10.1088/0953-8984/8/32/015.

65. W. Rehman, R. L. Milot, G. E. Eperon, C. Wehrenfennig, J. L. Boland, H. J. Snaith, M. B. Johnston, and L. M. Herz. "Charge-Carrier Dynamics and Mobilities in Formamidinium Lead Mixed-Halide Perovskites". *Advanced Materials* 27:48, 2015, p. 7938.
DOI: https://doi.org/10.1002/adma.201502969.

66. R. J. Elliott. "Intensity of Optical Absorption by Excitons". *Physical Review* 108:6, 1957, p. 1384.
DOI: 10.1103/PhysRev.108.1384.

67. M. Saba, M. Cadelano, D. Marongiu, F. Chen, V. Sarritzu, N. Sestu, C. Figus, M. Aresti, R. Piras, A. Geddo Lehmann, C. Cannas, A. Musinu, F. Quochi, A. Mura, and G. Bongiovanni. "Correlated electron–hole plasma in organometal perovskites". *Nature Communications* 5:1, 2014, p. 5049.
DOI: 10.1038/ncomms6049.

68. Y. Yamada, T. Nakamura, M. Endo, A. Wakamiya, and Y. Kanemitsu. "Photocarrier Recombination Dynamics in Perovskite $CH_3NH_3PbI_3$ for Solar Cell Applications". *Journal of the American Chemical Society* 136:33, 2014, p. 11610.
DOI: 10.1021/ja506624n.

69. K. Tanaka, T. Takahashi, T. Ban, T. Kondo, K. Uchida, and N. Miura. "Comparative study on the excitons in lead-halide-based perovskite-type crystals $CH_3NH_3PbBr_3$ $CH_3NH_3PbI_3$". *Solid State Communications* 127:9-10, 2003, p. 619.
DOI: 10.1016/S0038-1098(03)00566-0.

70. J. S. Manser, J. A. Christians, and P. V. Kamat. "Intriguing Optoelectronic Properties of Metal Halide Perovskites". *Chemical Reviews* 116:21, 2016, p. 12956.
DOI: 10.1021/acs.chemrev.6b00136.

71. V. D'Innocenzo, G. Grancini, M. J. P. Alcocer, A. R. S. Kandada, S. D. Stranks, M. M. Lee, G. Lanzani, H. J. Snaith, and A. Petrozza. "Excitons versus free charges in organo-lead tri-halide perovskites". *Nature Communications* 5:1, 2014, p. 3586.
DOI: 10.1038/ncomms4586.

72. K. Chen, A. J. Barker, M. E. Reish, K. C. Gordon, and J. M. Hodgkiss. "Broadband Ultrafast Photoluminescence Spectroscopy Resolves Charge Photogeneration via Delocalized Hot Excitons in Polymer:Fullerene Photovoltaic Blends". *Journal of the American Chemical Society* 135:49, 2013, p. 18502.
DOI: 10.1021/ja408235h.

73. C. Sheng, C. Zhang, Y. Zhai, K. Mielczarek, W. Wang, W. Ma, A. Zakhidov, and Z. V. Vardeny. "Exciton versus Free Carrier Photogeneration in Organometal Tri-

halide Perovskites Probed by Broadband Ultrafast Polarization Memory Dynamics". *Physical Review Letters* 114:11, 2015, p. 116601.
DOI: 10.1103/PhysRevLett.114.116601.

74. Y.-C. Hsiao, T. Wu, M. Li, Q. Liu, W. Qin, and B. Hu. "Fundamental physics behind high efficiency organo metal halide perovskite solar cells". *Journal of Materials Chemistry A* 3:30, 2015, p. 15372.
DOI: 10.1039/C5TA01376C.

75. M. N. Saha. "On a physical theory of stellar spectra". *Proceedings of the Royal Society of London. Series A, Containing Papers of a Mathematical and Physical Character* 99:697, 1921, p. 135.
DOI: 10.1098/rspa.1921.0029.

76. G. Xing, N. Mathews, S. S. Lim, N. Yantara, X. Liu, D. Sabba, M. Grätzel, S. Mhaisalkar, and T. C. Sum. "Low-temperature solution-processed wavelength-tunable perovskites for lasing". *Nature Materials* 13:5, 2014, p. 476.
DOI: 10.1038/nmat3911.

77. R. Cingolani, L. Calcagnile, G. Colí, R. Rinaldi, M. Lomoscolo, M. DiDio, A. Franciosi, L. Vanzetti, G. C. LaRocca, and D. Campi. "Radiative recombination processes in wide-band-gap II–VI quantum wells: the interplay between excitons and free carriers". *Journal of the Optical Society of America B* 13:6, 1996, p. 1268.
DOI: 10.1364/JOSAB.13.001268.

78. F. Deschler, M. Price, S. Pathak, L. E. Klintberg, D.-D. Jarausch, R. Higler, S. Hüttner, T. Leijtens, S. D. Stranks, H. J. Snaith, M. Atatüre, R. T. Phillips, and R. H. Friend. "High Photoluminescence Efficiency and Optically Pumped Lasing in Solution-Processed Mixed Halide Perovskite Semiconductors". *The Journal of Physical Chemistry Letters* 5:8, 2014, p. 1421.
DOI: 10.1021/jz5005285.

79. D. A. Valverde-Chávez, C. S. Ponseca, C. C. Stoumpos, A. Yartsev, M. G. Kanatzidis, V. Sundström, and D. G. Cooke. "Intrinsic femtosecond charge generation dynamics in single crystal $CH_3NH_3PbI_3$". *Energy & Environmental Science* 8:12, 2015, p. 3700.
DOI: 10.1039/C5EE02503F.

80. P. Piatkowski, B. Cohen, C. S. Ponseca, M. Salado, S. Kazim, S. Ahmad, V. Sundström, and A. Douhal. "Unraveling Charge Carriers Generation, Diffusion, and Recombination in Formamidinium Lead Triiodide Perovskite Polycrystalline Thin Film". *The Journal of Physical Chemistry Letters* 7:1, 2016, p. 204.
DOI: 10.1021/acs.jpclett.5b02648.

81. A. Jha, H.-G. Duan, V. Tiwari, P. K. Nayak, H. J. Snaith, M. Thorwart, and R. J. D. Miller. "Direct Observation of Ultrafast Exciton Dissociation in Lead Iodide Perovskite by 2D Electronic Spectroscopy". *ACS Photonics* 5:3, 2018, p. 852.
DOI: 10.1021/acsphotonics.7b01025.

82. Y. Zhai, C. X. Sheng, C. Zhang, and Z. V. Vardeny. "Ultrafast Spectroscopy of Photoexcitations in Organo-metal Trihalide Perovskites". *Advanced Functional Materials* 26:10, 2016, p. 1617.
DOI: 10.1002/adfm.201505115.

83. H. He, Q. Yu, H. Li, J. Li, J. Si, Y. Jin, N. Wang, J. Wang, J. He, X. Wang, Y. Zhang, and Z. Ye. "Exciton localization in solution-processed organolead trihalide perovskites". *Nature Communications* 7:1, 2016, p. 10896.
DOI: 10.1038/ncomms10896.

84. J. Aneesh, A. Swarnkar, V. Kumar Ravi, R. Sharma, A. Nag, and K. V. Adarsh. "Ultrafast Exciton Dynamics in Colloidal $CsPbBr_3$ Perovskite Nanocrystals: Biexciton Effect and Auger Recombination". *The Journal of Physical Chemistry C* 121:8, 2017, p. 4734.
DOI: 10.1021/acs.jpcc.7b00762.

85. N. S. Makarov, S. Guo, O. Isaienko, W. Liu, I. Robel, and V. I. Klimov. "Spectral and Dynamical Properties of Single Excitons, Biexcitons, and Trions in Cesium–Lead-Halide Perovskite Quantum Dots". *Nano Letters* 16:4, 2016, p. 2349.
DOI: 10.1021/acs.nanolett.5b05077.

86. C. de Weerd, L. Gomez, A. Capretti, D. M. Lebrun, E. Matsubara, J. Lin, M. Ashida, F. C. M. Spoor, L. D. A. Siebbeles, A. J. Houtepen, K. Suenaga, Y. Fujiwara, and T. Gregorkiewicz. "Efficient carrier multiplication in CsPbI3 perovskite nanocrystals". *Nature Communications* 9:1, 2018, p. 4199.
DOI: 10.1038/s41467-018-06721-0.

87. M. Lundstrom. *Fundamentals of Carrier Transport*. 2nd ed. Cambridge University Press, 2000.
DOI: 10.1017/CBO9780511618611.

88. K. A. Dill, S. Bromberg, and D. Stigter. *Molecular Driving Forces: Statistical Thermodynamics in Biology, Chemistry, Physics, and Nanoscience*. 2nd ed. Garland Science, 2010.
DOI: 10.4324/9780203809075.

89. L. M. Herz. "Charge-Carrier Dynamics in Organic-Inorganic Metal Halide Perovskites". *Annual Review of Physical Chemistry* 67:1, 2016, p. 65.
DOI: 10.1146/annurev-physchem-040215-112222.

90. J. Bisquert and I. Mora-Seró. "Simulation of Steady-State Characteristics of Dye Sensitized Solar Cells and the Interpretation of the Diffusion Length". *The Journal of Physical Chemistry Letters* 1:1, 2010, p. 450.
DOI: 10.1021/jz900297b.

91. G. Xing, N. Mathews, S. Sun, S. S. Lim, Y. M. Lam, M. Grätzel, S. Mhaisalkar, and T. C. Sum. "Long-Range Balanced Electron- and Hole-Transport Lengths in Organic Inorganic $CH_3NH_3PbI_3$". *Science* 342:6156, 2013, p. 344.
DOI: 10.1126/science.1243167.

92. Z. Guo, J. S. Manser, Y. Wan, P. V. Kamat, and L. Huang. "Spatial and temporal imaging of long-range charge transport in perovskite thin films by ultrafast microscopy". *Nature Communications* 6:1, 2015, p. 7471.
DOI: 10.1038/ncomms8471.

93. W. Tian, C. Zhao, J. Leng, R. Cui, and S. Jin. "Visualizing Carrier Diffusion in Individual Single-Crystal Organolead Halide Perovskite Nanowires and Nanoplates". *Journal of the American Chemical Society* 137:39, 2015, p. 12458.
DOI: 10.1021/jacs.5b08045.

94. S. D. Stranks, G. E. Eperon, G. Grancini, C. Menelaou, M. J. P. Alcocer, T. Leijtens, L. M. Herz, A. Petrozza, and H. J. Snaith. "Electron Hole Diffusion Lengths Exceeding 1 Micrometer in an Organo metal Trihalide Perovskite Absorber". *Science* 342:6156, 2013, p. 341.
DOI: 10.1126/science.1243982.

95. D. W. deQuilettes, S. Jariwala, S. Burke, M. E. Ziffer, J. T.-W. Wang, H. J. Snaith, and D. S. Ginger. "Tracking Photoexcited Carriers in Hybrid Perovskite Semiconductors: Trap-Dominated Spatial Heterogeneity and Diffusion". *ACS Nano* 11:11, 2017, p. 11488.
DOI: 10.1021/acsnano.7b06242.

96. R. Ciesielski, F. Schäfer, N. F. Hartmann, N. Giesbrecht, T. Bein, P. Docampo, and A. Hartschuh. "Grain Boundaries Act as Solid Walls for Charge Carrier Diffusion in Large Crystal MAPI Thin Films". *ACS Applied Materials & Interfaces* 10:9, 2018, p. 7974.
DOI: 10.1021/acsami.7b17938.

97. R. L. Milot, G. E. Eperon, H. J. Snaith, M. B. Johnston, and L. M. Herz. "Temperature Dependent Charge Carrier Dynamics in $CH_3NH_3PbI_3$ Perovskite Thin Films". *Advanced Functional Materials* 25:39, 2015, p. 6218.
DOI: 10.1002/adfm.201502340.

98. C. S. Ponseca, T. J. Savenije, M. Abdellah, K. Zheng, A. Yartsev, T. Pascher, T. Harlang, P. Chabera, T. Pullerits, A. Stepanov, J.-P. Wolf, and V. Sundström. "Organometal Halide Perovskite Solar Cell Materials Rationalized: Ultrafast Charge Generation, High and Microsecond-Long Balanced Mobilities, and Slow Recombination". *Journal of the American Chemical Society* 136:14, 2014, p. 5189.
DOI: 10.1021/ja412583t.

99. O. G. Reid, M. Yang, N. Kopidakis, K. Zhu, and G. Rumbles. "Grain-Size-Limited Mobility in Methylammonium Lead Iodide Perovskite Thin Films". *ACS Energy Letters* 1:3, 2016, p. 561.
DOI: 10.1021/acsenergylett.6b00288.

100. D. H. Kim, J. Park, Z. Li, M. Yang, J. Park, I. J. Park, J. Y. Kim, J. J. Berry, G. Rumbles, and K. Zhu. "300% Enhancement of Carrier Mobility in Uniaxial-Oriented Perovskite Films Formed by Topotactic-Oriented Attachment". *Advanced Materials* 29:23, 2017, p. 1606831.
DOI: 10.1002/adma.201606831.

101. Y. Chen, H. T. Yi, X. Wu, R. Haroldson, Y. N. Gartstein, Y. I. Rodionov, K. S. Tikhonov, A. Zakhidov, X. Y. Zhu, and V. Podzorov. "Extended carrier lifetimes and dif-

fusion in hybrid perovskites revealed by Hall effect and photoconductivity measurements". *Nature Communications* 7:1, 2016, p. 12253.
DOI: 10.1038/ncomms12253.

102. Q. Wang, Y. Shao, H. Xie, L. Lyu, X. Liu, Y. Gao, and J. Huang. "Qualifying composition dependent p and n self-doping in $CH_3NH_3PbI_3$". *Applied Physics Letters* 105:16, 2014, p. 163508.
DOI: 10.1063/1.4899051.

103. J. Lim, M. T. Hörantner, N. Sakai, J. M. Ball, S. Mahesh, N. K. Noel, Y.-H. Lin, J. B. Patel, D. P. McMeekin, M. B. Johnston, B. Wenger, and H. J. Snaith. "Elucidating the long-range charge carrier mobility in metal halide perovskite thin films". *Energy & Environmental Science* 12:1, 2019, p. 169.
DOI: 10.1039/C8EE03395A.

104. J. Lim, M. Kober-Czerny, Y.-H. Lin, J. M. Ball, N. Sakai, E. A. Duijnstee, M. J. Hong, J. G. Labram, B. Wenger, and H. J. Snaith. "Long-range charge carrier mobility in metal halide perovskite thin-films and single crystals via transient photo conductivity". *Nature Communications* 13:1, 2022, p. 4201.
DOI: 10.1038/s41467-022-31569-w.

105. C. La-o vorakiat, T. Salim, J. Kadro, M.-T. Khuc, R. Haselsberger, L. Cheng, H. Xia, G. G. Gurzadyan, H. Su, Y. M. Lam, R. A. Marcus, M.-E. Michel-Beyerle, and E. E. M. Chia. "Elucidating the role of disorder and free-carrier recombination kinetics in $CH_3NH_3PbI_3$ perovskite films". *Nature Communications* 6:1, 2015, p. 7903.
DOI: 10.1038/ncomms8903.

106. C. Wehrenfennig, G. E. Eperon, M. B. Johnston, H. J. Snaith, and L. M. Herz. "High Charge Carrier Mobilities and Lifetimes in Organolead Trihalide Perovskites". *Advanced Materials* 26:10, 2014, p. 1584.
DOI: 10.1002/adma.201305172.

107. J. Peng, Y. Chen, K. Zheng, T. Pullerits, and Z. Liang. "Insights into charge carrier dynamics in organo-metal halide perovskites: from neat films to solar cells". *Chemical Society Reviews* 46:19, 2017, p. 5714.
DOI: 10.1039/C6CS00942E.

108. Y. Chen, J. Peng, D. Su, X. Chen, and Z. Liang. "Efficient and Balanced Charge Transport Revealed in Planar Perovskite Solar Cells". *ACS Applied Materials & Interfaces* 7:8, 2015, p. 4471.
DOI: 10.1021/acsami.5b00077.

109. K. Miyata, T. L. Atallah, and X.-Y. Zhu. "Lead halide perovskites: Crystal-liquid duality, phonon glass electron crystals, and large polaron formation". *Science Advances* 3:10, 2017, e1701469.
DOI: 10.1126/sciadv.1701469.

110. M. I. Saidaminov, A. L. Abdelhady, B. Murali, E. Alarousu, V. M. Burlakov, W. Peng, I. Dursun, L. Wang, Y. He, G. Maculan, A. Goriely, T. Wu, O. F. Mohammed, and O. M. Bakr. "High-quality bulk hybrid perovskite single crystals within minutes by inverse temperature crystallization". *Nature Communications* 6:1, 2015, p. 7586.
DOI: 10.1038/ncomms8586.

111. N. F. Mott and R. W. Gurney. *Electronic processes in ionic crystals*. Clarendon Press, 1948.

112. B. Chen, C.-s. Lee, S.-t. Lee, P. Webb, Y.-c. Chan, W. Gambling, H. Tian, and W. Zhu. "Improved Time-of-Flight Technique for Measuring Carrier Mobility in Thin Films of Organic Electroluminescent Materials". *Japanese Journal of Applied Physics* 39:3R, 2000, p. 1190.
DOI: 10.1143/JJAP.39.1190.

113. G. Juška, N. Nekrašas, V. Valentinavičius, P. Meredith, and A. Pivrikas. "Extraction of photogenerated charge carriers by linearly increasing voltage in the case of Langevin recombination". *Physical Review B* 84:15, 2011, p. 155202.
DOI: 10.1103/PhysRevB.84.155202.

114. L. M. Herz. "Charge-Carrier Mobilities in Metal Halide Perovskites: Fundamental Mechanisms and Limits". *ACS Energy Letters* 2:7, 2017, p. 1539.
DOI: 10.1021/acsenergylett.7b00276.

115. S. Sze and K. K. Ng. *Physics of Semiconductor Devices: Sze/Physics*. John Wiley & Sons, Inc., Hoboken, NJ, USA, 2006.
DOI: 10.1002/0470068329.

116. H. Fröhlich. "Electrons in lattice fields". *Advances in Physics* 3:11, 1954, p. 325.
DOI: 10.1080/00018735400101213.

117. Z.-G. Yu. "Oscillatory Magnetic Circular Dichroism of Free-Carrier Absorption and Determination of the Rashba Dispersions in Hybrid Organic Inorganic Perovskites". *The Journal of Physical Chemistry Letters* 9:1, 2018, p. 1.
DOI: 10.1021/acs.jpclett.7b02902.

118. A. D. Wright, C. Verdi, R. L. Milot, G. E. Eperon, M. A. Pérez-Osorio, H. J. Snaith, F. Giustino, M. B. Johnston, and L. M. Herz. "Electron phonon coupling in hybrid lead halide perovskites". *Nature Communications* 7:1, 2016, p. 11755.
DOI: 10.1038/ncomms11755.

119. H. Diab, G. Trippé-Allard, F. Lédée, K. Jemli, C. Vilar, G. Bouchez, V. L. Jacques, A. Tejeda, J. Even, J.-S. Lauret, E. Deleporte, and D. Garrot. "Narrow Linewidth Excitonic Emission in Organic Inorganic Lead Iodide Perovskite Single Crystals". *The Journal of Physical Chemistry Letters* 7:24, 2016, p. 5093.
DOI: 10.1021/acs.jpclett.6b02261.

120. J. L. T. Waugh and G. Dolling. "Crystal Dynamics of Gallium Arsenide". *Physical Review* 132:6, 1963, p. 2410.
DOI: 10.1103/PhysRev.132.2410.

121. M. Sendner, P. K. Nayak, D. A. Egger, S. Beck, C. Müller, B. Epding, W. Kowalsky, L. Kronik, H. J. Snaith, A. Pucci, and R. Lovrinčić. "Optical phonons in methylammonium lead halide perovskites and implications for charge transport". *Materials Horizons* 3:6, 2016, p. 613.
DOI: 10.1039/C6MH00275G.

122. S. Draguta, S. Thakur, Y. V. Morozov, Y. Wang, J. S. Manser, P. V. Kamat, and M. Kuno. "Spatially Non-uniform Trap State Densities in Solution Processed Hybrid Perovskite Thin Films". *The Journal of Physical Chemistry Letters* 7:4, 2016, p. 715.
DOI: 10.1021/acs.jpclett.5b02888.

123. S. D. Stranks, V. M. Burlakov, T. Leijtens, J. M. Ball, A. Goriely, and H. J. Snaith. "Recombination Kinetics in Organic-Inorganic Perovskites: Excitons, Free Charge, and Subgap States". *Physical Review Applied* 2:3, 2014, p. 034007.
DOI: 10.1103/PhysRevApplied.2.034007.

124. D. P. McMeekin, G. Sadoughi, W. Rehman, G. E. Eperon, M. Saliba, M. T. Hörantner, A. Haghighirad, N. Sakai, L. Korte, B. Rech, M. B. Johnston, L. M. Herz, and

H. J. Snaith. "A mixed-cation lead mixed-halide perovskite absorber for tandem solar cells". *Science* 351:6269, 2016, p. 151.
DOI: 10.1126/science.aad5845.

125. N. K. Noel, S. D. Stranks, A. Abate, C. Wehrenfennig, S. Guarnera, A.-A. Haghighirad, A. Sadhanala, G. E. Eperon, S. K. Pathak, M. B. Johnston, A. Petrozza, L. M. Herz, and H. J. Snaith. "Lead-free organic–inorganic tin halide perovskites for photovoltaic applications". *Energy Environ. Sci.* 7:9, 2014, p. 3061.
DOI: 10.1039/C4EE01076K.

126. R. J. Nelson and R. G. Sobers. "Minority-carrier lifetimes and internal quantum efficiency of surface-free GaAs". *Journal of Applied Physics* 49:12, 1978, p. 6103.
DOI: 10.1063/1.324530.

127. P Langevin. "Sur la loi de recombination des ions". *Ann. Chim. Phys* 28, 1903, p. 433.

128. M. B. Johnston and L. M. Herz. "Hybrid Perovskites for Photovoltaics: Charge Carrier Recombination, Diffusion, and Radiative Efficiencies". *Accounts of Chemical Research* 49:1, 2016, p. 146.
DOI: 10.1021/acs.accounts.5b00411.

129. J.-C. Blancon, W. Nie, A. J. Neukirch, G. Gupta, S. Tretiak, L. Cognet, A. D. Mohite, and J. J. Crochet. "The Effects of Electronic Impurities and Electron-Hole Recombination Dynamics on Large-Grain Organic-Inorganic Perovskite Photovoltaic Efficiencies". *Advanced Functional Materials* 26:24, 2016, p. 4283.
DOI: 10.1002/adfm.201505324.

130. M. M. Ali, K. Minami, K. Ogura, T. Hosokawa, H. Kazama, T. Ozawa, T. Watanabe, Y. Carmel, V. L. Granatstein, W. W. Destler, R. A. Kehs, W. R. Lou, and D. Abe. "Absolute instability for enhanced radiation from a high-power plasma-filled backward-wave oscillator". *Physical Review Letters* 65:7, 1990, p. 855.
DOI: 10.1103/PhysRevLett.65.855.

131. B. Wu, H. T. Nguyen, Z. Ku, G. Han, D. Giovanni, N. Mathews, H. J. Fan, and T. C. Sum. "Discerning the Surface and Bulk Recombination Kinetics of Organic-Inorganic Halide Perovskite Single Crystals". *Advanced Energy Materials* 6:14, 2016, p. 1600551.
DOI: 10.1002/aenm.201600551.

132. Y. Yang, M. Yang, D. Moore, Y. Yan, E. Miller, K. Zhu, and M. Beard. "Top and bottom surfaces limit carrier lifetime in lead iodide perovskite films". *Nature Energy* 2:2, 2017, p. 16207.
DOI: 10.1038/nenergy.2016.207.

133. E. L. Unger, E. T. Hoke, C. D. Bailie, W. H. Nguyen, A. R. Bowring, T. Heumüller, M. G. Christoforo, and M. D. McGehee. "Hysteresis and transient behavior in current–voltage measurements of hybrid-perovskite absorber solar cells". *Energy Environ. Sci.* 7:11, 2014, p. 3690.
DOI: 10.1039/C4EE02465F.

134. Y. Yuan, J. Chae, Y. Shao, Q. Wang, Z. Xiao, A. Centrone, and J. Huang. "Photovoltaic Switching Mechanism in Lateral Structure Hybrid Perovskite Solar Cells". *Advanced Energy Materials* 5:15, 2015, p. 1500615.
DOI: 10.1002/aenm.201500615.

135. E. J. Juarez-Perez, R. S. Sanchez, L. Badia, G. Garcia-Belmonte, Y. S. Kang, I. Mora-Sero, and J. Bisquert. "Photoinduced Giant Dielectric Constant in Lead Halide Perovskite Solar Cells". *The Journal of Physical Chemistry Letters* 5:13, 2014, p. 2390.
DOI: 10.1021/jz5011169.

136. D. A. Egger, L. Kronik, and A. M. Rappe. "Theory of Hydrogen Migration in Organic-Inorganic Halide Perovskites". *Angewandte Chemie International Edition* 54:42, 2015, p. 12437.
DOI: 10.1002/anie.201502544.

137. C. Eames, J. M. Frost, P. R. F. Barnes, B. C. O'Regan, A. Walsh, and M. S. Islam. "Ionic transport in hybrid lead iodide perovskite solar cells". *Nature Communications* 6:1, 2015, p. 7497.
DOI: 10.1038/ncomms8497.

138. J Mizusaki, K Arai, and K Fueki. "Ionic conduction of the perovskite-type halides". *Solid State Ionics* 11:3, 1983, p. 203.
DOI: 10.1016/0167-2738(83)90025-5.

139. T.-Y. Yang, G. Gregori, N. Pellet, M. Grätzel, and J. Maier. "The Significance of Ion Conduction in a Hybrid Organic-Inorganic Lead-Iodide-Based Perovskite Photosensitizer". *Angewandte Chemie International Edition* 54:27, 2015, p. 7905.
DOI: 10.1002/anie.201500014.

140. J. M. Azpiroz, E. Mosconi, J. Bisquert, and F. De Angelis. "Defect migration in methylammonium lead iodide and its role in perovskite solar cell operation". *Energy & Environmental Science* 8:7, 2015, p. 2118.
DOI: 10.1039/C5EE01265A.

141. Y. Yuan, Q. Wang, Y. Shao, H. Lu, T. Li, A. Gruverman, and J. Huang. "Electric-Field-Driven Reversible Conversion Between Methylammonium Lead Triiodide Perovskites and Lead Iodide at Elevated Temperatures". *Advanced Energy Materials* 6:2, 2016, p. 1501803.
DOI: 10.1002/aenm.201501803.

142. Z. Xiao, Y. Yuan, Y. Shao, Q. Wang, Q. Dong, C. Bi, P. Sharma, A. Gruverman, and J. Huang. "Giant switchable photovoltaic effect in organometal trihalide perovskite devices". *Nature Materials* 14:2, 2015, p. 193.
DOI: 10.1038/nmat4150.

143. M. Saliba, T. Matsui, J.-Y. Seo, K. Domanski, J.-P. Correa-Baena, M. K. Nazeeruddin, S. M. Zakeeruddin, W. Tress, A. Abate, A. Hagfeldt, and M. Grätzel. "Cesium-containing triple cation perovskite solar cells: improved stability, reproducibility and high efficiency". *Energy & Environmental Science* 9:6, 2016, p. 1989.
DOI: 10.1039/C5EE03874J.

144. W. S. Yang, B.-W. Park, E. H. Jung, N. J. Jeon, Y. C. Kim, D. U. Lee, S. S. Shin, J. Seo, E. K. Kim, J. H. Noh, and S. I. Seok. "Iodide management in formamidinium lead halide based perovskite layers for efficient solar cells". *Science* 356:6345, 2017, p. 1376.
DOI: 10.1126/science.aan2301.

145. N. J. Jeon, H. Na, E. H. Jung, T.-Y. Yang, Y. G. Lee, G. Kim, H.-W. Shin, S. Il Seok, J. Lee, and J. Seo. "A fluorene-terminated hole-transporting material for highly efficient and stable perovskite solar cells". *Nature Energy* 3:8, 2018, p. 682.
DOI: 10.1038/s41560-018-0200-6.

146. H. Zhu, Y. Fu, F. Meng, X. Wu, Z. Gong, Q. Ding, M. V. Gustafsson, M. T. Trinh, S. Jin, and X.-Y. Zhu. "Lead halide perovskite nanowire lasers with low lasing thresholds and high quality factors". *Nature Materials* 14:6, 2015, p. 636.
DOI: 10.1038/nmat4271.

147. Z. Yang, Y. Deng, X. Zhang, S. Wang, H. Chen, S. Yang, J. Khurgin, N. X. Fang, X. Zhang, and R. Ma. "High-Performance Single-Crystalline Perovskite Thin-Film Photodetector". *Advanced Materials* 30:8, 2018, p. 1704333.
DOI: 10.1002/adma.201704333.

148. L. Protesescu, S. Yakunin, M. I. Bodnarchuk, F. Krieg, R. Caputo, C. H. Hendon, R. X. Yang, A. Walsh, and M. V. Kovalenko. "Nanocrystals of Cesium Lead Halide Perovskites ($CsPbX_3$, X = Cl, Br, and I): Novel Optoelectronic Materials Showing Bright Emission with Wide Color Gamut". *Nano Letters* 15:6, 2015, p. 3692.
DOI: 10.1021/nl5048779.

149. Z.-K. Tan, R. S. Moghaddam, M. L. Lai, P. Docampo, R. Higler, F. Deschler, M. Price, A. Sadhanala, L. M. Pazos, D. Credgington, F. Hanusch, T. Bein, H. J. Snaith, and R. H. Friend. "Bright light-emitting diodes based on organometal halide perovskite". *Nature Nanotechnology* 9:9, 2014, p. 687.
DOI: 10.1038/nnano.2014.149.

150. N. Wang, L. Cheng, R. Ge, S. Zhang, Y. Miao, W. Zou, C. Yi, Y. Sun, Y. Cao, R. Yang, Y. Wei, Q. Guo, Y. Ke, M. Yu, Y. Jin, Y. Liu, Q. Ding, D. Di, L. Yang, G. Xing, H. Tian, C. Jin, F. Gao, R. H. Friend, J. Wang, and W. Huang. "Perovskite light-emitting diodes based on solution-processed self-organized multiple quantum wells". *Nature Photonics* 10:11, 2016, p. 699.
DOI: 10.1038/nphoton.2016.185.

151. K. Lin, J. Xing, L. N. Quan, F. P. G. de Arquer, X. Gong, J. Lu, L. Xie, W. Zhao, D. Zhang, C. Yan, W. Li, X. Liu, Y. Lu, J. Kirman, E. H. Sargent, Q. Xiong, and Z. Wei. "Perovskite light-emitting diodes with external quantum efficiency exceeding 20 per cent". *Nature* 562:7726, 2018, p. 245.
DOI: 10.1038/s41586-018-0575-3.

152. Y. Cao, N. Wang, H. Tian, J. Guo, Y. Wei, H. Chen, Y. Miao, W. Zou, K. Pan, Y. He, H. Cao, Y. Ke, M. Xu, Y. Wang, M. Yang, K. Du, Z. Fu, D. Kong, D. Dai, Y. Jin, G. Li, H. Li, Q. Peng, J. Wang, and W. Huang. "Perovskite light-emitting diodes based on spontaneously formed submicrometre-scale structures
". *Nature* 562:7726, 2018, p. 249.
DOI: 10.1038/s41586-018-0576-2.

153. J. Li, X. Shan, S. G. R. Bade, T. Geske, Q. Jiang, X. Yang, and Z. Yu. "Single-Layer Halide Perovskite Light-Emitting Diodes with Sub-Band Gap Turn-On Voltage and High Brightness". *The Journal of Physical Chemistry Letters* 7:20, 2016, p. 4059. DOI: 10.1021/acs.jpclett.6b01942.

154. H. Deng, X. Yang, D. Dong, B. Li, D. Yang, S. Yuan, K. Qiao, Y.-B. Cheng, J. Tang, and H. Song. "Flexible and Semitransparent Organolead Triiodide Perovskite Network Photodetector Arrays with High Stability". *Nano Letters* 15:12, 2015, p. 7963. DOI: 10.1021/acs.nanolett.5b03061.

155. W. Hu, W. Huang, S. Yang, X. Wang, Z. Jiang, X. Zhu, H. Zhou, H. Liu, Q. Zhang, X. Zhuang, J. Yang, D. H. Kim, and A. Pan. "High-Performance Flexible Photodetectors based on High-Quality Perovskite Thin Films by a Vapor-Solution Method". *Advanced Materials* 29:43, 2017, p. 1703256. DOI: 10.1002/adma.201703256.

156. X. Zhang, S. Yang, H. Zhou, J. Liang, H. Liu, H. Xia, X. Zhu, Y. Jiang, Q. Zhang, W. Hu, X. Zhuang, H. Liu, W. Hu, X. Wang, and A. Pan. "Perovskite-Erbium Silicate Nanosheet Hybrid Waveguide Photodetectors at the Near-Infrared Telecommunication Band". *Advanced Materials* 29:21, 2017, p. 1604431. DOI: 10.1002/adma.201604431.

157. E. Yablonovitch, O. D. Miller, and S. R. Kurtz. "A great solar cell also needs to be a great LED: External fluorescence leads to new efficiency record". In: Orenas Castle, Sweden, 2013, p. 9. DOI: 10.1063/1.4794698.

158. W. Tress, N. Marinova, O. Inganäs, M. K. Nazeeruddin, S. M. Zakeeruddin, and M. Graetzel. "Predicting the Open-Circuit Voltage of $CH_3NH_3PbI_3$ Perovskite Solar Cells Using Electroluminescence and Photovoltaic Quantum Efficiency Spectra: the Role of Radiative and Non-Radiative Recombination". *Advanced Energy Materials* 5:3, 2015, p. 1400812. DOI: 10.1002/aenm.201400812.

159. D. Bi, W. Tress, M. I. Dar, P. Gao, J. Luo, C. Renevier, K. Schenk, A. Abate, F. Giordano, J.-P. Correa Baena, J.-D. Decoppet, S. M. Zakeeruddin, M. K. Nazeeruddin, M. Grätzel, and A. Hagfeldt. "Efficient luminescent solar cells based on tailored mixed-cation perovskites". *Science Advances* 2:1, 2016, e1501170. DOI: 10.1126/sciadv.1501170.

160. Z. Hameiri, A. Mahboubi Soufiani, M. K. Juhl, L. Jiang, F. Huang, Y.-B. Cheng, H. Kampwerth, J. W. Weber, M. A. Green, and T. Trupke. "Photoluminescence and electroluminescence imaging of perovskite solar cells: PL and EL imaging of perovskite". *Progress in Photovoltaics: Research and Applications* 23:12, 2015, p. 1697. DOI: 10.1002/pip.2716.

161. P. Lopez-Varo, J. A. Jiménez-Tejada, M. García-Rosell, S. Ravishankar, G. Garcia-Bel-monte, J. Bisquert, and O. Almora. "Device Physics of Hybrid Perovskite Solar cells: Theory and Experiment". *Advanced Energy Materials* 8:14, 2018, p. 1702772. DOI: 10.1002/aenm.201702772.

162. C. Murawski, K. Leo, and M. C. Gather. "Efficiency Roll-Off in Organic Light-Emitting Diodes". *Advanced Materials* 25:47, 2013, p. 6801. DOI: 10.1002/adma.201301603.

163. M. Yang, N. Wang, S. Zhang, W. Zou, Y. He, Y. Wei, M. Xu, J. Wang, and W. Huang. "Reduced Efficiency Roll-Off and Enhanced Stability in Perovskite Light-Emitting Diodes with Multiple Quantum Wells". *The Journal of Physical Chemistry Letters* 9:8, 2018, p. 2038. DOI: 10.1021/acs.jpclett.8b00600.

164. W. Zou, R. Li, S. Zhang, Y. Liu, N. Wang, Y. Cao, Y. Miao, M. Xu, Q. Guo, D. Di, L. Zhang, C. Yi, F. Gao, R. H. Friend, J. Wang, and W. Huang. "Minimising efficiency roll-off in high-brightness perovskite light-emitting diodes". *Nature Communications* 9:1, 2018, p. 608. DOI: \\10.1038/s41467-018-03049-7.

165. H. Kim, L. Zhao, J. S. Price, A. J. Grede, K. Roh, A. N. Brigeman, M. Lopez, B. P. Rand, and N. C. Giebink. "Hybrid perovskite light emitting diodes under intense electrical excitation". *Nature Communications* 9:1, 2018, p. 4893. DOI: 10.1038/s41467-018-07383-8.

166. P. Tyagi, R. Srivastava, L. I. Giri, S. Tuli, and C. Lee. "Degradation of organic light emitting diode: Heat related issues and solutions". *Synthetic Metals* 216, 2016, p. 40. DOI: 10.1016/j.synthmet.2015.10.016.

167. X. Dai, Z. Zhang, Y. Jin, Y. Niu, H. Cao, X. Liang, L. Chen, J. Wang, and X. Peng. "Solution processed, high performance light emitting diodes based on quantum dots". *Nature* 515:7525, 2014, p. 96.
DOI: 10.1038/nature13829.

168. M.-H. Kim, M. F. Schubert, Q. Dai, J. K. Kim, E. F. Schubert, J. Piprek, and Y. Park. "Origin of efficiency droop in GaN-based light-emitting diodes". *Applied Physics Letters* 91:18, 2007, p. 183507.
DOI: 10.1063/1.2800290.

169. H. Wang, Z. Chen, J. Hu, H. Yu, C. Kuang, J. Qin, X. Liu, Y. Lu, M. Fahlman, L. Hou, X. Liu, and F. Gao. "Dynamic Redistribution of Mobile Ions in Perovskite Light-Emitting Diodes". *Advanced Functional Materials* 31:8, 2021, p. 2007596.
DOI: 10.1002/adfm.202007596.

170. L. Zhao, J. Gao, Y. L. Lin, Y.-W. Yeh, K. M. Lee, N. Yao, Y.-L. Loo, and B. P. Rand. "Electrical Stress Influences the Efficiency of $CH_3NH_3PbI_3$ Perovskite Light Emitting Devices". *Advanced Materials* 29:24, 2017, p. 1605317.
DOI: 10.1002/adma.201605317.

171. R. Gegevičius, M. Franckevičius, J. Chmeliov, W. Tress, and V. Gulbinas. "Electroluminescence Dynamics in Perovskite Solar Cells Reveals Giant Overshoot Effect". *The Journal of Physical Chemistry Letters* 10:8, 2019, p. 1779.
DOI: 10.1021/acs.jpclett.9b00618.

172. H. J. Snaith, A. Abate, J. M. Ball, G. E. Eperon, T. Leijtens, N. K. Noel, S. D. Stranks, J. T.-W. Wang, K. Wojciechowski, and W. Zhang. "Anomalous Hysteresis in Perovskite Solar Cells". *The Journal of Physical Chemistry Letters* 5:9, 2014, p. 1511.
DOI: 10.1021/jz500113x.

173. H.-W. Chen, N. Sakai, M. Ikegami, and T. Miyasaka. "Emergence of Hysteresis and Transient Ferroelectric Response in Organo-Lead Halide Perovskite Solar Cells". *The Journal of Physical Chemistry Letters* 6:1, 2015, p. 164.
DOI: 10.1021/jz502429u.

174. W. Tress, N. Marinova, T. Moehl, S. M. Zakeeruddin, M. K. Nazeeruddin, and M. Grätzel. "Understanding the rate-dependent J–V hysteresis, slow time component, and aging in

$CH_3NH_3PbI_3$ perovskite solar cells: the role of a compensated electric field". *Energy & Environmental Science* 8:3, 2015, p. 995.
DOI: 10.1039/C4EE03664F.

175. A. Buin, P. Pietsch, J. Xu, O. Voznyy, A. H. Ip, R. Comin, and E. H. Sargent. "Materials Processing Routes to Trap-Free Halide Perovskites". *Nano Letters* 14:11, 2014, p. 6281.
DOI: 10.1021/nl502612m.

176. W.-J. Yin, T. Shi, and Y. Yan. "Unusual defect physics in $CH_3NH_3PbI_3$ perovskite solar cell absorber". *Applied Physics Letters* 104:6, 2014, p. 063903.
DOI: 10.1063/1.4864778.

177. E. Aydin, M. Bastiani, and S. Wolf. "Defect and Contact Passivation for Perovskite Solar Cells". *Advanced Materials* 31:25, 2019, p. 1900428.
DOI: 10.1002/adma.201900428.

178. Y. Shang, Y. Liao, Q. Wei, Z. Wang, B. Xiang, Y. Ke, W. Liu, and Z. Ning. "Highly stable hybrid perovskite light-emitting diodes based on Dion-Jacobson structure". *Science Advances* 5:8, 2019, eaaw8072.
DOI: 10.1126/sciadv.aaw8072.

179. J. H. Warby, B. Wenger, A. J. Ramadan, R. D. J. Oliver, H. C. Sansom, A. R. Marshall, and H. J. Snaith. "Revealing Factors Influencing the Operational Stability of Perovskite Light-Emitting Diodes". *ACS Nano* 14:7, 2020, p. 8855.
DOI: 10.1021/acsnano.0c03516.

180. K. Elkhouly, R. Gehlhaar, J. Genoe, P. Heremans, and W. Qiu. "Perovskite Light Emitting Diode Characteristics: The Effects of Electroluminescence Transient and Hysteresis". *Advanced Optical Materials* 8:23, 2020, p. 2000941.
DOI: 10.1002/adom.202000941.

181. J. Haruyama, K. Sodeyama, L. Han, and Y. Tateyama. "First-Principles Study of Ion Diffusion in Perovskite Solar Cell Sensitizers". *Journal of the American Chemical Society* 137:32, 2015, p. 10048.
DOI: 10.1021/jacs.5b03615.

182. E. Mosconi, D. Meggiolaro, H. J. Snaith, S. D. Stranks, and F. De Angelis. "Light-induced annihilation of Frenkel defects in organo-lead halide perovskites". *Energy & Environmental Science* 9:10, 2016, p. 3180.
DOI: 10.1039/C6EE01504B.

183. D. W. deQuilettes, W. Zhang, V. M. Burlakov, D. J. Graham, T. Leijtens, A. Osherov, V. Bulović, H. J. Snaith, D. S. Ginger, and S. D. Stranks. "Photo-induced halide redistribution in organic–inorganic perovskite films". *Nature Communications* 7:1, 2016, p. 11683.
DOI: 10.1038/ncomms11683.

184. C. Li, A. Guerrero, S. Huettner, and J. Bisquert. "Unravelling the role of vacancies in lead halide perovskite through electrical switching of photoluminescence". *Nature Communications* 9:1, 2018, p. 5113.
DOI: 10.1038/s41467-018-07571-6.

185. H. Jin, E. Debroye, M. Keshavarz, I. G. Scheblykin, M. B. J. Roeffaers, J. Hofkens, and J. A. Steele. "It's a trap! On the nature of localised states and charge trapping in lead halide perovskites". *Materials Horizons* 7:2, 2020, p. 397.
DOI: 10.1039/C9MH00500E.

186. Q. Dong, J. Mendes, L. Lei, D. Seyitliyev, L. Zhu, S. He, K. Gundogdu, and F. So. "Understanding the Role of Ion Migration in the Operation of Perovskite Light-Emitting Diodes by Transient Measurements". *ACS Applied Materials & Interfaces* 12:43, 2020, p. 48845.
DOI: 10.1021/acsami.0c14269.

187. K. Elkhouly, I. Goldberg, H. Boyen, A. Franquet, V. Spampinato, T. Ke, R. Gehlhaar, J. Genoe, J. Hofkens, P. Heremans, and W. Qiu. "Operationally Stable Perovskite Light Emitting Diodes with High Radiance". *Advanced Optical Materials*, 2021, p. 2100586.
DOI: 10.1002/adom.202100586.

188. T. Cheng, G. Tumen-Ulzii, D. Klotz, S. Watanabe, T. Matsushima, and C. Adachi. "Ion Migration Induced Degradation and Efficiency Roll-off in Quasi-2D Perovskite Light-Emitting Diodes". *ACS Applied Materials & Interfaces* 12:29, 2020, p. 33004.
DOI: 10.1021/acsami.0c06737.

189. Y. Guo, S. Apergi, N. Li, M. Chen, C. Yin, Z. Yuan, F. Gao, F. Xie, G. Brocks, S. Tao, and N. Zhao. "Phenylalkylammonium passivation enables perovskite light emitting diodes with record high-radiance operational lifetime: the chain length matters". *Nature Communications* 12:1, 2021, p. 644.
DOI: 10.1038/s41467-021-20970-6.

190. Y.-C. Zhao, W.-K. Zhou, X. Zhou, K.-H. Liu, D.-P. Yu, and Q. Zhao. "Quantification of light-enhanced ionic transport in lead iodide perovskite thin films and its solar cell applications". *Light: Science & Applications* 6:5, 2017, e16243.
DOI: 10.1038/lsa.2016.243.

191. Y. Deng, Z. Xiao, and J. Huang. "Light-Induced Self Poling Effect on Organometal Trihalide
Perovskite Solar Cells for Increased Device Efficiency and Stability". *Advanced Energy Materials* 5:20, 2015, p. 1500721.
DOI: 10.1002/aenm.201500721.

192. M. J. Trimpl, A. D. Wright, K. Schutt, L. R. V. Buizza, Z. Wang, M. B. Johnston, H. J. Snaith, P. Müller Buschbaum, and L. M. Herz. "Charge-Carrier Trapping and Radiative Recombination in Metal Halide Perovskite Semiconductors". *Advanced Functional Materials* 30:42, 2020, p. 2004312.
DOI: 10.1002/adfm.202004312.

193. R. Jasiūnas, R. Gegevičius, M. Franckevičius, V. Jašinskas, and V. Gulbinas. "Energy Barriers Restrict Charge Carrier Motion in MAPI Perovskite Films". *Advanced Optical Materials* 8:16, 2020, p. 2000036.
DOI: 10.1002/adom.202000036.

194. A. Devizis, K. Meerholz, D. Hertel, and V. Gulbinas. "Ultrafast charge carrier mobility dynamics in poly(spirobifluorene- c o -benzothiadiazole): Influence of temperature on initial transport". *Physical Review B* 82:15, 2010, p. 155204.
DOI: 10.1103/PhysRevB.82.155204.

195. B. Maynard, Q. Long, E. A. Schiff, M. Yang, K. Zhu, R. Kottokkaran, H. Abbas, and V. L. Dalal. "Electron and hole drift mobility measurements on methylammonium lead iodide perovskite solar cells". *Applied Physics Letters* 108:17, 2016, p. 173505.
DOI: 10.1063/1.4948344.

Notes

Vilniaus universiteto leidykla
Saulėtekio al. 9, III rūmai, LT-10222 Vilnius
El. p. info@leidykla.vu.lt, www.leidykla.vu.lt
bookshop.vu.lt, journals.vu.lt
Tiražas 40 egz.